

Mixed conducting perovskites and their solid state chemistry

Von der Naturwissenschaftlichen Fakultät
der Gottfried Wilhelm Leibniz Universität Hannover
zur Erlangung des Grades

Doktorin der Naturwissenschaften
Dr. rer. nat.

genehmigte Dissertation

von

Julia-Maria Martynczuk
(Diplom-Chemikerin)

geboren am 19.03.1981 in Hannover

2009

Referent: Prof. Dr. Jürgen Caro
Institut für Physikalische Chemie und Elektrochemie,
Leibniz Universität Hannover

Korreferent: Prof. Dr. Ludwig J. Gauckler
Departemente der Materialwissenschaft,
ETH Zürich

Tag der Promotion: 29.01.2009

Our great discovery was this:
God is Love, God is a Father!

Our heart opened up and reached out to Him
who loves us and makes of us
the very object of His love,
who even "counts the hair on our head".

Nothing happens without His consent:
happy or sad circumstances acquire a new meaning.

We cannot fear anything anymore.

We find a new hope, a new strength,
a new confidence:
we experience the Love of the One
who follows the history of mankind
as well as the small history of each one of us
with an immense Love.

All this is God's gift which makes us shout:

"We believe in Love".

from Chiara Lubich

Preface

The results of this thesis were achieved in the past three years during my work as a scientific assistant at the Institute of Physical Chemistry and Electrochemistry at the Gottfried Wilhelm Leibniz Universität Hannover under the supervision of Prof. Dr. Jürgen Caro. The financial support was granted by the Deutsche Forschungsgemeinschaft for the project FE 928 1-1/-2 under the guidance of Dr. Armin Feldhoff and Prof. Dr. Haihui Wang.

During my time as scientific assistant I contributed to 13 publications and 12 conferences with talks or (oral) posters, which are listed in the appendix. One of the posters (ICIM9, Lillehammer, Norway) was awarded as best poster in July 2006 and in June 2008 I obtained the Zonta Award for Young Scientists for excellent scientific performance and outstanding voluntary service. The following statement will point out my contributions to the particular research articles included in this thesis. The thesis comprises six selected research articles. Three of them are written by myself and in three of them I am co-author.

Foremost, I would like to acknowledge the fruitful discussions and the encouragement during the preparation of publications from my co-authors, particularly from Dr. Armin Feldhoff, Dr. Mirko Arnold and Prof. Dr. Jürgen Caro.

Two articles studying the synthetic process of $(\text{Ba}_{0.5}\text{Sr}_{0.5})(\text{Fe}_{0.8}\text{Zn}_{0.2})\text{O}_{3-\delta}$ perovskite-type oxide (BSFZ) are presented in chapter 2. The first article, *How $(\text{Ba}_{0.5}\text{Sr}_{0.5})(\text{Fe}_{0.8}\text{Zn}_{0.2})\text{O}_{3-\delta}$ and $(\text{Ba}_{0.5}\text{Sr}_{0.5})(\text{Co}_{0.8}\text{Fe}_{0.2})\text{O}_{3-\delta}$ perovskites form via an EDTA/citric acid complexing method*, was written by myself. All experimental results on BSFZ and data interpretation were done by me. I acknowledge the helpful cooperation with Dr. Armin Feldhoff on transmission electron microscopy (TEM). He introduced me to all TEM techniques and helped with any occurring problem. The contribution of Dr. Mirko Arnold was the X-ray diffraction data of $(\text{Ba}_{0.5}\text{Sr}_{0.5})(\text{Co}_{0.8}\text{Fe}_{0.2})\text{O}_{3-\delta}$ (BSCF). Additionally, I obtained support with the manuscript preparation from all co-authors.

The second article, *The sol-gel synthesis of perovskites by an EDTA/citrate complexing method involves nanoscale solid state reactions*, was written by Dr. Armin Feldhoff. I kindly acknowledge the cooperation with him on this publication. The sample preparation of sols, gels and powders, and the X-ray diffraction measurements and interpretation were done by me. Furthermore, I performed the thermodynamic experiments and calculations and I contributed to the manuscript preparation. The provision of a vacuum apparatus for the decarbonation measurements by Dr. Sebastian Hein from the Institute of Inorganic Chemistry of the Gottfried Wilhelm Leibniz Universität Hannover is appreciated.

The third chapter presents the impact of grain size and grain boundaries on the transport properties of electronic and ionic charge carriers in BSFZ and BSCF. The first article, *Influence of grain size on the oxygen permeation performance of perovskite-type $(\text{Ba}_{0.5}\text{Sr}_{0.5})(\text{Fe}_{0.8}\text{Zn}_{0.2})\text{O}_{3-\delta}$ membranes*, was written by myself and all investigations and data interpretation were done by me. I acknowledge the fruitful discussions with Dr. Mirko Arnold and Dr. Armin Feldhoff during manuscript preparation.

The elaboration of the second article in this assembly, *Grain boundaries as barrier for oxygen transport in perovskite-type membranes*, was done together with Dr. Mirko Arnold, Konstantin Efimov and Dr. Armin Feldhoff. The powder preparation, scanning electron microscopy (SEM) along with the determination of grain size distribution and the differential scanning calorimetry (DSC) were conducted by Konstantin Efimov and me in equal shares.

The following two articles presented in chapter 4 comprehend the investigation of the dependence of phase stability on valence and spin state for BSFZ and a $(\text{Ba}_{0.5}\text{Sr}_{0.5})(\text{Fe}_{1-x}\text{Al}_x)\text{O}_{3-\delta}$ perovskite system with previously unreleased composition. The first article, *Spin-state transition of iron in $(\text{Ba}_{0.5}\text{Sr}_{0.5})(\text{Fe}_{0.8}\text{Zn}_{0.2})\text{O}_{3-\delta}$ perovskite*, is the result of an efficient cooperation of many outstanding scientists. I am very glad to have contributed to the excellent in situ EELS investigations of Dr. Armin Feldhoff with sample and standards preparation and complementary investigations, which were SEM, differential thermoanalysis (DTA), thermogravimetric analysis (TGA) and (in situ) XRD. I am grateful to Prof. Dr. Harald Behrens from the Institute of Mineralogy at the Gottfried Wilhelm Leibniz Universität Hannover for putting his high pressure apparatus at my disposal and offering therefore, the possibility of the preparation of stoichiometric SrFeO_3 by filling the lattice with additional oxygen. I appreciate the possibility of cooperation with Dr. Ulrich Vogt for the measurements of the coefficient of thermal expansion with dilatometry, which were done by myself, at the Swiss Federal Laboratories for Materials Testing and Research (EMPA) in Dübendorf, Switzerland.

Within this chapter, the second article, *Aluminum doped perovskites as high performance oxygen permeation materials*, presenting a novel perovskite material with aluminum doping was written by me. The development of this material was my idea and sample preparation and TEM along with energy-dispersive X-ray spectroscopy (EDXS) were conducted by myself. I kindly acknowledge the fruitful cooperation with Dr. Mirko Arnold on the Rietveld refinements, with Prof. Dr. Vladimír Šepelák on Mössbauer spectroscopy and Dr. Armin Feldhoff on EELS and manuscript preparation. All other measurements and calculations included in the article were conducted by Fangyi Liang under my supervision.

Acknowledgments

I would like to express my grateful appreciation to all those who have contributed, directly or indirectly, to this thesis and made it a pleasure for me to work on it.

First, let me thank Prof. Dr. Jürgen Caro for the allocation of this research topic and the excellent mentoring throughout the entire thesis. He supported me in many different ways. For instance, he encouraged me to submit manuscripts to excellent journals, i.e. *Advanced Materials* or to apply for different awards. This was successful in the case of the Young Scientist Award for the best poster presentation at the 9th International Conference on Inorganic Membranes in Lillehammer, Norway in July 2006 and for the Zonta Award for Young Scientists, which I obtained due to his nomination in June 2008 for excellent scientific performance and outstanding voluntary service. I am profoundly impressed by his ability to focus on every problem or request and to solve it immediately. Moreover, I appreciate his very determined and uncomplicated manner.

Furthermore, I would like to thank Prof. Dr. Ludwig J. Gauckler from the Department of Materials of the ETH Zürich for his serious interest in my work and for the acceptance to conduct the second expertise. I am looking forward to working together with him in the future.

I am especially grateful to the supervisor of my work, Dr. Armin Feldhoff, who always offered me advice. I am deeply indebted to him for his professional support of my whole work during the past three years. I was able to benefit from his excellent knowledge regarding transmission electron microscopy in theory and application. Many helpful suggestions and critical questions simplified the elaboration of this thesis and upgraded my work. In addition, I acknowledge his promotion and understanding during my work.

I would like to express my gratitude to Dr. Mirko Arnold, Frank Steinbach, Konstantin Efimov, Oliver Czuprat, Heqing Jiang, and Fangyi Liang for their helpful input regarding my thesis and the nice atmosphere at work.

Prof. Dr. Haihui Wang provided assistance with the oxygen permeation experiments and discussions with him are kindly acknowledged.

I appreciate the possibility of cooperation with Dr. Ulrich Vogt for the measurements of the coefficient of thermal expansion at the Swiss Federal Laboratories for Materials Testing and Research (EMPA) in Dübendorf, Switzerland, where I spent two weeks in January 2008.

Prof. Dr. Vladimír Šepelák, Prof. Dr. Harald Behrens, Apl.-Prof. Dr. Claus H. Rüschler, Priv.-Doz. Dr. Thorsten M. Gesing, Dr. Sebastian Hein, Dipl.-Ing. Raphael Höver, Nina Ehlert, Falk Heinroth, and Lars Robben please accept my best thanks regarding your manifold measurements and support.

Exceptional thanks go to my colleagues Katrin Wessels and Inga Bannat, who always cheered me up enduring my moods and answered many questions during the time, we shared the "Schnucki" office. I am very happy about the nice atmosphere in the group and the many activities organized after work mainly by Frank Steinbach, Inga Bannat and Katrin Wessels. I was glad to have the possibility to organize the soft skills meeting together with Yvonne Selk and Oliver Czuprat. I want to express my sincere thanks to all other group members, especially Yvonne Gabbey-Uebe, Kerstin Janze, and Britta Seelandt. I acknowledge the great job done by the mechanical and electrical workshop consisting of Mr. Bieder, Mr. Egly, Mr. Becker, Mr. Picker, and Mr. Rogge and the computer and facility managers, Priv.-Doz. Dr. Grabow and Mr. Ribbe.

Finally, none of this would have been possible without the strong support of my friends and family, which I greatly appreciate.

Even though the list of people I would never want to miss in my life might be too long, here they are (and I hope they know what they mean to me): Laura and Andreas Krauze, Gudrun Baum, Katharina Rzeczowski, Heidi Rendelmann, Yvonne Dreimann, Alexandra and Julia Pietrzyk, Dirk von der Heide, Annemarie, Günter and Manuel Höver, Chiara Lubich and the Focolare. I remain in grateful recognition to Raphael Höver, for his continuous encouragement, understanding, and patience, especially during the demanding periods of my studies and this work.

To my parents, Stefania and Lech Martynczuk, and my sister, Alicja Krauze, who unremittingly supported me my whole life and made every effort to enable my education in both the soft and scientific skills, I owe a dept of immense gratitude. These people made this work possible.

Abstract

The presented thesis comprises six original research articles on the solid state chemistry of selected cubic perovskite-type oxides. Cobalt containing mixed conducting perovskite-type materials like $(\text{Ba}_{0.5}\text{Sr}_{0.5})(\text{Co}_{0.8}\text{Fe}_{0.2})\text{O}_{3-\delta}$ (BSCF) show exceptionally high oxygen fluxes. But serious long-term stability problems in the intermediate temperature (IT) range of 500-800 °C and a high coefficient of thermal expansion due to the flexible redox behavior of cobalt are reported. Thus, a great effort is put into the development of cobalt-free perovskite-type oxides. This thesis presents results concerning two novel promising cobalt-free perovskite materials containing iron, zinc or aluminum with the stoichiometries $(\text{Ba}_{0.5}\text{Sr}_{0.5})(\text{Fe}_{0.8}\text{Zn}_{0.2})\text{O}_{3-\delta}$ (BSFZ) and $(\text{Ba}_{0.5}\text{Sr}_{0.5})(\text{Fe}_{1-x}\text{Al}_x)\text{O}_{3-\delta}$ (BSFA). For an accurate atomic level understanding of the solid state chemistry integrative investigations, like oxygen permeation or X-ray diffraction, were combined throughout the whole thesis with microscopic studies derived from analytical electron microscopy.

The sol gel-based synthesis of the BSFZ perovskite-type oxide is presented in chapter 2 and compared to the first formation steps of BSCF. The nanometer-scale solid state reaction between the finely dispersed crystalline intermediates was examined. They were identified as mixed carbonate and mixed spinel reacting over a stuffed tridymite structure, a spinel, and ZnO to the final BSFZ perovskite-oxide. The profound knowledge of the perovskite formation process opens new ways to engage the microstructure of the underlying ceramic material. For example in the way, that the common calcination temperature for BSFZ can be decreased by 200 °C avoiding presintering.

Chapter 3 considers the transport properties of electronic and ionic charge carriers in BSFZ and BSCF in dependence of the ceramic's microstructure. The grain size distribution in the green compacts can be controlled by variation of calcination temperature in powder synthesis, and in the sintered membranes during ceramic production by variation of sintering time or using liquid phase sintering with BN as sintering aid. Grain boundaries in the membranes were found to be atomically thin and no amorphous or interfacial phase occurred. The oxygen permeation flux was lowered proportionally to the abatement of the average grain size. Larger grains in the sintered ceramic and a homogeneous grain size distribution are favorable for the oxygen permeation. Grain boundaries were identified as barriers for the bulk diffusion and thus for the oxygen permeation. BSFZ and BSCF are high mobility materials, but the transport rate of the oxygen permeation is limited predominantly by bulk diffusion.

The dependence of phase stability on valence and spin state for BSFZ and BSFA are investigated in chapter 4. An excellent phase stability demands a tailoring which enables pure high-spin states of the polyvalent ions, even if mixed valence states are present. A combination of in situ electron energy-loss and Mössbauer spectroscopy disclosed the redox behavior of iron in BSFZ during heating. A partial reduction of iron from a mixed valence state of Fe^{4+} (high-spin) and Fe^{3+} (low-spin) at room temperature to Fe^{3+} (high-spin) during heating was revealed. The gradual transition of the valence and spin state takes place at around 500 °C and thus, BSFZ is a highly attractive ceramic for IT applications. In BSFA the iron species are both in high-spin state already at room temperature. $(\text{Ba}_{0.5}\text{Sr}_{0.5})(\text{Fe}_{0.9}\text{Al}_{0.1})\text{O}_{3-\delta}$ shows the highest oxygen flux for all so far published iron and aluminum containing perovskites. This new composition with a less flexible redox behavior and a stable high-spin configuration of iron is expected to show outstanding performance for the IT range.

Keywords: Perovskite - Microstructure - Electron Microscopy

Zusammenfassung

Die vorliegende Arbeit beinhaltet sechs Forschungsarbeiten zur Festkörperchemie ausgewählter kubischer perowskitartiger Oxide. Kobalthaltige gemischtleitende Oxidkeramiken wie $(\text{Ba}_{0.5}\text{Sr}_{0.5})(\text{Co}_{0.8}\text{Fe}_{0.2})\text{O}_{3-\delta}$ (BSCF) weisen zwar hohe Sauerstoffflüsse auf, doch bei Untersuchungen der Langzeitstabilität zeigen sich Probleme im mittleren Temperaturbereich von 500-800 °C und der thermische Ausdehnungskoeffizient ist wegen des flexiblen Redoxverhaltens des Kobalts sehr hoch. Deshalb wird zur Zeit mit großem Aufwand an der Entwicklung neuer kobaltfreier Materialien gearbeitet. Diese Arbeit stellt Ergebnisse zu zwei neuen viel versprechenden eisen-, zink- oder aluminiumhaltigen Oxiden mit den Stöchiometrien $(\text{Ba}_{0.5}\text{Sr}_{0.5})(\text{Fe}_{0.8}\text{Zn}_{0.2})\text{O}_{3-\delta}$ (BSFZ) und $(\text{Ba}_{0.5}\text{Sr}_{0.5})(\text{Fe}_{1-x}\text{Al}_x)\text{O}_{3-\delta}$ (BSFA) vor. Für ein Verständnis bis zur atomaren Ebene wurden integrative und mikroskopische Untersuchungsmethoden kombiniert.

Die Sol-Gel basierte Synthese des BSFZ-Perowskiten wird in Kapitel 2 erläutert und mit der von BSCF verglichen. Die Festkörperreaktion zwischen den feinverteilten kristallinen Intermediaten wurde bis zur Nanometerebene untersucht. Die Intermediate wurden als gemischtes Karbonat und gemischter Spinell identifiziert, die über einen gestopften Tridymit, einen weiteren Spinell und Zinkoxid zum BSFZ reagieren. Das Wissen um die Perowskitbildung eröffnet neue Wege, um in die Mikrostruktur der späteren Keramik einzugreifen. Zum Beispiel konnte die Kalzinationstemperatur um 200 °C herabgesetzt werden, um das Vorsintern zu verhindern.

Kapitel 3 handelt von den Transporteigenschaften der elektronischen und ionischen Ladungsträger im BSFZ und BSCF in Abhängigkeit von der Mikrostruktur. Die Steuerung der Korngrößenverteilung im Grünkörper wird ermöglicht durch die Variation der Kalzinationstemperatur und in den gesinterten Membranen durch die Variation der Sinterzeit oder durch die Nutzung von Flüssigphasensintern mit Bornitrid als Sinteradditiv. Korngrenzen innerhalb der Membran sind atomar dünn und es treten keine amorphen Grenzflächenphasen auf. Der Sauerstofffluss nimmt proportional mit der Verkleinerung der Korngrößen ab. Große Körner in der gesinterten Keramik und eine homogene Korngrößenverteilung sind also vorteilhaft für die Sauerstoffpermeation. BSFZ und BSCF sind Materialien mit großer Sauerstoffmobilität, wobei der Sauerstofftransport bei den hier verwendeten Membrandicken hauptsächlich durch Diffusion limitiert ist.

Die Abhängigkeit der Phasenstabilität von der Valenz und dem Spinzustand für BSFZ und BSFA werden in Kapitel 4 untersucht. Eine exzellente Phasenstabilität wird nur erreicht, wenn auch bei gemischten Valenzen der reine High-Spin-Zustand der polyvalenten Ionen möglich ist. Die Kombination von In-situ-Elektronen-Energieverlust- und Mössbauerspektroskopie offenbaren das Redoxverhalten des Eisens in BSFZ beim Erhitzen. Die partielle Reduktion des Eisens von einem gemischten Fe^{4+} (high-spin)- und Fe^{3+} (low-spin)- Valenzzustand bei Raumtemperatur zu Fe^{3+} (high-spin) beim Erhitzen wurde festgestellt. Der graduelle Übergang des Valenz- und Spinzustandes findet bei etwa 500 °C statt und macht BSFZ damit zu einem hoch attraktiven Material für die Anwendung im mittleren Temperaturbereich. Im BSFA liegen die Eisenspezies bereits bei Raumtemperatur beide im High-Spin-Zustand vor. BSFA zeigt die höchsten Sauerstoffflüsse von allen bisher veröffentlichten eisen- und aluminiumhaltigen Perowskiten. Von dieser neuen Zusammensetzung mit weniger flexiblem Redoxverhalten und stabiler High-Spin-Konfiguration des Eisens wird eine außergewöhnliche Leistungsfähigkeit im mittleren Temperaturbereich erwartet.

Schlagwörter: Perowskit - Mikrostruktur - Elektronenmikroskopie

Contents

1	Guidelines	1
1.1	Perovskite-type oxides	1
1.1.1	Introduction to the topic	1
1.1.2	Perovskite structure and tolerance factor	4
1.2	Synthetic process and membrane preparation	7
1.2.1	Powders	7
1.2.2	Membranes	10
1.3	Oxygen permeation	12
1.3.1	Mixed ionic and electronic conductors	12
1.3.2	Oxygen permeation experiments	14
1.3.3	Effect of the microstructure	15
	Bibliography	17
2	Sol-gel based synthetic processes	23
2.1	Summary	23
2.2	How $(\text{Ba}_{0.5}\text{Sr}_{0.5})(\text{Fe}_{0.8}\text{Zn}_{0.2})\text{O}_{3-\delta}$ and $(\text{Ba}_{0.5}\text{Sr}_{0.5})(\text{Co}_{0.8}\text{Fe}_{0.2})\text{O}_{3-\delta}$ perovskites form via an EDTA/citric acid complexing method	24
2.3	The sol-gel synthesis of perovskites by an EDTA/citrate complexing method involves nanoscale solid state reactions	30
3	Grain size and grain boundaries	45
3.1	Summary	45
3.2	Influence of grain size on the oxygen permeation performance of perovskite-type $(\text{Ba}_{0.5}\text{Sr}_{0.5})(\text{Fe}_{0.8}\text{Zn}_{0.2})\text{O}_{3-\delta}$ membranes	46
3.3	Grain boundaries as barrier for oxygen transport in perovskite-type membranes	56
4	Valence and spin state	65
4.1	Summary	65
4.2	Spin-state transition of iron in $(\text{Ba}_{0.5}\text{Sr}_{0.5})(\text{Fe}_{0.8}\text{Zn}_{0.2})\text{O}_{3-\delta}$ perovskite	66
4.3	Aluminum doped perovskites as high performance oxygen permeation materials	82
	Publications and Conferences	I
	List of Figures	V
	Curriculum vitae	VII
	Erklärung zur Dissertation	IX

Chapter 1

Guidelines

1.1 Perovskite-type oxides

1.1.1 Introduction to the topic

In November 2008 the International Energy Agency released the actual World Energy Outlook 2008 [1,2] and declared that current energy trends are patently unsustainable: socially, environmentally and economically. Oil will remain the leading energy source, but the era of cheap oil is over. Oilfield decline is the key determinant of investment needs, because the oil and gas industry is undergoing lasting structural change, with national companies in the ascendancy (80% of production in 2030). It is also now well established that global warming, due to effluent gases emission and CO₂ in particular, is happening. To avoid abrupt and irreversible climate change we need a major decarbonisation of the world's energy system. Limiting temperature rise to 2 °C will require significant emission reductions in all regions and technological breakthroughs. The global warming situation is worsened by the continuously increasing power generation, since the world population keeps increasing at 1.2-2% per year [1–3].

These observations demonstrate that interest will rapidly increase regarding energy related environment concerns (Fig.1.1) and that energy is one of the main factors that must be considered in discussions of sustainable development. In response to the critical need for a cleaner energy technology, some potential solutions have evolved including energy conservation through improved energy efficiency, a reduction in the fossil fuels and an increase in the supply of environmentally friendly energy forms. This is leading to the use of renewable sources (water, sun, wind, biomass, geothermal, hydrogen) as well as technologies and an alternative to standard sources of energy: the fuel cells. A fuel cell is an energy conversion device that generates electricity and heat by electrochemically combining fuel (hydrogen) and oxidant gases (oxygen from the air) through electrodes and across an ion conducting electrolyte. The principal characteristic of a fuel cell is its ability to convert chemical energy directly into electrical energy giving much higher conversion efficiencies than any conventional thermo-mechanical system. The electrical efficiencies of fuel cells are superior to that of heat engines and the overall efficiency in the case of cogeneration of heat and electricity reaches 80% and higher for solid-oxide fuel cells (SOFCs) [4]. Thus, fuel cells are extracting more electricity from the same amount of fuel and operate in the case of hydrogen as fuel without combustion, so they are virtually pollution free. The emission of fuel cells running on hydrogen derived from a renewable source will be nothing but water va-

por. The fuel cell does not run down or require any recharging, unlike a battery it will produce energy as long as fuel is supplied. Fuel cells are presently under development for a variety of power generation applications.

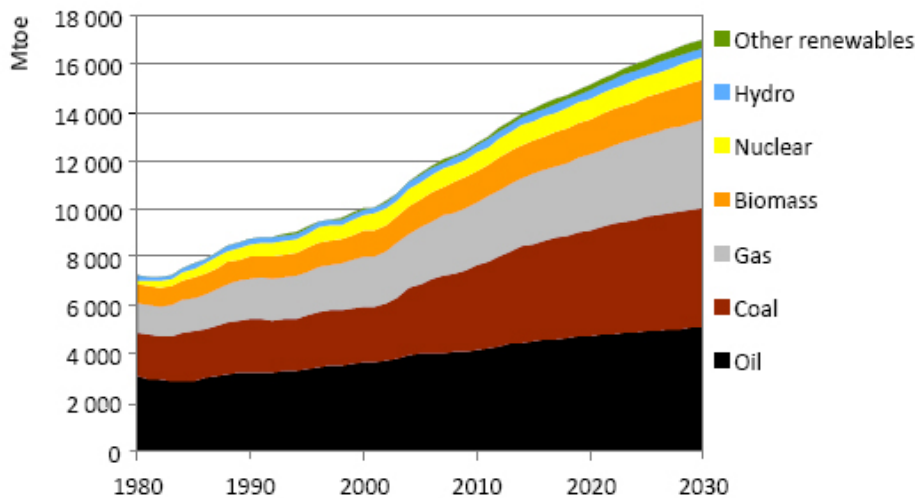


Figure 1.1: World energy demand (in Mtoe: Million tonnes of oil equivalent) expands by 45% between now and 2030 with an average rate of increase of 1.6% per year [1].

In 1839 Sir William Grove, a British lawyer and physicist, created the first fuel cell type based on reversing the electrolysis of water [5]. Ceramic fuel cells came much later and began with Nernst's discovery of solid oxide electrolytes in 1899 [6] and the operation of the first ceramic fuel cell at 1000 °C by Baur and Preis in 1937 [7]. Today, fuel cells are common in spaceflight, transportation and make sense for use as home power generation, large power generation and even as portable power for battery replacement [8]. They are sorted by their operating temperature and their classification is generally done according to the nature of the electrolyte used. In solid-oxide fuel cells the electrolyte consists of an oxygen ion conducting ceramic like yttria-stabilized zirconia (YSZ) and they are operated in a wide temperature range (500-1000 °C). The currently most widespread and investigated anode material for the use with hydrogen as fuel is a nickel/YSZ cermet. The state-of-the-art cathodes are $(La_xSr_{1-x})MnO_{3-\delta}$ for SOFCs operating at high temperature i.e. 800-1000 °C, or mixed conducting $(La_xSr_{1-x})(Co_yFe_{1-y})O_{3-\delta}$ for intermediate temperature operation, i.e. 500-800 °C. Among the variety of alternative materials, $(Sm_xSr_{1-x})CoO_{3-\delta}$ and $(Ba_xSr_{1-x})(Co_yFe_{1-y})O_{3-\delta}$ are perovskites that show very good oxygen reduction properties [9]. Perovskites are not only employed as cathode, but also as electrolyte or anode materials and even full ceramic intermediate-temperature solid-oxide fuel cells (IT-SOFCs) are possible [10–14].

In addition to the application in SOFCs ceramic membranes based on mixed ionic-electronic conductors (MIECs) with perovskite structure are used in many other industrial processes, where the supply or removal of oxygen to or from reaction mixtures with high selectivity and oxygen fluxes is needed. The separation of oxygen from air by ceramic membranes is a key technology. Perovskite-type oxides of the composition ABO_3 can host many different cations on the A- and B-sites that allow tuning conductivities from almost pure electronic to almost pure ionic (Figure 1.2, a detailed description of the structure will be provided in section 1.1.2). Thus, numerous

applications of MIECs with different elemental compositions have already been reported, e.g. separation of oxygen from air, partial oxidation of carbon hydrides and oxygen-enrichment in air [15–18]. Furthermore, perovskite materials offer in addition to oxygen separation membranes even a wider range of application in many different fields, which are listed in Chapter 2.2. Therefore, they have attracted much interest in the last two decades, and it is likely that perovskite-type membranes will find their way into the chemical process technology in the near future [15, 19].

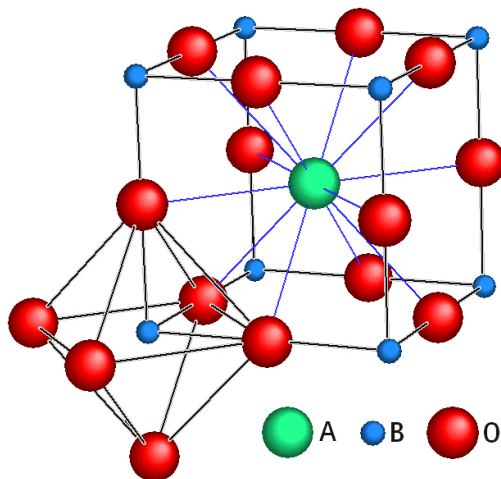


Figure 1.2: Structure of perovskite-type oxide.

In the large field of perovskite materials, some materials have stood out due to their exceptionally high oxygen fluxes and excellent phase stability. One of the highest oxygen permeation fluxes reported so far for a perovskite membrane exhibits the $(\text{Ba}_{0.5}\text{Sr}_{0.5})(\text{Co}_{0.8}\text{Fe}_{0.2})\text{O}_{3-\delta}$ perovskite-type oxide (BSCF), which is under intense investigation [10, 20–25]. But recently, serious stability problems for long-term periods with cobalt containing materials in the IT range below 900 °C due to the spin-state transition of the cobalt are discussed in the literature [26, 27]. Therefore, a great effort is put into the search for alternative materials and the development of cobalt-free perovskite-type oxides. This thesis presents results concerning two novel promising cobalt-free perovskite materials of $\text{A}^{II}\text{B}^{II/III/IV}\text{O}_{3-\delta}$ -type containing iron, zinc or aluminum with the stoichiometries $(\text{Ba}_{0.5}\text{Sr}_{0.5})(\text{Fe}_{0.8}\text{Zn}_{0.2})\text{O}_{3-\delta}$ (BSFZ) and $(\text{Ba}_{0.5}\text{Sr}_{0.5})(\text{Fe}_{1-x}\text{Al}_x)\text{O}_{3-\delta}$ (BSFA). Doping of the B-site of the perovskite structure with a metal with fixed valence state like the divalent zinc or trivalent aluminum leads to the diminution of non-stoichiometric oxygen variations and a more stable redox behavior of the material. The lattice expansion caused by the variation of temperature or chemical oxygen potential is reduced, but the oxygen permeability due to higher ionic conductivity improves. The BSFZ perovskite-type material was recently developed in our group to present an alternative to BSCF [28]. It showed high oxygen permeation fluxes ($2.55 \text{ mL min}^{-1} \text{ cm}^{-2}$ in the partial catalytic oxidation of methane to syngas (POM) for 1.25 mm thick membrane disks) and an excellent phase stability under low oxygen partial pressures ($p\text{O}_2 \leq 1 \times 10^{-8} \text{ Pa}$ in a 2% H_2 -Ar atmosphere). Furthermore, Wei et al. demonstrated the use of BSFZ as a cathode material in an IT-SOFC at 500–650 °C at power densities of up to 180 mW cm^{-2} and quantified the polarization resistances of symmetrical BSZF cathodes in air to be $0.23 \Omega \text{ cm}^2$, $0.48 \Omega \text{ cm}^2$, and $1.06 \Omega \text{ cm}^2$ at 700 °C, 650 °C, and 600 °C, respectively [29, 30].

Extensive research on BSFZ was conducted and the results are presented in the following chapters. In chapter 2 and 3 BSFZ was investigated in comparison to BSCF with regard to the synthetic process as well as to the influence of grain size distribution and grain boundaries on the oxygen permeation performance. Chapter 4 presents the characterization of the novel BSFA material and the findings concerning the spin states of iron in BSFZ and BSFA. These studies were aimed at the correlation of general and broad results obtained for the whole sample e.g. X-ray diffraction or oxygen permeation measurements with microscopic findings e.g. with transmission or scanning electron microscopy.

1.1.2 Perovskite structure and tolerance factor

To achieve a high oxygen permeation performance of ceramic materials perovskite-type oxides of the composition ABO_3 are often chosen. The flexibility of perovskites in accommodating a broad range of atomic substitutions on both A- and B-sites, provides a substantial opportunity for probing correlations between structure, bulk chemistry, and properties. The A- or B-sites can contain mixtures of two or more different atoms, what provides the control of the positional ordering of the cations in complex perovskites and the composition can be designed to stabilize new systems for potential application. The structure of perovskites can be described as a cubic closed packing of the A and oxygen ions with the B ions in the octahedron vacancies, shown in Figure 1.2, or in terms of close packing of AO_3 layers, where the B-site cations occupy 100% of the resultant BO_6 oxygen octahedra (Figure 1.3a and Figure 1.4a). When the AO_3 layers are arranged in cubic close packing, the BO_6 octahedra are connected exclusively through corner sharing without tilting, and the structure is termed a cubic perovskite. In an ideal cubic perovskite the A and B cations realize their equilibrium bond distances to oxygen without inducing any distortion of the unit cell and adopt the cubic space group $Pm\bar{3}m$. $SrTiO_3$ is commonly regarded as the archetypal cubic perovskite as its structure approaches closely that of the ideal ABO_3 compound.

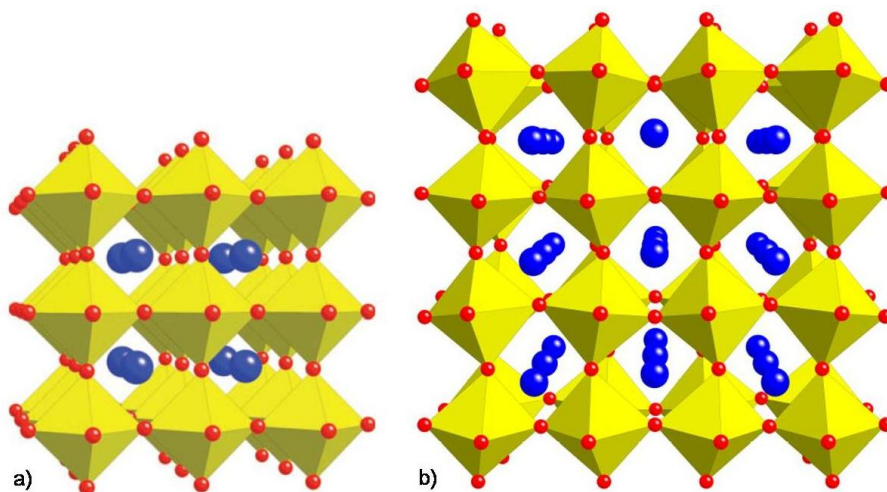


Figure 1.3: Perspective view of perovskite structure, a) ideal cubic perovskite, b) distorted perovskite with tilted BO_6 octahedra $t < 1$ [31].

Most perovskites are considered to be ionic compounds, and the ions comprising them can be described to a first approximation as spheres with the ionic radii r . A

good guide as to whether a given assembly of ions will adopt the perovskite structure is the tolerance factor t by Goldschmidt [32]. Following the Pythagorean Theorem ($a^2 + b^2 = c^2$), where a or b is the distance BOB ($2 \times (r_B + r_O)$) and c is the distance OAO ($2 \times (r_A + r_O)$), illustrated in Fig. 1.2), the tolerance factor is defined as the sum of the radii of the A-site cation and the oxygen ion divided by the sum of the radii of the B-site cation and the oxygen ion multiplied by $\sqrt{2}$. For the ideal cubic structure, t should equal one. It was adopted to double perovskites by Anderson [33] and can be calculated for ABO_3 with weighted arithmetic mean values for the cationic radii \bar{r} according to Feldhoff et al. [34]:

$$[2 \times (\bar{r}_A + r_O)]^2 = 2 \times [2 \times (\bar{r}_B + r_O)]^2 \quad (1.1)$$

$$2 \times (\bar{r}_A + r_O) = \sqrt{2} \times 2 \times (\bar{r}_B + r_O) \quad (1.2)$$

$$t = \frac{\bar{r}_A + r_O}{\sqrt{2} \times [\bar{r}_B + r_O]} \quad (1.3)$$

In many perovskites the A-O and B-O bond lengths are geometrically incompatible, and lower symmetry structures are stabilized. When the A cation is undersized, $t < 1$, the A-O distance can be shortened, and the coordination number of the A cation can be lowered through a correlated tilting of the surrounding BO_6 octahedra (Figure 1.3b). When the tolerance factor is >1 , the AO_3 layers typically adopt mixed cubic (c) and hexagonal (h), or pure hexagonal, close-packed stacking sequences. The introduction of hexagonal stacking is accompanied by face-sharing of adjacent BO_6 octahedra and by the formation of 90° BOB bond angles (Figure 1.4b). The more t deviates from unity, the less stable is the cubic perovskite [26, 31, 35, 36].

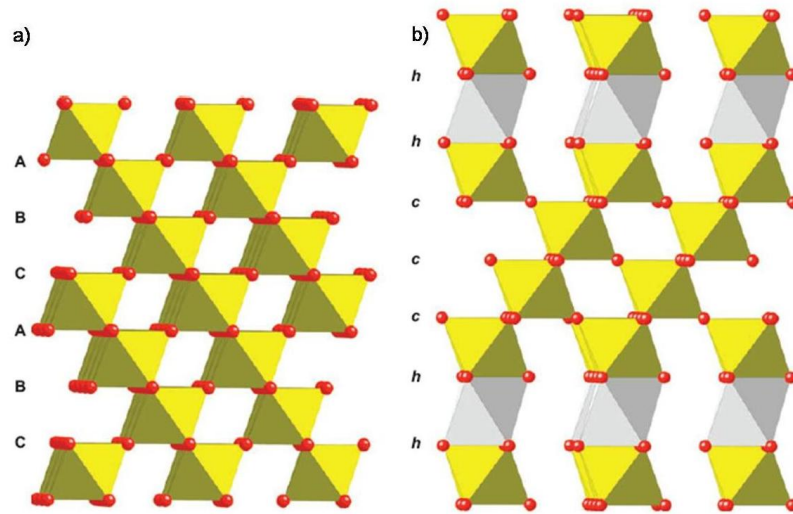


Figure 1.4: Perovskite structures viewed along (110): a) Ideal cubic with cubic close packing of AO_3 layers and resultant corner sharing of BO_6 octahedra, b) $t > 1$, cubic (c) and hexagonal (h) layers are indicated (A cations are omitted for clarity) [31].

Thus, the calculation of the tolerance factor for a desired perovskite composition is a first step to predict the structure. This was done for the perovskites included in this thesis at room temperature according to the weighted ionic radii presented by Shannon [37, 38] for both the cations of the B-site as well as for the A-site. Iron and cobalt were determined for each composition to be in 2+, 3+ or 4+ high-spin (HS) or low-spin (LS) state, aluminum in 3+, and zinc in 2+ oxidation state as reported in [39], chapter 2.3, and chapter 4.3 for the stoichiometries:

- $(\text{Ba}_{0.50}^{2+}\text{Sr}_{0.50}^{2+})(\text{Co}_{0.48}^{3+,HS}\text{Co}_{0.32}^{2+,HS}\text{Fe}_{0.20}^{3+,HS})\text{O}_{2.3}$ for BSCF with $t = 1.004$
- $(\text{Ba}_{0.50}^{2+}\text{Sr}_{0.50}^{2+})(\text{Fe}_{0.60}^{4+,HS}\text{Fe}_{0.20}^{3+,LS}\text{Zn}_{0.20}^{2+})\text{O}_{2.7}$ for BSFZ with $t = 1.030$
- $(\text{Ba}_{0.50}^{2+}\text{Sr}_{0.50}^{2+})(\text{Fe}_{0.29}^{4+,HS}\text{Fe}_{0.62}^{3+,HS}\text{Al}_{0.09}^{3+})\text{O}_{2.6}$ for BSFA0.1 with $t = 1.025$

Hence, cubic perovskite structures are expected for all three compositions and these calculations were verified, after the structures were found to really be cubic with $\text{Pm}\bar{3}\text{m}$ symmetry (chapter 2.3, 4.3 and [40]). However, this is only a simple approximation in order to provide an idea which structure might be formed, and a very important issue has not been taken into account. Importantly, the value of t is an ambiguous guide to structural type, and is certainly not an indicator of the space group that a particular perovskite will adopt, because factors other than ion size, e.g. degree of covalency, metal-metal interactions, Jahn-Teller and lone pair effects play a role in determining the space group and structure [36]. This aspect will be discussed further in chapter 4.

Table 1.1: Effective cationic radii based on $r(\text{VI}O^{2-}) = 140$ pm [37, 38] with coordination number (CN) and for iron and cobalt in high-spin (HS) and low-spin (LS) states.

Ion	CN	Ionic radius [pm]
Ba^{2+}	12	161
Sr^{2+}	12	144
Zn^{2+}	6	74
Al^{3+}	6	53.5
Fe^{4+} , HS	6	58.5
Fe^{3+} , HS	6	64.5
Fe^{3+} , LS	6	55
Co^{3+} , HS	6	61
Co^{3+} , LS	6	54.5
Co^{2+} , HS	6	74.5
Co^{2+} , LS	6	65

1.2 Synthetic process and membrane preparation

1.2.1 Powders

The characteristics of the powder have a remarkable effect on subsequent processing, like consolidation of the powder to a green body and firing to obtain the desired microstructure. Thus, powder synthesis is very important to the overall fabrication of ceramics (for more details see chapter 3). First, the choice of a powder preparation method should be considered, which will depend on the production cost and the capability of the method for achieving a certain set of characteristics. The methods available for powder preparation can be classified into gas-phase reactions, e.g. chemical vapor deposition, solid state reactions, e.g. melt casting or firing of powders, and liquid precursor methods, e.g. sol-gel processing [41–43]. All three methods are applied for perovskite synthesis, but in our particular case we chose the sol-gel processing as synthetic method. This preparation from liquid solution was aimed at the production of a homogeneous, high-purity powder with exactly defined composition for improved sinter abilities with rather low calcination and sintering temperatures. A schematic flow chart is displayed in Figure 1.5.

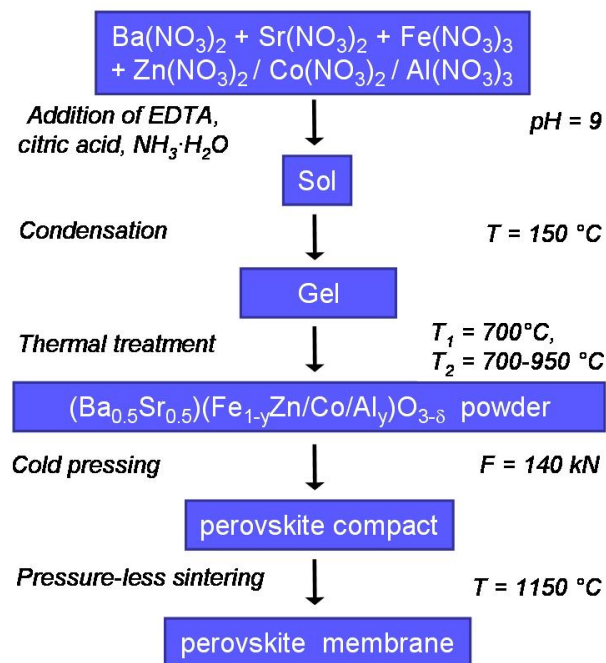


Figure 1.5: Flow chart of the sol-gel synthetic process for the perovskite preparation.

The synthesis of perovskite-type oxides from stoichiometric metal nitrates using a citrate process was first introduced by Marcilly et al. in 1970 [44]. Variants of this sol-gel procedure are widely used today and in this work a modification by Shao et al. with the addition of EDTA to the reaction in order to improve the dispersion of the metal cations was applied [20]. The liquid solution of the metal nitrates is transformed into a solid over sol, gel and calcination. The metal compounds are dispersed as very fine particles in the liquid (sol) and are converted into a highly viscous mass (gel). It is common to add a complexing agent like ethylene-diamine-

tetraacetic acid (EDTA) and a polymerization agent like citric acid. EDTA is chosen because of its high complex formation ability (section 2.3, Table 1), which avoids the partial segregation of the metal ions [45]. It offers six coordination sites for an octahedral complexation of the cation. The condensation of the citric acid leads to the formation of the polymerized network with particle sizes up to 10 nm. With increasing temperature to 150 °C mainly water and ammonia are evaporated and a three dimensional network is formed. After this gelation the metal complexes remain finely dispersed in a polymeric matrix, which was revealed by scanning transmission electron microscopy (STEM) in section 2.3, Figure 1. Afterwards, the gel is calcined firing the organics and the solid is formed over solid state reactions. The decrease in nitrogen and oxygen content during drying of the gel was monitored by energy-dispersive X-ray spectroscopy (EDXS). Figure 1.6 shows the drop of N-K_α and O-K_α X-ray lines relative to the Fe L_α line that refers to a non-volatile constituent of the gel [34].

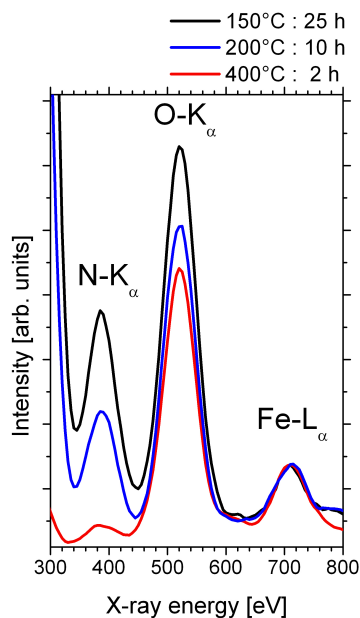


Figure 1.6: EDX spectra monitoring the decrease of nitrogen and oxygen content of the gel.

Despite the common use of sol-gel processes, details of the formation of the crystalline products are not investigated so far. Thus, the nano-scaled solid state reactions of the intermediates are discussed extensively in chapter 2. Section 2.2 points out the first crystalline intermediates in the synthesis of BSFZ compared to BSCF. A mixed carbonate ($\text{Ba}_{0.5}\text{Sr}_{0.5}\text{CO}_3$) as well as a mixed spinel ($(\text{Zn}_{0.6}\text{Fe}_{0.4})\text{Fe}_2\text{O}_4$ (BSFZ) or $(\text{Fe}_{0.6}\text{Co}_{0.4})\text{Co}_2\text{O}_4$ (BSCF)) are the dominant phases present in this stage of the reaction. When the reaction between the mixed carbonate and the mixed spinel proceeds, it was found to be more intricate. A more detailed investigation of the intermediate phases in BSFZ was done in section 2.3 showing the formation of a stuffed tridymite structure $\gamma\text{-(Ba}_{0.5}\text{Sr}_{0.5})\text{Fe}_2\text{O}_4$, a ZnFe_2O_4 spinel and ZnO. Thermodynamic measurements revealed that barium and strontium oxides are not evident during the perovskite formation due to a higher decomposition temperature of the nano-sized mixed carbonate than the perovskite formation temperature. The sol-gel method was

found to be an excellent method to produce finely dispersed powder particles, which can easily react to form the final solid. Particles on the nanometer scale are present in the solid state reaction and thus, very thin product layers are formed during the synthesis (section 2.2, Figure 1 and section 2.3, Figure 8). A solid state reaction in the classical sense occurs when local transport of matter is observed in crystalline phases. If the reactants are brought together at constant pressure and temperature in a closed system, then the reaction will take place spontaneously if the Gibbs free enthalpy of the system is thereby decreased. The transport of matter in the solid state, and thus the reactivity of solids, are dependent on the mobility of the individual particles (i.e. Ba, Sr, Fe, Zn, O) in the lattice. Since an ideally ordered crystal could only be moved as a whole, and the motion of individual ions from their lattice sites would not occur, every case of mass transport in a solid phase directly depends on deviations from ideal crystalline order. The higher the atomic disorder, the higher is the corresponding transport coefficient. If two substances react with one another to form one or more product phases which are separated from the reactants and from each other by phase boundaries, then a heterogeneous solid state reaction occurs [42, 46]. Following this definition the perovskite formation is a heterogeneous reaction and the mass transport can take place across phase boundaries between the carbonate, spinel, tridymite and oxides, which exhibit high atomic disorder.

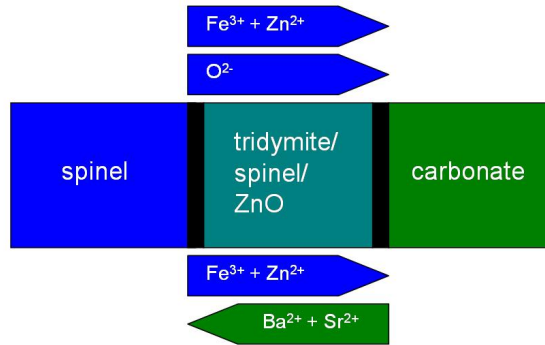


Figure 1.7: Schematic diagram showing the mechanism of formation of tridymite, spinel and ZnO between spinel and carbonate (phase boundaries in black).

Figure 1.7 illustrates schematically how the intermediate phases (tridymite, spinel and ZnO) are formed from the polycrystalline carbonate $(\text{Ba}_{0.5}\text{Sr}_{0.5})\text{CO}_3$ and mixed spinel $(\text{Zn}_{0.6}\text{Fe}_{0.4})\text{Fe}_2\text{O}_4$. The reaction product, first the tridymite/spinel and ZnO, second the perovskite, separates the reactants from one another, and the reaction proceeds by diffusion of the participating components through the reaction product. In this case the fluxes of the components in the reaction product are charged particles. Therefore, in order to preserve local electrical neutrality, the fluxes of the different ions must always be coupled with each other, either oppositely charged ions (Ba^{2+} , Sr^{2+} or Fe^{3+} , Zn^{2+} with O^{2-}) flow in the same direction (1: top of Figure 1.7), or ions with similar charges flow in opposite directions through the reaction product (Ba^{2+} , Sr^{2+} against Fe^{3+} , Zn^{2+}) (2: bottom of Figure 1.7). It should be mentioned at this point, that these are two possible mechanisms, since the reaction product can either be formed on the expense of only one educt (1) or on the expense of both educts (2) [42].

1.2.2 Membranes

To obtain an oxygen permeable membrane from the perovskite powder, the latter needs to be consolidated and afterwards sintered to a dense membrane. In the present work, the BSFZ, BSCF, and BSFA powders were uniaxially pressed with 140 kN to a green compact of ca. 1 mm thickness and 14 mm in diameter and condensed in a pressure-less single step sintering process at temperatures close under the melting point (ca. 1150 °C, Figure 1.5). The driving force for the sintering process is the lowering of the free energy of the system, which can be accomplished by reducing the surface free energy of the consolidated particles, by applying pressure or a chemical reaction. In the following, only the effects of reducing the surface free energy will be discussed due to the absence of an external stress or chemical reaction in the present work. The reduction of the free energy is consistent with the variation of the free enthalpy dG . For constant pressure dG is composed of the solid-vapor surface tension γ_{sv} with the surface area A_s , the solid-solid boundary tension γ_{ss} with the boundary area A_b and a part for the volume of the grain boundaries in the dense body ($\sum \mu_0 dN$):

$$dG = \gamma_{sv}dA_s + \gamma_{ss}dA_b + \sum \mu_0 dN \quad (1.4)$$

In the initial stage of the sintering process boundaries are formed due to the relocation of powder particles, because the solid-solid boundary energy is smaller than the solid-vapor surface energy ($\gamma_{ss} < \gamma_{sv}$). Afterwards, the porosity decreases with densification of the body (intermediate stage) and in the final stage the boundary area is further decreased due to grain coarsening during grain growth. Thus, the change in size and shape of the powder particles leads to a replacement of solid-vapor surface energy with solid-solid boundary energy [41,47].

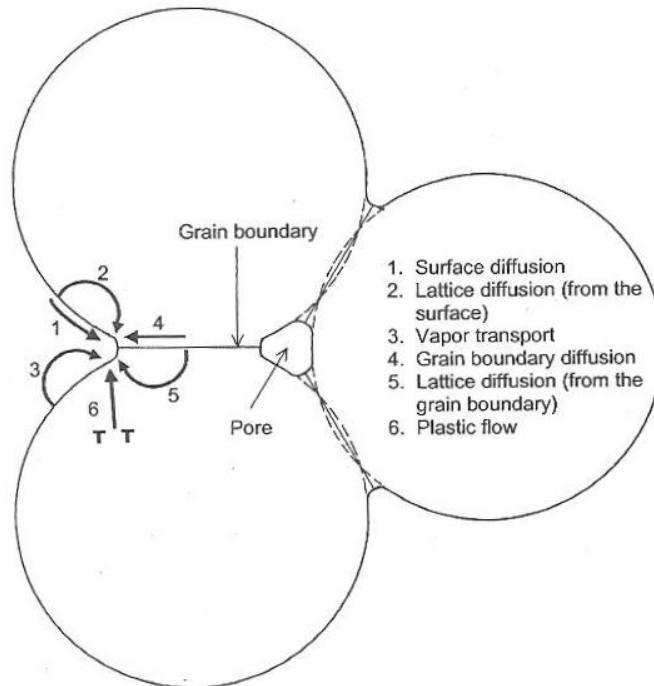


Figure 1.8: Mechanisms during the sintering. Only 1 to 3 lead to densification, but all cause the necks to grow and so influence the rate of densification [41].

As mentioned above the sintering process can be described in three stages, which are further specified in the following part. During the initial stage the particles are relocated and the number of next neighbors is increased. New grain boundaries are formed and according to the two-sphere model the grain junctions are filled leading to a neck growth between the grains and approach of the grain centers. Sintering occurs by diffusional transport of matter along definite paths from regions of higher chemical potential (source of matter) to regions of lower chemical potential (sink). The six different mechanisms of sintering for a system of three particles are illustrated in Figure 1.8: Mechanism 1 (surface diffusion), mechanism 2 (lattice diffusion), and mechanism 3 (vapor transport) can only lead to coarsening and neck growth without densification (nondensifying mechanisms). They reduce the curvature of the neck surface and thus, the rate of the densifying mechanisms (4-6). Mechanism 4 (grain boundary diffusion), mechanism 5 (lattice diffusion from the grain boundary), and mechanism 6 (plastic flow) lead to densification. Densification and coarsening are often discussed in terms of competing mechanisms since coarsening reduces the driving force for the densification, which is the desired process. Up to 65% of the maximum density are achieved at the initial stage.

The intermediate stage starts when the grains are not moving anymore due to the highest coordination possible and the pores reached their equilibrium shape dictated by the surface and the grain boundary tension (Figure 1.9), where ψ is the dihedral angle. The pore phase is still continuous. A reduction in the pore cross section is accomplished by steps 1, 4, 5 of Figure 1.8, whereas only steps 4 and 5 can contribute to densification. Continuous porosity is replaced by isolated pores and the intermediate stage is taken to end when 90% of the theoretical density is reached. When grains start to grow at the expense of other grains and isolated pores at the grain corners are eliminated, the sintering process reaches the final stage. The density further increases up to 95%-98% and coarse grains form. If pores become trapped inside a grain, they are difficult to remove from the ceramic. Thus, it is important to avoid the inclusion of pores into the grains to achieve high density ceramics, which are therefore prepared starting with small particles and with relatively low heating rates during the sintering process in order to remove the pores from the solid before they are included into the grains [41, 47].

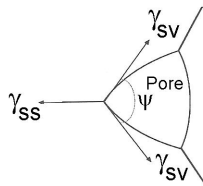


Figure 1.9: Equilibrium shape of a pore in a polycrystalline solid [41].

The knowledge of the sintering process is very important for the preparation of ceramic membranes with different microstructure, what is described further in chapter 3. Due to the investigation regarding the synthetic process of the perovskite powder (chapter 2) we were able to start from smaller grain sizes for the ceramic production and with the variation of sintering time for green compacts the grain size of the ceramics was controlled. The impact of the changes of the grain size distribution on the oxygen transport through the ceramic membranes is also discussed in section 1.3.3 and in section 3.2. In section 3.3, we introduce the investigations on

the liquid phase sintering of BSFZ and BSCF ceramic membranes with boron nitride (BN) as a sintering aid with regards to controlling the grain size distribution of these ceramics with similar relative densities. Liquid phase sintering is another way to influence the microstructure of the sintered ceramics and has been described in detail by Rahaman [41]. It is a widespread method which is used to achieve high density ceramics. Due to the introduction of a liquid phase during the sintering process, matter transport for densification as described above is facilitated. We applied the transient liquid phase sintering, in which the liquid is completely removed in contrast to the persistent liquid phase sintering, where the liquid additive remains in the ceramic.

1.3 Oxygen permeation

1.3.1 Mixed ionic and electronic conductors

According to section 1.1.1 we already know that separation of oxygen from air by ceramic membranes is a key technology and membranes based on MIECs with perovskite structure are used in many industrial processes, where the supply or removal of oxygen to or from reaction mixtures with high selectivity and oxygen fluxes is needed, e.g. in SOFCs. To achieve good oxygen permeation we use perovskites which have equal amounts of barium and strontium on the A-site and iron, cobalt, zinc, or aluminum on the B-site. The replacement of the B^{4+} ion by a lower oxidation state ion causes an oxygen deficit δ and thus oxygen vacancies in the perovskite structure are caused (Figure 1.10a). This is the property which is most important for the oxygen and electron conductivity.

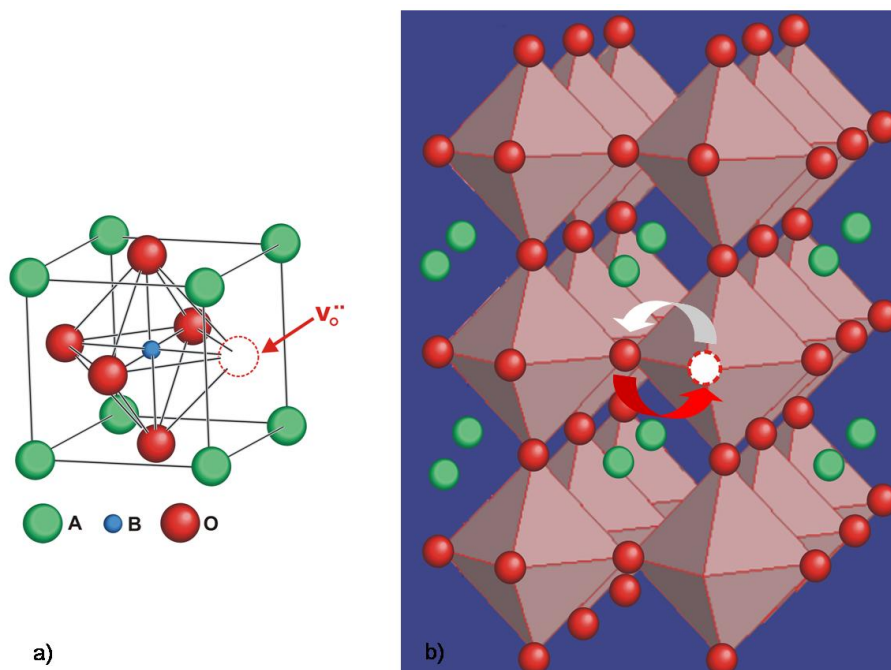
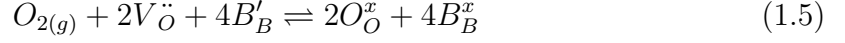


Figure 1.10: Oxygen vacancy $V_O^{..}$ in the perovskite structure (a) and the mechanism for the oxygen transport through change of places (b).

Due to the oxygen vacancies introduced in the lattice the oxygen transport occurs through a change of places and high oxygen permeability is achieved (Figure 1.10b).

Using the Kröger-Vink notation for structure elements [48] and the assumption that the oxygen deficit δ is determined only by the presence of double ionized lattice oxygen vacancies the oxygen insertion during permeation can be described as:



The oxygen removal on the other side of the membrane follows the equation read in the reverse direction [49]. The oxygen transport can also be described in terms of electron holes h^\bullet and delocalized electrons denoted as e^- with the equations at the bottom of Figure 1.11. The driving force for the oxygen transport in one direction through the membrane is the chemical potential gradient $\nabla\mu_{O_2}$ along the membrane. For example one side of the membrane is exposed to air with a high oxygen partial pressure p_A and the other side to helium with a low oxygen partial pressure of p_P . The chemical potential on the air side $\mu_{O_2}^A$ is much higher than on the permeation side ($\mu_{O_2}^P$) and thus the oxygen ions are incorporated into the perovskite lattice and permeate through the membrane by change of places. The oxygen flux is charge compensated by the simultaneous counteracting flux of delocalized electrons occupying energy states in electron bands (ambipolar diffusion).

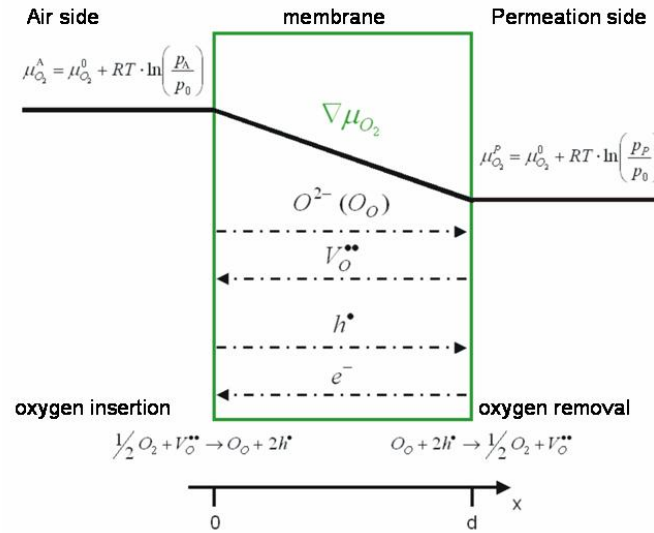


Figure 1.11: Principle of oxygen permeation through a perovskite membrane. $\nabla\mu_{O_2}$ is the chemical potential gradient between the air side with high oxygen partial pressure p_A and the permeation side with low oxygen partial pressure p_P . The chemical potential on the air side $\mu_{O_2}^A$ is much higher than on the permeation side ($\mu_{O_2}^P$).

The transport of oxygen through MIECs is commonly described using Wagner's theory [50, 51], which is restricted to the simultaneous transport of a single ionic-type defect (ionic conductivity) and a single electronic-type defect (electronic conductivity) that are ideally diluted and do not interact. The oxygen flux j_{O_2} is dependent on the electrical conductivity σ_{el} , the ionic conductivity σ_{ion} , and the oxygen chemical potential μ_{O_2} :

$$j_{O_2} = -\frac{1}{4^2 F^2} \frac{\sigma_{ion} \sigma_{el}}{\sigma_{ion} + \sigma_{el}} \nabla \mu_{O_2} \quad (1.6)$$

This equation is valid as long as the surface exchange reactions on both sides of the membrane are fast and therefore have no influence on the oxygen transport through the membrane. For the chemical potential μ_{O_2} a linearity is assumed and the gradient $\nabla\mu_{O_2}$ has to be locally constant. Integration of equation 1.6 over the thickness L without deviation of the flux and using the equation $\nabla\mu_{O_2} = \frac{\partial RT \ln p_{O_2}}{\partial x}$ leads to the usual Wagner-Equation (1.7), where p_P denotes the oxygen partial pressure of the low chemical potential side and p_A denotes the oxygen partial pressure of the high chemical potential side, and L is the membrane thickness:

$$j_{O_2} = -\frac{RT}{4^2 F^2 L} \int_{\ln p_A}^{\ln p_P} \frac{\sigma_{ion} \sigma_{el}}{\sigma_{ion} + \sigma_{el}} d \ln p_{O_2} \quad (1.7)$$

The oxygen ionic conductivity is much lower compared to the electronic conductivity in perovskite-type oxides according to Bouwmeester [19]. Therefore, the oxygen ionic conduction is the rate limiting step, and equation 1.7 can be simplified to:

$$j_{O_2} = -\frac{RT}{4^2 F^2 L} \int_{\ln p_A}^{\ln p_P} \sigma_{ion} d \ln p_{O_2} \quad (1.8)$$

Hence, it is important to consider the influence of the microstructure of the ceramic on the oxygen ionic conductivity in the interpretation of the oxygen permeation. Nevertheless, two different processes, bulk transport and surface exchange, contribute to the oxygen permeation. The oxygen permeation flux is mainly dominated by the bulk transport as long as the membrane thickness does not drop below a critical value, which is referred to as the critical membrane thickness. Further discussion of this aspect will be provided in section 1.3.3 and 3.2. These considerations are important for the comparison of permeation experiments. In order to draw meaningful conclusions from permeation experiments each studied membrane needs to be of equal thickness, which should be higher than the critical membrane thickness making the bulk transport the rate determining process.

1.3.2 Oxygen permeation experiments

The oxygen permeation was measured in a high-temperature permeation cell using a setup as illustrated in Figure 1.12. Disc-shaped membranes were gas tight sealed onto a ceramic tube (e.g. with gold paste). After sealing, gas flow rates were delivered to the reactor by mass flow controllers and continuously read by an on-line gas chromatograph. Air was fed to the air side (high oxygen chemical potential) and He and Ne as the internal standard gases were fed to the permeation side (low oxygen chemical potential) in order to transport the permeated oxygen away from the membrane and thus to maintain the gradient of the oxygen chemical potential across the membrane. The absolute flow of the effluents rate was determined by using neon as an internal standardization. The permeation flux through the membrane could then be calculated by the fraction of O_2 in the effluents and the determination of the effective permeation area of the membrane. The membranes used have a diameter of 14 mm and a thickness of ca. 1 mm. Usually, permeation experiments are conducted in a temperature range from 750 to 950°C. For a further description of such experiments, the reader is referred to chapters 3 and 4.

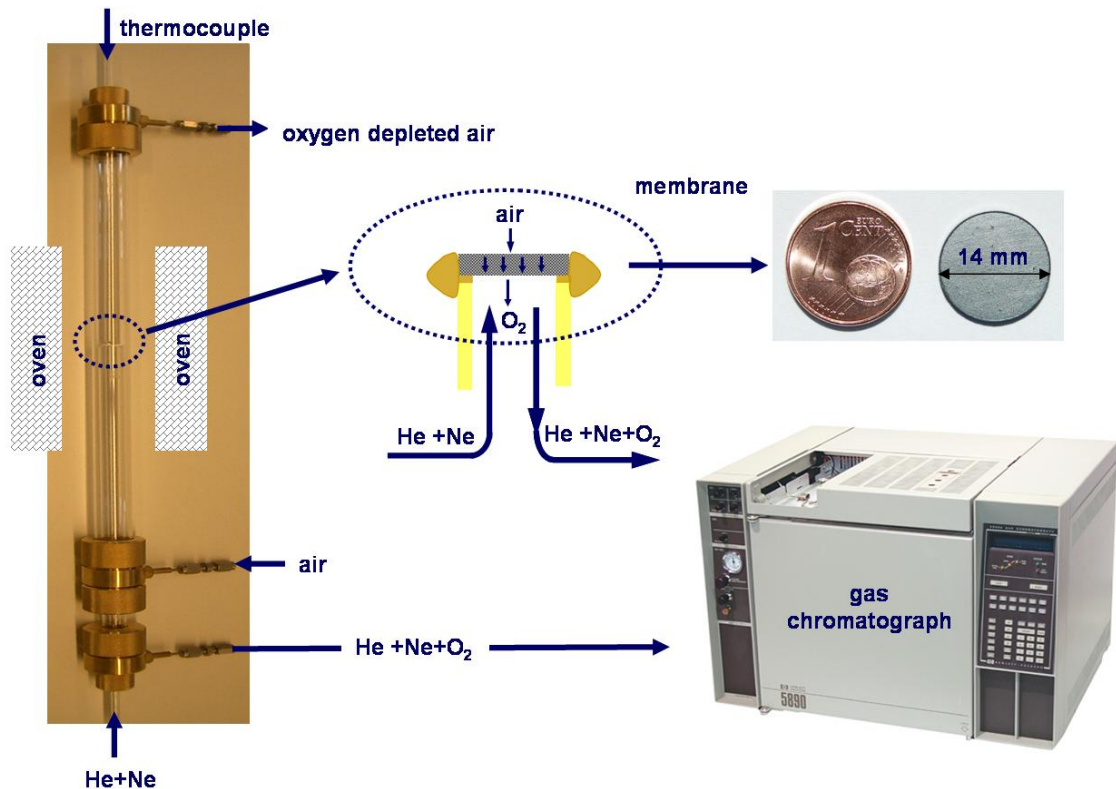


Figure 1.12: Oxygen permeation measurement setup for disc membranes with the high-temperature permeation cell (left), the closer look on the membrane and the sealing (middle) and a disc membrane and the on-line gas chromatograph (right).

1.3.3 Effect of the microstructure

This section deals with the influence of the microstructure of the ceramic membrane on the oxygen transport through it. Perovskite-type membranes for oxygen separation are polycrystalline and therefore consist of a large number of single crystals connected by grain boundaries. The grain size and grain boundary distribution and inhomogeneous grain and grain boundary compositions have to be considered. Since amorphous phases or inclusions at the grain boundary seem to act as high diffusivity paths [52,53], the influence of grain and grain boundary distribution is contradictory. The influence of microstructure cannot be generalized and clearly depends on the chemical nature of grains and grain boundaries, the powder synthesis and the ceramic process. The increase of grain size leads to an enhanced oxygen permeation for several materials, but to a decrease in oxygen permeation for others (for details see section 3.2). This contradiction might be caused by a lack of important additional information. Like already explained above, two different processes, bulk transport and surface exchange, contribute to the oxygen permeation. The oxygen permeation flux is mainly dominated by the bulk transport as long as the membrane thickness does not drop below a critical value, which is referred to as the critical membrane thickness, L_c . Membranes need to be of equal thickness, which should be higher than the critical membrane thickness making the bulk transport the rate determining process [54]. For surface exchange diffusion smaller grains are favorable due to bigger surface area. Thus, in surface exchange controlled processes an increase in oxygen permeation is expected

Bibliography

- [1] International Energy Agency. World Energy Outlook 2008, Presentation to the Press, *OECD/IEA*, London, 12th November 2008.
- [2] International Energy Agency. World Energy Outlook 2008, Fact Sheet, *IEA/AIE*, Paris, 2008.
- [3] A.B. Stambouli and E. Traversa. Fuel cells, an alternative to standard sources of energy. *Renewable and Sustainable Energy Reviews*, 6:297–306, 2002.
- [4] L. Carrette, K.A. Friedrich, and U. Stimming. Fuel cells - fundamentals and applications. *Fuel Cells*, 1:5–39, 2001.
- [5] W.R. Grove. On a new voltaic combination. *Philos. Mag.*, 13:430–431, 1838.
- [6] W. Nernst. Über die elektrolytische Leitung fester Körper bei sehr hohen Temperaturen. *Z. Elektrochem.*, 6:41–43, 1899.
- [7] E. Baur and H. Preis. Über die Brennstoff-Ketten mit Festleitern. *Z. Elektrochem.*, 43:727–732, 1937.
- [8] A. Bieberle-Hütter, D. Beckel, A. Infortuna, U.P. Muecke, J.L.M. Rupp, L.J. Gauckler, S. Rey-Mermet, P. Muralt, N.R. Bieri, N. Hotz, M.J. Stutz, D. Poulidakos, P. Heeb, P. Müller, A. Bernard, R. Gmür, and T. Hocker. A micro-solid oxide fuel cell system as battery replacement. *J. Power Sources*, 177:123–130, 2008.
- [9] L.J. Gauckler, D. Beckel, B.E. Buegler, E. Jud, U.P. Muecke, M. Prestat, J.L.M. Rupp, and J. Richter. Solid oxide fuel cells: Systems and materials. *Chimia*, 58:837–850, 2004.
- [10] Z. Shao and S. Haile. A high-performance cathode for the next generation of solid-oxide fuel cells. *Nature*, 431:170–173, 2004.
- [11] A. Esquirol, N.P. Brandon, J.A. Kilner, and M. Mogensen. Electrochemical characterization of $\text{La}_{0.6}\text{Sr}_{0.4}\text{Co}_{0.2}\text{Fe}_{0.8}\text{O}_3$ cathodes for intermediate-temperature SOFCs. *J. Electrochem. Soc.*, 151:A1847–A1855, 2004.
- [12] S. Tao and J.T.S. Irvine. A stable, easily sintered proton-conducting oxide electrolyte for moderate-temperature fuel cells and electrolyzers. *Adv. Mater.*, 18:1581–1584, 2006.
- [13] Q.X. Fu, F. Tietz, and F. Stöver. $\text{La}_{0.4}\text{Sr}_{0.6}\text{Co}_{1-x}\text{Fe}_x\text{O}_{3-\delta}$ perovskites as anode materials for solid oxide fuel cells. *J. Electrochem. Soc.*, 153:D74–D83, 2006.

- [14] M.-F. Hsu, L.-J. Wu, J.-M. Wu, Y.-H. Shiu, and K.-F. Lin. Solid oxide fuel cell fabricated using all-perovskite materials. *Electrochem. Solid-State Lett.*, 9:A193–A195, 2006.
- [15] J. Caro. Membranreaktoren für die katalytische Oxidation. *Chemie Ingenieur Technik*, 78:899–912, 2006.
- [16] H. Wang, Y. Cong, X. Zhu, and W. Yang. Oxidative dehydrogenation of propane in a dense tubular membrane reactor. *React. Kinet. Catal. Lett.*, 79:351–356, 2003.
- [17] C. Hamel, A. Seidel-Morgenstern, T. Schiestel, S. Werth, H. Wang, C. Tablet, and J. Caro. Experimental and modeling study of the O₂-enrichment by perovskite fibers. *AIChE J.*, 52:3118–3125, 2003.
- [18] H. Wang, S. Werth, T. Schiestel, and J. Caro. Perovskite hollow-fiber membranes for the production of oxygen-enriched air. *Angew. Chemie Int. Ed.*, 44:6906–6909, 2005.
- [19] H.J.M. Bouwmeester and A.J. Burggraaf. Dense ceramic membranes for oxygen separation. In A.J. Burggraaf and L. Cot, editors, *Fundamentals of inorganic membrane science and technology*. Elsevier, Amsterdam, 1st edition, 1996.
- [20] Z.P. Shao, W.S. Yang, Y. Cong, H. Dong, J.H. Tong, and G.X. Xiong. Investigation of the permeation behavior and stability of a (Ba_{0.5}Sr_{0.5})(Co_{0.8}Fe_{0.2})O_{3-δ} oxygen membrane. *J. Membr. Sci.*, 172:177–188, 2000.
- [21] A.C. van Veen, M. Rebeilleau, D. Farrusseng, and C. Mirodatos. Studies on the performance stability of mixed conducting BSCFO membranes in medium temperature oxygen permeation. *Chem. Comm.*, 2003:32–33, 2003.
- [22] H. Wang, C. Tablet, A. Feldhoff, and J. Caro. Investigation of phase structure, sintering, and permeability of perovskite-type (Ba_{0.5}Sr_{0.5})(Co_{0.8}Fe_{0.2})O_{3-δ} membranes. *J. Membr. Sci.*, 262:20–26, 2005.
- [23] J. Caro, H.H. Wang, C. Tablet, A. Kleinert, A. Feldhoff, T. Schiestel, M. Kilgus, P. Kölsch, and S. Werth. Evaluation of perovskites in hollow fibre and disk geometry in catalytic membrane reactors and in oxygen separators. *Catal. Today*, 118:128–135, 2006.
- [24] A. Yan, M. Cheng, Y.L. Dong, W.S. Yang, V. Maragou, S.Q. Song, and P. Tsakaras. Investigation of a (Ba_{0.5}Sr_{0.5})(Co_{0.8}Fe_{0.2})O_{3-δ} based cathode IT-SOFC I. The effect of CO₂ on the cell performance. *Appl. Catal., B*, 66:64–71, 2006.
- [25] W. Lei and S.M. Haile. Electrochemical impedance spectroscopy of mixed conductors under a chemical potential gradient: a case study of Pt|SDC|BSCF. *Phys. Chem. Chem. Phys.*, 10:865–883, 2008.
- [26] M. Arnold, T.M. Gesing, J. Martynczuk, and A. Feldhoff. Correlation of the formation and the decomposition process of the BSCF perovskite at intermediate temperatures. *Chem. Mater.*, 20:5851–5858, 2008.

-
- [27] S. Švarcová, K. Wiik, J. Tolchard, H.J.W. Bouwmeester, and T. Grande. Structural instability of cubic perovskite $(\text{Ba}_x\text{Sr}_{1-x})(\text{Co}_{1-y}\text{Fe}_y)\text{O}_{3-\delta}$. *Solid State Ionics*, 178:1787–1791, 2008.
- [28] H. Wang, C. Tablet, A. Feldhoff, and J. Caro. A cobalt-free oxygen-permeable membrane based on the perovskite-type oxide $(\text{Ba}_{0.5}\text{Sr}_{0.5})(\text{Fe}_{0.8}\text{Zn}_{0.2})\text{O}_{3-\delta}$. *Adv. Mater.*, 17:1785–1788, 2005.
- [29] B. Wei, Z. Lü, X. Huang, Z. Liu, J. Miao, N. Li, and W. Su. $(\text{Ba}_{0.5}\text{Sr}_{0.5})(\text{Fe}_{0.8}\text{Zn}_{0.2})\text{O}_{3-\delta}$ perovskite oxide as a novel cathode for intermediate-temperature solid-oxide fuel cell. *J. Am. Ceram. Soc.*, 90:2264–3366, 2007.
- [30] B. Wei, Z. Lü, X. Huang, Z. Liu, J. Miao, N. Li, and W. Su. Synthesis, electrical and electrochemical properties of $(\text{Ba}_{0.5}\text{Sr}_{0.5})(\text{Fe}_{0.8}\text{Zn}_{0.2})\text{O}_{3-\delta}$ perovskite oxide for IT-SOFC cathode. *J. Power Sourc.*, 176:1–8, 2008.
- [31] P.K. Davies, H. Wu, A.Y. Borisevich, I.E. Molodetsky, and L. Farber. Crystal chemistry of complex perovskites: New cation-ordered dielectric oxides. *Annu. Rev. Mater. Res.*, 38:369–401, 2008.
- [32] V.M. Goldschmidt. Die Gesetze der Krystallochemie. *Naturwissenschaften*, 14:477–485, 1926.
- [33] M.T. Anderson, K.B. Greenwood, G.A. Taylor, and K.R. Poeppelmeier. B-cation arrangements in double perovskites. *Prog. Solid State Chem.*, 22:197–233, 1993.
- [34] A. Feldhoff, J. Martynczuk, and H. Wang. Advanced $(\text{Ba}_{0.5}\text{Sr}_{0.5})(\text{Fe}_{0.8}\text{Zn}_{0.2})\text{O}_{3-\delta}$ perovskite-type ceramics as oxygen selective membranes: Evaluation of the synthetic process. *Prog. Solid State Chem.*, 35:339–353, 2007.
- [35] U. Müller. *Anorganische Strukturchemie*. B.G. Teubner Verlag, Wiesbaden, 4th edition, 2004.
- [36] R.H. Mitchell. *Perovskites: Modern and ancient*. Almaz Press Inc., Ontario, 1st edition, 2002.
- [37] R.D. Shannon and C.T. Prewitt. Effective ionic radii in oxides and fluorides. *Acta Crystallogr.*, 25:925–946, 1969.
- [38] R.D. Shannon. Revised effective ionic radii and systematic studies of interatomic distances in halides and chalcogenides. *Acta Crystallogr.*, 32:751–767, 1976.
- [39] M. Arnold and Q. Xu and D. Tichelaar and A. Feldhoff. Local charge disproportion in a high performance perovskite, *Chem. Mater.*, 2008, submitted.
- [40] S. McIntosh, J.F. Vente, W.G. Haije, D.H.A. Blank, and H.J.M. Bouwmeester. Oxygen stoichiometry and chemical expansion of $(\text{Ba}_{0.5}\text{Sr}_{0.5})(\text{Co}_{0.8}\text{Fe}_{0.2})\text{O}_{3-\delta}$ measured by in situ neutron diffraction. *Chem. Mater.*, 18:2187–2193, 2006.
- [41] M.N. Rahaman. *Ceramic Processing and Sintering*. CRC Press/Taylor and Francis Group, Boca Raton, 2nd edition, 2003.
-

- [42] H. Schmalzried. *Solid State Reactions*. Verlag Chemie, Weinheim, 2nd edition, 1981.
- [43] L. Smart and E. Moore. *Einführung in die Festkörperchemie*. Vieweg, Braunschweig/Wiesbaden, 2nd edition, 1997.
- [44] C. Marcilly, P. Courty, and B. Delmon. Preparation of highly dispersed mixed oxides and oxide solid solutions by pyrolysis of amorphous organic precursors. *J. Am. Ceram. Soc.*, 53:56–57, 1970.
- [45] R.H.E. van Doorn, H. Kruidhof, A. Nijmeijer, L. Winnubst, and A.J. Burggraaf. Preparation of $\text{La}_{0.3}\text{Sr}_{0.7}\text{CoO}_{3-\delta}$. *J. Mater. Chem.*, 8:2109–2112, 1998.
- [46] K. Hauffe. *Reaktionen in und an festen Stoffen*. Springer-Verlag, Berlin, 2nd edition, 1966.
- [47] R.W. Cahn and P. Haasen. *Physical Metallurgy*. Elsevier Science BV, North Holland, 4th edition, 1996.
- [48] F. A. Kröger and H. J. Vink. Relations between the concentrations of imperfections in crystalline solids. In F. Seitz and D. Turnbull, editors, *Solid State Physics*. Academic Press, New York, 3rd edition, 1956.
- [49] M.H.R. Lankhorst, H.J.M. Bouwmeester, and H. Verweij. Thermodynamics and transport of ionic and electronic defects in crystalline oxides. *J. Am. Ceram. Soc.*, 80:2175–2197, 1997.
- [50] C. Wagner. Beitrag zur Theorie des Anlaufvorgangs. *Z. Phys. Chem. B*, 21:25–41, 1933.
- [51] C. Wagner. Beitrag zur Theorie des Anlaufvorgangs II. *Z. Phys. Chem. B*, 32:447–462, 1936.
- [52] G. Etchegoyen, T. Chartier, A. Julian, and P. Del-Gallo. Microstructure and oxygen permeability of a $\text{La}_{0.6}\text{Sr}_{0.4}\text{Fe}_{0.9}\text{Ga}_{0.1}\text{O}_{3-\delta}$ membrane containing magnesia as dispersed second phase particles. *J. Membr. Sci.*, 268:86–95, 2006.
- [53] S. Diethelm, J. van Herle, J. Sfeir, and P. Buffat. Influence of microstructure on oxygen transport in perovskite type membranes. *Br. Ceram. Trans.*, 103:147–152, 2004.
- [54] H.J.M. Bouwmeester, H. Kruidhof, and A.J. Burggraf. Importance of the surface exchange kinetics as rate limiting step in oxygen permeation through mixed-conducting oxides. *Solid State Ionics*, 72:185–194, 1994.
- [55] J. Maier. Transport in electroceramics: micro- and nano-structural aspects. *J. Euro. Ceram. Soc.*, 24:1251–1257, 2004.
- [56] J. Maier. *Physical Chemistry of Ionic Materials: Ions and Electrons in Solids*. John Wiley & Sons, Chichester, 1st edition, 2004.
- [57] Y.-M. Chiang and T. Tagaki. Grain-boundary chemistry of barium-titanate and strontium-titanate. 1. High-temperature equilibrium space-charge. *J. Am. Ceram. Soc.*, 73:3278–3285, 1990.

-
- [58] I. Denk, J. Claus, and J. Maier. Electrochemical investigations of SrTiO₃ boundaries. *J. Electrochem. Soc.*, 144:3526–3536, 1997.
- [59] X. Guo, J. Fleig, and J. Maier. Separation of electronic and ionic contributions to the grain boundary conductivity in acceptor-doped SrTiO₃. *J. Electrochem. Soc.*, 148:J50–J53, 2001.
- [60] X. Guo and J. Maier. Grain boundary blocking effect in zirconia: a schottky barrier analysis. *J. Electrochem. Soc.*, 148:E121–E126, 2001.
- [61] J. Jamnik and J. Maier. Chemical diffusion through grain boundaries in mixed conductors. *J. Electrochem. Soc.*, 145:1762–1767, 2001.
- [62] S. Kim and J. Maier. On the conductivity mechanism of nanocrystalline ceria. *J. Electrochem. Soc.*, 149:373–383, 2002.
- [63] M. Leonhardt, J. Jamnik, and J. Maier. In situ monitoring and quantitative analysis of oxygen diffusion through schottky-barriers in SrTiO₃ bicrystals. *Electrochem. Solid-State Lett.*, 2:333–335, 1999.
- [64] G.E. Pike and C.H. Seager. DC voltage dependence of semiconductor grain-boundary resistance. *J. Appl. Phys.*, 50:3414–3422, 1979.
- [65] R. Waser. Bulk conductivity, defect chemistry of acceptor-doped strontium titanate in the quenched state. *J. Am. Ceram. Soc.*, 74:1934–1940, 1991.

Chapter 2

Sol-gel based synthetic processes

2.1 Summary

This chapter reveals the sol gel-based synthesis of the complex $(\text{Ba}_{0.5}\text{Sr}_{0.5})(\text{Fe}_{0.8}\text{Zn}_{0.2})\text{O}_{3-\delta}$ perovskite-type oxide (BSFZ) in comparison to the first formation steps of $(\text{Ba}_{0.5}\text{Sr}_{0.5})(\text{Co}_{0.8}\text{Fe}_{0.2})\text{O}_{3-\delta}$ (BSCF). The advantage of the utilized sol gel-based EDTA/citric acid complexing method is the fine-scale intermixing of the reaction partners, which leads to a nanometer-scale solid state reaction between finely dispersed crystalline intermediates. Thus, it was essential to conduct an extensive transmission electron microscopic study using high resolution (HRTEM) and energy-filtered transmission electron microscopy (EFTEM), scanning transmission electron microscopy (STEM) in high-angle annular dark-field (HAADF), selected-area electron diffraction (SAED) and electron energy-loss spectroscopy (EELS) with an emphasis on energy-loss near-edge structures (ELNES). These methods were accomplished by scanning electron microscopy (SEM) and X-ray diffraction (XRD).

In the first article we determined the first crystalline intermediates in the synthesis of the two distinct $\text{ABO}_{3-\delta}$ perovskites to be a complex spinel of the later B-site ions and a complex carbonate in the aragonite polymorph of the later A-site ions. This profound knowledge of the perovskite formation process opens new ways to engage the microstructure of the underlying ceramic material, for example in the way, that the common calcination temperature for BSFZ can be decreased from 950 °C to 750 °C avoiding presintering.

The second article presents a more detailed investigation of the intermediate phases in BSFZ. The reaction between the mixed carbonate $(\text{Ba}_{0.5}\text{Sr}_{0.5})\text{CO}_3$ and the mixed spinel $(\text{Zn}_{0.6}\text{Fe}_{0.4})\text{Fe}_2\text{O}_4$ was found to be more intricate, as it does not lead directly to the perovskite structure, but a stuffed tridymite structure $\gamma\text{-(Ba}_{0.5}\text{Sr}_{0.5})\text{Fe}_2\text{O}_4$, a ZnFe_2O_4 spinel and ZnO are formed. Supplementary, the question, why barium and strontium oxides are not evident during the perovskite formation, was resolved. Thermodynamic measurements disclosed the decomposition temperature of the nano-sized mixed carbonate being at about 40 °C higher than the perovskite formation temperature. Hence, the described reaction sequence between spinel and carbonate over stuffed tridymite to the final perovskite structure was confirmed.

2.2 How $(\text{Ba}_{0.5}\text{Sr}_{0.5})(\text{Fe}_{0.8}\text{Zn}_{0.2})\text{O}_{3-\delta}$ and $(\text{Ba}_{0.5}\text{Sr}_{0.5})(\text{Co}_{0.8}\text{Fe}_{0.2})\text{O}_{3-\delta}$ perovskites form via an EDTA/citric acid complexing method

Julia Martynczuk, Mirko Arnold, Haihui Wang, Jürgen Caro,
and Armin Feldhoff

Advanced Materials 19, 2134-2140 (2007)

How the $(\text{Ba}_{0.5}\text{Sr}_{0.5})(\text{Fe}_{0.8}\text{Zn}_{0.2})\text{O}_{3-\delta}$ and $(\text{Ba}_{0.5}\text{Sr}_{0.5})(\text{Co}_{0.8}\text{Fe}_{0.2})\text{O}_{3-\delta}$ perovskites form by the EDTA/citric acid complexing method**

By Julia Martynczuk, Mirko Arnold, Haihui Wang, Juergen Caro, and Armin Feldhoff*

Nowadays, numerous perovskite materials with different elemental compositions bear a meaning for therewith affiliated applications. Perovskite-based ceramics are applied for combustion of VOCs (volatile organic compounds), vehicular emission control, electrical pulse induced resistance-change and electric field devices, high-frequency capacitors, plasma activation of CO_2 , electro- and thermochromic devices and microwave applications like mobile communication systems and satellite broadcast systems¹. Furthermore, there is an interest in perovskites for the chemical synthesis of ammonia at atmospheric pressure, ammonia oxidation and the application as nanoparticles². The electrochemical importance of perovskite oxides is apparent in the case of solid-oxide fuel cells (SOFC)³. After their first employment as cathode materials, perovskites are now used as electrolyte and anode materials; and in the end full intermediate-temperature SOFCs are prepared⁴. Ceramics with both ionic and electronic conductivities are often of perovskite-type. The basic work was done by Teraoka et al., who proposed $(\text{La}_{1-x}\text{Sr}_x)(\text{Co}_{1-y}\text{Fe}_y)\text{O}_{3-\delta}$ as a membrane material with an high oxygen permeability⁵. The oxygen permeation property⁶ is used for the separation of oxygen from air, partial oxidation of methane, ethane and propane and oxygen-enrichment in air⁷.

Instead of the classical solid state synthesis route, that is the blending and firing of powdered reactants, perovskite-type oxides of complex stoichiometries are nowadays widely synthesised by wet chemical methods like the combined citric acid and EDTA (ethylene-diamine-tetraacetic acid) complexing method⁸, that is investigated here and was first used by Shao et al.⁹. The synthesis of mixed oxides by the decomposition of complex organic mixtures has been introduced in the 1960s by Paris et al.¹⁰. Some years later Marcilly et al. described the first preparation of a perovskite-type oxide from the respective metal nitrates in a citrate process¹¹. Until now the single stages of the latter described synthesis route, which maintains a fine-scale intermixing of the cations during all processing steps, are investigated insufficiently although this is essential to open ways to utilize the full potential of the material and to optimize the functional properties.

In our group the novel perovskite-type material $(\text{Ba}_{0.5}\text{Sr}_{0.5})(\text{Fe}_{0.8}\text{Zn}_{0.2})\text{O}_{3-\delta}$ has been developed¹². It shows high oxygen permeation fluxes ($2.55 \text{ mL min}^{-1} \text{ cm}^{-2}$ in the partial catalytic oxidation of methane to syngas (POM) for 1.25 mm thick membrane disks) and an excellent phase stability under low oxygen partial pressures ($p_{\text{O}_2} < 1 \cdot 10^{-8} \text{ Pa}$ in a 2 % H_2 -Ar atmosphere)¹³. The doping of the B site of the perovskite structure with a divalent metal like zinc, which exhibits a constant oxidation state, leads to the elimination of non-stoichiometric oxygen variations and lattice expansion caused by variations of the temperature or the chemical potential of oxygen. The procedure of the EDTA/citric acid complexing synthesis route is usually a low temperature heating of the sol until gelation followed by a heat treatment resulting in a pure perovskite powder. This workflow was interrupted by quenching samples for a stepwise structure analysis. The relevant stages from the gel to the pure perovskite powder are the crystallisation of the amorphous gel at about 550 to

600 °C, the initiation of the perovskite structure formation at 600 to 650 °C and the total disappearance of the intermediates at 750 °C. Due to this stepwise refinement it was possible to determine crystalline intermediates formed during the preparation of a $(\text{Ba}_{0.5}\text{Sr}_{0.5})(\text{Fe}_{0.8}\text{Zn}_{0.2})\text{O}_{3-\delta}$ perovskite as a two phase mixture of ultra-finely dispersed $(\text{Zn}_{0.6}\text{Fe}_{0.4})\text{Fe}_2\text{O}_4$ spinel and $(\text{Ba}_{0.5}\text{Sr}_{0.5})\text{CO}_3$ carbonate in aragonite modification as intermediates. It is interesting to note that there is obviously a pre-arrangement in groups of cations according to the later A (barium and strontium) and B (iron and zinc) sites in the perovskite on a nano-scale.

This finding was verified by the following characterization methods. First, we proof the nano-scale location of the perovskite formation between the intermediates by imaging it in the transmission electron microscope (TEM) for ten different conglomerations with homogeneous results. The specimen used was prepared like described in the experimental part of a quenched powder calcined at 750 °C for 2h (Fig. 5c). The exemplary TEM bright-field micrograph images the reaction pathway from spinel and carbonate to perovskite (Fig. 1a). Crystal sizes are of about 100 nm as is evidenced by TEM dark-field imaging. Having a particle with spinel and carbonate crystals neighbouring, the perovskite is formed at their expense. The identification of the three phases was carried out by electron energy-loss spectroscopy (EELS), energy-filtered transmission electron microscopy (EFTEM) (Figs. 1b-e) and selected-area electron diffraction (SAED). The presence of an Fe-L_{2,3} edge and the characteristic energy-loss near-edge structure (ELNES) of the O-K ionization edge in the top spectrum identify the spinel (Fig. 1b). The carbonate structure is specified by the bottom spectrum using Ba-M_{4,5} white lines and different characteristics of the O-K-ELNES. In the middle the O-K, the Fe-L_{2,3} and the Ba-M_{4,5} edge identify the perovskite structure. The accurate location of the different particles is illustrated by Figs. 1c-e showing high elemental concentrations of iron and barium by bright contrast and different colours, respectively. The particle in the middle contains a high amount of iron (white in c, blue in e) but no barium whereas the bottom particle comprises no iron but barium (white in d, green in e). The perovskite appears with moderate bright contrast in Figs. 1c, d and a green/blue mixture in Fig. 1e. For a more detailed specification, an investigation on the particular compounds was carried out by EELS in different energy ranges.

Electron energy-loss spectroscopy offers not only information

[*] J. Martynczuk, M. Arnold, Prof. J. Caro, Dr. A. Feldhoff
Institute of Physical Chemistry and Electrochemistry
Leibniz Universität Hannover
Callinstr. 3-3a, 30167 Hannover, Germany
E-mail: armin.feldhoff@pci.uni-hannover.de
Prof. H. Wang
College of Chemical and Energy Engineering
South China University of Technology
Guangzhou, 510640, P.R. China

[**] The authors acknowledge gratefully funding by the Deutsche Forschungsgemeinschaft (DFG) under grant FE 928/1-1.

about the elements contained in the compound, but also about their chemical environment. The inelastic scattered electrons can be resolved energy-dependant, and the resulting energy distribution with its characteristic ionization edges and energy-loss near-edge structures allows conclusions on the element itself and, moreover, on its bonds to other elements¹⁴.

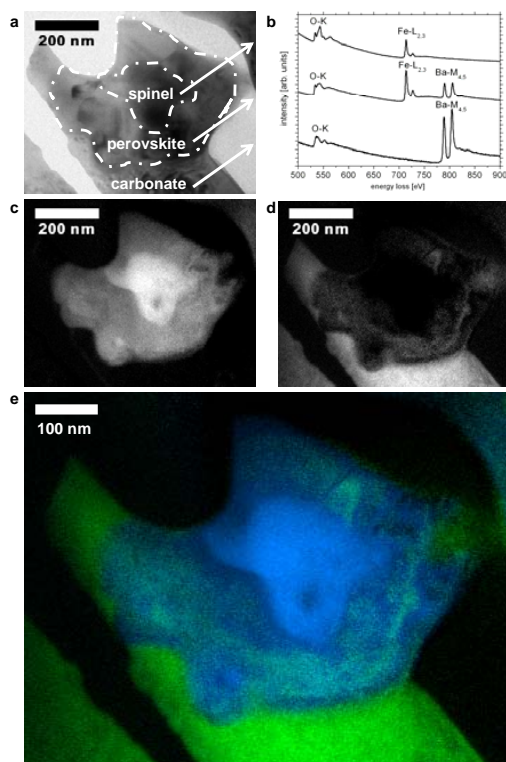


Figure 1. Transmission electron micrographs showing the formation of the perovskite phase between the intermediates. a, Insight into the EDTA/citric acid complexing synthesis of the $(\text{Ba}_{0.5}\text{Sr}_{0.5})(\text{Fe}_{0.8}\text{Zn}_{0.2})\text{O}_{3.5}$ perovskite. Crystalline intermediates identified as $(\text{Zn}_{0.8}\text{Fe}_{0.4})\text{Fe}_2\text{O}_4$ spinel and $(\text{Ba}_{0.5}\text{Sr}_{0.5})\text{CO}_3$ carbonate in the aragonite modification by transmission electron microscopy. b, Identification of these three phases by electron energy-loss spectroscopy (EELS) (top: spinel, middle: perovskite, bottom: carbonate). c-e, Accurate location of the different particles illustrated by energy-filtered transmission electron micrographs showing high elemental concentrations by bright contrast (c: iron, d: barium) or in different colours (e: blue = iron, green = barium).

The specification of the carbonate structure comes to the fore by Figs. 2b-d showing three EEL spectra in different energy ranges. Two peaks in the C-K near-edge structure (290 eV, 300 eV, Fig. 2b) originate from excitations of carbon 1s electrons into unoccupied non-binding π^* and σ^* orbitals¹⁵. They reflect directly the presence of C=O double bonds and C-O single bonds in the carbonate ion (Fig. 2a). At 272 eV and 282 eV an Sr-M_{2,3} ionization edge emerges. The low-loss spectrum in Fig. 2c is characterized by Ba-O_{2,3} and Sr-N_{2,3} edges at 15-29 eV. A Ba-N_{4,5} edge appears at 95 eV. O-K and Ba-M_{4,5} edges are shown in Fig. 2d. The fine structure of the O-K edge at 532 eV is in good agreement with that reported for SrCO₃¹⁵. Furthermore, neither an Fe-M_{2,3} edge is present at 54 eV nor an Fe-M_{2,3} edge arises at 708 eV.

The spinel is indicated by two EEL spectra in Figs. 2e and f: in the low loss region by the presence of an Fe-M_{2,3} edge at 54 eV and at higher energy losses by Fe-L_{2,3} white lines (708 eV,

721 eV)¹⁶. The characteristic ELNES of the O-K ionization edge is typical for spinels¹⁷ and distinctly different from the one obtained for the carbonate in Fig. 2c. Barium and strontium edges at 15-29 eV and 781 eV are not found.

The formation of the perovskite between the spinel and carbonate phases is evidenced by Figs. 2g and h. The low-loss spectrum shows Ba-O_{2,3} and Sr-N_{2,3} edges at 15-29 eV. Additionally, an Fe-M_{2,3} edge is found at 54 eV. At higher energies the Fe-L_{2,3} (708 eV, 721 eV) and Ba-M_{4,5} (781 eV, 796 eV) white lines appear. In addition, the characteristic O-K ELNES confirms the perovskite structure¹⁸.

Exemplary SAED pattern of the three phases involved in the formation of the perovskite are shown in Figure 3. For the carbonate in aragonite modification (Fig. 3a) along the [-1,7,-2] zone axis three different lattice plane distances of $d = 1.77 \text{ \AA}$, $d = 2.32 \text{ \AA}$ and $d = 2.85 \text{ \AA}$ are indicated. The spinel exhibits lattice plane distances of $d = 4.22 \text{ \AA}$ and $d = 2.98 \text{ \AA}$ along [0,0,1] zone axis. The orientation of a perovskite particle along [1,-3,2] zone axis resulted in lattice plane distances of $d = 1.77 \text{ \AA}$, $d = 1.61 \text{ \AA}$, $d = 2.28 \text{ \AA}$ and $d = 1.32 \text{ \AA}$.

As the basis of these results we reason that the perovskite structure comprises of spinel and carbonate at their expense in a solid state reaction. Further on, we expect that the grain sizes of the primarily formed perovskite crystals are in the same range as those of the crystalline intermediates and coarsen afterwards with evolving time during temperature treatment.

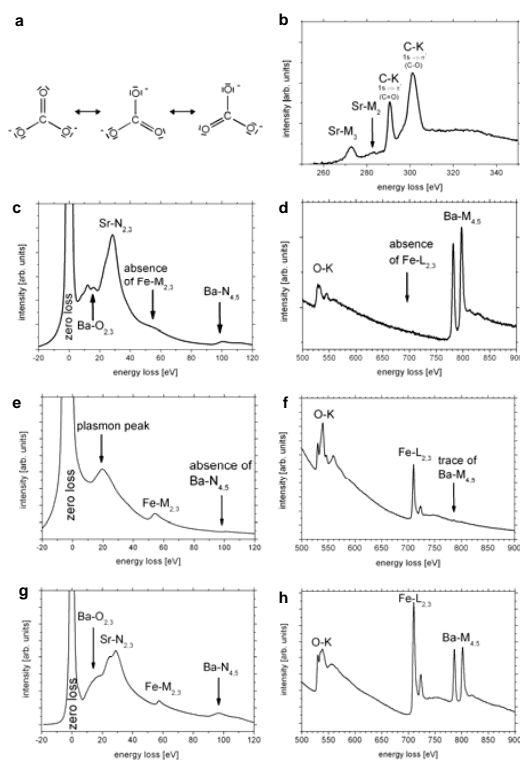


Figure 2. Identification of intermediates by elements and their chemical environment a-d, Carbonate structure specified by three EEL spectra in different energy ranges by a closer look at the energy-loss near-edge structures (ELNES) at ionization edges for barium, strontium, carbon and oxygen. e,f, Spinel indicated by two EEL spectra: in the low-loss region and at higher energy losses by Fe-edges and the characteristic ELNES of the O-K ionization edge g,h, Formation of perovskite evidenced by two EEL spectra. The low-loss spectrum shows Ba-O_{2,3}, Sr-N_{2,3} and Fe-M_{2,3} edges. At higher energies the characteristic O-K ELNES confirms the perovskite structure.

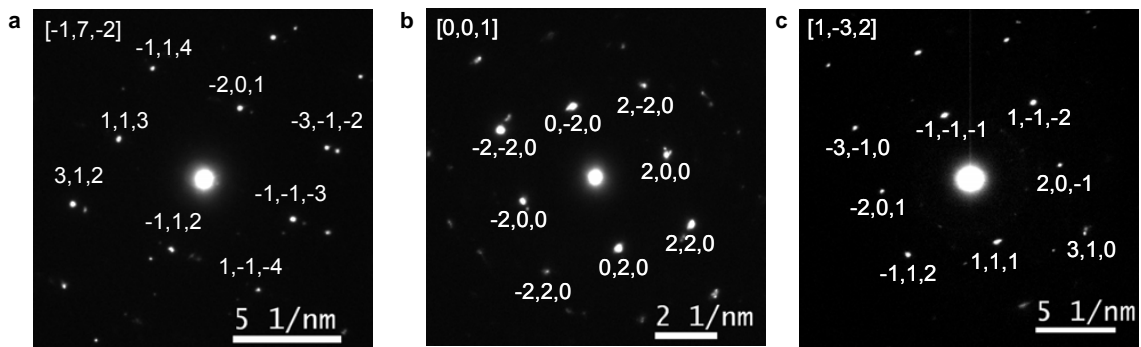
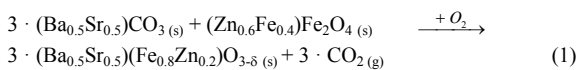


Figure 3. Selected-area electron diffraction (SAED) of the three phases: a, carbonate along $[-1,7,-2]$ zone axis and lattice plane distances of $d = 1.77 \text{ \AA}$ ($3,1,2$; $-1,1,4$; $-3,-1,-2$; $1,-1,-4$), $d = 2.32 \text{ \AA}$ ($1,1,3$; $-1,-1,-3$), $d = 2.85 \text{ \AA}$ ($-2,0,1$; $-1,1,2$), b, spinel along $[0,0,1]$ zone axis and lattice plane distances of $d = 4.22 \text{ \AA}$ ($0,-2,0$; $2,0,0$; $0,2,0$; $-2,0,0$), $d = 2.98 \text{ \AA}$ ($2,-2,0$; $2,2,0$; $-2,2,0$; $-2,-2,0$), c, perovskite along $[1,-3,2]$ zone axis and lattice plane distances of $d = 1.77 \text{ \AA}$ ($2,0,-1$; $-2,0,1$), $d = 1.61 \text{ \AA}$ ($-1,1,2$; $1,-1,-2$), $d = 2.28 \text{ \AA}$ ($1,1,1$; $-1,-1,-1$), $d = 1.32 \text{ \AA}$ ($3,1,0$; $-3,-1,0$).

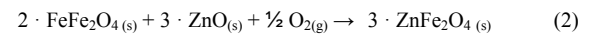
The grain size distribution of the perovskite particles is of high importance for the later properties of the hence synthesized ceramic. The smaller the grains of the powder underlying the green compact of the later ceramic are, the merrier is the sintering behaviour like lower sintering temperature and shorter time, less pores and highly dense ceramics can be obtained. Thus, it is essential to spy out the optimized calcination procedure to get a perovskite powder of high purity, but as small grains as possible.

During the calcination process the organic compounds are burned step by step under the elimination of CO_3^{2-} , NO_3^- and NH_4NO_3 . This can be confirmed by thermo gravimetry¹⁹. After crystallisation of the amorphous gel at about 550 to $600 \text{ }^\circ\text{C}$, no nitrogen containing compounds are found anymore, what indicates the total release of NO_x . Figures 4a, b show scanning electron micrographs (SEM) of a powder calcined at $650 \text{ }^\circ\text{C}$ for two hours, containing estimated by the XRD intensities approximately equal amounts of intermediates and perovskite. At the initiation of the perovskite structure formation at 600 to $650 \text{ }^\circ\text{C}$, an evaporation of CO_2 caused by the decomposition of the carbonate is observed. Due to this evaporation, the powder is getting porous, but the grain sizes remain in the range of 400 nm and smaller. The total disappearance of the intermediates is observable after calcination at $750 \text{ }^\circ\text{C}$ for ten hours (Fig. 4c, d). The grain coarsening is slightly proceeded to grain sizes up to 700 nm . The calcination at $950 \text{ }^\circ\text{C}$ for two hours produces a powder run through a coarsening of grains to sizes of around a micrometer. On account of the grain growth at the expense of smaller grains the powder gets more and more porous. Figure 4f images the pre-sintering in some parts of the powder. Based on these results a chemical equation for the solid state reaction between the intermediates has been established:



This finding confirms that the primarily formed perovskite crystals possess grain sizes of the same range as those of the crystalline intermediates and that the usual calcination at superior temperatures is not required, even not desirable due to grain coarsening during further heat treatment. Additionally, the pre-sintering of the powder should be avoided in order to facilitate the pressing of the green compact for the ceramic production. Why is the perovskite directly formed without the formation of barium strontium oxides? The decomposition of the carbonate can take place just if it forces a CO_2 potential that is higher than the one in the surrounding atmosphere. The decomposition temperature for the $(\text{Ba}_{0.5}\text{Sr}_{0.5})\text{CO}_3$, which was calculated by the thermodynamic data of the barium and strontium carbonate (Supplementary Information 1), is $808 \text{ }^\circ\text{C}$ and thus higher than the temperature of the perovskite formation. Zinc and iron do not form carbonates

because calculated by thermodynamic data (Supplementary Information 1), in ambient air, zinc carbonate and iron carbonate are not stable above $10 \text{ }^\circ\text{C}$ and $27 \text{ }^\circ\text{C}$, respectively. Including kinetic factors which inhibit the decomposition process the measured temperature for zinc carbonate is in the range of 250 to $290 \text{ }^\circ\text{C}$ and above $300 \text{ }^\circ\text{C}$ for iron carbonate²⁰. Among the iron oxides, the spinel phase is the most stable phase in the relevant temperature range as can be seen from ΔG curves²¹. In presence of Zn, however, the incorporation of Zn^{2+} into the spinel is energetically favourable as ΔG_R lies in the range of -190 to -130 kJ/mole for 500 to $800 \text{ }^\circ\text{C}$ for the reaction²²:



The basis of the perovskite formation process of $(\text{Ba}_{0.5}\text{Sr}_{0.5})(\text{Fe}_{0.8}\text{Zn}_{0.2})\text{O}_{3-\delta}$ is now evidenced, and this knowledge provides new possibilities to optimize the ceramic synthesis. But how general are these results? To verify the assumption that the perovskite oxide formation in an EDTA/citric acid complexing synthesis route might proceed over analogous crystalline intermediates, the $(\text{Ba}_{0.5}\text{Sr}_{0.5})(\text{Co}_{0.8}\text{Fe}_{0.2})\text{O}_{3-\delta}$ perovskite, which is a promising reduced-temperature cathode for SOFCs²³, was also investigated. It was found that after gelation the first crystalline phases were a $(\text{Ba}_{0.5}\text{Sr}_{0.5})\text{CO}_3$ carbonate in the aragonite modification and an $(\text{Fe}_{0.6}\text{Co}_{0.4})\text{Co}_2\text{O}_4$ spinel documented by X-ray diffraction. The diffraction pattern in Figure 5a was measured of a $(\text{Ba}_{0.5}\text{Sr}_{0.5})(\text{Co}_{0.8}\text{Fe}_{0.2})\text{O}_{3-\delta}$ perovskite powder after calcination at $600 \text{ }^\circ\text{C}$ for two hours. In comparison to the diffraction pattern above (Fig. 5b), detected for a $(\text{Ba}_{0.5}\text{Sr}_{0.5})(\text{Fe}_{0.8}\text{Zn}_{0.2})\text{O}_{3-\delta}$ powder run though the same temperature treatment, it badges that the identified phase coincide with a difference in the spinel lattice caused by the diverse cations. With this result we can expect that the perovskite oxide synthesis with EDTA/citric acid complexing methods can proceed with the formation of a spinel and carbonate after the gelation.

For the $(\text{Ba}_{0.5}\text{Sr}_{0.5})(\text{Fe}_{0.8}\text{Zn}_{0.2})\text{O}_{3-\delta}$ perovskite oxide two diffraction pattern in Figure 5c and d exhibit the reaction pathway from the intermediates $(\text{Ba}_{0.5}\text{Sr}_{0.5})\text{CO}_3$ and $(\text{Zn}_{0.6}\text{Fe}_{0.4})\text{Fe}_2\text{O}_4$ towards the perovskite. Upgrading the calcination temperature step by step no other phase transition is detected and the perovskite formation to the expense of the carbonate and the spinel can be observed continuously. This was investigated in steps of $10 \text{ }^\circ\text{C}$ from 600 to $750 \text{ }^\circ\text{C}$ and is shown for the heat treatment from two hours at $600 \text{ }^\circ\text{C}$ to two hours at $750 \text{ }^\circ\text{C}$ to finally pure perovskite at ten hours at $750 \text{ }^\circ\text{C}$. With increasing sizes of crystallites the perovskite reflexes narrow during calcinations indicating a grain coarsening that was also observed by electron microscopy.

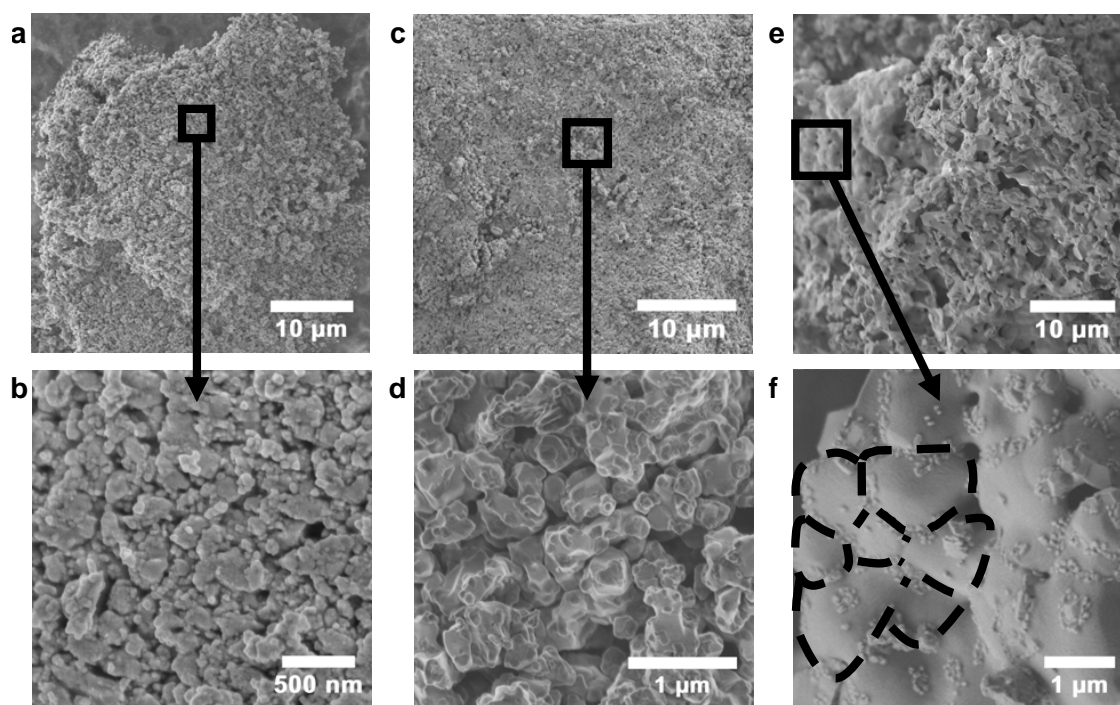


Figure 4. Grain coarsening and gaseous release during calcination at higher temperatures a,b, Scanning electron micrographs (SEM) of an approximately equal amount of intermediates and perovskite containing powder calcined at 650 °C for two hours. Grains are at a size of 400 nm and smaller. c,d, Pure perovskite powder in the SEM after calcination at 750 °C for ten hours. Sizes of the grains are up to 700 nm. The powder gets highly porous because of the release of gaseous CO₂ (Equation 1). e,f, Grain coarsening of perovskite powders to 1 micron after calcination at 950 °C for two hours.

Advanced TEM methods together with SEM and XRD can give important new insight into the initial formation of a perovskite phase. A profound knowledge of the perovskite formation process opens new ways to engage into the microstructure of the underlying ceramic material e.g. to fine tune both grain stoichiometries and grain boundaries in the ceramic material and therewith to optimize the sintering behaviour like lower sintering temperature and shorter time, to get less pores and highly dense ceramics.

We achieved a structural determination of the fine-scale intermixed intermediates formed during the perovskite preparation by employing an EDTA/citrate process as spinel and carbonate in aragonite modification. Thus, a pre-arrangement in groups of cations according to the later A and B sites in the perovskite structure is indicated. TEM and EFTEM as well as EELS provide evidence that the perovskite structure is formed in a nano-scale solid state reaction between the above mentioned intermediates and at their expense. For this purpose not only the elemental composition of the three phases was determined but also the near-edge structures were considered for chemical environment cognition and liken with current literature.

Grain sizes obtained in different perovskite synthesis steps show that the primarily formed perovskite crystals are of the same size as the intermediates and coarsen afterwards during temperature treatment. The common calcination temperature of 950 °C can be decreased to 750 °C to avoid pre-sintering and therewith facilitate the pressing of the green compact for the ceramic production.

In the synthesis of two distinct perovskite oxides by a EDTA/citric acid complexing method it was evidenced that the perovskites form in nano-scale solid state reactions between finely dispersed crystalline intermediates and that the first crystalline intermediates are a complex spinel of the later B site ions and a

complex carbonate of the later A site ions of the perovskite. Hence, it is expected that perovskite oxide syntheses via EDTA/citric acid complexing methods go on generally with the formation of a spinel and carbonate after the gelation.

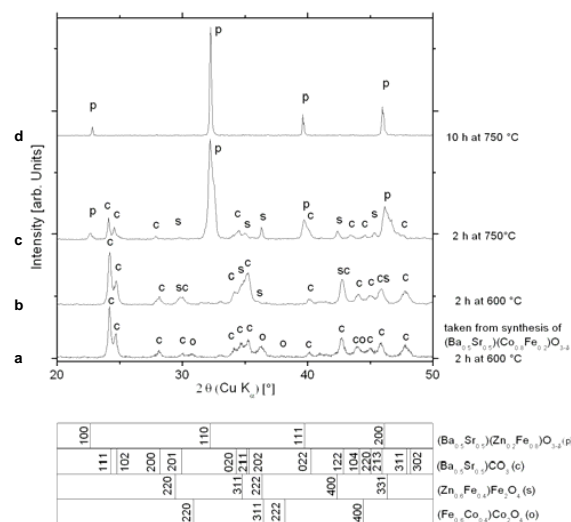


Figure 5. Analogy with synthesis of another perovskite and development from intermediates to perovskite. X-ray diffraction pattern for (Ba_{0.5}Sr_{0.5})(Co_{0.8}Fe_{0.2})O_{3-δ} at 600 °C for two hours provides evidence that the perovskite formation proceeds over analogous intermediates (spinel and carbonate) like for the synthesis of (Ba_{0.5}Sr_{0.5})(Fe_{0.8}Zn_{0.2})O_{3-δ}. The latter is formed by treatments of two hours at 600 °C over two hours at 750 °C to 10 hours at 750 °C. The intermediates start to vanish due to the formation of the perovskite.

Experimental

A synthesis method with combined citric acid and EDTA acid as the complexing agents was applied. A given amount of Ba(NO₃)₂ powder was dissolved in an aqueous solution of Zn(NO₃)₂, Fe(NO₃)₃, and Sr(NO₃)₂, followed by the addition of EDTA acid. After agitation for a certain time, a proper amount of citric acid was introduced, with the molar ratio of EDTA acid : citric acid : total of metal cations controlled at around 1:1.5:1. After addition of NH₃·H₂O, the pH value of the solution was adjusted in the range of 6 to 9 by the addition of supplementary NH₃·H₂O. Water was evaporated with stirring in the temperature range of 120 - 150 °C. After evaporation for several hours the transparent solution transformed into a dark purple gel. Further heat treatments were applied at temperatures up to 950 °C.

Transmission electron microscopy (TEM) was performed at 200 kV on a field-emission instrument of the type JEOL JEM-2100F with an ultra-high resolution pole piece (C_s = 0.5 mm) that provides a point-resolution better than 0.19 nm. Moreover, the microscope was equipped with an energy filter of the type Gatan GIF 2001 with a 1k-CCD camera. The filter was employed to acquire energy-filtered transmission electron micrographs (EFTEM) and electron energy-loss spectra (EELS) with a special emphasis on energy-loss near-edge structures (ELNES) at ionization edges. Powders were prepared for TEM investigations by crushing them by mortar and pestle and afterwards epoxy gluing them between two silicon single crystals. Further preparation was made by cutting 1×1.5×3 mm pieces and polishing them on polymer embedded diamond lapping films to 0.01×1×2.5 mm, approximately. Finally, Ar⁺ ion sputtering was employed at 3 kV (Gatan, model 691 PIPS, precision ion polishing system) under shallow incident angles of 4-8 degrees until electron transparency was achieved.

Scanning electron microscopy (SEM) was employed on a field-emission instrument of the type JEOL JSM-6700F. Secondary electron (SE) micrographs were taken at low excitation voltages in the range of 0.5 to 2 kV.

X-ray diffraction (XRD) was performed on a Philips X'pert - MPD instrument using monochromator-filtered Cu-K_α radiation at 40 kV and 40 mA, receiving slit of 0.15mm and count times of 3 s/step. Data were collected in a step-scan mode in the range of 20° - 50° with intervals of 0.03°. Data for interpretation were taken from the PDF-2 database with PDF numbers FeFe₂O₄ [19-629], ZnFe₂O₄ [22-1012], CoFe₂O₄ [3-864], BaCO₃ [45-1471], SrCO₃ [5-418], SrFeO_{3-x} [34-641], BaFeO₃ [147-180]. Lattice parameters for the exact stoichiometries have been calculated according to homogeneous solid solutions.

- [1] a) S. Irusta, M. P. Pina, M. Menéndez, J. Santamaria, *Catal. Lett.* **1998**, 54, 69, b) N. Labhsetwar, R. B. Biniwale, R. Kumar, S. Rayalu, S. Devotta, *Catal. Surv. Asia* **2006**, 10, 55, c) X. Chen, J. Strozier, N. J. Wu, A. Ignatiev, Y. B. Nian, *New J. Phys.* **2006**, 8, 229, d) C. H. Ahn, J.-M. Trisconne, J. Mannhart, *Nature* **2003**, 424, 1015, e) D. Dimos, C. H. Mueller, *Annu. Rev. Mater. Sci.* **1998**, 28, 397, f) R. Li, Q. Tang, S. Yin, T. Sato, *Plasma Chem. Plasma Process.* **2006**, 28, 267, g) V. Thangadurai, W. Weppner, *J. Electrochem. Soc.* **2004**, 151, H1, h) P. Laffez, M. Zaghrioui, L. Reversat, P. Ruello, *Appl. Phys. Lett.* **2006**, 89, 081909, i) T. Liu, X.-Z. Zhao, W. Chen, *J. Am. Ceram. Soc.* **2006**, 89, 1153.
- [2] a) Z.-J. Li, R.-Q. Liu, J.-D. Wang, Y.-H. Xie, F. Yue, *J. Solid State Electrochem.* **2005**, 9, 201, b) J. Pérez-Ramírez, B. Vigeland, *Angew. Chem. Int. Ed.* **2005**, 44, 1112, c) Y. Mao, S. S. Wong, *Adv. Mater.* **2005**, 17, 2194, d) A. Weidenkaff, *Adv. Eng. Mater.* **2004**, 6, 709.
- [3] H. Yokokawa, N. Sakai, T. Kawada, M. Dokiya, *Solid State Ionics* **1992**, 52, 43.
- [4] a) A. Esquirol, N. P. Brandon, J. A. Kilner, M. Mogensen, *J. Electrochem. Soc.* **2004**, 151, A1847, b) S. Tao, J. T. S. Irvine, *Adv. Mater.* **2006**, 18, 1581, c) T. Ishihara, *Bull. Chem. Soc. Jpn.* **2006**, 76, 1155, d) Q. X. Fu, F. Tietz, D. Stöver, *J. Electrochem. Soc.* **2006**, 153, D74, e) M.-F. Hsu, L.-J. Wu, J.-M. Wu, Y.-H. Shiu, K.-F. Lin, *Electrochem. Solid-State Lett.* **2006**, 9, A193, f) S. Tao, J. T. S. Irvine, J. A. Kilner, *Adv. Mater.* **2005**, 17, 1734.
- [5] H. Teraoka, H.-M. Zhang, S. Furukawa, N. Yamazoe, *Chem. Lett.* **1985**, 11, 1743.
- [6] R. Merkle, J. Maier, H. J. M. Bouwmeester, *Angew. Chem. Int. Ed.* **2004**, 43, 5069.
- [7] a) M. Liu, V. Joshi, Y. Shen, K. Krist, *US Patent* **1993**, 5, 273,628, b) U. Balachandran, J. T. Dusek, R. L. Mieville, R. B. Poeppl, M. S. Kleefisch, S. Pei, T. P. Kobylinski, C. A. Udovich, A. C. Bose *Appl. Catal., A* **1995**, 133, 19, c) H. Wang, Y. Cong, W. Yang, *J. Membr. Sci.* **2002**, 209, 143, d) H. Wang, Y. Cong, X. Zhu, W. Yang, *React. Kinet. Catal. Lett.* **2003**, 79, 351, e) C. Hamel, A. Seidel-Morgenstern, T. Schiestel, S. Werth, H. Wang, C. Tablet, J. Caro, *AIChE J.* **2006**, 52, 3118, f) H. Wang, S. Werth, T. Schiestel, J. Caro, *Angew. Chemie Int. Ed.* **2005**, 44, 6906.
- [8] H. J. M. Bouwmeester, A. J. Burggraaf, in *Fundamentals of Inorganic Membrane Science and Technology*, Vol. 4, (Eds: A. J. Burggraaf, L. Cot) Elsevier Science B.V., Amsterdam, Netherlands **1996**, Ch. 10.
- [9] Z. Shao, W. Yang, Y. Cong, H. Dong, J. Tong, G. Xiong, *J. Membr. Sci.* **2000**, 172, 177.
- [10] J. Páris, R. Páris, *Bull. Soc. Chim. Fr.* **1965**, 4, 1138.
- [11] C. Marcilly, P. Courty, B. Delmon, *J. Am. Ceram. Soc.* **1970**, 53, 56.
- [12] H. Wang, G. Grubert, C. Tablet, J. Caro, *Patent*, **2005**, EP 0402056.
- [13] H. Wang, C. Tablet, A. Feldhoff, J. Caro, *Adv. Mater.* **2005**, 17, 1785.
- [14] M. M. Disko, C. C. Ahn, B. Fultz, in *Electron Energy Loss Spectrometry in Materials Science*, 2nd Ed. TMS, Warrendale, Pennsylvania **2001**.
- [15] J. L. Mansot, V. Golabkan, L. Romana, T. Césaire, *J. Microsc.* **2003**, 210, 110.
- [16] L. A. J. Garvie, P. R. Buseck, *Nature* **1998**, 396, 667.
- [17] a) C. C. Calvert, A. Brown, R. Brydson, *J. Electron Spectrosc. Rel. Phenom.* **2005**, 143, 173, b) F. T. Docherty, A. J. Craven, D. W. McComb, J. Skakle, *Ultramicroscopy* **2001**, 86, 273.
- [18] A. S. Sefat, G. Amow, M.-Y. Wu, G. A. Botton, J. E. Greedan, *J. Solid State Chem.* **2005**, 178, 1008.
- [19] a) H. M. Zhang, T. Teraoka, N. Yamazoe, *Chem. Lett.* **1987**, 4, 665, b) R. H. E. van Doorn, H. Kruidhof, A. Nijmeijer, L. Winnubst, A. J. Burggraaf, *J. Mater. Chem.* **1998**, 8, 2109.
- [20] a) A. M. Gadalla, *Int. J. Chem. Kinet.* **1984**, 16, 1471. b) R. J. Meyer, *Gmelin Handbook of Inorganic Chemistry*, 8th edition, Syst. Nr. 59, Fe, Tl. B, Chemie, Berlin, **1932**, 508.
- [21] R.A. Swalin, *Thermodynamics of Solids*, Wiley, New York, p. 84, **1962**.
- [22] I. Barin, F. Sauer, G. Patzki, *Thermochemical Data of Pure Substances*, 3rd edition, Vol. I & Vol. II, VCH Weinheim, **1995**.
- [23] Z. Shao, S. M. Haile, *Nature* **2004**, 431, 170.

2.3 The sol-gel synthesis of perovskites by an EDTA/citrate complexing method involves nanoscale solid state reactions

Armin Feldhoff, Mirko Arnold, Julia Martynczuk,

Thorsten M. Gesing, and Haihui Wang

Solid State Sciences 10, 689-701 (2008)

Available online at www.sciencedirect.com

Solid State Sciences 10 (2008) 689–701

www.elsevier.com/locate/ssscie

The sol–gel synthesis of perovskites by an EDTA/citrate complexing method involves nanoscale solid state reactions

A. Feldhoff^{a,*}, M. Arnold^a, J. Martynczuk^a, Th.M. Gesing^b, H. Wang^{a,c}

^a Institute of Physical Chemistry and Electrochemistry, Leibniz Universität Hannover, Callinstraße 3-3A, D-30167 Hannover, Germany

^b Institute of Mineralogy, Leibniz Universität Hannover, Welfengarten 1, D-30167 Hannover, Germany

^c College of Chemical and Energy Engineering, South China University of Technology, Guangzhou 510640, PR China

Received 26 January 2007; received in revised form 1 June 2007; accepted 19 November 2007

Available online 28 January 2008

On the occasion of the 75th birthday of Prof. Schmalzried.

Abstract

Nowadays, sol–gel procedures are well established in the synthesis of complex oxides as they allow to obtain phase pure products and to control precisely their stoichiometry. This quality makes them a tool of choice for the preparation of perovskite-type oxides. To optimize the functional properties of these materials, it is essential to set accurately their possible complex stoichiometries. However, details of the formation of the perovskite crystal remain obscure. Different stages of an ethylene-diamine-tetraacetic acid (EDTA)/citrate-gel based synthesis process for mixed conducting $(\text{Ba}_{0.5}\text{Sr}_{0.5})(\text{Fe}_{0.8}\text{Zn}_{0.2})\text{O}_{3-\delta}$ of cubic perovskite structure are elucidated. The combination of analytical transmission electron microscopy with X-ray diffraction reveals that the perovskite-type oxide is formed already at moderate temperatures at around 700 °C via nanoscale solid state reactions between finely-dispersed crystalline intermediates identified as a spinel and a carbonate. The reaction scheme, however, is intricate and includes stuffed tridymite structures as transient phases. The ultrafine intermixing of extremely small reactants makes EDTA/citrate-gel based procedures superior to classical solid state routes with respect to applications that demand phase purity and stoichiometry control.

© 2007 Elsevier Masson SAS. All rights reserved.

Keywords: Sol–gel synthesis; Perovskite; Reaction mechanism; Transmission electron microscopy; Carbonate; Spinel; Stuffed tridymite; Rietveld refinement; Ellingham diagram

1. Introduction

Conventionally, complex oxides are prepared by the solid state route that is the blending of powdered reactants, mostly oxides and carbonates, and their firing at temperatures as high as 1200 °C. At these high temperatures the loss of the most volatile component may easily occur leading to non-stoichiometric products with decreased functional properties.

Alternative chemical synthesis processes have been introduced in the 1960s by the thermal decomposition of stirred metal–organic complexes that employ distinctly lower temperatures in the range of 600–700 °C [1,2,3]. All these processes rely on the chemistry of gels that contain all the cations in the desired ratios [4,5]. Even though variants of these sol–gel procedures are widely used today, details of the formation of the final crystalline product are still little known. The combined ethylene-diamine-tetraacetic acid (EDTA)/citrate complexing method under investigation has been introduced some years ago [6]. It has been shown elsewhere [7–9] that complex oxides of cubic perovskite structure are formed in nanoscale solid state reactions between carbonate and spinel intermediates. The general reaction scheme has been outlined for the perovskite stoichiometries $(\text{Ba}_{0.5}\text{Sr}_{0.5})(\text{Fe}_{0.8}\text{Zn}_{0.2})\text{O}_{3-\delta}$ and

* Corresponding author. Tel.: +49 511 762 2940; fax: +49 511 762 19121.

E-mail addresses: armin.feldhoff@pci.uni-hannover.de (A. Feldhoff), mirko.arnold@pci.uni-hannover.de (M. Arnold), julia.martynczuk@pci.uni-hannover.de (J. Martynczuk), tm.gesing@mineralogie.uni-hannover.de (Th.M. Gesing), haihui.wang@pci.uni-hannover.de, wanghh@scut.edu.cn (H. Wang).

$(\text{Ba}_{0.5}\text{Sr}_{0.5})(\text{Co}_{0.8}\text{Fe}_{0.2})\text{O}_{3-\delta}$. The present study is devoted to details of the formation of the Zn-containing perovskite that turns out to be intricate on the atomic scale.

2. Materials and methods

The synthesis process is evaluated for a perovskite-type oxide that is a prospective membrane material for oxygen separation technologies [10–12] or electrode material for solid oxide fuel cells [13]. In the temperature range of 700–950 °C, $(\text{Ba}_{0.5}\text{Sr}_{0.5})(\text{Fe}_{0.8}\text{Zn}_{0.2})\text{O}_{3-\delta}$ [14,15] is a mixed electron and oxygen conductor that provides high oxygen fluxes and exhibits an excellent phase stability even under low oxygen partial pressures, superior to other compositions.

The processing route employs both citric acid and EDTA as the complexing and gelation agents [6] and has been adapted for the specific stoichiometry under investigation. Proper amounts of $\text{Ba}(\text{NO}_3)_2$, $\text{Sr}(\text{NO}_3)_2$, $\text{Fe}(\text{NO}_3)_3$, and $\text{Zn}(\text{NO}_3)_2$ were dissolved in water followed by the addition of citric acid, EDTA and NH_3 . In the temperature range of 120–150 °C, the reaction mixture was then heated under constant stirring to obtain a purple-coloured gel. Afterwards, the gel was pre-calcined for 1 h at 700 °C. The pre-calcined powders were grounded and heated at temperatures up to 750 °C with a heating rate of 3 °C/min. Intermediates as well as final products were analyzed by several techniques that are described below.

X-ray diffraction (XRD) was conducted in a $\theta/2\theta$ geometry on a Philips X'pert-MPD instrument using monochromated $\text{Cu K}\alpha_{1,2}$ radiation at 40 kV and 40 mA, receiving slit of 0.15 mm and count times of 5 s/step. Data were collected in a step-scan mode in the 2θ range of 20–50° with intervals of 0.03°.

Data for interpretation were taken from the ICDD PDF-2 database with PDF numbers FeFe_2O_4 [19-629], ZnFe_2O_4 [22-1012], Fe_2O_3 [33-664], SrFeO_{3-x} [34-641], and BaFeO_{3-x} [147-180]. Lattice parameters for the exact stoichiometries have been calculated according to homogeneous solid solutions. To index experimental data related to $(\text{Ba}_{0.5}\text{Sr}_{0.5})\text{CO}_3$, the structure has been described with unit cell parameters according to Ref. [16]. To index data related to $(\text{Ba}_{1-x}\text{Sr}_x)\text{Fe}_2\text{O}_4$, the structure has been described in space group $\text{Cmc}2_1$ (No. 36) based on the structure given in Ref. [17].

For structure refinements of the product phase, X-ray powder diffraction data were collected on a Bruker AXS D8 Advance diffractometer using a transmission geometry, a Göbel mirror and $\text{Cu K}\alpha_{1,2}$ radiation. Six thousand data points were collected with a step width of 0.02° in the 2θ range from 20° to 140°. XRD powder data Rietveld refinements were carried out by using TOPAS 3.0 (Bruker AXS) software. During refinements, general parameters such as the scale factor, seven background parameters and the zero point of the counter were optimized. Profile shape calculations were carried out on the basis of standard instrumental parameters using the fundamental parameter method implemented in the program, varying also the average crystal size (integral breadth) and the strain parameter ϵ_0 (FWHM based strain calculation assuming intermediate strain broadening modelled by a Voigt

function giving $\Delta d/2\theta$ with a 50% probability). Additionally, the cell parameter and the displacement parameters were refined. In the case of site occupation with mixed atoms, linear constraints were used for occupancy (occupancy of atom B is equivalent to 1.0 minus occupancy of atom A) and displacement parameters (atoms on the same position have the same displacement parameter).

Transmission electron microscopy (TEM) and scanning transmission electron microscopy (STEM) were performed at 200 kV on a field-emission instrument of the type JEOL JEM-2100F. The microscope was equipped with an ultra-high-resolution pole piece that provides a point-resolution better than 0.19 nm (spherical aberration constant $C_s = 0.5$ mm, chromatic aberration constant $C_c = 0.5$ mm) and allowed to make high-resolution transmission electron microscopy (HRTEM). STEM was conducted in high-angle annular dark-field (HAADF) contrast that allows to obtain mass-thickness information. The microscope was equipped with an energy filter of the type Gatan GIF 2001 with a 1k charge-coupled-device (CCD) camera. The filter was used to enhance the dynamics in selected area electron diffraction (SAED) pattern by elastic filtering with a bandwidth of 15 eV. The filter was employed as well to acquire electron energy-loss spectra (EELS) of core-loss energies with a special emphasis on energy-loss near-edge structures (ELNES) at ionization edges. To obtain elemental maps via energy-filtered transmission electron microscopy (EFTEM), the three-window technique was utilized with 40 eV energy slit and power law model [18]. For the Fe-L edge energy slits were centered at 643, 683 eV (pre-edge) and 728 eV (post-edge). To avoid any overlap with Fe-L signals, for the Ba-M edge energy slits were centered at 661, 751 eV (pre-edge) and 801 eV (post-edge). Individual exposure times were 30 s, respectively. Elemental analysis by energy-dispersive X-ray spectroscopy (EDXS) was made using an Oxford Instruments INCA-200-TEM system with an ultra-thin window that was attached to the microscope.

To obtain specimen for TEM, dried gel was crushed in ethanol by mortar and pestle. The suspension was dropped from a pipette to a 300-mesh copper-supported carbon foil (Quantifoil) that was placed on a piece of filter paper to wick away excess ethanol. Calcined powders were prepared for TEM investigations by epoxy gluing them between two pieces of silicon wafer. These sandwiches were cut into $1 \times 1.5 \times 3$ mm rectangular pieces and polished in cross-section on polymer embedded diamond lapping films down to $0.01 \times 1 \times 2.5$ mm, approximately (Allied High Tech, Multiprep). Thinned sandwiches were glued onto a copper slot grid, respectively, and Ar^+ ion sputtered at 3 kV under an incident angle of 6° (Gatan, model 691 PIPS, precision ion polishing system) until electron transparency was achieved.

A quantity of 2 g of pure $(\text{Ba}_{0.5}\text{Sr}_{0.5})\text{CO}_3$ powder and $(\text{Zn}_{0.6}\text{Fe}_{0.4})\text{Fe}_2\text{O}_4$ powder was synthesized by the EDTA/citrate method, and phase purity and crystal size were determined by SEM (JEOL JSM-6700F), respectively. Experimental determination of the CO_2 equilibrium pressure above the carbonate as a function of temperatures was performed in

a quartz glass equipment flanged to a turbo molecular pump. After sealing and evacuating the equipment from atmospheric pressure to 1 Pa and heating to 700 °C, the pressure was measured with a Pirani gage in steps of 50 °C up to 1000 °C after equilibration times of ca. 1/2 h, respectively.

3. Results and discussion

3.1. Early stages

Gelation takes place in the temperature range of 120–150 °C due to the release of water and is accompanied by the evaporation of ammonia. This leads to a decrease of the nitrogen and oxygen content as it is shown elsewhere [7]. Fig. 1 shows a magnification series of Z-contrast HAADF micrographs of the gel after 18 h at 150 °C. The gel is characterized by a fine dispersion of metal complexes (high Z) in a polymerized network (low Z). Individual metal atoms or clustered metal complexes give rise to strong electron scattering

and thus bright contrast in the micrographs. The polymeric matrix composed of atoms with much lower scattering cross-sections appears with grey contrast. Concerning the stability constants for the complex formation K given logarithmically in Table 1, the distinctly higher K -values for EDTA for all four cations make a total complexation with EDTA most likely. On the contrary, the citric acid contributes to the gelation, and formation of a polymeric network, by a condensation due to the esterification of the alcohol group of the citric acid molecule with the carboxyl group of another citric acid molecule or an EDTA molecule. In Fig. 1a and b some relatively large clusters of metal complexes with sizes of around 15 nm are present. Predominantly, cluster sizes are distinctly smaller as it can be seen in Fig. 1c and d. An eminent fraction of clusters is around 5 nm in size. Moreover, the close-up in Fig. 1d shows structural details with sizes of just 1 nm that hint to the presence of very small individual clusters of metal complexes. In conclusion, the sol–gel method prevails a very fine intermixing of metal cations on the nanometer scale.

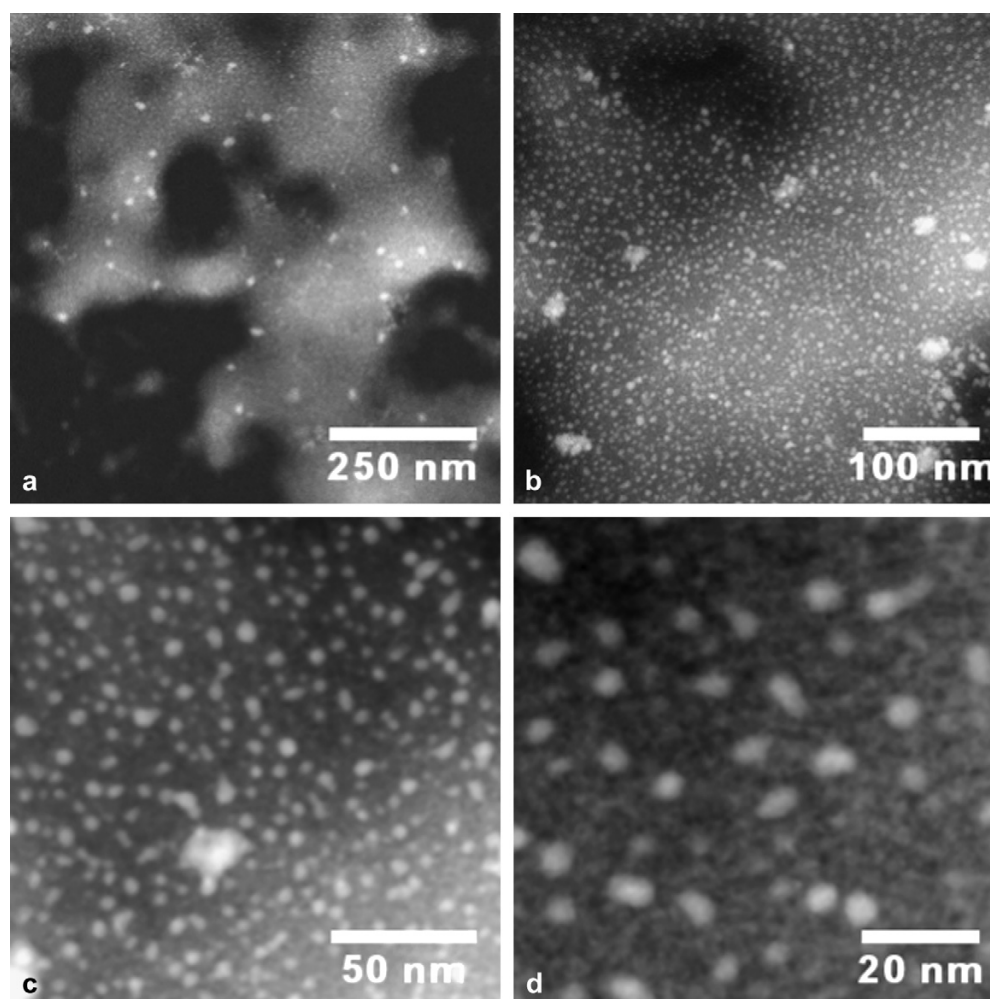


Fig. 1. Magnification series in high-angle annular dark-field contrast of the gel after 18 h at 150 °C.

Table 1
Complex forming constants of metal cations (from Refs. [19,20])

	EDTA, log <i>K</i>	Citric acid, log <i>K</i>
Ba ²⁺	7.86	2.73
Sr ²⁺	8.74	3.02
Fe ³⁺	25.1	11.2
Zn ²⁺	16.5	4.76

3.2. Crystalline intermediates and perovskite

During further heating the gel starts to crystallize at about 550–600 °C under the formation of intermediate phases that can be detected by XRD. Typical diffraction pattern after 1 h at 700 °C are given for three preparations in Fig. 2a–c showing reflections from an aragonite-type carbonate (Fig. 2a,c and f) and spinel-type (Zn_{0.6}Fe_{0.4})Fe₂O₄ oxide (Fig. 2b,c and g). During cumulated further heat treatments of the powder in

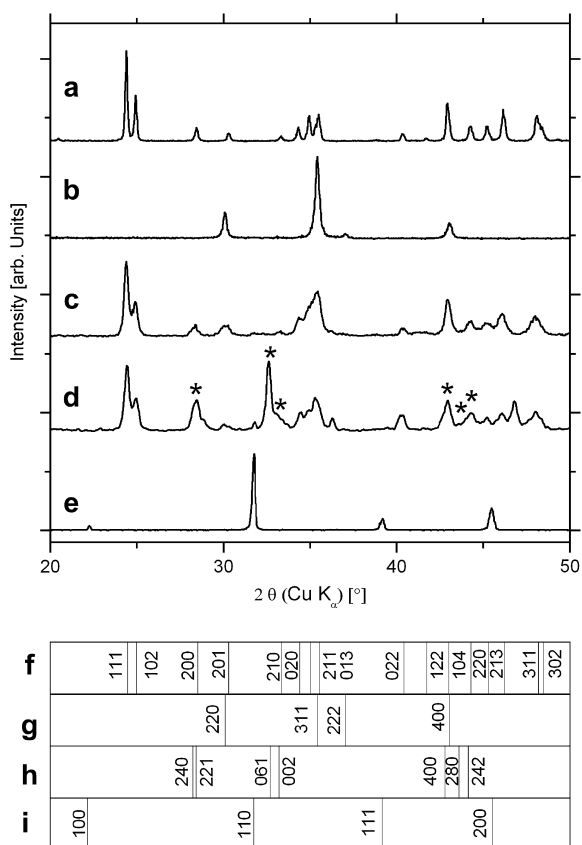
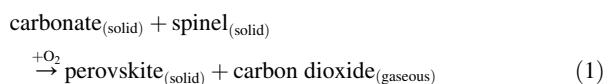


Fig. 2. X-ray powder diffraction of intermediates and perovskite. (a) Taken from the synthesis of (Ba_{0.5}Sr_{0.5})CO₃ after 10 h at 750 °C, (b) taken from the synthesis of (Zn_{0.6}Fe_{0.4})Fe₂O₄ after 1 h at 700 °C, (c–e) taken from the synthesis of (Ba_{0.5}Sr_{0.5})(Fe_{0.8}Zn_{0.2})O_{3–δ} after (c) 1 h at 700 °C, (d) additional 12 h at 700 °C, (e) additional 10 h at 750 °C. (f–i) Assignment of diffraction lines for different phases: (f) aragonite-type (Ba_{0.5}Sr_{0.5})CO₃ carbonate, (g) (Zn_{0.6}Fe_{0.4})Fe₂O₄ spinel, (h) γ-(Ba_{0.5}Sr_{0.5})Fe₂O₄, (i) perovskite-type (Ba_{0.5}Sr_{0.5})(Fe_{0.8}Zn_{0.2})O_{3–δ}.

Fig. 2c, the reflections of the intermediate phases become smaller, reflections of a further transient phase of stuffed tridymite-type oxide arise (Fig. 2d), and finally the perovskite structure is formed (Fig. 2e).

Fig. 2d shows an XRD pattern after heating the powder additionally 12 h at 700 °C. The reflections of the intermediates are less pronounced and broad reflections of a Ba–Sr–Fe oxide dominate (marked by stars), which can be compared to a γ-(Ba_{0.5}Sr_{0.5})Fe₂O₄-type phase (Fig. 2h). More details concerning the transient phase are discussed below in context of Fig. 7. After additional heating for 10 h at 750 °C, the intermediate and transient phases are completely vanished and a pure perovskite powder is obtained (Fig. 2e and i).

The XRD analysis points to a solid state reaction in the nanoscale powder between the intermediates of the following simplified type:



The liberation of gaseous CO₂ is manifested in the evolution of a porous sponge-like solid that has been investigated by scanning electron microscopy [7,8]. Details of this reaction are, however, more intricate as it is manifested in additional transient phases. All involved phases are discussed in the following.

3.2.1. Rietveld refinement of the (Ba_{0.5}Sr_{0.5})(Fe_{0.8}Zn_{0.2})O_{3–δ} product

The stoichiometry of the product has been determined by EDXS during TEM experiments to be close to (Ba_{0.5}Sr_{0.5})(Fe_{0.8}Zn_{0.2})O_{3–δ} as is described elsewhere [14]. By XRD (Fig. 3), the perovskite was found to crystallize in the cubic space group *Pm-3m* (No. 221) with a lattice parameter of 0.39900(2) nm. Barium and strontium were refined on the same crystallographic position 1a (0,0,0) with 52(2)% occupation for the barium atoms corresponding to the chemical analysis and a displacement parameter of *B* = 1.4(1). Iron (80%) and zinc (20%) were calculated on the 1b (1/2,1/2,1/2) position showing a high displacement of *B* = 2.4(1). An individual refinement of the occupancy parameters for this position is not possible. An equivalent high displacement of *B* = 3.1(5) was found for the oxygen atoms on the 3c (0,1/2,1/2) site. These higher displacement parameters correspond to a strain parameter of $\epsilon_0 = 0.157(5)$ expressing the high distortion in the structure caused by the mixed occupancy of the anionic positions in combination with the oxygen deficit introduced by the lower 2+ charge of the zinc atoms in relation to the 2+/3+/4+ charge value of iron atoms. Refining the occupancy parameters of the oxygen atoms, only 81(2)% could be found. This could be a hint for a mainly 2+/3+ oxidation state for the iron atoms, but it has to be taken into account that the error for the occupancy parameter is difficult to calculate caused by the high scattering power of the cations in the structure. The refinement converged to reliability factors of *R*_{WP} = 0.053 and *P*_P = 0.042 for the pattern with a goodness of fit = 1.01, a Durban–Watson parameter of 1.92, and Bragg *R*-value of

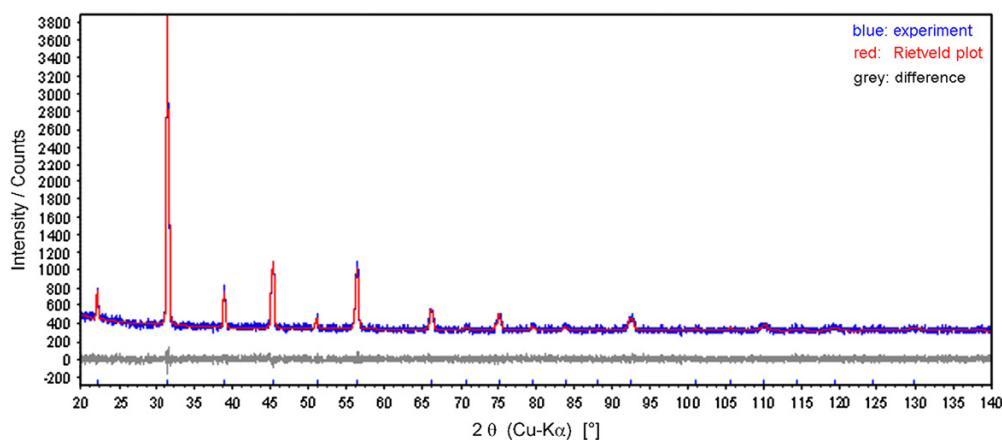


Fig. 3. Rietveld plot of $(\text{Ba}_{0.5}\text{Sr}_{0.5})(\text{Fe}_{0.8}\text{Zn}_{0.2})\text{O}_{3-\delta}$. The observed (blue) and calculated (red) intensities together with the difference between the observed and calculated pattern (grey) as well as the possible reflex position (tick marks) are given.

0.007 for the perovskite structure. Further details could be taken from CSD-No. 418850 [40]. Additionally, the average crystal size was found to be 56(2) nm ($L_{\text{Vol-IB}}$).

3.2.2. The mixed carbonate $(\text{Ba}_{0.5}\text{Sr}_{0.5})\text{CO}_3$

Very detailed considerations on the structure of the aragonite-type $(\text{Ba}_{0.5}\text{Sr}_{0.5})\text{CO}_3$ carbonate are given elsewhere [7]. XRD pattern of the mixed carbonate indicates unit cell parameters $a = 0.62450$ nm, $b = 0.52020$ nm, and $c = 0.86420$ nm in space group $Pnma$ (No. 62) which agrees well with data according to Ref. [16] but deviates slightly from values given by us elsewhere [7]. However, regarding the stability of the carbonate at the applied temperatures, an Ellingham diagram has been examined which is based on calculations that are valid for bulk phases [7]. For nanocrystalline powders, the influence of the surface cannot be neglected, and the Thomson–Freundlich equation [21] predicts a higher chemical potential of carbon dioxide, μ_{CO_2} , with respect to bulk phases. Consequently, the decarbonation temperature will decrease with decreasing particle size.

Thus, a pure $(\text{Ba}_{0.5}\text{Sr}_{0.5})\text{CO}_3$ powder with crystal sizes below 100 nm has been synthesized, and CO_2 equilibrium pressures have been measured. In the temperature range of 850–1000 °C, the CO_2 pressure above the nano-sized carbonate increases from about 100 Pa to 2.3 kPa. Data points have been connected with a spline function, and within the experimental error, the experimental curve lies slightly above the estimation from the Ellingham diagram (Fig. 4a). Considering the corresponding chemical potential, μ_{CO_2} , each experimental data point has been put into the Ellingham diagram in Fig. 4b by squared points. Their positions deviate slightly to higher values compared to the calculated mixed carbonate in bulk phase (dashed line) are interpolated by the respective solid line.

In contrast to the presentation in Ref. [7], the calculated Ellingham diagram in Fig. 4b gives directly the chemical potential of carbon dioxide, μ_{CO_2} , in dependence of the temperature.

Different partial pressures of CO_2 are considered as well as equilibrium values over mixtures of carbonates (BaCO_3 , SrCO_3) and rocksalt-type oxides (BaO , SrO). The line that presents μ_{CO_2} above a mixture of $(\text{Ba}_{0.5}\text{Sr}_{0.5})\text{CO}_3$ and $(\text{Ba}_{0.5}\text{Sr}_{0.5})\text{O}$ is assumed to lie symmetrically between those of the simple carbonate/oxide mixtures, indicated by a dashed line.

As mentioned above, liberated CO_2 can easily evaporate through the porous sponge-like body of the reaction product. As all experiments were done under ambient atmospheres, it is assumed that isobaric conditions apply; with the partial pressure of CO_2 being that in air, $p_{\text{CO}_2} = 30$ Pa. The carbonate would thermally decompose if its oxidation forces a chemical potential of CO_2 that is higher than in the surrounding atmosphere. Considering bulk $(\text{Ba}_{0.5}\text{Sr}_{0.5})\text{CO}_3$, a decomposition temperature of 808 °C is read from Fig. 4b as the intersection point of the “ p_{CO_2} in air” line with the respective carbonate line (dashed). Considering the experimental data points (square brackets), the line valid for the nano-sized carbonate is shifted up by approximately 4 kJ/mol (solid line) so that the decomposition temperature lies at about 790 °C. The analysis indicates that the decarbonation temperature of the nano-sized carbonate is decreased by ca. 20 °C with respect to bulk carbonate. But it is still approximately 40 °C higher than the highest applied temperature of 750 °C, and thus stability considerations support the solid state reaction pathway that is given in Eq. (1).

However, in powder reactions the reaction interface is large; especially if nanoscale powders are considered. This can lead to the liberation of large amounts of heat [23,24] and consequently to local overheating. Despite the moderate heating rate of 3 °C/min up to a nominal maximum temperature of just 750 °C makes it unlikely that in any of the experiments discussed here, the decomposition temperature of the carbonate (ca. 790 °C) has been exceeded. This is supported also by the fact that there have been observed in nanoscale reactions neither BaO nor SrO nor $(\text{Ba}_{0.5}\text{Sr}_{0.5})\text{O}$.

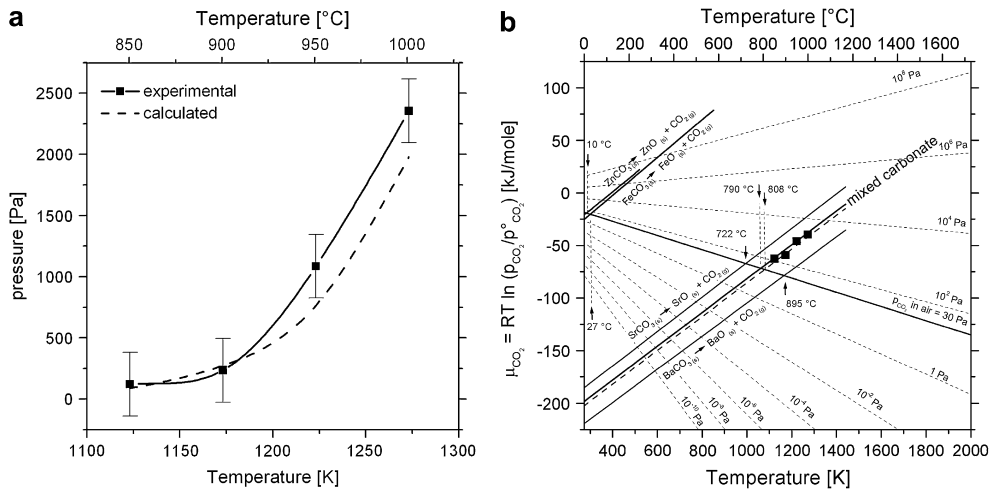


Fig. 4. (a) Experimental and calculated equilibrium CO₂ pressures above (Ba_{0.5}Sr_{0.5})CO₃ as a function of temperature, (b) chemical potential of CO₂ versus temperature plots for different partial pressures including equilibrium values above barium and strontium carbonates. Experimental data are added as squares. Calculations have been made after thermodynamic data [22] with reference to standard conditions ($p_{\text{CO}_2}^0 = 101.3 \text{ kPa}$).

Fig. 4b contains also μ_{CO_2} plots for ZnCO₃ and FeCO₃ to illustrate that a formation of these carbonates do not play any role in the solid state reaction scheme.

3.2.3. The complex spinel (Zn_{0.6}Fe_{0.4})Fe₂O₄

To prove the formation of the (Zn_{0.6}Fe_{0.4})Fe₂O₄ spinel during the perovskite synthesis, the sol–gel method was

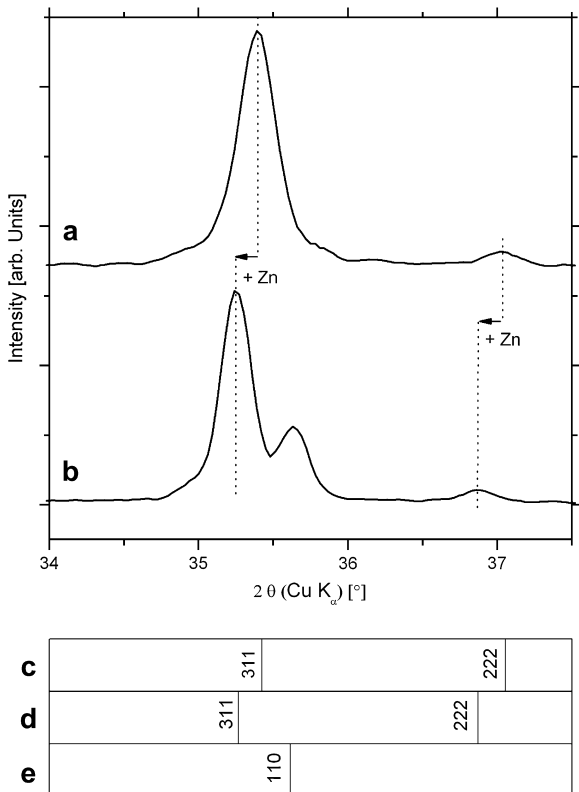


Fig. 5. X-ray powder diffraction: taken from the synthesis of (Zn_{0.6}Fe_{0.4})Fe₂O₄ (a) after 1 h at 700 °C, (b) after 10 h at 750 °C, (c) Fe₂O₃ (magnetite), (d) ZnFe₂O₄ (franklinite), (e) α-Fe₂O₃ (hematite).

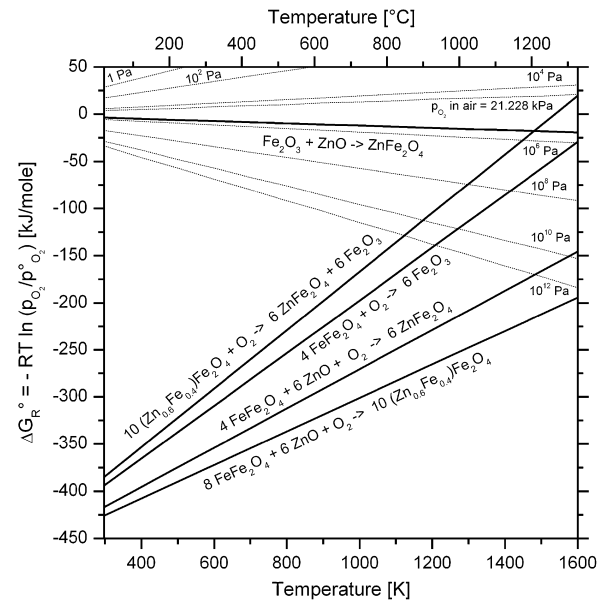


Fig. 6. Thermodynamic calculations for the system Zn–Fe–O under different O₂ partial pressures [22]. Free enthalpy of formation for the (Zn_{0.6}Fe_{0.4})Fe₂O₄ spinel has been calculated in consideration of the activities according to Ref. [26]. Standard free enthalpies of O₂ versus temperature plots for different partial pressures are shown with dashed lines in the range of 1–10¹² Pa ($p_{\text{O}_2}^0 = 101.3 \text{ kPa}$). All reactions illustrated proceed under atmosphere conditions (p_{O_2} in air = 21.3 kPa).

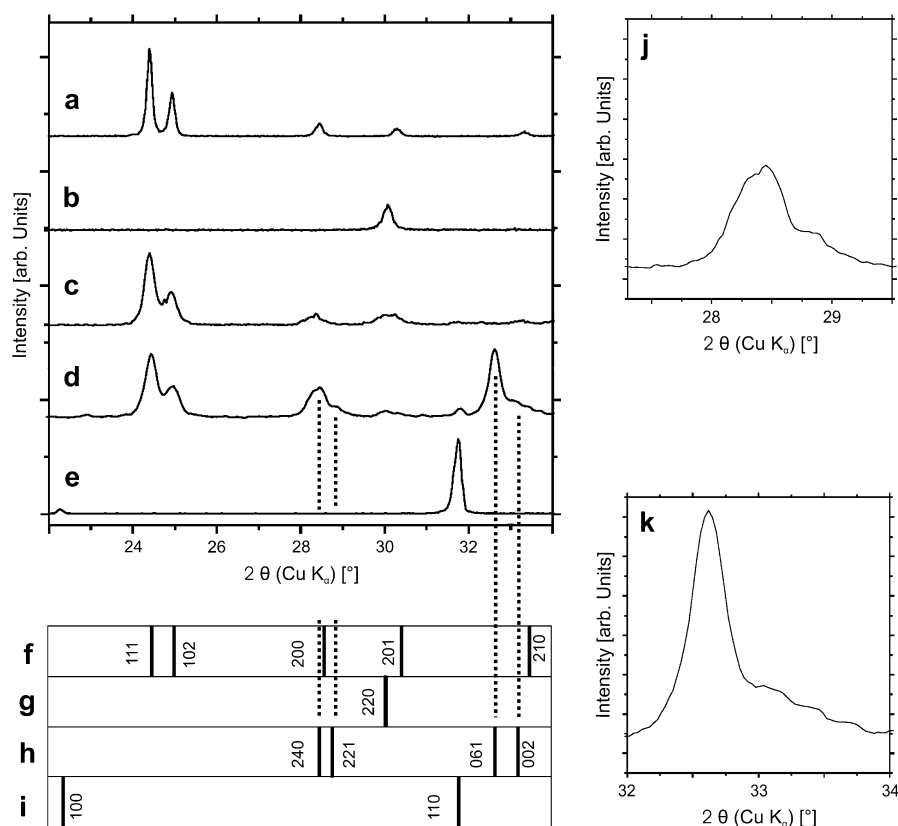


Fig. 7. Close-up X-ray powder diffraction of intermediates and perovskite in the 2θ range between 22° and 34° . (a) Taken from the synthesis of $(\text{Ba}_{0.5}\text{Sr}_{0.5})\text{CO}_3$ after 10 h at 750°C , (b) taken from the synthesis of $(\text{Zn}_{0.6}\text{Fe}_{0.4})\text{Fe}_2\text{O}_4$ after 1 h at 700°C . (c–e) taken from the synthesis of $(\text{Ba}_{0.5}\text{Sr}_{0.5})(\text{Fe}_{0.8}\text{Zn}_{0.2})\text{O}_{3-\delta}$ after (c) 1 h at 700°C , (d) additional 12 h at 700°C , (e) additional 10 h at 750°C . (f–i) Assignment of diffraction lines for different phases: (f) aragonite-type $(\text{Ba}_{0.5}\text{Sr}_{0.5})\text{CO}_3$ carbonate, (g) $(\text{Zn}_{0.6}\text{Fe}_{0.4})\text{Fe}_2\text{O}_4$ spinel, (h) γ - $(\text{Ba}_{0.5}\text{Sr}_{0.5})\text{Fe}_2\text{O}_4$, (i) perovskite-type $(\text{Ba}_{0.5}\text{Sr}_{0.5})(\text{Fe}_{0.8}\text{Zn}_{0.2})\text{O}_{3-\delta}$. (j) close-up of peaks related to 240 and 221 of $(\text{Ba}_{1-x}\text{Sr}_x)\text{Fe}_2\text{O}_4$, (k) close-up of peaks 061 and 002 of $(\text{Ba}_{1-x}\text{Sr}_x)\text{Fe}_2\text{O}_4$.

performed without barium and strontium. After calcination for 1 h at 700°C the formation of a $(\text{Zn}_{0.6}\text{Fe}_{0.4})\text{Fe}_2\text{O}_4$ spinel was confirmed by XRD measurements (Fig. 2b) and EDXS. Fig. 5a (1 h at 700°C) shows details of the diffraction pattern in the 2θ range of 34 – 37.5° , in the vicinity of the most intense (311) spinel reflex. After heat treatment in air for additional 10 h

Table 2
Crystallographic data for γ - $(\text{Ba}_{0.5}\text{Sr}_{0.5})\text{Fe}_2\text{O}_4$

Atom	Site	x	y	z	Occ
Ba	4(a)	0	0.1307	0.2500	0.5
Sr	4(a)	0	0.1307	0.2500	0.5
Ba	4(a)	0	0.6173	0.2270	0.5
Sr	4(a)	0	0.6173	0.2270	0.5
Fe	8(b)	0.2776	0.0424	0.7320	1
Fe	8(b)	0.2913	0.2803	0.7740	1
O	8(b)	0.2430	0.0370	0.4030	1
O	8(b)	0.2250	0.1230	0.9170	1
O	8(b)	0.2913	0.2090	0.4170	1
O	4(a)	0	0.4530	0.2260	1
O	4(a)	0	0.2800	0.2260	1

Space group $Cmc2_1$ (No. 36) with $a = 0.8448$ nm, $b = 1.9050$ nm, $c = 0.5390$ nm (unit cell dimensions according to Ref. [17]).

at 750°C , the (311) and (222) spinel reflexes shift by about 0.14° to smaller diffraction angles 2θ . That indicates an incorporation of a larger ion like Zn^{2+} for Fe^{2+} (61 pm \rightarrow 75 pm [25]) into the A site of the spinel structure. A slightly larger shift in the diffraction angle 2θ by about 0.16° is noticed between FeFe_2O_4 (Fig. 5c) and ZnFe_2O_4 (Fig. 5d) that corresponds to an increase of the unit cell dimension from 0.8394 to 0.8442 nm. Additionally, another reflection occurs at 35.6° (see Fig. 5b), which was identified with attention to complementary diffraction peaks in the 2θ range of 20 – 60° (Fig. 2b) as belonging to α - Fe_2O_3 (hematite, Fig. 5e). In conclusion, the $(\text{Zn}_{0.6}\text{Fe}_{0.4})\text{Fe}_2\text{O}_4$ spinel formed at 700°C decomposes in the absence of $(\text{Ba}_{0.5}\text{Sr}_{0.5})\text{CO}_3$ carbonate at higher temperatures to a spinel with ZnFe_2O_4 stoichiometry and Fe_2O_3 as hematite.

To check whether this conclusion is in agreement with thermodynamics, calculations have been performed, the results of which are displayed in Fig. 6. Free enthalpy of formation for the $(\text{Zn}_{0.6}\text{Fe}_{0.4})\text{Fe}_2\text{O}_4$ spinel has been calculated considering the activities according to Ref. [26]. Because the graph for ΔG_R lies lower than that for O_2 partial pressure in air (p_{O_2} in air = 21.228 kPa), dashed line in Fig. 6, the oxidation

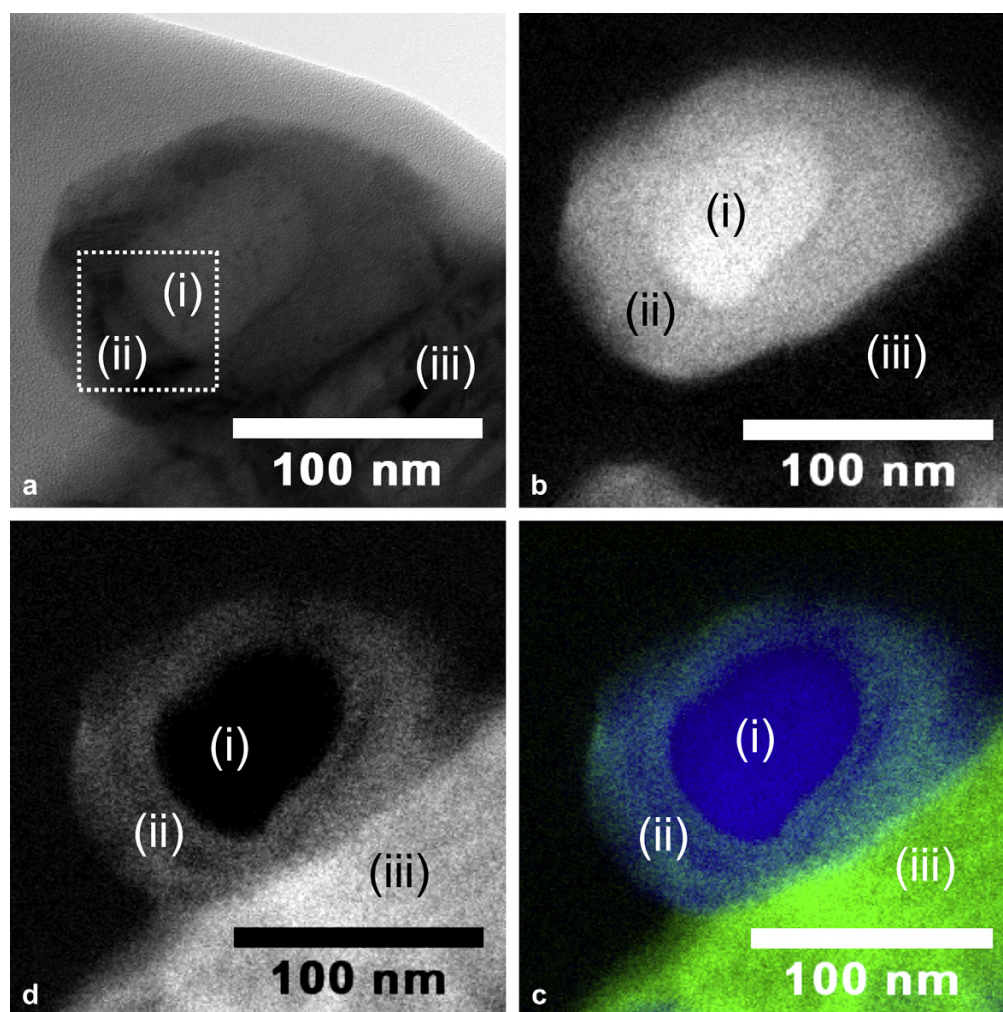


Fig. 8. Transmission electron micrographs showing the formation of the $(\text{Ba}_{1-x}\text{Sr}_x)\text{Fe}_2\text{O}_4$ phase between the ZnFe_2O_4 spinel and $(\text{Ba}_{0.5}\text{Sr}_{0.5})\text{CO}_3$ carbonate in the aragonite modification. (a) Bright-field micrograph with indicated area of high-resolution TEM, of Fig. 9, (b–c) location of the different particles illustrated by energy-filtered transmission electron micrographs showing high elemental concentrations by bright contrast: (b) iron, (c) barium, (d) location of the different particles illustrated by energy-filtered transmission electron micrographs showing high elemental concentrations by different colours (blue = iron, green = barium).

of the $(\text{Zn}_{0.6}\text{Fe}_{0.4})\text{Fe}_2\text{O}_4$ spinel to ZnFe_2O_4 and Fe_2O_3 takes place at atmospheric conditions in the whole temperature range of 20–1300 °C. Due to the fact that all graphs in Fig. 6 are below the “ p_{O_2} in air” line, these reactions proceed regarding thermodynamics. In the presence of zinc oxide, the iron spinel favours to form the $(\text{Zn}_{0.6}\text{Fe}_{0.4})\text{Fe}_2\text{O}_4$ or ZnFe_2O_4 spinels, and in its absence hematite is formed. However, in presence of zinc oxide, the reaction of hematite to ZnFe_2O_4 spinel is thermodynamically advantageous, too. Strictly speaking, these thermodynamic considerations are valid for bulk phases only and not for nanoscale powders. But with the contemplations that have been made in context of Fig. 4, all ΔG_{R} curves in Fig. 6 would be shifted slightly down to represent the situation for nanopowders. Anyway, the relative stabilities of the different phases would not be affected.

Recapitulatory, the $(\text{Zn}_{0.6}\text{Fe}_{0.4})\text{Fe}_2\text{O}_4$ spinel is not the most stable spinel in the Zn–Fe–O system due to its decomposition at elevated temperatures. Thus, it is essential that the reaction towards the perovskite with the carbonate takes place immediately after the formation of the $(\text{Zn}_{0.6}\text{Fe}_{0.4})\text{Fe}_2\text{O}_4$ spinel.

3.2.4. Complex (Ba,Sr)-Fe oxide intermediates

As investigated by XRD pattern, crystalline intermediates that are formed during the synthesis process are $(\text{Zn}_{0.6}\text{Fe}_{0.4})\text{Fe}_2\text{O}_4$ spinel and $(\text{Ba}_{0.5}\text{Sr}_{0.5})\text{CO}_3$ carbonate in the aragonite modification. Against our previous assumption, the final perovskite might be formed directly between the spinel and the carbonate [7,8], we now deliver results that indicate a more complex reaction pathway. This is due to the consideration of quenched specimen that represents earlier intermediate stages in that

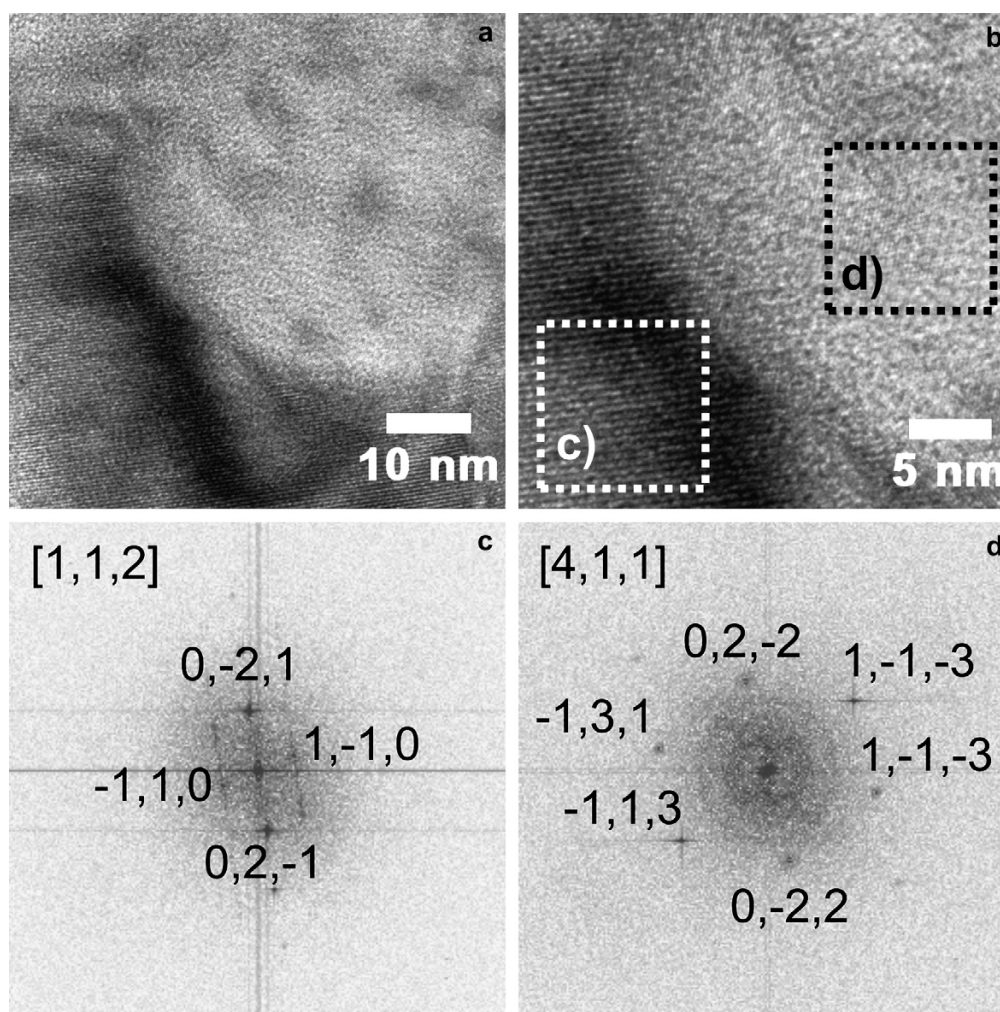


Fig. 9. (a and b) High-resolution transmission electron micrographs as indicated in Fig. 8a. (c) Diffraction data via FFT related to ZnFe_2O_4 spinel. (d) Diffraction data via FFT related to $(\text{Ba}_x\text{Sr}_{1-x})\text{Fe}_2\text{O}_4$.

the perovskite structure is not yet clearly developed compared to Refs. [7,8]. Fig. 7 displays XRD patterns given in Fig. 2 with special emphasize on the 2θ range between 22° and 35° . A first glance on the XRD pattern of Fig. 2d might lead to the conclusion the perovskite structure is already evident in the intermediate powder. Against this, a detailed examination of the XRD pattern in Fig. 7d indicates that a different phase is formed in the first place. The XRD pattern of Fig. 7d could be satisfactorily indexed by a mixed oxide, namely $(\text{Ba}_{1-x}\text{Sr}_x)\text{Fe}_2\text{O}_4$. Oxides of this kind have been intensively discussed by several authors in the past decades [17,27–31]. These oxides can be regarded as stuffed tridymite structures which are build of six-membered rings of corner-sharing FeO_4 -tetrahedra while the arrangement of the tetrahedra corners within the rings determine the crystal structure [27]. Because of the particular arrangement of the FeO_4 -tetrahedra within these structures, a channel-like network is evident

which can be occupied by the larger Ba^{2+} (160 pm [25]) and Sr^{2+} (144 pm [25]) ions, respectively. We found that the orthorhombic crystal structure of $\gamma\text{-BaFe}_2\text{O}_4$ fits best to the obtained XRD pattern [26].

In order to index XRD pattern as well as HRTEM micrographs, the structure has been described in space group $Cmc2_1$ (No. 36), see Table 2. It differs from $Bb2_1m$ given in Ref. [17] by a permutation of the crystal axes. At this point, it has to be stressed, that the investigated phases are determined within a mixture that contains at least three different phases. Additionally, it should be considered that the ideal stoichiometry of $\gamma\text{-BaFe}_2\text{O}_4$ should not be found in the reaction sequence, due to the cation ratio that has been applied in the reaction mixture. Thus, various stoichiometries like $(\text{Ba}_{1-x}\text{Sr}_x)\text{Fe}_2\text{O}_4$ should be evident. The existence of crystals with various, slightly different, lattice parameter can be concluded from Fig. 7j and k as many reflections for the same

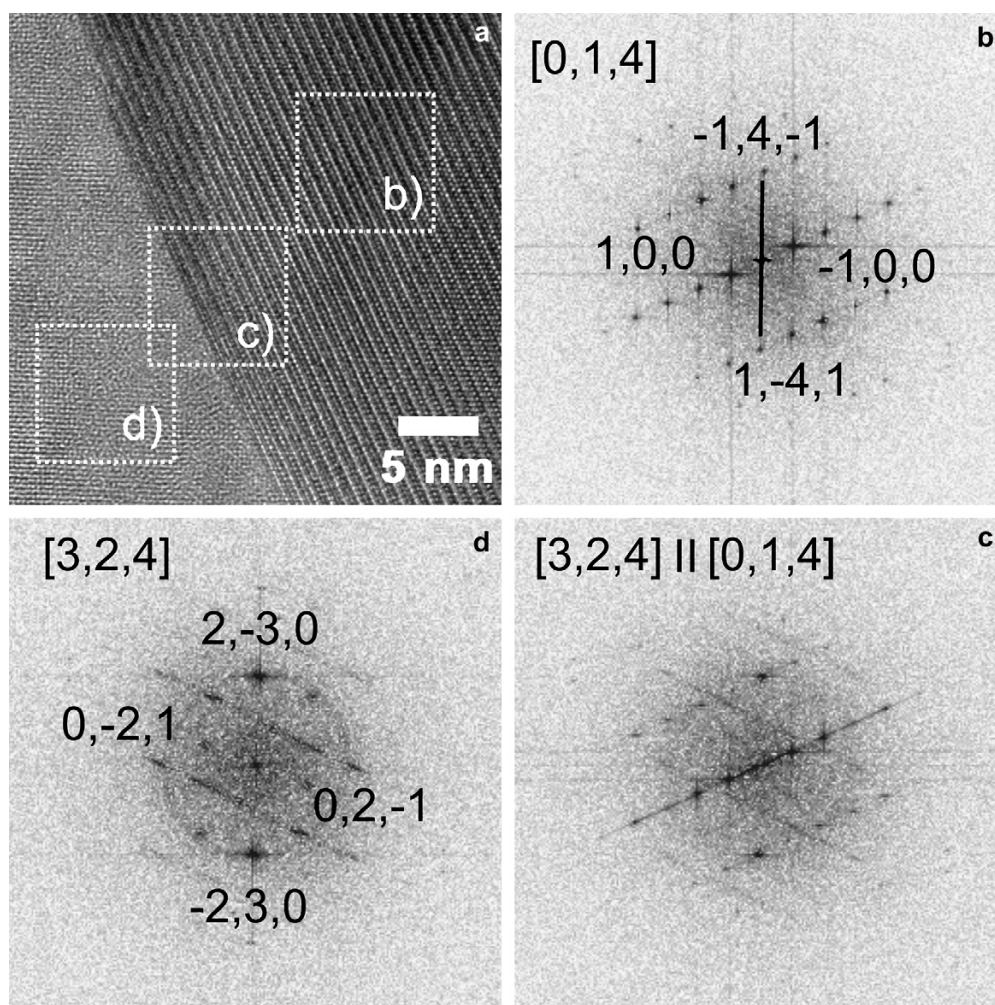


Fig. 10. (a) High-resolution transmission electron micrograph of contact zone of two $(\text{Ba}_x\text{Sr}_{1-x})\text{Fe}_2\text{O}_4$ grains. (b–d) Diffraction data via FFT related to grains as indicated in (a).

plane are observed. This seems to be reasonable as similar structures like $(\text{Ba}_{0.5}\text{Sr}_{0.5})\text{Fe}_2\text{O}_4$ have been already described [28], and they show polymorphism [29]. In order to support XRD findings, TEM bright-field experiments have been conducted with powders as in the XRD pattern in Fig. 7d. Fig. 8 shows a TEM micrograph exhibiting the reaction zone between ZnFe_2O_4 spinel (i), the above mentioned $(\text{Ba}_{1-x}\text{Sr}_x)\text{Fe}_2\text{O}_4$ phase (ii) and $(\text{Ba}_{0.5}\text{Sr}_{0.5})\text{CO}_3$ carbonate (iii). Energy-filtered TEM (EFTEM) micrographs of this particle display the cation distributions by colours. Obviously, the inner core (i) contains no barium, whereas barium is evident in the border (ii) as well as in site (iii). Contrary to barium, iron can be found in the inner core as well in the border (ii) but not in site (iii). EFTEM investigations have been confirmed by quantitative EDXS of respective specimen areas. It has been found that the inner core (i) exhibits a stoichiometry like ZnFe_2O_4 , whereas no zinc can be found in the border (ii)

and in site (iii). Further proof for this supposition can be found in Fig. 9a and b in which HRTEM micrographs of the contact zone between ZnFe_2O_4 and $(\text{Ba}_{1-x}\text{Sr}_x)\text{Fe}_2\text{O}_4$ are displayed. Structure determinations have been conducted via two-dimensional fast Fourier transformation (FFT) of the corresponding areas (Fig. 9c and d). The indexed pattern in Fig. 9c and d give hint to an orientation relationship between spinel (c) and stuffed tridymite (d) of the following type: $(0,2,-2)_c \parallel (0,-2,1)_d$ and $[4,1,1]_c \parallel [1,1,2]_d$. These findings agree well with the observations displayed in Figs. 5 and 6. Below 1400 °C, the $(\text{Zn}_{0.6}\text{Fe}_{0.4})\text{Fe}_2\text{O}_4$ spinel structure tends to separate into ZnFe_2O_4 and Fe_2O_3 with hematite structure (Fig. 6). Taken this into account, it can be concluded, that the $(\text{Ba}_{1-x}\text{Sr}_x)\text{Fe}_2\text{O}_4$ phase has been grown at the expense of the Fe_2O_3 which is one reaction product of the spinel separation. In order to underline the assumption of the formation of a $(\text{Ba}_{1-x}\text{Sr}_x)\text{Fe}_2\text{O}_4$ phase, several other particles have been investigated with respect to

this phase. Fig. 10a displays an HRTEM micrograph exhibiting two grains of the $(\text{Ba}_{1-x}\text{Sr}_x)\text{Fe}_2\text{O}_4$ phase, but in different orientation. As it can be seen from FFTs in Fig. 10b–d, the grain related to (b) is viewed along the $[0,1,4]$ zone axis, while grain related to (d) is viewed along $[3,2,4]$. Thus, $(-1,4,-1)_b \parallel (0,-2,3)_d$ and $[0,1,4]_b \parallel [3,2,4]_d$. Additionally, Fig. 10d shows an FFT of the contact zone as indicated in Fig. 10c. Fig. 11 displays an HRTEM micrograph of the same grain as in Fig. 10d now viewed along the $[2,1,2]$ zone axis instead of $[3,2,4]$ (after tilting the sample holder). Summing up the above findings, we postulate a rather complicated reaction sequence. After formation of spinel and carbonate, the formation of a $(\text{Ba}_{1-x}\text{Sr}_x)\text{Fe}_2\text{O}_4$ phase is postulated. Considering that the spinel structure (B_3O_4) consists only of type-B cations (according to the perovskite terminology ABO_3) it is not surprising that structures like AB_2O_4 are evident which can be understood as intermediate compositions regarding the type-A cation concentration in the spinel and the perovskite. After prolonged reaction time, the diffusion processes, which have to be studied in more detail, between ZnFe_2O_4 spinel and the $(\text{Ba}_{1-x}\text{Sr}_x)\text{Fe}_2\text{O}_4$ phase might finally lead to the perovskite structure.

EEL spectra of the phases under consideration are given in Fig. 12a–d in the energy-loss range of 500–850 eV. These show up O-K, Fe-L_{2,3}, and Ba-M_{4,5} ionization edges. The relative intensities of Fe-L_{2,3} and Ba-M_{4,5} white lines clearly show that the stuffed tridymite structure (Fig. 12b) contains more iron relative to barium compared to the perovskite structure (Fig. 12a). The oxygen K-edge reveals characteristic signatures of the different phases that are shown in more detail in Fig. 12e–h. The O-K ELNES of Fig. 12a,c,d,e,g, and h correspond to fingerprints given in the literature for spinel [32,33], carbonate [34], and perovskite [35], respectively. The stuffed tridymite structure shows after a pronounced leading peak a peak doublet (arrows in Figs. 12b and f) and is in good agreement with the spectral signature given in Ref. [36] for CaAl_2O_4 that is structurally related.

4. Conclusions

It is evidenced that in the sol–gel based synthesis route employed here, the cubic perovskite-type $(\text{Ba}_{0.5}\text{Sr}_{0.5})(\text{Fe}_{0.8}\text{Zn}_{0.2})\text{O}_{3-\delta}$ is formed in a nanoscale solid state reaction between finely-dispersed crystalline intermediates, i.e. a $(\text{Ba}_{0.5}\text{Sr}_{0.5})\text{CO}_3$ carbonate and a $(\text{Zn}_{0.6}\text{Fe}_{0.4})\text{Fe}_2\text{O}_4$ spinel. Obviously, the reaction pathway goes from cubic spinel over transient phases of orthorhombic stuffed tridymite-type finally to cubic perovskite-type. XRD and TEM snapshots on quenched samples reveal some details of the intricate reaction mechanism on the atomic scale, however, not all questions can be answered satisfactorily.

The technologically so important spinel/perovskite interfaces or superstructures [37,38] might suggest that a simple topotactic arrangement of both cubic structures, spinel and perovskite, with low lattice misfit could be expected in these nanoscale solid state reactions. Our investigations make clear that this is not the case. In the quenched specimens from different stages of the synthesis process, we may find even additional phases that could be different from the so far found ones. For instance in the analogous synthesis of a cobalt containing cubic perovskite-type oxide, $(\text{Ba}_{0.5}\text{Sr}_{0.5})(\text{Co}_{0.8}\text{Fe}_{0.2})\text{O}_{3-\delta}$, tetragonally distorted perovskite phases are involved [9].

From a general point of view it is nebulous how the spinel structure with FeO_4 and ZnO_4 tetrahedra and FeO_6 octahedra transforms to stuffed tridymite structures with FeO_4 -tetrahedra and finally to a perovskite structure with FeO_6 and ZnO_6 octahedra. Zinc seems to be squeezed first into a ZnFe_2O_4 spinel and then probably into ZnO what was seen in some quenched specimen [7]. Incorporation of zinc into the perovskite structure occurs obviously late in the reaction sequence. At which stage, and how, this proceeds is not understood. In addition, the stuffed tridymite $(\text{Ba,Sr})\text{-Fe}_2\text{O}_4$ -type phases show polymorphism [29] so that in very detail everything is undoubtedly even more intricate. And, in these technologically so important

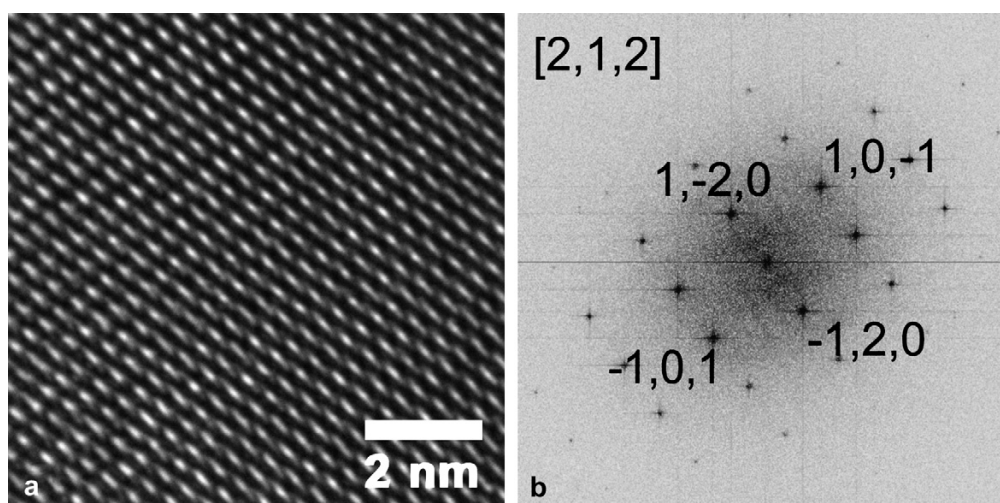


Fig. 11. (a) High-resolution transmission electron micrograph of $(\text{Ba,Sr}_{1-x})\text{Fe}_2\text{O}_4$ grain as in Fig. 9d viewed along different zone axis. (b) Diffraction data via FFT.

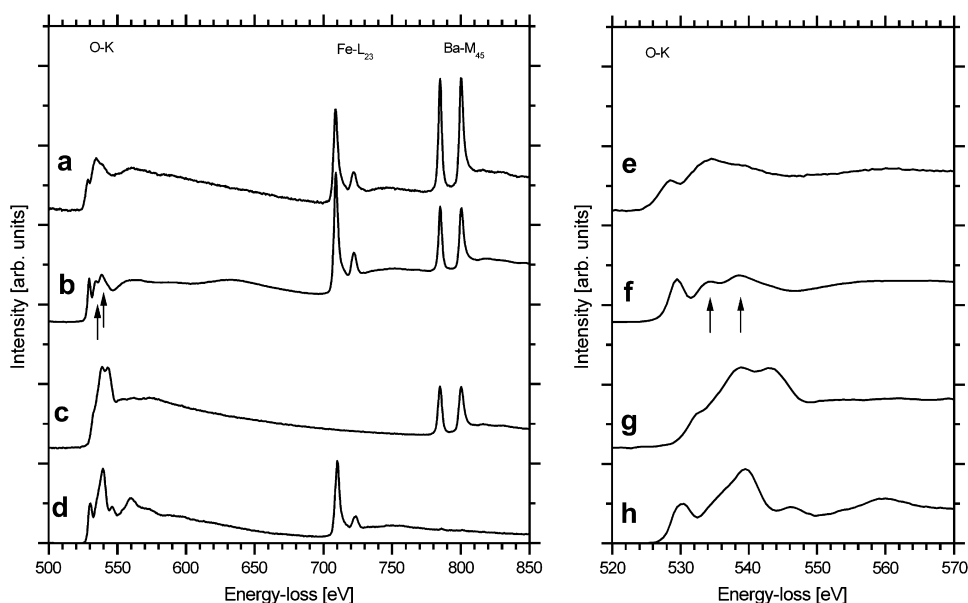


Fig. 12. Electron energy-loss spectra showing O-K, Fe-L_{2,3} and Ba-M_{4,5} ionization edges and O-K energy-loss near-edge structures of different phases. (a and e) Perovskite-type (Ba_{0.5}Sr_{0.5})(Fe_{0.8}Zn_{0.2})O_{3-δ}, (b and f) stuffed tridymite-type (Ba_xSr_{1-x})Fe₂O₄, (c and g) (Ba_{0.5}Sr_{0.5})CO₃ carbonate, (d and h) (Zn_{0.6}Fe_{0.4})Fe₂O₄ spinel.

nanoscale powder reactions, mechanisms are more difficult to understand than in bulk solid state reactions by principle [39].

All in all it is somehow astonishing that the sol–gel procedure passes the same intermediate phases (carbonate and spinel) that are employed in classical solid state routes. However, several advantages of the sol–gel procedure are evident. Starting from the solution over the gel to the crystalline intermediates a nanoscale intermixing of cations is preserved that is the key to homogeneous products of complex stoichiometries.

Solid state reactions in minute reaction couples form tiny product layers and thus do not require the activation of long range diffusion processes. So, the reaction temperature can be kept below the decomposition temperature of the relevant carbonate. Conclusively, the reaction pathway is different from the classical solid route, even if the same type of reaction couples are employed. Reaction temperatures distinctly below 1000 °C diminish the risk of the evaporation of the most volatile constituents (in the systems under investigation Co or Zn) and are thus advantageous for the synthesis of homogeneous products of complex stoichiometries. Moreover, low reaction temperatures lead to nanoscale grains that are favourable with respect to several demands.

Acknowledgements

The authors acknowledge gratefully funding by the Deutsche Forschungsgemeinschaft (DFG) under grant FE 928-1. Thanks are given to Dr. Sebastian Hein for assistance in decarbonation experiments. Fruitful discussions with Prof. Jürgen Caro are appreciated.

References

- [1] J. Pâris, R. Pâris, Bull. Soc. Chim. Fr. 4 (1965) 1795.
- [2] M.P. Pechini, US Patent 3 330 697, 1967.
- [3] C. Marcilly, P. Courty, B. Delmon, J. Am. Ceram. Soc. 53 (1970) 56.
- [4] Y.G. Metlin, Y.D. Tretyakov, J. Mater. Chem. 4 (11) (1994) 1659.
- [5] D. Segal, J. Mater. Chem. 7 (8) (1997) 1297.
- [6] Z.P. Shao, W.S. Yang, Y. Cong, H. Dong, J.H. Tong, G.X. Xiong, J. Membr. Sci. 172 (2000) 177.
- [7] A. Feldhoff, J. Martynczuk, H. Wang, Prog. Solid State Chem. 35 (2007) 339.
- [8] J. Martynczuk, M. Arnold, H. Wang, J. Caro, A. Feldhoff, Adv. Mater. 19 (2007) 2134.
- [9] M. Arnold, H. Wang, A. Feldhoff, J. Am. Ceram. Soc., doi:10.1111/j.1551-2916.2007.01932.x.
- [10] J. Kilner, S. Benson, J. Lane, D. Waller, Chem. Ind. 17 (1997) 907.
- [11] H. Wang, C. Tablet, A. Feldhoff, J. Caro, J. Membr. Sci. 262 (2005) 20.
- [12] M. Arnold, H. Wang, A. Feldhoff, J. Membr. Sci. 293 (2007) 44.
- [13] Z. Shao, S.M. Haile, Nature 431 (2004) 170.
- [14] H. Wang, C. Tablet, A. Feldhoff, J. Caro, Adv. Mater. 17 (2005) 1785.
- [15] H. Wang, G. Grubert, C. Tablet, J. Caro, EU Patent EP 1 630 148, 2006.
- [16] I.A. Kiselva, A.R. Kotelnikov, K.V. Martynov, L.P. Ogordova, Ju.K. Kabalov, Phys. Chem. Miner. 21 (1994) 392.
- [17] H. Mitsuda, S. Mori, C. Okazaki, Acta Crystallogr. B 27 (1971) 1263.
- [18] R.F. Egerton, Electron Energy-Loss Spectroscopy in the Electron Microscope, Plenum Press, New York, 1986.
- [19] R.M. Smith, A.E. Martell, Critical Stability Constants, vol. 6, Plenum Press, New York, 1989, pp. 96–99, 356–358.
- [20] A.E. Martell, R.M. Smith, Critical Stability Constants, vol. 5, Plenum Press, New York, 1982, 330.
- [21] R.A. Swalin, Thermodynamics of Solids, John Wiley & Sons, New York, 1962.
- [22] I. Barin, F. Sauert, G. Patzki, Thermochemical Data of Pure Substances, third ed., vols. I and II, VCH, Weinheim, 1995.
- [23] H. Schmalzried, Solid State Reactions. In: Monographs in Modern Chemistry, vol. 12, Verlag Chemie, Weinheim, 1981.

- [24] M.N. Rahaman, *Ceramic Processing and Sintering*, second ed. Marcel Dekker, New York, 2003.
- [25] R.D. Shannon, *Acta Crystallogr. A* 32 (1976) 751.
- [26] A.A. Lykasov, V.V. D'yachuk, *Inorg. Mater.* 29 (1993) 786.
- [27] W. Leib, H.K. Müller-Buschbaum, *Z. Anorg. Allg. Chem.* 538 (1986) 71.
- [28] S. Meriani, G. Slocari, *Acta Crystallogr. B* 26 (1970) 1184.
- [29] S. Meriani, *Acta Crystallogr. B* 28 (1972) 1241.
- [30] E. Lucchini, D. Minichelli, S. Meriani, *Acta Crystallogr. B* 29 (1973) 919.
- [31] W. Hörkner, H.K. Müller-Buschbaum, *J. Inorg. Nucl. Chem.* 38 (1976) 983.
- [32] F.T. Docherty, A.J. Craven, D.W. McComb, J. Skakle, *Ultramicroscopy* 86 (2001) 273.
- [33] C.C. Calvert, A. Brown, R. Brydson, *J. Electron Spectrosc. Relat. Phenom.* 143 (2005) 173.
- [34] J.L. Mansot, V. Golabkan, L. Romana, T. Césaire, *J. Microsc.* 210 (2003) 110.
- [35] A.S. Sefat, G. Amow, M.Y. Wu, G.A. Botton, J.E. Greendan, *J. Solid State Chem.* 178 (2005) 1008.
- [36] N. Jiang, *J. Appl. Phys.* 100 (2006) 13703.
- [37] G. Chern, C. Cheng, *J. Vac. Sci. Technol. A* 17 (1999) 1097.
- [38] H. Zheng, J. Wang, S.E. Lofland, Z. Ma, L. Mohaddes-Ardabili, T. Zhao, L. Salamanca-Riba, S.R. Shinde, S.B. Ogale, F. Bai, D. Viehland, Y. Jia, D.G. Schlom, M. Wuttig, A. Roytburd, R. Ramesh, *Science* 3003 (2004) 661.
- [39] H. Schmalzried, *Angew. Chem.* 8 (1963) 353.
- [40] Additional material to this paper can be ordered to the CSD-No. 418850, names of the authors, and citations of the paper at the Fachinformationszentrum Karlsruhe, Gesellschaft für wissenschaftlich-technische Information mbH, D-76344 Eggenstein-Leopoldshafen, Germany.

Chapter 3

Grain size and grain boundaries

3.1 Summary

The results presented in the following two sections consider the transport properties of electronic and ionic charge carriers in BSFZ and BSCF, which are examined via SEM, HRTEM, EELS and energy-dispersive X-ray spectroscopy (EDXS), differential scanning calorimetry (DSC), XRD and oxygen permeation measurements.

In the first article the effect of grain size distribution on the permeation performance of BSFZ membranes is investigated by variation of calcination temperature in powder synthesis and sintering time for membranes. We are able to control the grain sizes in the green compact and thus, in the sintered membranes during ceramic production. An increase in dwell time during sintering results in larger grains at the surface as well as in the bulk of the membrane as long as the grains are in good contact from the stage of green compact production. Grain boundaries were found to be atomically thin without any interfacial phases. Larger grains in the sintered ceramic and a homogeneous grain size distribution are favorable for the oxygen permeation. Grain boundaries were identified as barriers for the bulk diffusion and thus for the oxygen permeation, because the increase in grain size is accompanied by a decrease of grain boundary ratio. This leads to the conclusion that the transport rate of the oxygen permeation is limited predominantly by bulk diffusion and that BSFZ is a high mobility material. The second article describes the effect of microstructure on the oxygen permeation performance of BSFZ and BSCF using liquid phase sintering with BN as sintering aid. Prior to sintering BN with concentrations up to 10 mol-% was added to the perovskite powders and dense ceramic membranes of BSFZ and BSCF were successfully prepared without any remaining boron after sintering. The sintering temperature could be lowered by 50-100 °C. The membranes exhibit excellent phase stability. The addition of BN as sintering aid turned out as an other suitable method to decrease the grain size of both membrane materials, BSFZ as well as BSCF, and the findings of the first section of this chapter were confirmed. The oxygen permeation flux was lowered proportionally to the abatement of the average grain size with increasing BN addition. Due to the fact that no amorphous material or interfacial phase were found to be incorporated at the grain boundaries, we come to the conclusion that a lattice misfit between the grains and associated straining of regions near to grain boundaries have a negative impact on the oxygen ion transport.

3.2 Influence of grain size on the oxygen permeation performance of perovskite-type $(\text{Ba}_{0.5}\text{Sr}_{0.5})(\text{Fe}_{0.8}\text{Zn}_{0.2})\text{O}_{3-\delta}$ membranes

Julia Martynczuk, Mirko Arnold, and Armin Feldhoff

Journal of Membrane Science 322, 375-382 (2008)



Influence of grain size on the oxygen permeation performance of perovskite-type $(\text{Ba}_{0.5}\text{Sr}_{0.5})(\text{Fe}_{0.8}\text{Zn}_{0.2})\text{O}_{3-\delta}$ membranes

Julia Martynczuk*, Mirko Arnold, Armin Feldhoff

Institute of Physical Chemistry and Electrochemistry, Leibniz Universität Hannover, Callinstr. 3-3a, D-30167 Hannover, Germany

ARTICLE INFO

Article history:

Received 18 April 2008

Received in revised form 22 May 2008

Accepted 30 May 2008

Available online 8 June 2008

Keywords:

Perovskite membrane

Grain size distribution

Microstructure

BSFZ

Oxygen permeation

ABSTRACT

The effect of grain size distribution in perovskite-type $(\text{Ba}_{0.5}\text{Sr}_{0.5})(\text{Fe}_{0.8}\text{Zn}_{0.2})\text{O}_{3-\delta}$ (BSFZ) ceramics on their oxygen permeation behaviour has been investigated by variation of calcination temperature in powder production and sintering time for the ceramics. The membranes were examined via scanning electron microscopy (SEM), transmission electron microscopy (TEM) and oxygen permeation experiments. We found that the dwell time during sintering has an important influence on the microstructure of the ceramic. The longer the dwell time, the further proceeds the grain coarsening, which affects the oxygen permeation in a positive way and leads to an enhanced permeation. Supplementary, decreasing calcination temperature in perovskite powder synthesis delivers fine powders with grain sizes less than one micrometer and thus smaller grains in the ceramic. Unfortunately, the grain size distribution in sintered membranes is not constant through membrane cross-sections since grains in the bulk are smaller compared to those at the surface which is not favorable for the oxygen permeation of the ceramics. The activation energy was determined to be in the range of 51–53 kJ/mol and its variation does not exhibit a dependence of grain size changes. High-resolution transmission electron microscopy proved that grain boundaries are atomically thin without any interfacial phases. We come to the conclusion that the transport rate of the oxygen permeation is limited predominantly by bulk diffusion and due to the fact that grain boundaries in BSFZ act as barriers for bulk diffusion, this material is a high mobility material.

© 2008 Elsevier B.V. All rights reserved.

1. Introduction

Various applications demand ceramic materials that exhibit both high ionic and electronic conductivities. Perovskite-type oxides of the composition ABO_3 can host a lot of different cations on the A and B sites and thus they can show conductivities from almost pure electronic to almost pure ionic. P-type electron conductors usually exhibit high electronic conductivity and low O_2 conductivity. The introduction of lower valence state ions into the perovskite structure induces oxygen vacancies leading to an improved ionic conductivity benefiting the oxygen permeability. Recently, a novel perovskite material of $\text{A}^{\text{II}}\text{B}^{\text{IV}}\text{O}_3$ -type with the stoichiometry $(\text{Ba}_{0.5}\text{Sr}_{0.5})(\text{Fe}_{0.8}\text{Zn}_{0.2})\text{O}_{3-\delta}$ (BSFZ) has been developed that shows high oxygen permeation fluxes (membrane disks: $\sim 2.55 \text{ mL min}^{-1} \text{ cm}^{-2}$ for the partial catalytic oxidation of methane to syngas (POM)) as well as an excellent phase stability under a 2% H_2 -Ar atmosphere with an oxygen par-

tial pressure $p\text{O}_2$ of less than $1 \times 10^{-8} \text{ Pa}$ [1,2]. Doping of the B site of the perovskite structure with a divalent metal like zinc leads to the diminution of non-stoichiometric oxygen variations and lattice expansion caused by the variation of temperature or chemical oxygen potential and improves the oxygen permeability due to higher ionic conductivity. Wei et al. [3] showed with impedance spectroscopy that BSFZ is a mixed conductor that can provide simultaneous transport of oxygen ions and electrons.

The oxygen transport properties are the major reason for the various applications of polycrystalline perovskite materials, e.g. in oxygen separation or solid oxide fuel cells (SOFC) [4–8]. It has often been ignored that these properties are largely influenced by differences in the microstructure of the material, i.e. grain size and grain boundary distribution or inhomogeneous grain and grain boundary composition. Recently, some research was done by different groups to elucidate its importance and to address the dependence of the oxygen permeation on the microstructure. Since amorphous phases or inclusions at the grain boundary seem to act as high diffusivity paths [9,10], the influence of grain and grain boundary distribution is contradictory.

* Corresponding author. Tel.: +49 511 762 3555; fax: +49 511 762 19121.
E-mail address: julia.martynczuk@pci.uni-hannover.de (J. Martynczuk).

The influence of microstructure cannot be generalized and clearly depends on the chemical nature of grains and grain boundaries, the powder synthesis and the ceramic process. For example there is no homogeneous explanation for the following findings: the increase of grain size leads to an enhanced oxygen permeation for $\text{LaCoO}_{3-\delta}$, $\text{La}_{0.3}\text{Sr}_{0.7}\text{CoO}_{3-\delta}$, and $\text{La}_{0.6}\text{Sr}_{0.4}\text{Co}_{0.2}\text{Fe}_{0.8}\text{O}_{3-\delta}$ [11–14], but to a decrease in oxygen permeation for $\text{La}_{0.5}\text{Sr}_{0.5}\text{FeO}_{3-\delta}$, $\text{La}_{0.1}\text{Sr}_{0.9}\text{Co}_{0.9}\text{Fe}_{0.1}\text{O}_{3-\delta}$, and $\text{La}_{0.6}\text{Sr}_{0.4}\text{Fe}_{0.9}\text{Ga}_{0.1}\text{O}_{3-\delta}$ [15–17]. This contradiction might be caused by missing of important additional information which should always be considered. The first information needed is L_c , the characteristic thickness of the ceramic below which the oxygen flux will be predominantly controlled by surface exchange kinetics. If the ceramic exceeds L_c , the transport rate of the oxygen permeation is not limited anymore by surface exchange but predominantly by bulk diffusion [18]. It is obvious that the grain size and grain boundary ratio play an important role in the acceleration of the diffusion processes. For surface exchange diffusion smaller grains are favorable due to bigger surface area. Thus in surface exchange controlled processes an increase in oxygen permeation is expected with decreasing grain size, what explains the behaviour of $\text{La}_x\text{Sr}_{1-x}\text{Fe}_y\text{Ga}_{1-y}\text{O}_{3-\delta}$. Etchegoyen et al. and Kim et al. proved independently that the oxygen flux is controlled by a surface exchange mechanism and the oxygen exchange coefficient increases significantly when the average grain size on membrane surface decreases [17,19]. Comparable findings were made for $\text{SrCo}_{0.8}\text{Fe}_{0.2}\text{O}_{3-\delta}$. Zhang et al. [20] found a dependence of increasing permeation with decreasing grain size and Bouwmeester et al. [18] suggested already in 1994 that the oxygen flux is affected by the surface exchange kinetics. $\text{SrCo}_{0.8}\text{Fe}_{0.2}\text{O}_{3-\delta}$ is a good example to show that the incorporation of either an additional A (e.g. Ba) or B (e.g. Cu, Cr or Al) cation into the ABO_3 perovskite structure can totally invert the behaviour. Contradictory to the prior findings a positive correlation between bigger grains and the oxygen permeation was found for $\text{Ba}_{0.5}\text{Sr}_{0.5}\text{Co}_{0.8}\text{Fe}_{0.2}\text{O}_{3-\delta}$ by Wang et al. and Arnold et al. [21,22] as well as for $\text{SrCo}(\text{Fe},\text{M})\text{O}_{3-\delta}$ (M = Cu or Cr) and $\text{SrFe}(\text{Al})\text{O}_{3-\delta}\text{-SrAl}_2\text{O}_4$ composites by Kharton et al. [23,24]. It is disputable if this change in behaviour is just ascribable to an increase of the characteristic thickness due to the new cations or if there are also other aspects to consider.

Joachim Maier is engaged in the influence of crystal defects on the transport properties in electro ceramics [25]. He found that interfaces (e.g. grain boundaries) exhibit their own defect chemistry and special mobilities, and can hence, provide fast pathways or obstacles in addition to space charge effects. There is a differentiation between high and low mobility materials. In high mobility materials usually the bulk structure is optimized for point defect motion and then a structural modification as occurring in the grain boundary is likely to depress the mobility. Whereas for materials with very low mobilities in the bulk any structural perturbation is likely to increase the mobility significantly. For acceptor doped oxides like Fe doped SrTiO_3 , Y-doped ZrO_2 or CeO_2 , a positive space charge potential occurs at grain boundaries and hence, severe depletion effects at the grain boundary are observed [26–33]. This implies the depletion of oxygen vacancies (decreasing ionic conductivity) and holes. At high oxygen partial pressures the presence and mobility of both carriers is important for an effectively neutral mass transport. This leads to a pronounced chemical resistance of a grain boundary with respect to oxygen transport across it. Hence, the variation of the grain boundary ratio provides information about the nature of the material (low or high mobility) depending on the grain boundaries as depletion or accumulation layers, but also the characteristic thickness of the material should be taken into account.

2. Experimental

A synthetic method with combined citric acid and ethylenediamine-tetraacetic acid (EDTA) as the complexing agents was applied (Fig. 1). A given amount of $\text{Ba}(\text{NO}_3)_2$ powder was dissolved in an aqueous solution of $\text{Zn}(\text{NO}_3)_2$, $\text{Fe}(\text{NO}_3)_3$, and $\text{Sr}(\text{NO}_3)_2$, followed by the addition of EDTA acid. After agitation for a certain time, a proper amount of citric acid was introduced, with the molar ratio of EDTA acid: citric acid: total of metal cations controlled at around 1:1.5:1. After addition of $\text{NH}_3\cdot\text{H}_2\text{O}$, the pH value of the solution was adjusted at around 9 by the addition of supplementary $\text{NH}_3\cdot\text{H}_2\text{O}$. Water was evaporated with stirring at 150°C . After evaporation for several hours the transparent solution transformed into a dark purple gel. Further heat treatments were applied at temperatures up to 950°C . The fine-scale mixed intermediates appearing during the perovskite synthesis were determined as $(\text{Zn}_{0.2}\text{Fe}_{0.8})\text{Fe}_2\text{O}_4$ spinel and $(\text{Ba}_{0.5}\text{Sr}_{0.5})\text{CO}_3$ carbonate in aragonite modification followed by the formation of stuffed tridymite structures as transient phases. The perovskite structure formation was found to be completed at calcination at 800°C for 10 h with grain size diameters up to 700 nm. The calcination at 950°C for 10 h produces a powder run through a coarsening of grains to sizes of around a micrometer [34–37]. Thus, a variation of the calcination temperature was used to adjust the grain sizes of the as-synthesized perovskite. The calcined powders were uniaxially pressed under 140 kN into pellets and sintered pressurelessly at 1150°C to ceramic discs of 14 mm in diameter and a thickness of around 1.15 mm.

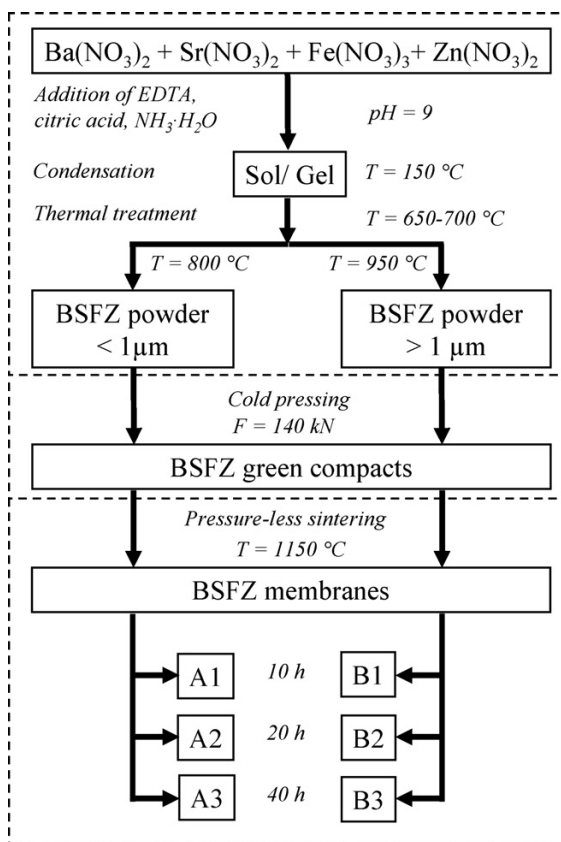


Fig. 1. Scheme of the membrane fabrication.

The oxygen permeation was measured in a high-temperature permeation cell [21]. Discs were sealed onto a ceramic tube with gold-paste (conducting 130 paste, C5754, Heraeus) at 950 °C for 2 h. After sealing, gas flow rates were delivered to the reactor by mass flow controllers (Bronckhorst Hi-Tech) and continuously read by an on-line gas chromatograph (Agilent Technologies, HP 6890, equipped with a Carboxen 1000 column). Air was fed at a rate of 150 mL min⁻¹ to the air side; He (29.0 mL min⁻¹, 99.995%) and Ne (1.0 mL min⁻¹, 99.995%) as the internal standard gases were fed to the sweep side. The absolute flow of the effluents rate was determined by using neon as an internal standardization. For that purpose the concentration of neon in effluents was measured. Since the flow rate of neon is known it is thus possible to calculate the total effluents flow rate. Nitrogen was also detected in the effluents by the gas chromatograph because of slight imperfections in the sealing, and the leakage of oxygen was subtracted in the calculation of the oxygen permeation flux. The relative leakage of O₂ was found to be less than 8%. The permeation flux through the membrane could then be calculated by the fraction O₂ in the effluents and the determination of the effective permeation area of the membrane.

The density was determined by the Archimedes principle using a Sartorius balance model BP211D with a resolution of 0.01 mg completed by a support for the determination of density.

Scanning electron microscopy (SEM) was employed on a field-emission instrument of the type JEOL JSM-6700F. Secondary electron (SE) micrographs were taken at a low excitation voltage of 2 kV. In order to analyze the microstructure of the sintered membranes, SEM was conducted on both surfaces and on fracture surfaces, and grain size distributions were evaluated. Fracture surfaces were etched with aqueous HCl (2 M) for 2–5 s in order to visualize grain boundaries. An EDX spectrometer of the type Oxford Instruments INCA-300 with ultra-thin window was used for elemental analysis. Adobe Photoshop CS2 (Version 9.0) and ImageJ (1.33 u) was used as image analysis software for the determination of the grain size distribution.

X-ray diffraction (XRD) was measured with a Philips X'pert-MPD instrument using monochromator-filtered Cu K α radiation at 40 kV and 40 mA, receiving slit of 0.15 mm and count times of 3 s per step. Data were collected in a step-scan mode in the range of 20–50° with intervals of 0.03°.

Additionally, TEM was conducted at 200 kV with a JEOL JEM-2100F-UHR field-emission instrument equipped with a Gatan GIF 2001 energy filter and a 1k-CCD camera. EDXS was carried out by a light-element detector using the Cliff–Lorimer quantification technique (INCA 200 TEM, Oxford Instruments). Furthermore, the specimen for TEM investigations was prepared as follows. First, pieces of 1 mm × 1.5 mm × 3 mm were cut out of the membrane followed by covering of both sides with silicon single crystal using epoxy. Accordingly, the protected membrane pieces were polished on polymer embedded diamond lapping films down to 0.02 mm × 1 mm × 3 mm and epoxy-glued onto a copper slot grid. Electron transparency was achieved by Ar⁺ ion sputtering at 3 kV under incident angles of 6° and 4° (Gatan, model 691 PIPS).

3. Results and discussion

The effect of grain size distribution on the oxygen permeation behaviour has been investigated by variation of calcination temperature and sintering time, but a constant membrane thickness. The powder calcined at 800 °C had an average grain size of 700 nm and led to membranes A1–3. Membranes A1 had average surface grain areas of 377 μm^2 and bulk grain areas of 9 μm^2 (Table 1). Fig. 2 displays the different grain sizes by SEM micrographs of the surface (a), fracture surface (b), and the cross-section (c) etched

2 s with hydrochloric acid. Due to the faster etching of the grain boundaries the grains of the fracture surface are visible but at the same time they seem more loosely. With shorter time of etching the grain boundaries of the single grains are not visible and the grains are in good contact, but a grain size determination is not possible. From the grain size distribution of surface and bulk (Fig. 2d) it is obvious that it has been possible to synthesize membranes with distinctly smaller grains in the bulk than at the surface starting from powders with small particles (A1–3). Fig. 2c gives evidence of a sandwich-effect. There is a region of approximately 160 μm depth of big grains, similar to those at the surface, followed by a changeover to the smaller grains in the bulk (marked by a horizontal line). This effect is also observed for membranes A2 and A3. Supplementary, the sintering temperature and dwell time influence the final microstructure of the ceramic. The ceramics pressed out of small size powder (A1–3) have been sintered for different times at 1150 °C (Fig. 1). As can be seen from Table 1 the grain coarsening in the bulk of the membrane proceeds slower than at the surface (A1 to A2). But after a dwelling time of 40 h the bulk grains seem to grow at the expense of the surface grains, thus, the average surface grain area becomes smaller due to increasing average bulk grain area.

To receive larger grains in the sintered ceramics, the calcination temperature of the powder has been changed to 950 °C and the dwell time for the sintering was elongated (B1–3). The membrane B1 was prepared from a powder with a calcination temperature of 950 °C for 10 h with grain sizes of around a micrometer and a dwell time of 10 h at 1150 °C during sintering. The average grain area of the membrane was determined as 435 μm^2 at the surface and 302 μm^2 for the bulk. The average grain area for the surface increased from 435 over 652 to 1029 μm^2 . This effect has also been observed for the bulk from 302 over 609 to 781 μm^2 . Fig. 3a and b show some grains of the surface and the fracture surface of B3 etched 2 s with hydrochloric acid. The grains are visible due to the faster etching of the grain boundaries, but the grain surfaces are also etched a little (etching cavity), what should not be mistaken as porosity. Fig. 3d illustrates that the grain size distribution for the surface is similar to that in the bulk. A slight difference between bulk and surface grain sizes remains, but SEM investigations show, that the sandwich-effect, where the smaller bulk grains merge into the bigger surface grains is negligible. The relative densities shown in Table 2 lie in a reasonable range like reported elsewhere [21]. Although there is a slight trend to higher densification with grain coarsening from B1 to B3, the grain size distribution at the surface is similar to that in the bulk. In contrast to that the grain size distribution for A1 points out that the grains at the surface have a bigger size than in the bulk, but a difference in density is not the explanation. According to the initial stage model for the sintering process [38], which consists of two spheres in contact, it is very important for the formation of sintering necks during the sintering process to have grains in good contact, because for the densifying mechanisms the model accounts for interpenetration of the spheres (i.e., shrinkage) as well as neck growth. It might be necessary to increase the pressure during uniaxial pressing of the membranes for small size powders to avoid big differences in grain size distribution, since the volume reduction of small size powders during pressing is greater than for powders with bigger grain sizes and thus the contact between single perovskite powder grains might be worse in a powder with small grains compared to larger grains leading to a deceleration of the sintering process and thus to smaller grains in the final membrane. Fig. 4 illustrates that for the membranes of kind B an increase in dwell time during sintering results in larger grains at the surface as well as in the bulk, whereas for membranes A1–A3 the dwell time has a slight influence on the surface grain size and hardly any modification of the grain sizes of

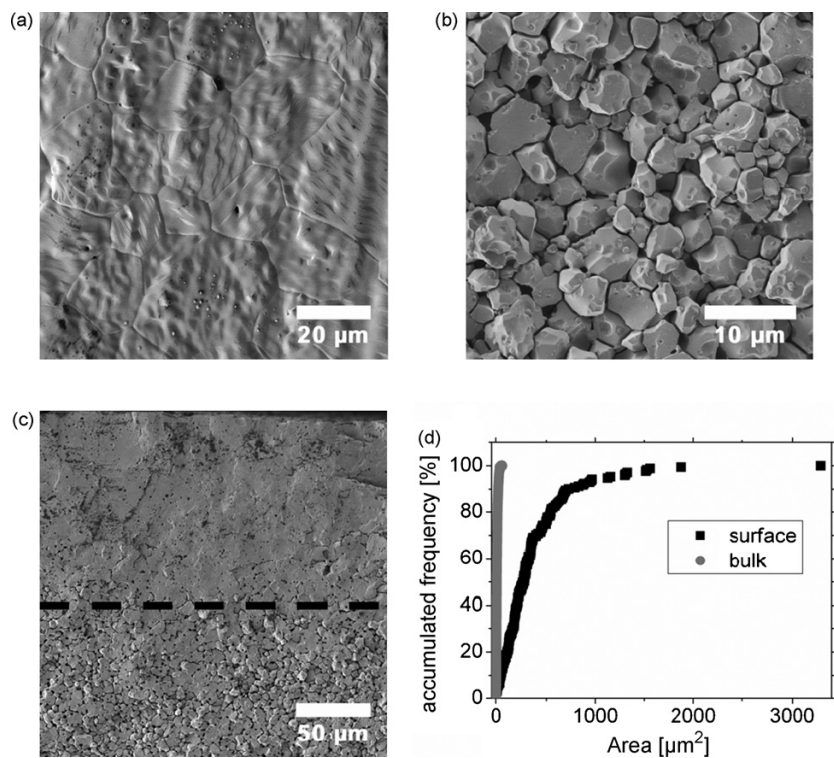


Fig. 2. SEM micrographs of A1 and grain size distribution: (a) surface, (b) fracture surface (bulk) etched 2 s with HCl (2 M), (c) cross-section etched 2 s with HCl (2 M) and (d) grain size distribution of surface and bulk.

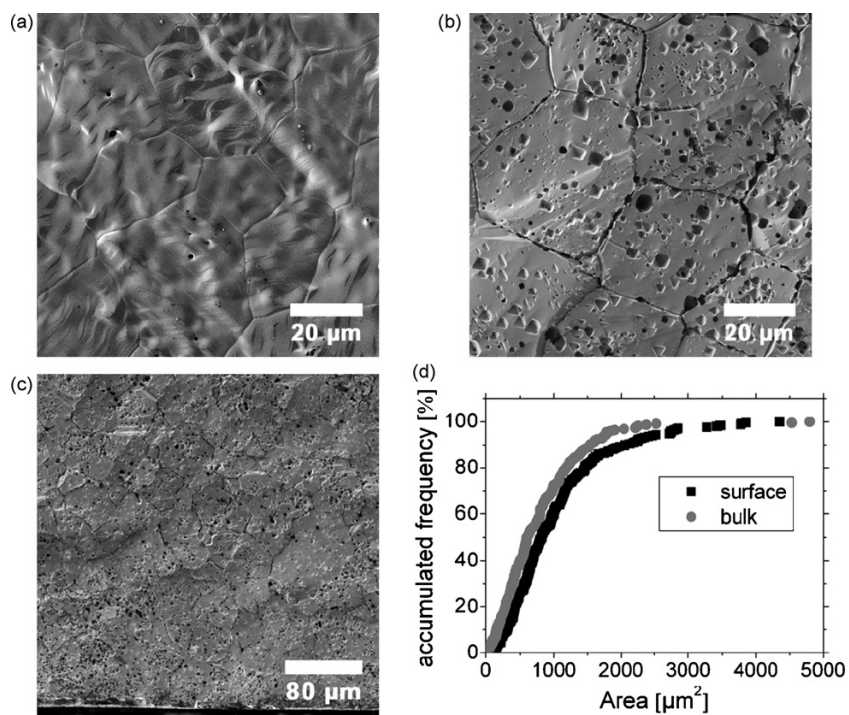
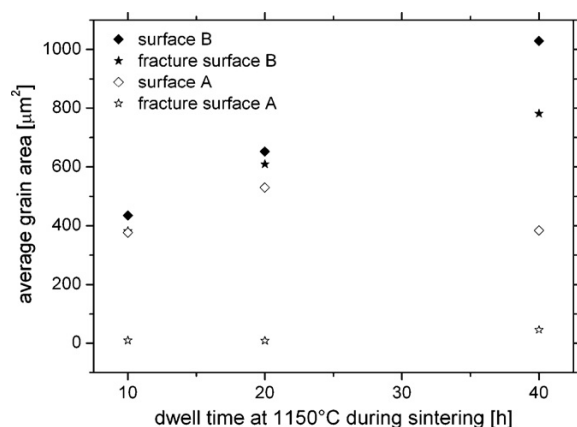


Fig. 3. SEM micrographs of membrane B3 and grain size distribution: (a) surface, (b) fracture surface (bulk) etched 2 s with HCl (2 M), (c) cross-section etched 2 s with HCl (2 M) and (d) grain size distribution of surface and bulk.

Table 1
Average grain area and synthesis conditions for membranes A1–3 and B1–3

	Powders Calcination 10 h at (°C)	Membranes		
		Average grain area		Dwell time at 1150 °C during sintering (h)
		Surface (μm^2)	Bulk (μm^2)	
A1	800	377	9	10
A2		530	8	20
A3		384	46	40
B1	950	435	302	10
B2		652	609	20
B3		1029	781	40

**Fig. 4.** Plot of the average grain area in dependence of the dwell time at 1150 °C during sintering for each of the three membranes of kind A and B for the surface and fracture surface.

the bulk is evident. When the grains in the A membranes are in poor contact from the beginning of the sintering process, then an extension of the dwell time during sintering does not result in a progression of the sintering process.

To make sure that the materials were all cubic perovskite-type without any impurities, XRD was applied to all powders and to all membrane surfaces. There was no evidence for impurities and therefore please find comparable data with Rietveld refinement published in [37]. Cross-sections of the membranes were analysed by EDXS, and no impurities or non-stoichiometries in the material composition were found. An example for an EDX spectrum is shown in [2].

Furthermore, the nature of grain boundaries has been evidenced by transmission electron microscopy (TEM). Membrane B3 was chosen because it showed the highest oxygen permeation. Fig. 5a–c shows high-resolution micrographs at three rising magnifications of a grain boundary of two grains with different zone axes. Fig. 5d and e shows the selected area electron diffraction (SAED) taken

with an 120 nm aperture of the left and right grain, respectively, which allows the determination of the zone axes of [201] for the grain at the left side and [001] for the grain at the right side. In this example the two lattice planes at the grain boundary are (010) and the grains are twisted with respect to each other by a dislocation angle of approximately 26° (Fig. 5b). The grain boundaries were found to be atomically thin without any interfacial phases (Fig. 5c) and the right grain merges into the left grain by leaving some planes unpaired, which is necessary to accommodate the dislocation angle of 26°. Comparable findings were already made for membranes of kind B1 [35].

It is very interesting to see the impact of the grain size distribution on the oxygen permeation (Fig. 6a). Membranes A1–3 with lower calcination temperature (800 °C) exhibit lower oxygen permeation abilities. The permeation increases with dwell time, but remains below that of B1. Thus, it is not favorable for the oxygen permeation to start from smaller grains in the green compact with the applied sintering conditions. But in principle the BSFZ synthesis provides the possibility of the preparation of nano-scale powders, which might be more favorable for the membrane abilities with different pressing or sintering conditions. Nevertheless, the increase of the dwell time for green compacts is expedient. For B2 and B3 with dwell times of 20 and 40 h, respectively, the oxygen permeation has been significantly enhanced. For 950 °C the oxygen permeation for B3 is with 1.08 mL/min cm² higher than that for B1 (0.96 mL/min cm²) and B2 (1.06 mL/min cm²). Comparable results have been found for $\text{Ba}_{0.5}\text{Sr}_{0.5}\text{Co}_{0.8}\text{Fe}_{0.2}\text{O}_{3-\delta}$ membranes [21]. Wang et al. found that the oxygen permeation flux increased considerably with the increase of the grain size.

For the determination of the activation energy Fig. 6b shows the logarithmic plot for the oxygen permeation flux depending on the inverse temperature. Regression analysis gives values for the activation energy E_a in the range of 50–60 kJ/mol, which are listed in Table 2. Actually E_a lies between 51 and 53 kJ/mol and just the value for A2 is an outlier with 59 kJ/mol. The variation of the activation energy does not exhibit a dependence of grain size changes, whereas the oxygen permeation flux increases with increasing grain size, what is illustrated by Fig. 7 for the sintered membranes at 950 °C permeation temperature.

Table 2
Experimental conditions, thickness, relative density (Archimedes method) and calculated activation energies for membranes A1–3 and B1–3 from 820 to 950 °C

	Dwell time at 1150 °C during sintering (h)	Thickness of membrane (mm)	Relative density (%)	Activation energy, E_a (kJ/mol)
A1	10	1.17	96	53
A2	20	1.15	96	53
A3	40	1.15	96	51
B1	10	1.15	94	51
B2	20	1.15	95	59
B3	40	1.15	96	53

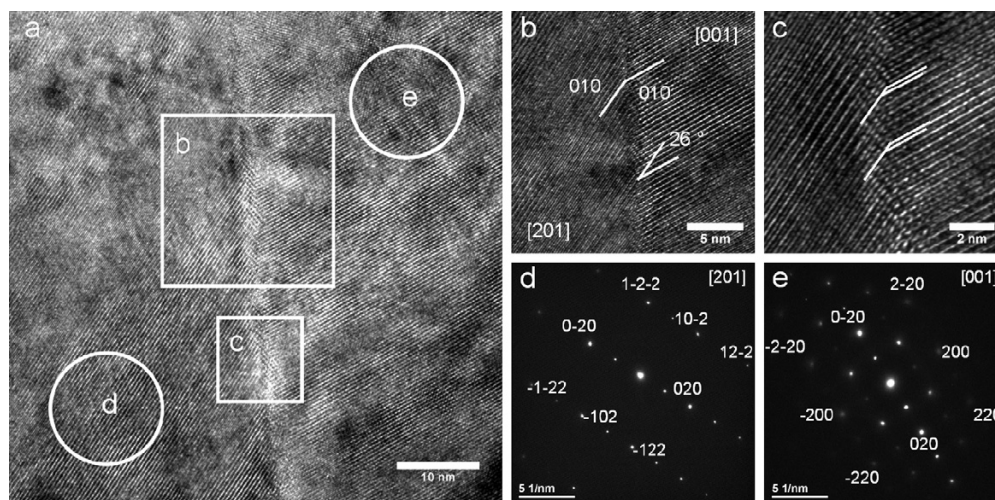


Fig. 5. TEM of a grain boundary in B3: (a–c) HRTEM at three different magnifications, (d) and (e) SAED of the left and right grain, respectively.

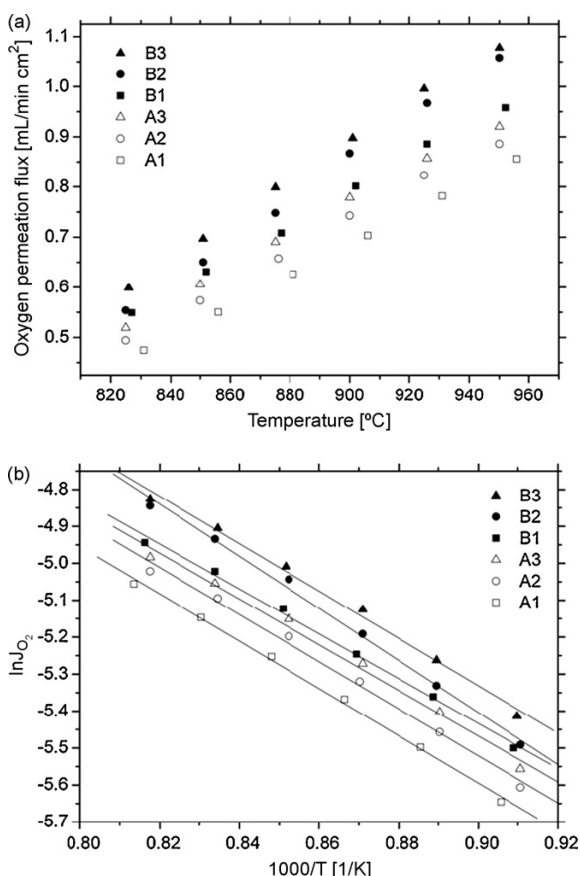


Fig. 6. Oxygen permeation measurements: (a) oxygen permeation flux in the temperature regime of 825–950 °C for six different membranes and (b) logarithmic plot for the oxygen permeation flux depending on the inverse temperature, and linear fittings.

Due to the fact that the thickness of the membranes (Table 2) was not significantly changed, the transport mechanism control – surface exchange or bulk diffusion – is expected to be the same for all investigated membranes. For surface exchange diffusion smaller grains are favorable due to bigger surface area thus in surface exchange controlled processes an increase in oxygen permeation is expected with decreasing grain size. The finding that the oxygen permeation is enhanced with increasing grain sizes leads to the conclusion that the ceramic exceeds L_c and the transport rate of the oxygen permeation is not limited by surface exchange but predominantly by bulk diffusion [18]. An increase in grain size is accompanied by a decrease of grain boundary ratio, thus grain boundaries in BSFZ act as barriers for the bulk diffusion and thus for the oxygen permeation. Following the theory of Maier [25] this material is a high mobility material, because the bulk structure is optimized for point defect motion and a structural modification as occurring in the grain boundary is likely to depress the mobility due to a pronounced chemical resistance

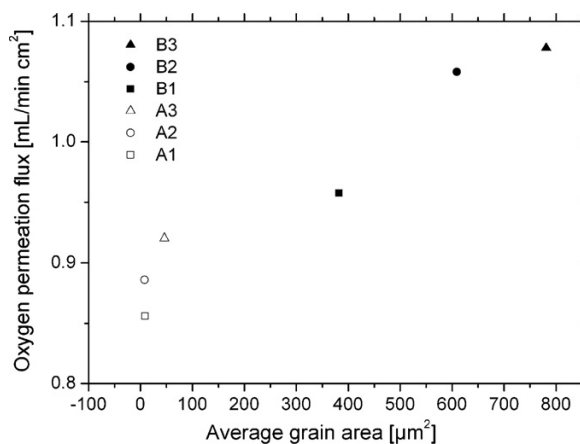


Fig. 7. Oxygen permeation flux of sintered membranes at 950 °C in dependence of the average grain area of the bulk.

of the grain boundary with respect to oxygen transport across it.

4. Conclusion

A variation of the calcination temperature of the as-synthesized perovskite powder in a sol–gel based process was used to control the grain sizes for the green compact for the ceramic production. Due to these grain size variations in the starting powder, we were able to control the grain sizes in the sintered ceramic. Membranes with distinctly smaller grains in the bulk than at the surface were synthesized. Supplementary, the sintering temperature and dwell time during sintering influence the final microstructure of the ceramic. An increase of dwell time produced membranes with larger grains in the sintered ceramics. For membranes of kind A (calcination of the powder at 800 °C for 10 h) the dwell time has a slight influence on the surface grain size and hardly any modification of the grain sizes of the bulk is evident. This can be explained by the poor contact of the grains in the green compact from the beginning of the sintering process. Whereas, for membranes of kind B (calcination of the powder at 950 °C for 10 h) an increase in dwell time during sintering results in larger grains at the surface as well as in the bulk. High-resolution transmission electron microscopy proved that grain boundaries are atomically thin without any interfacial phases.

The oxygen permeation can be enhanced by an increase of the dwell time during sintering of the membrane. This has been shown for both kinds of ceramics. A second finding is that a huge difference in grain size distribution between surface and fracture surface resulting in a sandwich-effect, where the size differences have to be balanced, leads to a decrease in oxygen permeation. Thus, it is not favorable for the oxygen permeation to start from smaller grains in the green compact with the applied pressing and sintering conditions. The activation energy was determined to be in the range of 51–53 kJ/mol with an outlier at 59 kJ/mol and its variation does not exhibit a dependence of grain size changes. The finding that the oxygen permeation is increased with increasing grain sizes leads to the conclusion that the transport rate of the oxygen permeation is limited predominantly by bulk diffusion. An increase in grain size is accompanied by a decrease of grain boundary ratio, thus grain boundaries in $(\text{Ba}_{0.5}\text{Sr}_{0.5})(\text{Fe}_{0.8}\text{Zn}_{0.2})\text{O}_{3-\delta}$ act as barriers for the bulk diffusion and thus for the oxygen permeation. Following [25] this material is a high mobility material.

Acknowledgements

The authors greatly acknowledge financial support by DFG grant number FE 928/1-2 and fruitful discussions with Prof. Jürgen Caro.

References

- [1] H. Wang, G. Grubert, C. Tablet, J. Caro, Sauerstofftransportierende Oxidkeramiken. Patent Application, EP 1630148/05102708.4 (2005).
- [2] H. Wang, C. Tablet, A. Feldhoff, J. Caro, A cobalt-free oxygen-permeable membrane based on the perovskite-type oxide $\text{Ba}_{0.5}\text{Sr}_{0.5}\text{Zn}_{0.2}\text{Fe}_{0.8}\text{O}_{3-\delta}$, *Adv. Mater.* 17 (2005) 1785–1788.
- [3] B. Wei, Z. Lu, X. Huang, Z. Liu, J. Miao, N. Li, W. Su, $\text{Ba}_{0.5}\text{Sr}_{0.5}\text{Zn}_{0.2}\text{Fe}_{0.8}\text{O}_{3-\delta}$ perovskite oxide as a novel cathode for intermediate-temperature solid-oxide fuel cells, *J. Am. Ceram. Soc.* 90 (10) (2007) 3364–3366.
- [4] H.J.M. Bouwmeester, A.J. Burggraaf, Dense ceramic membranes for oxygen separation, in: A.J. Burggraaf, L. Cot (Eds.), *Fundamentals of Inorganic Membrane Science and Technology*, Elsevier, Amsterdam, 1996, p. 435.
- [5] R. Merkle, J. Maier, H.J.M. Bouwmeester, A linear free energy relationship for gas–solid interactions: Correlation between surface rate constant and diffusion coefficient of oxygen tracer exchange for electron-rich perovskites, *Angew. Chem. Int. Ed.* 43 (2004) 5069–5073.
- [6] C. Hamel, A. Seidel-Morgenstern, T. Schiestel, S. Werth, H. Wang, C. Tablet, J. Caro, Experimental and modelling study of the O_2 -enrichment by perovskite fibers, *AIChE J.* 52 (2006) 3118–3125.
- [7] H. Yokokawa, N. Sakai, T. Kawada, M. Dokiya, Thermodynamic stabilities of perovskite oxides for electrodes and other electrochemical materials, *Solid State Ionics* 52 (1992) 43–56.
- [8] Z. Shao, S. Haile, A high-performance cathode for the next generation of solid-oxide fuel cells, *Nature* 431 (2004) 170–173.
- [9] S. Diethelm, J. van Herle, J. Sfeir, P. Buffat, Influence of microstructure on oxygen transport in perovskite type membranes, *Br. Ceram. Trans.* 103 (2004) 147–152.
- [10] G. Etchegoyen, T. Chartier, A. Julian, P. Del-Gallo, Microstructure and oxygen permeability of a $\text{La}_{0.6}\text{Sr}_{0.4}\text{Fe}_{0.9}\text{Ga}_{0.1}\text{O}_{3-\delta}$ membrane containing magnesia as dispersed second phase particles, *J. Membr. Sci.* 268 (2006) 86–95.
- [11] V.V. Kharton, E.N. Naumovich, A.V. Kovalevsky, A.P. Viskup, F.M. Figueiredo, I.A. Bashmakov, F.M.B. Marques, Mixed electronic and ionic conductivity of $\text{LaCo}(\text{M})\text{O}_3$ (M = Ga, Cr, Fe or Ni), IV. Effect of preparation method on oxygen transport in $\text{LaCoO}_{3-\delta}$, *Solid State Ionics* 138 (2000) 135–148.
- [12] V.V. Kharton, F.M. Figueiredo, A.V. Kovalevsky, A.P. Viskup, E.N. Naumovich, A.A. Yaremchenko, I.A. Bashmakov, F.M.B. Marques, Processing, microstructure and properties of $\text{LaCoO}_{3-\delta}$ ceramics, *J. Euro. Ceram. Soc.* 21 (2001) 2301–2309.
- [13] V.V. Kharton, A.V. Kovalevsky, A.A. Yaremchenko, F.M. Figueiredo, E.N. Naumovich, A.L. Shaulo, F.M.B. Marques, Surface modification of $\text{La}_{0.3}\text{Sr}_{0.7}\text{CoO}_{3-\delta}$ ceramic membranes, *J. Membr. Sci.* 195 (2002) 277–287.
- [14] P. Zeng, R. Ran, Z. Chen, H. Gu, Z. Shao, J.C. Diniz da Costa, S. Liu, Significant effects of sintering temperature on the performance of $\text{La}_{0.6}\text{Sr}_{0.4}\text{Co}_{0.2}\text{Fe}_{0.8}\text{O}_{3-\delta}$ oxygen selective membranes, *J. Membr. Sci.* 302 (2007) 171–179.
- [15] S. Diethelm, J. van Herle, J. Sfeir, P. Buffat, Correlation between oxygen transport properties and microstructure in $\text{La}_{0.5}\text{Sr}_{0.5}\text{FeO}_{3-\delta}$, *J. Eur. Ceram. Soc.* 25 (2005) 2191–2196.
- [16] H. Kusaba, Y. Shibata, K. Sasaki, Y. Teraoka, Surface effect on oxygen permeation through dense membrane of mixed-conductive LSCF perovskite-type oxide, *Solid State Ionics* 177 (2006) 2249–2253.
- [17] G. Etchegoyen, T. Chartier, P. Del-Gallo, Oxygen permeation in $\text{La}_{0.6}\text{Sr}_{0.4}\text{Fe}_{0.9}\text{Ga}_{0.1}\text{O}_{3-\delta}$ dense membrane: effects of surface microstructure, *J. Solid State Electrochem.* 10 (2006) 597–603.
- [18] H.J.M. Bouwmeester, H. Kruidhof, A.J. Burggraaf, Importance of the surface exchange kinetics as rate limiting step in oxygen permeation through mixed-conducting oxides, *Solid State Ionics* 72 (1994) 185–194.
- [19] S. Kim, S. Wang, X. Chen, Y.L. Yang, N. Wu, A. Ignatiev, A.J. Jacobsen, B. Abeles, Oxygen surface exchange in mixed ionic electronic conductors: application to $\text{La}_{0.5}\text{Sr}_{0.5}\text{Fe}_{0.8}\text{Ga}_{0.2}\text{O}_{3-\delta}$, *J. Electrochem. Soc.* 147 (6) (2000) 2398–2406.
- [20] K. Zhang, Y.L. Yang, D. Ponnusamy, A.J. Jacobson, K. Salama, Effect of microstructure on oxygen permeation in $\text{SrCo}_{0.8}\text{Fe}_{0.2}\text{O}_{3-\delta}$, *J. Mater. Sci.* 34 (1999) 1367–1372.
- [21] H. Wang, C. Tablet, A. Feldhoff, J. Caro, Investigation of phase structure, sintering, and permeability of perovskite-type $\text{Ba}_{0.5}\text{Sr}_{0.5}\text{Co}_{0.8}\text{Fe}_{0.2}\text{O}_{3-\delta}$ membranes, *J. Membr. Sci.* 262 (2005) 20–26.
- [22] M. Arnold, J. Martynczuk, K. Efimov, H. Wang, A. Feldhoff, Grain boundaries as barrier for oxygen transport in perovskite-type membranes, *J. Membr. Sci.* 316 (2008) 137–144.
- [23] V.V. Kharton, V.N. Tikhonovich, L. Shuangbao, E.N. Naumovich, A.V. Kovalevsky, A.P. Viskup, I.A. Bashmakov, A.A. Yaremchenko, Ceramic microstructure and oxygen permeability of $\text{SrCo}(\text{Fe},\text{M})\text{O}_{3-\delta}$ (M = Cu or Cr) perovskite membranes, *J. Electrochem. Soc.* 145 (1998) 1363–1373.
- [24] V.V. Kharton, A.V. Kovalevsky, A.A. Yaremchenko, F.M.M. Snijders, J.F.C. Coymans, J.J. Luyten, A.A. Markov, J.R. Frade, F.M.B. Marques, Oxygen transport and thermomechanical properties of $\text{SrFe}(\text{Al})\text{O}_{3-\delta}$ – SrAl_2O_4 composites: microstructural effects, *J. Solid State Electrochem.* 10 (2006) 663–673.
- [25] J. Maier, Transport in electroceramics: micro- and nano-structural aspects, *J. Euro. Ceram. Soc.* 24 (2004) 1251–1257.
- [26] R. Waser, Bulk conductivity, defect chemistry of acceptor-doped strontium titanate in the quenched state, *J. Am. Ceram. Soc.* 74 (1991) 1934–1940.
- [27] X. Guo, J. Fleig, J. Maier, Separation of electronic and ionic contributions to the grain boundary conductivity in acceptor-doped SrTiO_3 , *J. Electrochem. Soc.* 148 (2001) J50–J53.
- [28] X. Guo, J. Maier, Grain boundary blocking effect in zirconia: a Schottky barrier analysis, *J. Electrochem. Soc.* 148 (2001) E121–E126.
- [29] G.E. Pike, C.H. Seager, DC voltage dependence of semiconductor grain-boundary resistance, *J. Appl. Phys.* 50 (1979) 3414–3422.
- [30] Y.-M. Chiang, T. Tagaki, Grain-boundary chemistry of barium-titanate and strontium-titanate. 1. High-temperature equilibrium space-charge, *J. Am. Ceram. Soc.* 73 (1990) 3278–3285.
- [31] I. Denk, J. Claus, J. Maier, Electrochemical investigations of SrTiO_3 boundaries, *J. Electrochem. Soc.* 144 (1997) 3526–3536.
- [32] M. Leonhardt, J. Jamnik, J. Maier, In situ monitoring and quantitative analysis of oxygen diffusion through Schottky-barriers in SrTiO_3 bicrystals, *Electrochem. Solid-State Lett.* 2 (1999) 333–335.
- [33] S. Kim, J. Maier, On the conductivity mechanism of nanocrystalline ceria, *J. Electrochem. Soc.* 149 (2002) 373–383.
- [34] J. Martynczuk, H. Wang, M. Arnold, A. Feldhoff, Influence of processing conditions on the microstructure and function of $\text{Ba}_{0.5}\text{Sr}_{0.5}\text{Fe}_{0.8}\text{Zn}_{0.2}\text{O}_{3-\delta}$ membranes, in: R. Bredeken, et al. (Eds.), *Proc. 9th Int. Conf. on Inorganic Membranes, SINTEF, Lillehammer, Norway, 2006*, pp. 503–506.
- [35] A. Feldhoff, J. Martynczuk, H. Wang, Advanced $\text{Ba}_{0.5}\text{Sr}_{0.5}\text{Fe}_{0.8}\text{Zn}_{0.2}\text{O}_{3-\delta}$ perovskite-type ceramics as oxygen selective membranes: Evaluation of the synthetic process, *Prog. Solid State Chem.* 35 (2007) 339–353.

- [36] J. Martynczuk, M. Arnold, H. Wang, J. Caro, A. Feldhoff, How $(\text{Ba}_{0.5}\text{Sr}_{0.5})(\text{Fe}_{0.8}\text{Zn}_{0.2})\text{O}_{3-\delta}$ and $(\text{Ba}_{0.5}\text{Sr}_{0.5})(\text{Co}_{0.8}\text{Fe}_{0.2})\text{O}_{3-\delta}$ perovskites form via an EDTA/citric acid complexing method, *Adv. Mater.* 19 (2007) 2134–2140.
- [37] A. Feldhoff, M. Arnold, J. Martynczuk, Th. Gesing, H. Wang, The sol-gel synthesis of perovskites by EDTA/citrate complexing method involves nanoscale solid state reactions, *Solid State Sci.* (2008), doi:10.1016/j.solidstatesciences.2007.11.030.
- [38] M.N. Rahaman, *Ceramic Processing and Sintering*, second Edition, CRC Press Taylor & Francis Group, Boca Raton, London, New York, 2003, p. 486.

3.3 Grain boundaries as barrier for oxygen transport in perovskite-type membranes

Mirko Arnold, Julia Martynczuk, Konstantin Efimov,
Haihui Wang, and Armin Feldhoff

Journal of Membrane Science 316, 137-144 (2008)

Available online at www.sciencedirect.com

Journal of Membrane Science 316 (2008) 137–144

**Journal of
MEMBRANE
SCIENCE**
www.elsevier.com/locate/memsci

Grain boundaries as barrier for oxygen transport in perovskite-type membranes

 Mirko Arnold^{a,*}, Julia Martynczuk^a, Konstantin Efimov^a, Haihui Wang^b, Armin Feldhoff^a
^a Institute of Physical Chemistry and Electrochemistry, Leibniz Universität Hannover, Callinstr. 3-3A, D-30167 Hannover, Germany^b College of Chemical and Energy Engineering, South China University of Technology, Guangzhou 510640, PR China

Received 6 July 2007; received in revised form 27 September 2007; accepted 1 October 2007

Available online 6 October 2007

Abstract

Perovskite-type membranes of $(\text{Ba}_{0.5}\text{Sr}_{0.5})(\text{Co}_{0.8}\text{Fe}_{0.2})\text{O}_{3-\delta}$ (BSCF) and $(\text{Ba}_{0.5}\text{Sr}_{0.5})(\text{Fe}_{0.8}\text{Zn}_{0.2})\text{O}_{3-\delta}$ (BSFZ) were successfully prepared via liquid-phase sintering using BN as sintering aid. The obtained membranes were examined via powder X-ray diffraction pattern (XRD), differential scanning calorimetry (DSC), scanning electron microscopy (SEM), transmission electron microscopy (TEM) and oxygen permeation experiments. It has emerged that the use of BN as sintering aid lowers sintering temperatures in order to obtain dense membranes with relative densities in the range of 93–96% as proven by the Archimedes method. It was further shown that the perovskite structure could be maintained after sintering with BN. Additionally, BN was completely removed from the sintered membranes. Investigation of the microstructure revealed that the average grain size of the membranes was influenced by the amount of BN added prior the sintering process. It was found that large amounts of BN effectively lower the average grain size. Oxygen permeation experiments have shown that the lower the average grain size the lower the oxygen permeation performance, particularly in the case of BSCF. Transmission electron microscopy revealed that no evidence for an amorphous layer or any other interfacial phase in the grain boundary is present.

© 2007 Elsevier B.V. All rights reserved.

Keywords: BSCF; BSFZ; Oxygen permeation; Grain boundaries; Transmission electron microscopy; Perovskite; Liquid-phase sintering; BN; Grain size distribution

1. Introduction

Nowadays, mixed ionic–electronic conductors (MIECs) with perovskite structure are applied in many different processes as they allow to selectively separate oxygen from gaseous mixtures. Due to their intrinsic mixed conductivity, they are of great interest for many industrial processes in which a constant supply or removal of oxygen to or from reaction mixtures is required [1]. Applications such as the usage of MIEC as cathode material in solid-oxide fuel cells as well as in the production of oxygen enriched air and in the conversion of hydrocarbons to synthesis gas have been reported [2–6]. Major advantages of these membranes are their almost infinite permselectivity and remarkable high oxygen fluxes in the range observed on microporous materials [1].

Within the MIECs, $(\text{Ba}_{0.5}\text{Sr}_{0.5})(\text{Co}_{0.8}\text{Fe}_{0.2})\text{O}_{3-\delta}$ (BSCF) is regarded to be one of the most promising materials as mem-

branes made of it show high oxygen permeation fluxes and excellent phase stability even under low oxygen partial pressures and reducing gas atmospheres [7–9]. Recently, a new perovskite system $(\text{Ba}_{0.5}\text{Sr}_{0.5})(\text{Fe}_{0.8}\text{Zn}_{0.2})\text{O}_{3-\delta}$ (BSFZ) was invented which also exhibits excellent phase stability and remarkably high oxygen fluxes [10–12]. As these perovskite systems display two of the state-of-the-art materials, they are of special interest and thus investigated regarding their microstructure and oxygen permeation performance in the presented study.

Several groups have reported that the microstructure and thus the relation between bulk and grain boundary oxygen ion diffusivity within dense ceramic membranes significantly influences the oxygen permeation performance [13–19]. Different perovskite systems were studied in these reports and no clear trend is visible whether the transport along grain boundaries displays a barrier or acts as a pathway for fast oxygen transport. Diethelm et al. found for $(\text{La}_{0.5}\text{Sr}_{0.5})\text{FeO}_{3-\delta}$ that the larger the obtained grains – and thus the fewer the grain boundaries – the smaller the observed oxygen permeation performance [13–14]. Similar findings were reported for $\text{LaCoO}_{3-\delta}$ by Kharton and Marques [15]. Contrary to that, in ceramics

* Corresponding author. Tel.: +49 511 762 4896; fax: +49 511 762 19121.

E-mail address: mirko.arnold@pci.uni-hannover.de (M. Arnold).

of $\text{Ca}(\text{Ti}_{0.8}\text{Fe}_{0.2})\text{O}_{3-\delta}$ – prepared by mechanical activation – grain boundaries are suggested to act as a barrier for oxygen permeation [16]. Most remarkably, opposite results were found within the system $(\text{Ba}_{1-x}\text{Sr}_x)(\text{Co}_{0.8}\text{Fe}_{0.2})\text{O}_{3-\delta}$. The end member $\text{Sr}(\text{Co}_{0.8}\text{Fe}_{0.2})\text{O}_{3-\delta}$ provides improved oxygen permeation performance by decreasing the average grain size, whereas for $(\text{Ba}_{0.5}\text{Sr}_{0.5})(\text{Co}_{0.8}\text{Fe}_{0.2})\text{O}_{3-\delta}$ opposite observations have been obtained [17–19]. As several parameters during the preparation influence the properties of the membrane, the effect of the microstructure on the oxygen permeation has to be studied more systematically. This could be done by varying the microstructure in different perovskite systems via the same way, i.e. the sintering temperature and dwelling time. Additionally, care has to be taken by comparing results, if the raw perovskite powder has been prepared in different ways, which might also influence the properties of the final membrane.

In this study, we have applied a liquid-phase sintering to obtain BSCF and BSFZ membranes using BN as sintering aid. The method was described by Ho on the BaTiO_3 perovskite system [20]. It was shown that the application of BN as sintering aid allows to lowering the sintering temperature, and no incorporation of boron into the perovskite lattice was observed. Due to the fact that during the sintering process a liquid-phase is eminent in the membrane, a lowering of the average grain size is expected [21]. In order to study the changes in microstructure and its influence on the oxygen permeation performance, membranes of BSCF and BSFZ with varying BN content during sintering were prepared. Investigations of the microstructure were carried out by scanning electron microscopy (SEM) combined with energy-dispersive X-ray spectroscopy (EDXS). Transmission electron microscopy (TEM) along with EDXS and electron energy-loss spectroscopy (EELS) was conducted to examine the microstructure and elemental composition of grain boundaries. Additionally, differential scanning calorimetry (DSC), X-ray diffraction (XRD) and oxygen permeation experiments as well as relative density measurements were applied for characterization purposes.

2. Experimental

BSCF and BSFZ powders were synthesized via a combined citrate and ethylene-diamine-tetraacetic acid (EDTA) complexing method according to Shao et al. [9]. Proper amounts of $\text{Ba}(\text{NO}_3)_2$, $\text{Sr}(\text{NO}_3)_2$, $\text{Co}(\text{NO}_3)_2 \cdot 6(\text{H}_2\text{O})$, $\text{Fe}(\text{NO}_3)_3 \cdot 9(\text{H}_2\text{O})$, and $\text{Zn}(\text{NO}_3)_2 \cdot 2(\text{H}_2\text{O})$ were dissolved in water, followed by the addition of citric acid, EDTA and $\text{NH}_3 \cdot (\text{H}_2\text{O})$. The reaction mixtures were then heated under constant stirring to obtain a purple-coloured gel. Afterwards the gels were pre-calcined for 2 h at 700 °C. The pre-calcined powders were grounded and finally fired for 10 h at 950 °C to get the pure perovskite phases. The pure perovskite powders were then carefully grounded together with certain amounts of hexagonal-BN (space group: $P6_3/mmc$ (194), $a = 2.5044 \text{ \AA}$, $c = 6.6562 \text{ \AA}$; Powder Diffraction File: 34–421, average particle size of $\varnothing = 1 \text{ \mu m}$): 2.5, 5, 7.5, and 10 mol%. The grounded powders were then coldly pressed under 140–150 kN for 20 min to prepare “green” membranes which were finally sintered at 1050 °C (BSCF) and 1100 °C (BSFZ)

with a dwelling time of 10 h in an ambient air atmosphere. In order to estimate the optimal sintering temperature, the melting point of each membrane was measured via (DSC) on a SETSYS TGA-DSC instrument. Relative densities of the sintered membranes were acquired via the Archimedes method on a Sartorius balance model BP 211D with a resolution of 0.01 mg equipped with compatible attachment.

To study the oxygen permeation performance of the sintered membranes, several permeation experiments were carried out on a self-made high temperature permeation cell which is described in detail elsewhere [18]. Discs of BSCF and BSFZ ($\varnothing = 14 \text{ mm}$, thickness = 1.15 mm) were sealed onto a ceramic tube with gold-paste (conducting paste, C5754, Heraeus) at 950 °C for 2 h. After sealing, gas flow rates were delivered to the reactor by mass flow controllers (Bronkhorst Hi-Tech) and continuously read by an on-line gas chromatograph (Agilent Technologies, HP 6890, equipped with a Carboxen 1000 column). The feed side (outer site of the ceramic tube onto the membrane was sealed) of the membrane was flushed with synthetic air. On the sweep side (inner site of the ceramic tube onto the membrane was sealed) pure helium and neon were applied. The total flow rate on the feed side of the membrane was set to be 150 ml/min, and the total flow rate on the sweep side to 30 ml/min. The absolute flow rate of the permeate stream (sweep plus permeated oxygen plus leakage) was determined by using neon as an internal standardization. The permeate stream (consisting of helium, oxygen, nitrogen, and neon) was examined by gas chromatography. For each component a quantitative calibration with known standards was conducted. Thus, the area of each component chromatogram was directly related to a certain percentage of this component. As the supplied sweep flow rate (i.e. helium and neon with no permeated oxygen) was known, it was thus possible to determine the total permeate flow rate from the concentration of neon in the permeate stream. The total leakage (<5%) was calculated by the amount of nitrogen, i.e. the percentage nitrogen found in the permeate stream was treated as the leakage. The related amount of oxygen was then subtracted from the total oxygen in the chromatogram leading to the net permeated oxygen. The permeation flux through the membrane could then be calculated by the fraction O_2 in the effluents and the determination of the effective permeation area of the membranes. Permeation experiments were conducted in the temperature range from 800 to 925 °C with steps of 25 °C. For each temperature step, an equilibrium time of 60 min was set. The actual temperature was measured slightly above the membranes.

In order to analyze the microstructure of the sintered membranes, SEM combined with EDXS as well as XRD were conducted on both surfaces and on fracture surfaces. Grain size distributions were evaluated by SEM on a JEOL JSM-6700F field-emission instrument using a secondary electron detector (SE) at an accelerating voltage of 2 kV. Fracture surfaces were etched with aqueous HCl (2 M) for 2–5 s in order to visualize grain boundaries. EDX spectra were obtained at an accelerating voltage of 15 kV using a light-element detector (INCA 300, Oxford Instruments). To determine the crystal structure of sintered membranes, XRD were conducted with monochromated $\text{Cu K}\alpha_1$ radiation in the range of 20–50° 2θ at room temperature

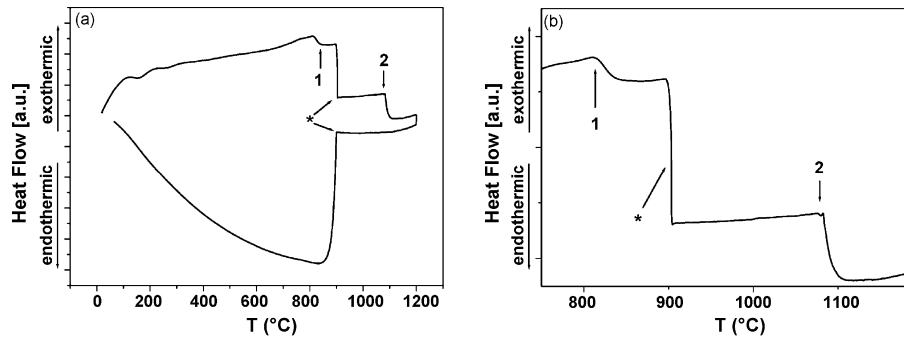


Fig. 1. DSC data obtained from a “green” BSCF membrane containing 10 mol% BN in a synthetic air atmosphere. The asterisk indicate a sensitivity switch of the instrument.

(Philips X’Pert-PW1710) on surfaces and grounded membranes. Powder XRD data for interpretation were taken from literature, ZnO: ICDD database PDF number [36–1451], BSCF [22], BSFZ [23].

Additionally, TEM was conducted at 200 kV with a JEOL JEM-2100F-UHR field-emission instrument equipped with a Gatan GIF 2001 energy filter and a 1k-CCD camera in order to obtain EEL spectra. EDXS was carried out by a light-element detector using the Cliff–Lorimer quantification technique (INCA 200 TEM, Oxford Instruments). Furthermore, the specimen for TEM investigations was prepared as follows. First, pieces of 1 mm × 1 mm × 2 mm were cut out of the membrane followed by covering of both sides with silicon single crystal using epoxy. Accordingly, the protected membrane pieces were polished on polymer embedded diamond lapping films down to 0.02 mm × 1 mm × 2 mm and glued onto a copper slot grid. Electron transparency was achieved by Ar⁺ ion sputtering at 3 kV under incident angles of 6° and 4° (Gatan, model 691 PIPS).

3. Results and discussion

Fig. 1a and b shows DSC data obtained from a “green” BSCF membrane containing 10 mol% BN in a synthetic air atmosphere. Around 800 °C (point 1), BN starts to oxidise yielding in B₂O₃ as indicated by an endothermic process. As B₂O₃ starts to melt immediately after oxidisation, we postulate that the endothermic process of oxidisation covers the endothermic melting process. Thus, the heat flow of this melting process is not directly visible. At 1078 °C (point 2), an endothermic heat flow is observed, which is clearly related to the melting process of the membrane followed by the decomposition of the melt.

For both materials, BSCF and BSFZ, respectively, excellent phase maintenance after sintering with BN has been observed as it can be concluded by comparing the obtained XRD pattern with those obtained from pure BSCF and BSFZ powders [22,23] as visible in Fig. 2a and b. Despite the fact the perovskite structure could be maintained even after sintering with BN, small amounts of CoO have been found in the BSCF membrane that was sintered with 10 mol% (not visible in XRD pattern but confirmed by EDXS of the fracture surface). In the case of BSFZ membranes that were sintered with 7.5 and 10 mol% small amounts of ZnO

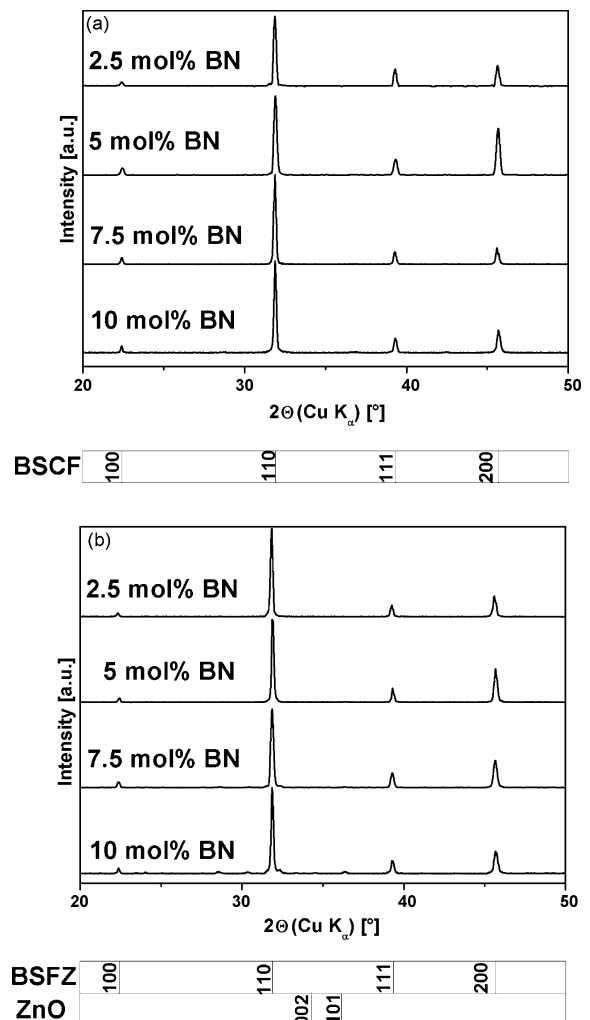


Fig. 2. XRD pattern taken of sintered membranes (surfaces) as synthesized: (a) BSCF, (b) BSFZ. XRD data obtained of pure BSCF and BSFZ and ZnO are displayed for comparison.

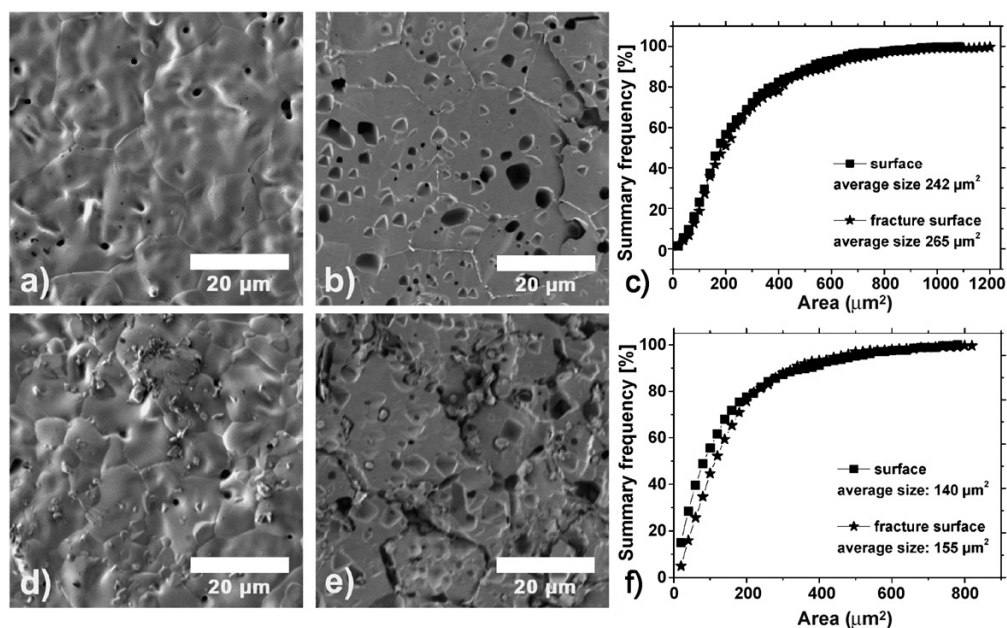


Fig. 3. SEM micrographs showing surfaces and fracture surfaces of sintered BSCF membranes (a–f). (a) Surface, (b) fracture surface, and (c) grain size distribution of a BSCF membrane containing 2.5 mol% BN. (d) Surface, (e) fracture surface, and (f) grain size distribution of a BSCF membrane containing 10 mol% BN.

have been detected on the surface as shown in Fig. 2b. Additionally, two unidentified reflections with very low intensities at $28.6^\circ 2\theta$ and $30.4^\circ 2\theta$ were found in these membranes.

In order to examine the microstructure of the sintered membranes, SEM was conducted on both surfaces and fracture surfaces on each membrane (Figs. 3 and 4). Fig. 3 displays SEM

micrographs and corresponding grain size distributions of BSCF membranes after sintering with 2.5 mol% BN (a–c) and with 10 mol% BN (d–f) for 10 h at 1050°C , respectively. As it can be seen in Fig. 3, dense membranes of BSCF sintered with BN have been achieved with low level of porosity even if the sintering temperature was decreased to 1050°C . Wang et al. found

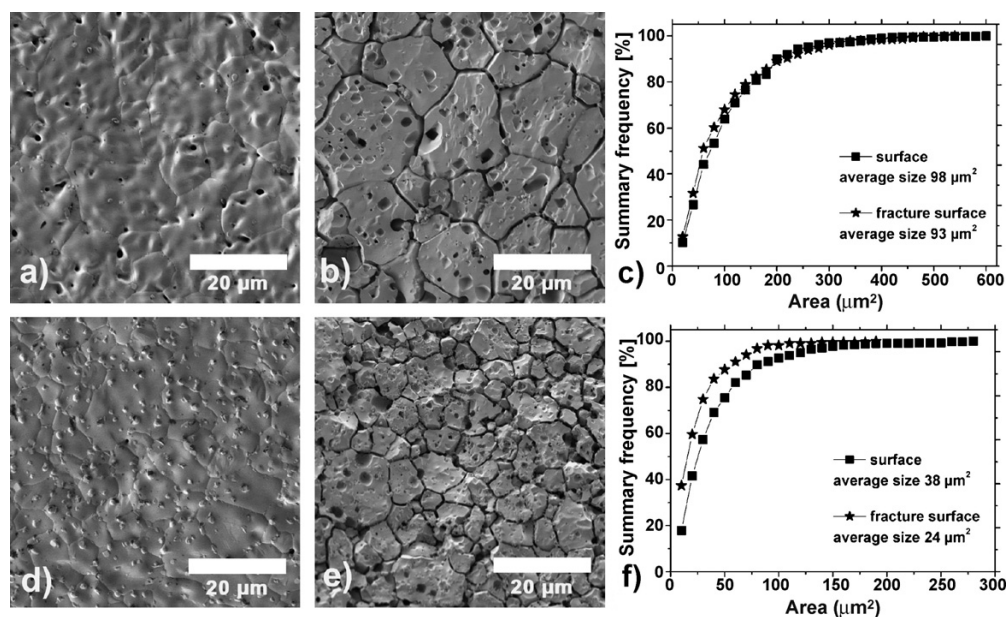


Fig. 4. SEM micrographs showing surfaces and fracture surfaces of sintered BSFZ membranes (a–f). (a) Surface, (b) fracture surface, and (c) grain size distribution of a BSFZ membrane containing 2.5 mol% BN. (d) Surface, (e) fracture surface, and (f) grain size distribution of a BSFZ membrane containing 10 mol% BN.

Table 1
Summary of melting points of membranes after sintering with indicated mol% BN obtained via DSC

BSCF (mol% BN)	T_{melt} (°C)	BSFZ (mol% BN)	T_{melt} (°C)
2.5	1131	2.5	1218
5	1102	5	1161
7.5	1088	7.5	1142
10	1078	10	1117

that sintering temperatures of at least 1150 °C were needed to obtain dense BSCF membranes with negligible porosity [18]. Obviously, the sintering aid BN helped to lower the sintering temperature of the prepared dense membranes. This was confirmed by DSC, as the melting point of the membranes was decreased using BN as sintering aid. A summary of the melting temperatures of the sintered BSCF and BSFZ membranes is given in Table 1.

Quantitative evaluation of the grain size distribution via SEM have shown that the addition of large amounts of BN lead to a decrease of the average grain size (Fig. 3c and f). The average grain size of BSCF-membranes sintered with 2.5 mol% BN has been determined to be 242 μm^2 at the surface and 265 μm^2 at the fracture surface, respectively. Contrary, membranes sintered with 10 mol% exhibit average grain sizes of 140 μm^2 (surface) and 155 μm^2 (fracture surface). In the case of 10 mol% BN, small particles of CoO ($\sim 1 \mu\text{m}^2$) have been found on the fracture surface as confirmed by EDXS.

Similar experiments were conducted for membranes of BSFZ. It has emerged, that melting temperatures of BSFZ membranes with BN as sintering lie generally up to 70 °C higher than that for the BSCF membranes (Table 1). In Fig. 4, SEM micrographs and grain size distributions of membranes after sintering with 2.5 mol% BN (a–c) and membranes sintered with 10 mol% BN are displayed (d–f). As for the case of BSCF, BSFZ membranes sintered with BN exhibit a low level of porosity and the same trend for the average grain size was found as for the BSCF membranes: The higher the amount of added BN the lower the average grain size. The average grain size of membranes sintered with 2.5 mol% has been determined to be 98 μm^2 (surface) and 93 μm^2 (fracture surface) compared to 38 μm^2 (surface) and 24 μm^2 (fracture surface) if 10 mol% BN was added (Fig. 4c and f). It has to be noted that small particles ($\sim 1 \mu\text{m}^2$) of ZnO (Fig. 4d) were found on the membrane surface after sintering with 7.5 and 10 mol% BN, respectively. Table 2 summarizes average grain sizes found in each membrane and it clearly demonstrates that increasing the amount of BN as

Table 3
Relative densities of BSCF and BSFZ membranes after sintering obtained by the Archimedes method

mol% BN	BSCF (%)	BSFZ (%)
10	94	92
7.5	96	94
5	96	95
2.5	93	93

sintering aid leads to a decrease in the average grain size. Additionally, it has to be emphasized that no boron has been found by EDXS in the surface or in the fracture surface in membranes of BSCF and BSFZ, respectively. Relative densities, displayed in Table 3, of the sintered membranes by the Archimedes method are estimated to vary randomly from 93 to 96% which display reasonable values as reported elsewhere [18].

As already found by Wang et al. [18], grain boundaries may affect the oxygen permeation in BSCF membranes in a negative manner. Therefore, oxygen permeation experiments were conducted in order to determine the influence of the average grain size (and thus the impact of grain boundaries) on the oxygen transport through the perovskite membranes. Fig. 5a and b displays the temperature-dependent oxygen permeation flux of BSCF and BSFZ membranes sintered with varying BN content. For all membranes, an almost linear slope for the oxygen permeation is observed in the temperature regime studied here. BSCF membranes sintered with 2.5 mol% BN exhibit an oxygen permeation performance that varies from 1.50 ml/min cm^2 at 850 °C to 2.60 ml/min cm^2 at 925 °C. As the amount of BN was increased during sintering, a diminution of the oxygen permeation flux has been observed (0.80 ml/min cm^2 at 850 °C to 1.60 ml/min cm^2 at 925 °C for 10 mol% BN added). In the case of BSFZ membranes sintered with BN, the oxygen permeation performance is not as strongly affected by the addition of BN as in the case of BSCF. Up to 7.5 mol% BN added as sintering aid no change in the oxygen permeation performance could be found and its ranges from 0.40 ml/min cm^2 (850 °C) to 0.85 ml/min cm^2 (925 °C) which is in the same order of magnitude as reported for membranes without sintering aid [10]. Only if the BN addition was set to 10 mol%, a distinct diminution in the oxygen permeation performance has been observed, as the oxygen permeation flux is found to range between 0.37 ml/min cm^2 (850 °C) and 0.80 ml/min cm^2 (925 °C) in this case.

In order to better visualize the dependence of oxygen permeation performance on the amount BN added to the membranes

Table 2
Summary of average grain sizes in sintered membranes with varying BN content

BSCF			BSFZ		
mol% BN	Area (μm^2) (surface)	Area (μm^2) (fracture surface)	mol% BN	Area (μm^2) (surface)	Area (μm^2) (fracture surface)
2.5	242	265	2.5	98	93
5	250	218	5	68	69
7.5	216	199	7.5	46	33
10	140	155	10	38	24

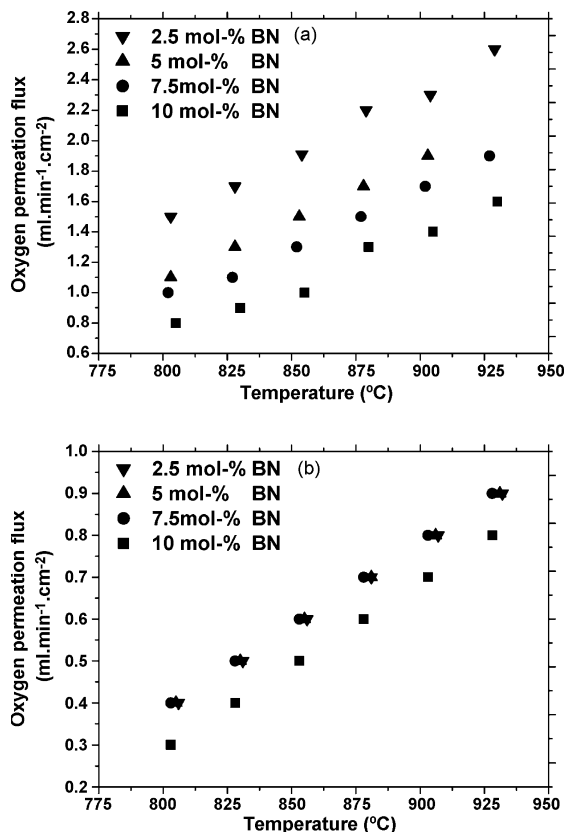


Fig. 5. Temperature-dependent oxygen permeation flux of sintered membranes with different BN content: (a) BSCF, (b) BSFZ. Conditions: feed synthetic air flow rate 150 ml/min, sweep flow rate 30 ml (helium 29 ml/min, neon 1 ml/min).

before sintering, oxygen permeation fluxes are plotted against the BN content and the average grain size on the surface at fixed temperature (Fig. 6a and b). At a temperature of 900 °C the oxygen permeation decreases from 2.30 ml/min cm² (2.5 mol% BN) down to 1.40 ml/min cm² (10 mol% BN) for BSCF membranes, whereas the oxygen permeation flux of BSFZ membranes range from 0.80 down to 0.70 ml/min cm² at 900 °C (Fig. 6a). The influence of the average grain size of the membranes on the oxygen permeation performance is displayed in Fig. 6b. For the case of BSCF membranes a decrease of the oxygen permeation flux from 2.30 down to 1.40 ml/min cm² is observed whereas the corresponding average grain size ranges from 265 to 155 μm² at the fracture surface. It should be stressed that the oxygen permeation performance decreases proportionally to the average grain size. In order to draw a general conclusion, membranes that have been sintered without boron nitride were also studied. Permeation experiments show that membranes consisting of an average grain size of 468 μm² (surface) and 430 μm² (fracture surface) exhibit an oxygen flux of 2.70 ml/min cm² at 900 °C, which is in excellent agreement with results discussed above.

In the case of BSFZ, the oxygen permeation flux varies from 0.77 to 0.72 ml/min cm² at 900 °C whereas the average grain size at the fracture surface ranges from 93 to 24 μm².

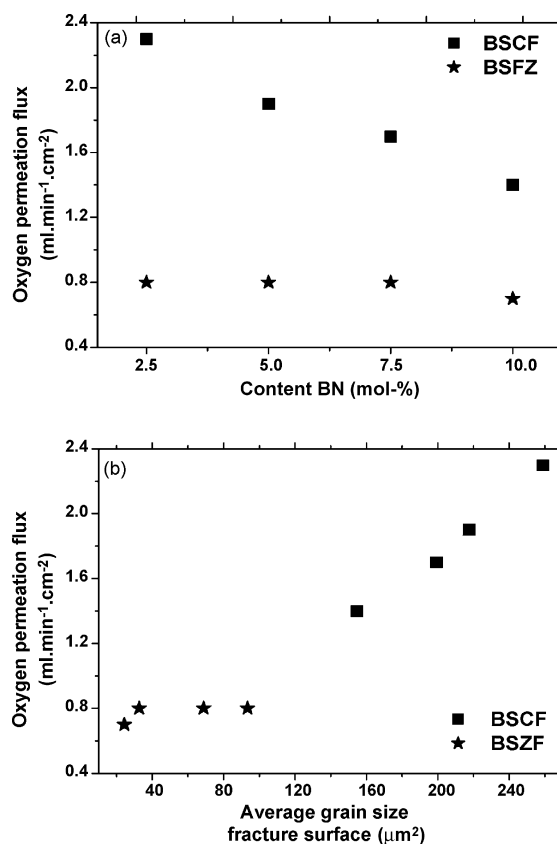


Fig. 6. Oxygen permeation flux of sintered membranes with different BN content at 900 °C. (a) Oxygen permeation flux in dependence of BN content and (b) oxygen permeation flux in dependence of average grain size at fracture surface. Conditions: feed synthetic air flow rate 150 ml/min, sweep flow rate 30 ml (helium 29 ml/min, neon 1 ml/min).

Again, membranes without BN addition were prepared. It was found that a membrane with an average grain size of 435 μm² (surface) and 317 μm² (fracture surface) show an oxygen permeation flux of 0.80 ml/min cm² at 900 °C, which is higher than in the case of the membrane sintered with 2.5 mol% BN (oxygen permeation flux for this membrane: 0.77 ml/min cm²).

In the case of BSCF, it is obvious that the larger the grain sizes the greater the oxygen permeation flux. This is in good agreement with findings of Wang et al. who also found a positive correlation between larger grains and higher oxygen permeation flux [18]. BSFZ membranes do not exhibit an influence of the average grain size that is as strong as for BSCF membranes.

In order to achieve a better understanding of the microstructure at the grain boundaries, an HRTEM study was conducted on a BSCF membrane which was sintered with 10 mol% BN as it is shown in Fig. 7. A TEM micrograph of two BSCF grains which can be discriminated by bright contrast is displayed in Fig. 7a. BSCF stoichiometry of these two grains has been confirmed by an EDXS analysis. For that purpose an ovally shaped convergent electron beam was used. The convergent beam mode allows to acquire as much signal as possible from the grain boundary.

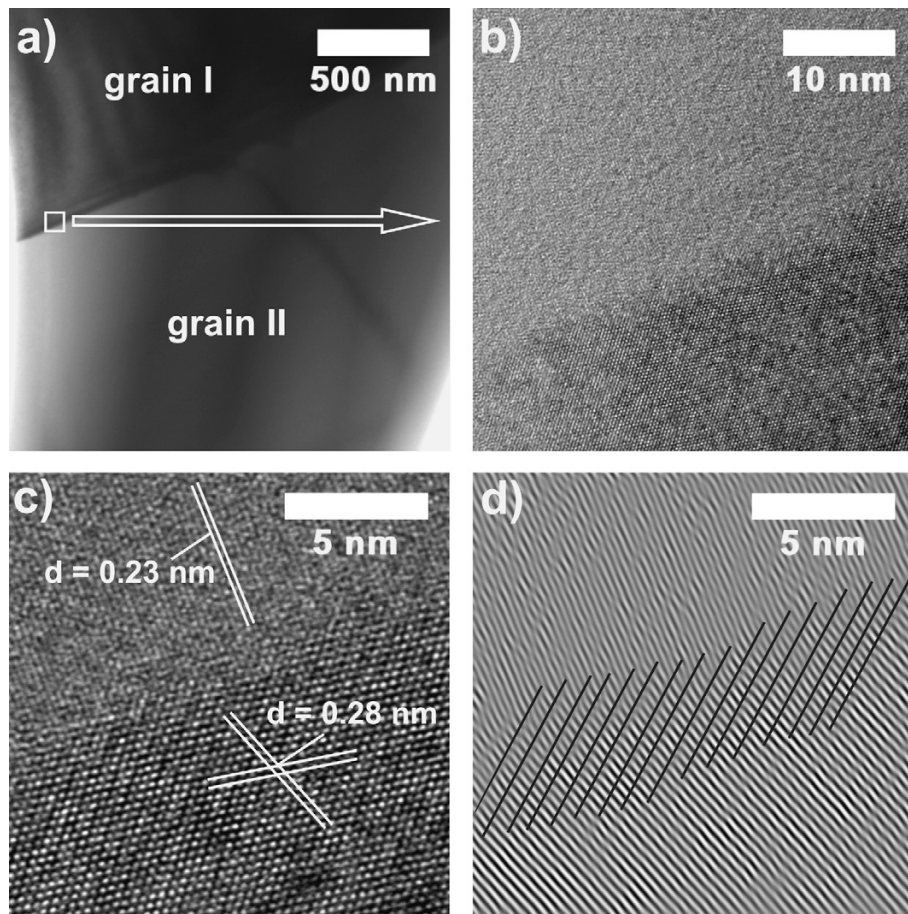


Fig. 7. TEM micrographs obtained from a BSCF membrane containing 10 mol% BN showing two different grains (a–d). (a) TEM bright-field micrograph, (b and c) HRTEM micrographs, and (d) inverse FFT of HRTEM micrograph as shown in (c). Black lines indicate direction of Moiré pattern.

From the EDXS analysis no difference in the elemental composition of grain I, grain II, and the grain boundary have been found as it can be seen in Table 4. As EDXS might not be the most sophisticated method to elucidate light elements like boron, electron-energy loss spectroscopy (EELS) was also conducted. Even via EELS, no boron could be found. Fig. 7b and c show HRTEM micrographs of a selected part of this grain boundary. Neither an interfacial phase nor an amorphous layer has been found to be located between the two grains as it can be seen in Fig. 7c. No zone axis could be determined for grain I but the observed plane spacing was determined to be 0.23 nm which is related to the (1,1,1)-plane of BSCF. The zone axis of grain

II was found to be [1,1,1]. Thus, the grain boundary displays the contact zone between (1,1,1)-planes of grain I and (1,1,0)-planes of grain II whereas the angle between these planes is determined to be 21° . An inverse fast-Fourier transformation (based on (1,1,1) of grain I and (1,1,0) of grain II) was conducted which is shown in Fig. 7d. As indicated by black lines, Moiré pattern has been observed indicating an overlap of approximately 6 nm of grain I and grain II. As the contrast of the lattice planes do not abate towards the contact zone, no indication for an amorphous layer is given. Diethelm et al. suggested that in the case of $(\text{La}_{0.5}\text{Sr}_{0.5})\text{FeO}_{3-\delta}$ an amorphous layer at the most of 0.5 nm may be prominent [13,14]. As reported for this material, smaller average grain sizes promote the oxygen permeation flux. Thus, the amorphous layer may act as fast diffusion pathway. This finding could further deliver an explanation for the blocking effect of the grain boundaries in the study presented here, as we believe no amorphous or interfacial layer is eminent in the grain boundaries of BSCF. Feldhoff et al. [11] reported even in BSCF the grain boundaries are atomically thin containing no second phase, which underlines the findings presented here.

Table 4
Quantitative analysis of elemental composition by EDXS of grain I, grain II and grain boundary as shown in Fig. 7

Element	Grain I (atom%)	Grain II (atom%)	Grain boundary (atom%)
Ba	28	29	28
Sr	24	23	25
Co	37	37	36
Fe	11	11	11

4. Conclusion

Dense ceramic membranes of BSCF and BSFZ with BN as sintering aid were successfully prepared via liquid-phase sintering. It has emerged that using BN as sintering aid the sintering temperature could be lowered down to 1050 °C in the case of BSCF membranes and down to 1100 °C in the case of the BSFZ membranes. It is also shown that the obtained membranes exhibit excellent phase stability after sintering with only very few impurities and no boron remained in the membranes after the sinter process. For both membrane materials BSCF and BSFZ, an increase of the added amount BN lead to a decrease of the average grain size. Oxygen permeation experiments delivered evidence that membranes containing particularly larger grains exhibit a better oxygen permeation performance. This effect is especially pronounced in the case of BSCF membranes in which the oxygen permeation flux is lowered proportionally to the abatement of the average grain size. A TEM study gives first indication that no amorphous material or interfacial phase is incorporated at the grain boundaries. That leads to the assumption that a lattice misfit between the grains and associated straining of grain boundary near regions could have negative impact on the oxygen ion transport. Considering former reports on the correlation of microstructure and oxygen permeation, future investigations should focus on the microstructure of the grain boundaries as their nature may give a better understanding of the oxygen permeation through dense ceramic membranes.

Acknowledgements

The authors greatly acknowledge the financial support by the Deutsche Forschungsgemeinschaft (DFG) under grant number FE 928/1-1 and fruitful discussions with Prof. Jürgen Caro.

References

- [1] H.J.M. Bouwmeester, A.J. Burggraaf, Dense ceramic membranes for oxygen separation, in: A.J. Burggraaf, L. Cot (Eds.), *Fundamentals of Inorganic Membrane Science and Technology*, Elsevier, Amsterdam, 1996, p. 435.
- [2] Z.P. Shao, S. Haile, A high-performance cathode for the next generation of solid-oxide fuel cells, *Nature* 431 (2004) 170.
- [3] H. Wang, S. Werth, T. Schiestel, J. Caro, Perovskite hollow-fibre membranes for the production of oxygen-enriched air, *Angew. Chem. Int.* 44 (2005) 6906.
- [4] C.S. Cheng, S.J. Feng, S. Ran, D.C. Zhu, W. Liu, H.J.M. Bouwmeester, Conversion of methane to syngas by a membrane-based oxidation-reforming process, *Angew. Chem. Int. Ed.* 115 (2003) 5354.
- [5] W. Zhu, W. Han, G. Xiong, W. Yang, Mixed reforming of heptane to syngas in the $\text{Ba}_{0.5}\text{Sr}_{0.5}\text{Co}_{0.8}\text{Fe}_{0.2}\text{O}_{3-\delta}$ membrane reactor, *Catal. Today* 104 (2005) 149.
- [6] B. Wei, Z. Lü, X. Huang, Z. Liu, J. Miao, N. Li, W. Su, $\text{Ba}_{0.5}\text{Sr}_{0.5}\text{Zn}_{0.2}\text{Fe}_{0.8}\text{O}_{3-\delta}$ Perovskite oxide as novel cathode for intermediate-temperature solid-oxide fuel cells, *J. Am. Ceram. Soc.* 90 (2007) 3364.
- [7] H. Wang, C. Tablet, W. Yang, J. Caro, In situ high temperature X-ray diffraction studies of mixed ionic and electronic conducting perovskite-type membranes, *Mater. Lett.* 59 (2005) 3750.
- [8] S. McIntosh, J.F. Vente, W.G. Haije, D.H.A. Blank, H.J.M. Bouwmeester, Oxygen stoichiometry and chemical expansion of $\text{Ba}_{0.5}\text{Sr}_{0.5}\text{Co}_{0.8}\text{Fe}_{0.2}\text{O}_{3-\delta}$ measured by in situ neutron diffraction, *Chem. Mater.* 18 (2006) 2187.
- [9] Z.P. Shao, W.S. Yang, Y. Cong, H. Dong, J.H. Tong, G.X. Xiong, Investigation on the permeation behaviour and stability of a $\text{Ba}_{0.5}\text{Sr}_{0.5}\text{Co}_{0.8}\text{Fe}_{0.2}\text{O}_{3-\delta}$ oxygen membrane, *J. Membr. Sci.* 172 (2000) 177.
- [10] H. Wang, C. Tablet, A. Feldhoff, J. Caro, A cobalt-free oxygen-permeable membrane based on the perovskite-type oxide $\text{Ba}_{0.5}\text{Sr}_{0.5}\text{Zn}_{0.2}\text{Fe}_{0.8}\text{O}_{3-\delta}$, *Adv. Mater.* 17 (2005) 1785.
- [11] A. Feldhoff, J. Martynczuk, H. Wang, Advanced $\text{Ba}_{0.5}\text{Sr}_{0.5}\text{Zn}_{0.2}\text{Fe}_{0.8}\text{O}_{3-\delta}$ perovskite-type ceramics as oxygen selective membranes: evaluation of the synthetic process, *Prog. Solid State Chem.* 35 (2007) 339.
- [12] J. Martynczuk, M. Arnold, H. Wang, J. Caro, A. Feldhoff, How $(\text{Ba}_{0.5}\text{Sr}_{0.5})(\text{Fe}_{0.8}\text{Zn}_{0.2})\text{O}_{3-\delta}$ and $(\text{Ba}_{0.5}\text{Sr}_{0.5})(\text{Co}_{0.8}\text{Fe}_{0.2})\text{O}_{3-\delta}$ perovskites form via an EDTA/citric acid complexing method, *Adv. Mater.* 19 (2007) 2134.
- [13] S. Diethelm, J. Van herle, J. Sfeir, P. Buffat, Correlation between oxygen transport properties and microstructure in $\text{La}_{0.5}\text{Sr}_{0.5}\text{FeO}_{3-\delta}$, *J. Eur. Ceram. Soc.* 25 (2005) 2191.
- [14] S. Diethelm, J. Van herle, J. Sfeir, P. Buffat, Influence of microstructure on oxygen transport in perovskite type membranes, *Br. Ceram. Trans.* 103 (2004) 147.
- [15] V.V. Kharton, F.M.B. Marques, Mixed ionic–electronic conductors: effect of ceramic microstructure on transport properties, *Curr. Opin. Solid State Mater. Sci.* 6 (2002) 261.
- [16] A.L. Shaula, R.O. Fuentes, F.M. Figueiredo, V.V. Kharton, F.M.B. Marques, J.R. Frade, Grain size effects on oxygen permeation in submicrometric $\text{CaTi}_{0.8}\text{Fe}_{0.2}\text{O}_{3-\delta}$ ceramics obtained by mechanical activation, *J. Eur. Ceram. Soc.* 25 (2005) 2613.
- [17] K. Zhang, Y.L. Yang, D. Ponnusamy, A.J. Jacobson, K. Salama, Effect of microstructure on oxygen permeation in $\text{SrCo}_{0.8}\text{Fe}_{0.2}\text{O}_{3-\delta}$, *J. Mater. Sci.* 34 (1999) 1367.
- [18] H. Wang, C. Tablet, A. Feldhoff, J. Caro, Investigation of phase structure, sintering, and permeability of perovskite-type $\text{Ba}_{0.5}\text{Sr}_{0.5}\text{Co}_{0.8}\text{Fe}_{0.2}\text{O}_{3-\delta}$ membranes, *J. Membr. Sci.* 262 (2005) 20.
- [19] J.F. Vente, S. McIntosh, W.G. Haije, H.J.M. Bouwmeester, Properties and performance of $\text{Ba}_{0.5}\text{Sr}_{0.5}\text{Co}_{0.8}\text{Fe}_{0.2}\text{O}_{3-\delta}$ materials for oxygen transport membranes, *J. Solid State Electrochem.* 10 (2006) 581.
- [20] I.C. Ho, Semiconducting barium titanate ceramics prepared by boron-containing liquid-phase sintering, *J. Am. Ceram. Soc.* 77 (1994) 829.
- [21] M.N. Rahaman, *Ceramic Processing and Sintering*, second ed., Marcel Dekker Inc, New York, Basel, 2004.
- [22] H. Koster, F.H.B. Mertins, Powder diffraction of the cubic $(\text{Ba}_{0.5}\text{Sr}_{0.5})(\text{Co}_{0.8}\text{Fe}_{0.2})\text{O}_{3-\delta}$, *Powder Diffr.* 18 (2003) 56.
- [23] A. Feldhoff, M. Arnold, J. Martynczuk, T. Gesing, H. Wang, The sol–gel synthesis of perovskites by an EDTA/citrate complexing method involves nanoscale solid state reactions, *Solid State Sci.*, submitted for publication.

Chapter 4

Valence and spin state

4.1 Summary

The dependence of phase stability on valence and spin state for BSFZ and a $(\text{Ba}_{0.5}\text{Sr}_{0.5})(\text{Fe}_{1-x}\text{Al}_x)\text{O}_{3-\delta}$ (BSFA) perovskite system ($0 \leq x \leq 0.2$) with previously unreleased composition is investigated in this chapter. An excellent phase stability of perovskite-based membranes demands a tailoring which enables pure high-spin states of the polyvalent cations during experimental conditions, even if mixed valence states are present. For an accurate atomic level understanding of the redox behavior a combination of in situ EELS and Mössbauer spectroscopy is necessary. Further characterization of the materials was conducted by SEM, TEM, EDXS, differential thermoanalysis (DTA), thermogravimetric analysis (TGA), in situ XRD, dilatometry and oxygen permeation experiments.

The first article deals with the redox behavior of iron in BSFZ during heating. It revealed a mixed valence state of 3.75+ (75% Fe^{4+} in high-spin state and 25% Fe^{3+} predominantly in low-spin state) at room temperature and a reduction of iron to 3.25+ (25% Fe^{4+} and 75% Fe^{3+} both in high-spin state) during heating to 900 °C. The reason for the transition from a mixed low- and high-spin to a pure high-spin state of Fe^{3+} is the decreasing hybridization of Fe 3d - O 2p orbitals because of thermal expansion. The gradual transition of the valence and spin state takes place under 500 °C and correlates with anomalies of weight-loss, due to release of oxygen, and thermal expansion behavior monitored by X-ray diffraction and dilatometry. Thus, above 500 °C BSFZ is a highly attractive ceramic for intermediate temperature applications (IT: 500-800 °C).

The second article introduces and characterizes a novel BSFA perovskite-type oxide. Cubic perovskites were successfully synthesized for aluminum contents up to 9-10%. A higher fraction of Fe^{4+} instead of Fe^{3+} is replaced by Al^{3+} and the iron species are both in high-spin state. The observed lattice expansion with increasing aluminum fraction can be explained due to the abatement of covalent character in the bonding of Fe-O. High temperature stability of the materials up to 1350 °C is revealed by in situ XRD and TG/DTA measurements. $(\text{Ba}_{0.5}\text{Sr}_{0.5})(\text{Fe}_{0.9}\text{Al}_{0.1})\text{O}_{3-\delta}$ as oxygen permeation material shows the highest oxygen flux for all so far published iron and aluminum containing perovskites. In comparison to cobalt containing materials, which show serious stability problems at IT, this new composition with a less flexible redox behavior and a stable high-spin configuration of iron is expected to show an improved long-term stability and thus, an outstanding performance for the IT range.

4.2 Spin-state transition of iron in (Ba_{0.5}Sr_{0.5})(Fe_{0.8}Zn_{0.2})O_{3- δ} perovskite

Armin Feldhoff, Julia Martynczuk, Mirko Arnold,
Maxym Myndyk, Ingo Bergmann, Vladimir Šepelák,
Wolfgang Gruner, Ulrich Vogt, Angelika Hähnel,
and Jörg Woltersdorf

Journal of the American Ceramic Society (submitted)

Spin-state transition of iron in $(\text{Ba}_{0.5}\text{Sr}_{0.5})(\text{Fe}_{0.8}\text{Zn}_{0.2})\text{O}_{3-\delta}$ perovskite

Armin Feldhoff*, Julia Martynczuk, Mirko Arnold,
*Institut für Physikalische Chemie und Elektrochemie,
 Leibniz Universität Hannover, D-30167 Hannover, Germany*

Maxym Myndyk, Ingo Bergmann†, Vladimir Šepelák‡
*Institut für Physikalische und Theoretische Chemie,
 Technische Universität Braunschweig, D-38104 Braunschweig, Germany*

Wolfgang Gruner,
*Leibniz-Institut für Festkörper- und Werkstoffforschung Dresden,
 D-01069 Dresden, Germany*

Ulrich Vogt,
EMPA, Materials Science & Technology, CH-8600 Dübendorf, Switzerland

Angelika Hähnel, and Jörg Woltersdorf,
Max-Planck-Institut für Mikrostrukturphysik, D-06120 Halle, Germany

Abstract

The redox behavior of iron during heating of a high-performance perovskite for ceramic oxygen separation membranes was studied by combined electron energy-loss (EELS, esp. ELNES) and Mössbauer spectroscopic *in situ* methods. At room temperature, the iron in $(\text{Ba}_{0.5}\text{Sr}_{0.5})(\text{Fe}_{0.8}\text{Zn}_{0.2})\text{O}_{3-\delta}$ (BSFZ) is in a mixed valence state of 75 % Fe^{4+} in the high-spin state and 25 % Fe^{3+} predominantly in the low-spin state. When heated to 900 °C, a slight reduction of iron is observed that increases the quantity of Fe^{3+} species. However, the dominant occurrence is a gradual transition in the spin-state of trivalent iron from a mixed low-spin/high-spin to a pure high-spin configuration. In addition, a remarkable amount of hybridization is found in the Fe-O bonds that are highly polar rather than purely ionic. The coupled valence/spin-state transition correlates with anomalies in thermogravimetry and thermal expansion behavior observed by X-ray diffraction and dilatometry, respectively. Since the effective cationic radii depend not only on the valence but also on the spin-state, both have to be considered when estimating

under which conditions a cubic perovskite will tolerate specific cations. It is concluded that an excellent phase stability of perovskite-based membrane materials demands a tailoring which enables pure high-spin states under operational conditions, even if mixed valence states are present. The low spin-state transition temperature of BSFZ provides that all iron species are in a pure high-spin configuration already above ca. 500 °C making this ceramic highly attractive for intermediate temperature applications (500 - 800 °C).

1 Introduction

Ceramic membranes can provide remarkable oxygen permeation fluxes at infinite selectivity without the need of external electrodes when they are based on heavily doped anion deficient cubic perovskite-type $\text{A}_{1-x}\text{A}'_x\text{B}_{1-y}\text{B}'_y\text{O}_{3-\delta}$ oxides exhibiting mixed oxygenion and electron conductivities at elevated temperatures (500 - 1000 °C).¹ While the partial conductivity of electrons is distinctly higher than that of oxygen ions,^{1,2} the oxygen deficit δ correlates directly with the obtainable permeation flux via the concentration of disordered oxygen vacancies. The perovskite lattice can tolerate a remarkable number of vacant oxygen sites if a reducible transition metal cation is located at the crystallographic B site in the center of the BO_6 octaeder. Upon heating under constant pressure, entropy may free up even more oxygen from a previously

*Corresponding author, E-mail: armin.feldhoff@pci.uni-hannover.de

†Now at Suzuki Laboratory, Institute of Multidisciplinary Research for Advanced Materials, Tohoku University, Sendai 980-8577, Japan

‡On leave from the Institute of Geotechnics, Slovak Academy of Sciences, SK-04353 Košice, Slovak Republic

equilibrated perovskite. The quantity of released oxygen may be quite high as the requirement of charge neutrality is no longer preserved solely by small concentrations of cation vacancies but by the possibly flexible redox behavior of the B site cation(s). However, one requirement for the oxygen vacancies to be mobile is to preserve a cubic perovskite structure,³ where the redox behavior of the B site cation(s) plays the key role as well. Hence, a better understanding of the redox behavior can be used to tailor improved membrane materials with excellent phase stability under strongly reducing conditions.

The pioneering work of Teraoka et al. in the 1980s⁴⁻⁷ exceeded the already high standards for obtainable oxygen fluxes. As a consequence, the search for high-flux materials (i.e., exhibiting oxygen permeation fluxes of one to two orders of magnitude higher than cubically stabilized zirconia equipped with shortcircuit external electrodes^{4,8}) focused until today mostly on complex perovskites hosting cobalt on their crystallographic B site. The current state-of-the-art material with respect to oxygen permeation and phase stability above 900 °C is $(\text{Ba}_{0.5}\text{Sr}_{0.5})(\text{Co}_{0.8}\text{Fe}_{0.2})\text{O}_{3-\delta}$ (BSCF).^{3,9-11} Recently, *in situ* high-temperature electron energy-loss spectroscopy (HT-EELS) on BSCF has shown that cobalt is reduced from an average formal oxidation state of 2.6+ to 2.2+ and iron from 3.0+ to 2.8+, if BSCF is heated in the vacuum chamber of a transmission electron microscope (TEM) from room temperature to 950 °C.¹² The average valence of the B site cations, 2.7+ at room temperature and 2.3+ at 950 °C, give oxygen contents $3 - \delta$ of 2.3 and 2.2, respectively. That is in good agreement with oxygen stoichiometries estimated by thermogravimetric analysis (TGA) and neutron powder diffraction.¹³ The experiments in¹² however, give direct proof of the easier reducibility of cobalt over iron in a highly doped perovskite-type oxide. Also, comparative TGA of different perovskite-type materials indicate that during heating the polyvalent B-site cobalt ions are reduced far more easily than iron, manganese or nickel.¹⁴

The flexible redox behavior of cobalt provides on the one hand high oxygen fluxes at high temperatures. On the other hand it leads to two major problems hindering the reliable use of the BSCF material (and cobaltites in general) under important technical requirements. First, it causes a large coefficient of thermal expansion (CTE) that can lie in the range of $20 - 24 \times 10^6 \cdot \text{K}^{-1}$ over a wide temperature range.^{13,15} The resulting dilatation causes huge thermal stresses and thus cracks form easily in the membranes, especially if operated at steep oxygen potential gradients. The steep gradients are obtained by making the cross-section of supported or self-standing membranes very thin (i.e., $< 200 \mu\text{m}$).¹⁵⁻¹⁷ This is of interest to increase flux densities for the design of compact membrane units. Second, the valence instability of cobalt introduces inherent phase instability to the

cobaltites at intermediate temperatures (ITs, ca. 500 - 800 °C).^{9,18,19} This is due to a coupled valence/spin-state transition of cobalt, and cobaltites containing CoO_6 octaeder with Co^{3+} in low-spin configuration tend to prefer face sharing (contributions of hexagonal stacking) rather than corner sharing (cubic stacking).¹⁹ The breakdown of the cubic perovskite structure principally limits the long-time stability of the BSCF material under the conditions required for the operation of a membrane material in the IT range. The IT range, however, is of special interest for membrane-based dehydrogenation processes in the synthesis of basic chemicals like ethylene²⁰ and propylene²¹ at high selectivity, and for the novel concept of solid oxide fuel cells (SOFCs).²²

Recently, the search for alternative materials has led to the development of the cobalt-free perovskite-type oxide $(\text{Ba}_{0.5}\text{Sr}_{0.5})(\text{Fe}_{0.8}\text{Zn}_{0.2})\text{O}_{3-\delta}$ (BSFZ).^{23,24} Wang et al.²⁴ demonstrated its potential for use in a membrane reactor for the partial oxidation of methane (POM) at 900 °C. The reported oxygen permeation flux of $2.5 \text{ ml} \cdot \text{min}^{-1} \cdot \text{cm}^{-2}$ on 1.25 mm-thick membranes at 900 °C indicates a high conductivity as well as high surface exchange rates for oxygen. Wei et al.^{25,26} quantified the latter by measuring low polarization resistances of 0.22, 0.46, and $0.98 \Omega \cdot \text{cm}^2$ at 700, 650, and 600 °C, respectively. They also use BSFZ as a cathode material in an IT-SOFC at 500 - 650 °C at power densities up to $180 \text{ mW} \cdot \text{cm}^{-2}$. The room temperature structure of BSFZ has been refined in a cubic unit cell ($a = 0.3990(0) \text{ nm}$) by the Rietveld method.²⁷ *In situ* X-ray diffraction (XRD) has shown that BSFZ remains in the cubic structure if heated to 900 °C in air or in low oxygen partial pressures down to $10 \times 10^{-7} \text{ Pa}$.²⁴ Good phase stability of cubic BSFZ in the IT range is implied by the observation that it can be synthesized by a sol gel-based method in the pure phase at 750 °C.²⁷⁻²⁹ This is contrary to the cobaltite BSCF that requires higher temperatures in an analogous synthesis (950 °C).^{19,30} The present work focuses on a thorough atomic level understanding of electronic effects in the redox behaviour of the BSFZ perovskite. Combined *in situ* electron energy-loss spectroscopy (EELS) and Mössbauer spectroscopy show that a coupled $\text{Fe}^{4+}/\text{Fe}^{3+}$ valence and Fe^{3+} low-spin to high-spin transition play a key role. This is reflected in anomalies found in integrative investigations of temperature-dependent weight-losses and lattice dilatations.

2 Experimental

The BSFZ material was synthesized from nitrate precursors via an ethylenediamine-tetraacetic acid (EDTA)/citrate acid complexing method at 950 °C for 10 hours as described in detail elsewhere.²⁷⁻²⁹ BSFZ ceramics were sintered at 1150 °C for 10 hours and

shaped by cutting, grinding, and polishing into disks approximately 3 mm in diameter and 80 μm in thickness. To obtain TEM specimens, these disks were dimple grinded from one side to a residual thickness of 10 μm (dimple grinder, model 656, Gatan Inc.). Finally, Ar^+ ion sputtering was employed at 3 kV under an incident angle of 6 degrees (PIPS, precision ion polishing system, model 691, Gatan Inc., Pleasanton (CA), USA) until electron transparency was achieved.

To obtain a standard for Fe^0 , a metallic iron wire 0.25 mm in diameter (purity 99.99+ %, Chempur) was polished on polymer-embedded diamond foils to a thickness of 50 μm using 1,2-propanediol as a lubricant. The bar was epoxy-glued onto a copper slot grid ($1 \times 2 \text{ mm}$; 50 μm) and then ion-milled with 3kV- Ar^+ . The specimen was immediately transferred from the vacuum chamber of the ion mill to the transmission electron microscope (TEM). To prevent the undesired influence of local oxidation of thin specimen areas on the observed EEL fine structures near the $\text{L}_{2,3}$ ionization edge of iron (Fe- $\text{L}_{2,3}$ ELNES), it was carefully checked for the absence of any O-K signal in EEL and energy dispersive X-ray (EDX) spectra.

Commercial powders of FeTiO_3 (purity 99.8 %, Alfa Aesar, CAS-Nr. 12022-71-8) and $\alpha\text{-Fe}_2\text{O}_3$ (>95 %, Riedel-de-Haen, CAS-Nr. 1309-37-1) were used as standards for Fe^{2+} and Fe^{3+} , respectively. FeTiO_3 (ilmenite) is a more reliable standard for Fe^{2+} than FeO (wüstite), as the latter is often iron deficient and consists of Fe_{1-x}O with noticeable contributions of Fe^{3+} .³¹

To obtain a standard for Fe^{4+} , a procedure similar to those chosen in^{32,33} was applied; although here an EDTA/citrate acid complexing method (like for the synthesis of the BSFZ material) instead of a solid-state process was used to synthesize $\text{SrFeO}_{3-\delta}$. Phase purity was confirmed by XRD. Subsequently, stoichiometric SrFeO_3 was observed by filling the lattice with additional oxygen. The additional oxygen was inserted into the lattice using KClO_4 in a gold capsule with an internal oxygen pressure of approximately 9 bar (six-fold excess) in an autoclave under 1.2 kbar and 530 $^\circ\text{C}$ for 22 h. All standards were carefully checked by Mössbauer spectroscopy to exhibit just the desired iron valence. For TEM, the powders were crushed, dispersed in ethanol, dropped onto copper-supported holey carbon films, and dried.

TEM investigations at room temperature (JEM-2100F-UHR, $C_S = 0.5 \text{ mm}$, $C_C = 1.2 \text{ mm}$, JEOL Ltd., Tokyo, Japan) and at high temperature (CM20 FEG Super TWIN microscope, $C_S = 1.2 \text{ mm}$, $C_C = 1.2 \text{ mm}$, Philips, Eindhoven, Netherlands) were performed at 200 kV with the specimen at $2-4 \times 10^{-5} \text{ Pa}$. Both microscopes were equipped with a post-column imaging filter (GIF, Gatan Inc.) employing a 1024 x 1024 pixel charge-coupled device (CCD) camera and a light-element energy-dispersive X-ray spectrometer. The Schottky-type emitter gave a full width at half maximum (FWHM) of the zero-loss peak of 1 eV. Cal-

ibration of the GIF drift tubes was done using the first maximum of the Ni- L_3 edge of a NiO standard (853 eV³⁴). The energy dispersion of the spectrometer setup at nominally 0.1 eV/pixel was calibrated by acquiring the zero-loss peak with an offset of 50 eV given to the calibrated drift tube and without any offset. All EEL spectra were taken in diffraction-coupled mode. Magnifications of the TEMs were set in combination with a 2 mm entrance aperture of the GIF so that ca. 150 nm circular areas were analyzed. These were carefully chosen to be thin and in the case of powder specimens were not supported locally by a carbon film. An objective aperture was inserted to limit the collection half-angle to ca. 32 mrad, respectively. This means that the dipole selection rule primarily applies and restricts, with respect to parity and angular momentum, the nature of empty states to be probed. In principle this provides measurement of the site, spin-state, and symmetry of the selective ions. To measure the absolute position of core-loss details, pairs of core-loss and low-loss spectra were acquired with 10 s exposure, while the switching of energy ranges was made within a few seconds by removing offsets to the drift tube of the GIF (O-K: 530 eV; Fe- $\text{L}_{2,3}$: 710 eV; Ba- $\text{M}_{4,5}$: 780 eV;). Illumination was almost parallel but was adjusted for low-loss acquisition by defocusing the condenser lens (CL-3) to avoid overexposure of the CCD camera. The CM20FEG was equipped with a double tilting heating holder (model 652-Ta, Gatan Inc.). Heating from room temperature to 900 $^\circ\text{C}$ was done with a ramp of ca. 5 $^\circ\text{C} \cdot \text{min}^{-1}$, and the specimen was equilibrated at the respective temperature for 15 min before acquiring *in situ* EEL spectra.

Scanning electron microscopy (SEM) was made on a field-emission instrument at 2 kV (JSM-6700F, JEOL Ltd., Tokyo, Japan).

Mössbauer spectroscopic measurements were performed in transmission geometry using a conventional spectrometer in constant acceleration mode. *In situ* spectra were taken in the temperature range of 20 $^\circ\text{C}$ to 900 $^\circ\text{C}$ in air. BSFZ powder specimen was fixed on a quartz support (a 200 m thick plate). A $^{57}\text{Co}/\text{Rh}$ γ -ray source was used. The velocity scale of the spectra was calibrated relative to ^{57}Fe in Rh. 'Recoil' spectral analysis software³⁵ was used for the quantitative evaluation of the Mössbauer spectra. The Voigt-based fitting method provided distributions of hyperfine parameters for multiple species in a spectrum.

Differential thermoanalysis (DTA) and TGA were measured on 99.5 mg calcined BSFZ powder in a DTA/TG crucible of Al_2O_3 from 20 - 1400 $^\circ\text{C}$ with a heating rate of 5 $^\circ\text{C}/\text{min}$ under an air flowrate of 100 $\text{ml} \cdot \text{min}^{-1}$ (STA 429 CD, Netsch, Selb, Germany). The oxygen content of calcined BSFZ powder was measured by the carrier gas hot extraction method with a commercial oxygen analyser (TC 436DR, Leco, St. Joseph, USA). The powders were weighed (about 20 mg) into a metallic capsule of nickel (0.4 g) with

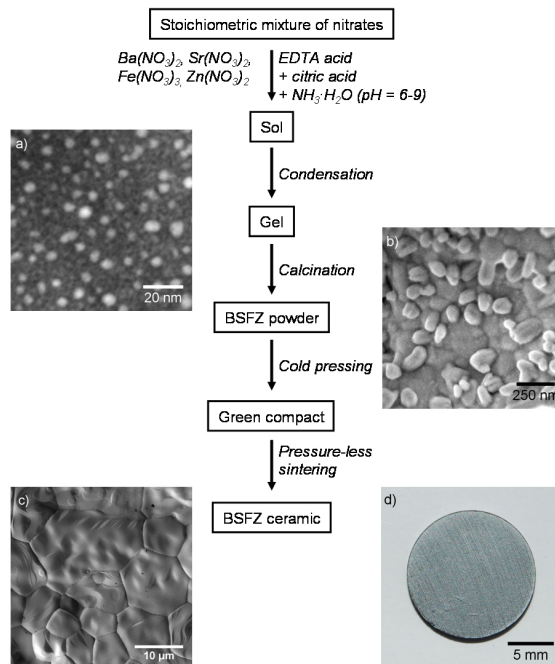


Figure 1: From nano to macro. Outline of the sol gel-based synthetic process with snapshots of different steps: (a) STEM-HAADF of the gel showing finely dispersed and cross-linked metal-organic complexes, (b) SEM of calcined perovskite powder, (c) SEM surface view of grain structure in sintered BSFZ ceramic, (d) photograph of a disk membrane.

the addition of a tin tablet (0.2 g). This pressed package was dropped into an outgassed high temperature graphite crucible that was electrically heated with a power-time-program. Two infrared selective detectors registered simultaneously the formed reaction species CO and CO_2 . The calibration was carried out with ZrO_2 for the CO detector and with carbon dioxide gas dosing for the CO_2 detector. A reproducibility of 0.5 % relative standard deviation (RSD) for this method has been shown for many oxides.³⁶

In situ high-temperature XRD measurements were performed with monochromator-filtered $Cu-K\alpha$ radiation ($K_{\alpha 2}/K_{\alpha 1}$: 0.5) at 40 kV and 40 mA with a receiving slit of 0.19 mm (X'pert-MPD instrument, Philips). Data were collected in a step-scan mode in the range of $29-33^\circ 2\theta$ with intervals of 0.02° and count times of 30 s per step. The sample was tested in an HT cell (HDK 2.4 with REP 2000, Edmund Bühler, Hechingen, Germany) with a Pt-Rh holder, which has no reflexes in the applied 2θ range. The applied temperature range was 30 - 1000 $^\circ C$ with $3^\circ \cdot min^{-1}$ in air and an equilibrium time of 30 min for each data acquisition. The maximum of the (110) reflex was estimated by a combined Gaussian and Lorentzian fitting and the cell parameters were refined by using TOPAS-Academic V4.1 (Coelho Software, Brisbane, Australia).

Measurements of the linear thermal expansion of BSFZ ceramics were conducted in the 20 - 1000 $^\circ C$

range, using a difference dilatometer with inductive transducers (DIL 802L, Bähr, Hüllhorst, Germany). Quartz specimens were used for calibration and as inert bodies. To study the influence of p_{O_2} , the expansion measurements were carried out in a flowing gas atmosphere of argon (0.5 Pa O_2) and argon/ O_2 mixtures under different O_2 partial pressures. In all cases, dense rods ($5 \times 2 \times 15 mm^3$) with polished frontal faces were successively heated and cooled two times at the rate $5 K \cdot min^{-1}$. The coefficient of thermal expansion (CTE) follows directly from these measurements as for the cubic perovskite the strain tensor is fully determined by a single scalar.³⁷

3 Results and discussion

Figure 1 illustrates the sol gel-based synthetic process for BSFZ starting from an aqueous solution of stoichiometric amounts of nitrates with EDTA, citric acid, and ammonia. The stage of the gel (after 18 h at 150 $^\circ C$) is characterized by an ultrafine dispersion of cross-linked metal-organic complexes (bright features in Fig. 1a). The fine-scale intermixing is considered a major advantage over classical solid-state routes if a homogeneous product of complex stoichiometry is desired, as in case of BSFZ. After calcination, the BSFZ perovskite is a fine powder with grains of nanoscale

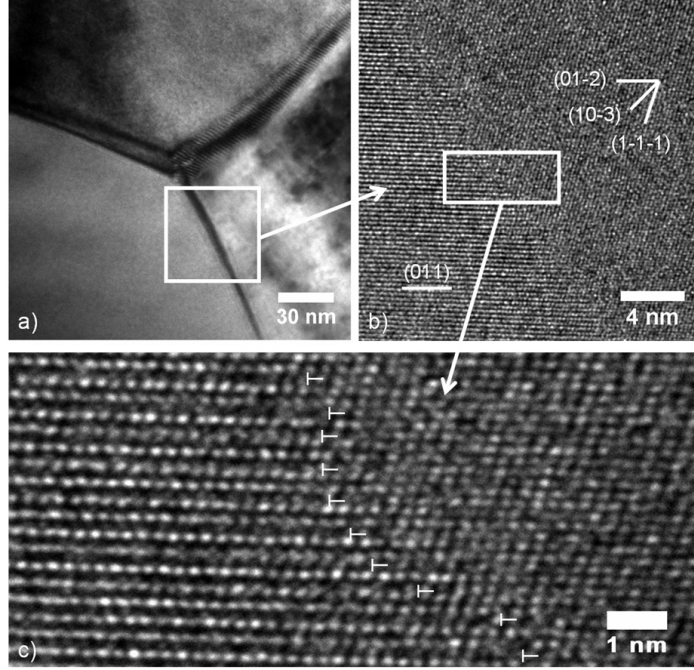


Figure 2: Details of a grain boundary in a BSFZ ceramic: (a) TEM bright-field of a triple junction, (b) HRTEM with indices assigned to lattice planes, (c) HRTEM with indication of unpaired atomic planes.

size that are eventually sintered together (Fig. 1b). After green compacting and sintering at ambient pressure, a BSFZ ceramic is obtained with grain sizes in the order of several tens of micrometers (Fig. 1c). Ceramic membranes for oxygen permeation experiments are disks having 14 mm diameter and 1.2 mm thickness (Fig. 1d) or fibers having a diameter of 1 mm and a wall thickness of $150 \mu\text{m}$.³⁸

The grain boundaries in sintered membranes are atomically thin, with the absence of any interfacial phase. A typical example is shown in Fig. 2. The lattice misfit between the (011) lattice planes of grain A (0.282 nm) and the (01 $\bar{2}$) lattice planes of grain B (0.178 nm) is accommodated by misfit dislocations (marked by T's in Fig. 2c). Obviously, it is energetically favorable to reduce strain by leaving every third (01 $\bar{2}$) atomic plane of grain B unpaired, and thus loose coherency. In^{39,40} it was shown that this kind of grain boundary acts as a barrier for oxygen permeation. In the present article, however, we focus on the bulk properties of the BSFZ material during temperature-induced reduction.

It is therefore essential to have a look at the electronic states or bands in the BSFZ material (Fig. 3). The location of the O-2p states just a few eV below the partly filled Fe-3d states means a small electronic oxygen ligand to iron charge transfer energy $\Delta_{dp} = \epsilon_{Fe-3d} - \epsilon_{O-2p}$.⁴¹ This causes partial hybridization in the Fe-O bonds that become strongly polar

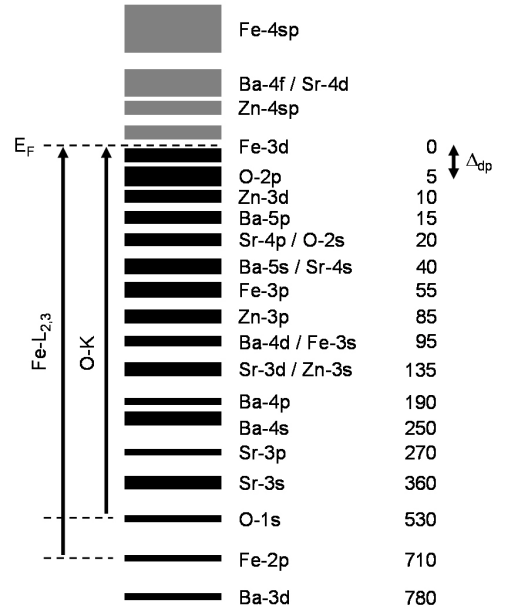


Figure 3: Schematic sketch of the electronic states or energy bands in the cubic BSFZ perovskite with binding energies down to 780 eV. Electronic transitions from O-1s and Fe-2p into unoccupied states above the Fermi level E_F indicate the origin of O K- and Fe $L_{2,3}$ -ELNES.

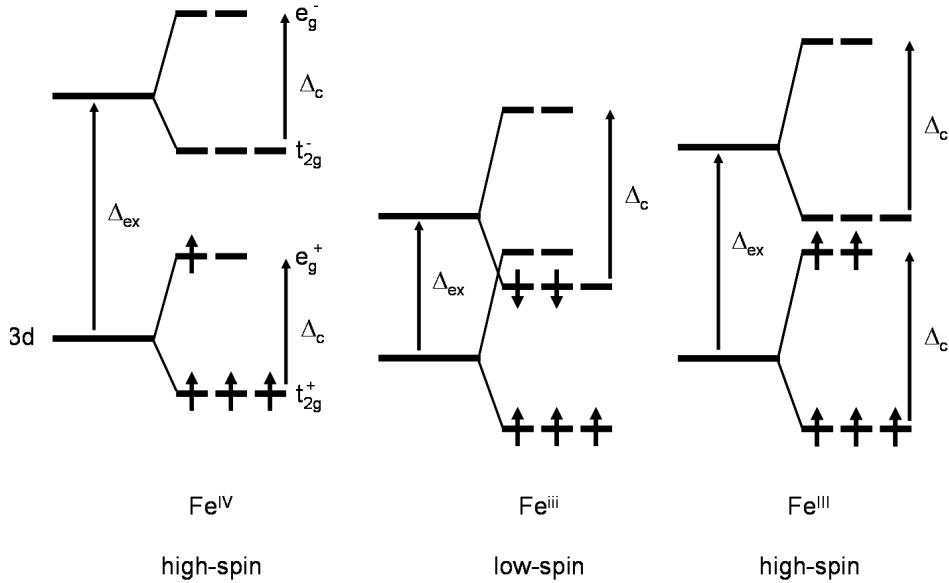


Figure 4: Electronic configurations for iron ions in an octahedral ligand field.

rather than purely ionic. For the same reason, hybridization of O-2p with unoccupied Zn-4sp, Ba-4f, Sr-4d, and Fe-4sp is expected (see Fig. 3). Because the occupied O-2p and Zn-3d states are energetically similar, an anomalous valence band cation-d-anion-p hybridization is expected as well.⁴²

Starting with an ionic model for iron allows important details of the electronic structure to be derived. The average d electron energy is given by the electrostatic Madelung energy of the ions. Due to intra-atomic exchange coupling, indistinguishable electrons in the partly filled ten d orbitals cause a splitting by Δ_{ex} .⁴³ This splits the d states for majority spin " $+$ " and minority spin " $-$ " (Fig. 4). It has to be taken into account that iron is octahedrally coordinated by oxygen in the cubic perovskite structure. Thus, the additional crystal field splitting Δ_c of the two sets of five d orbitals into three t_{2g} and two e_g orbitals, respectively, has to be considered. Depending on the relative magnitude of Δ_{ex} and Δ_c there are different electronic configurations, three of which are shown in Fig. 4: high-spin Fe^{IV} with $3d_{HS}^4 = (t_{2g}^+)^3(e_g^+)^1$, low-spin Fe^{III} with $3d_{LS}^5 = (t_{2g}^+)^3(t_{2g}^-)^2$, and high-spin Fe^{III} with $3d_{HS}^5 = (t_{2g}^+)^3(e_g^+)^2$. Consider that the amount of hybridization is different for the three configurations. The e_g orbitals are directed to the ligand, giving a large overlap with O-2p orbitals. The t_{2g} orbitals point towards the corners of the cubic unit cell and overlap less with the O-2p orbitals. It can be assumed that the amount of hybridization of e_g is twice that of t_{2g} ⁴⁴ due to a stronger overlap with O-2p orbitals. As a consequence e_g -derived bands are broader than t_{2g} -derived bands, even though both bands are narrow.

Figure 5 shows the room temperature L_{2,3} energy-loss near-edge structures (ELNESs) of iron in different compounds exhibiting pure valence states⁴⁵ compared to the BSFZ material (grey curves). Because of Fe-2p spin-orbit coupling, the overall spectral shapes are similar for all iron species with an intense peak at around 708 - 710 eV (L₃) and a less intense peak at 721 - 723 eV (L₂). Respective spectra in Fig. 5 match those obtained for FeO (Fe²⁺), LaFeO₃ (Fe³⁺), and SrFeO₃ (Fe⁴⁺) by X-ray absorption near-edge structures (XANES) and by multi-electron configuration interaction calculations.^{46,47} These findings show that the chemical shift between Fe⁰, Fe²⁺, Fe³⁺, and Fe⁴⁺ is in the range of 2 eV, making accurate measurement of the absolute position of fine structure details essential. Positions of the first peak (L₃) in the Fe-L_{2,3} ELNES in Fig. 5 were estimated by the weighted centroid's abscissa, based on the non-linear least squares fitting of multiple Gaussian functions (see¹²), respectively. The first peak in the Fe⁰ L_{2,3}-ELNES has its centroid's abscissa at 708.1 eV, and the whole spectrum is in agreement with the one presented in.⁴⁸ The centroid's abscissa of the L₃ peak of FeTiO₃ (Fe²⁺) is located at 709.3 eV and that of α -Fe₂O₃ (Fe³⁺) at 710.8 eV. The high-energy shoulders of the L₃ and L₂ peaks of Fe²⁺ as well as the low-energy shoulders of the L₃ and L₂ peaks of Fe³⁺ are usually taken as indications of a high-spin state of iron in the crystal field of the oxygen ligand, respectively.^{49,50} The L₃ peak of SrFeO₃ (Fe⁴⁺) has its centroid's abscissa at 710.7 eV. The centroid's abscissa of the first peak in the Fe L_{2,3}-ELNES of the BSFZ material is at 710.6 eV and coincides with that of the Fe³⁺ and Fe⁴⁺ standards. The L₂ peak centroid's abscissa is at 723.0 eV. The over-

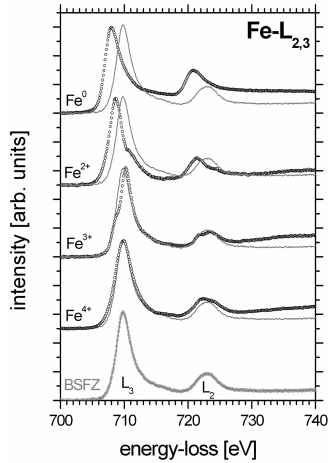


Figure 5: Room temperature ELNES of iron $L_{2,3}$ for different ionization states: Fe^0 (metallic iron), Fe^{2+} ($FeTiO_3$), Fe^{3+} ($\alpha-Fe_2O_3$), and Fe^{4+} ($SrFeO_3$). Gray curves refer to a BSFZ ceramic. Spectra are background subtracted, scaled to the same height of the respective maximum, and vertically shifted for clarity.

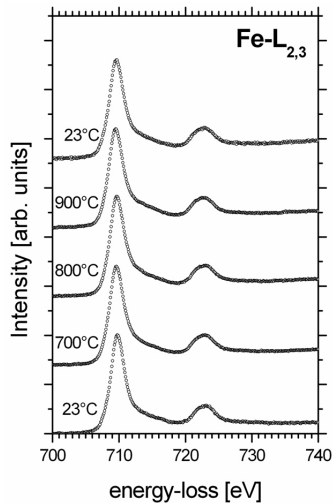


Figure 6: *In situ* iron $L_{2,3}$ -ELNES of a BSFZ ceramic. Spectra are background subtracted, scaled to the same height of the first maximum, and vertically shifted for clarity.

all shape and position of the $L_{2,3}$ -ELNES suggests an Fe^{4+}/Fe^{3+} mixed valence of iron in the BSFZ material at room temperature. It is noted that other spectral regions of the BSFZ material are shown in.²⁹ Because the L_3 and L_2 peaks in all the oxides presented do not split significantly it is concluded that the crystal field splitting Δ_c and the intra-atomic exchange splitting Δ_{ex} having nearly identical values (cf. Fig. 4). However, the first peak in the $L_{2,3}$ -ELNES of the Fe^{2+} and Fe^{3+} standards still shows some splitting. In contrast, this peak does not show any separation for the Fe^{4+} standard (3.5 eV) or BSFZ (2.8 eV), and the full width at half maximum is just 3.5 eV and 2.8 eV, respectively. Hence, the energy difference $|\Delta_{ex} - \Delta_c|$ in BSFZ is even smaller than for all investigated oxide standards. Moreover, it is concluded that the absolute values of Δ_{ex} and Δ_c are small compared to the actual energy resolution of 1 eV in the experiments. That means that the e_g^+ and t_{2g}^- states are positioned almost at the same energy leading to the competition of high- and low-spin states and the eventual break down of Hund's rule.⁴³

The ELNES of $Fe-L_{2,3}$ and O K-edges of the BSFZ material were monitored from room temperature to 900 °C. Significant changes in shape or energy position were not observed. Some *in situ* spectra of $Fe-L_{2,3}$ are shown in Fig. 6. Over the entire temperature range they show similar features to those discussed for the BSFZ spectrum in Fig. 5 with the same peak width and separations, indicating that iron stays in an Fe^{4+}/Fe^{3+} mixed valence state during the *in situ* experiment. Pre-peak A (522 - 530.5 eV) originates from transitions of O-1s electrons into the unoccupied Fe-3d fraction that have 2p character due to hybridization with O-2p orbitals.^{12,44,51,52} If compared with,^{42,53,54} peak B (530.5 - 546 eV) can be assigned to Zn-4sp, Ba-4f, and Sr-4d orbitals hybridized with O-2p orbitals (see Fig. 3). Feature C (above 546 eV) are unoccupied Fe-4s and Fe-4p states weakly hybridized with O-2p orbitals (see Fig. 3). Neither fitting procedures^{12,51} or integration of intensities gave a trend in the relative amount of pre-peak A as a function of temperature. Integration revealed that the relative amount of the pre-peak A intensities in the spectral range from 522 - 546 eV scatters from 13 - 15%. It is concluded that the amount of O-2p hybridization with Fe-3d relative to that with other metal cations does not change with the bond length expansion associated with lattice dilatation during heating of BSFZ. However, a shoulder in the high-energy flank of peak B is noted at high temperatures, and it remains present after cooling of the specimen to room temperature. It must be noted that if the heating occurs in the vacuum chamber of a TEM, the reverse filling oxygen in the perovskite lattice will not reach the initial level. A more accurate designation of the spectral features in the high-energy flank of peak B would require band structure calculations for this complex perovskite that is beyond the

scope of this work. Nevertheless, because the pre-peak A does not show splitting, it is emphasized once again that the energies Δ_{ex} and Δ_c as well as their difference $|\Delta_{ex} - \Delta_c|$ are small in BSFZ under all experimental conditions.

Room temperature Mössbauer spectra of a BSFZ powder before and after heat treatments in air up to 900 °C are almost identical (see Fig. 8). However, a small difference is noted that hints to some irreversibility in the oxygen release and pick-up process. The room temperature spectra are well fitted by the superposition of three subspectra (Fig. 8, bottom). Based on their isomer shifts ($IS_{\text{blue}} = -0.19$ mm/s, $IS_{\text{red}} = 0.26$ mm/s) and on their symmetric quadrupole splitting ($QS_{\text{blue}} = 0.48$ mm/s, $QS_{\text{red}} = 1.11$ mm/s) these blue and red subspectra are attributed to Fe^{IV} , $(t_{2g}^+)^3(e_g^+)^1$, and Fe^{III} ions, $(t_{2g}^+)^3(e_g^+)^2$, respectively, both in octahedral coordination and high-spin configurations.^{55,56} The isomer shift of the third subspectrum ($IS_{\text{green}} = 0.53$ mm/s) can be attributed to Fe^{iii} , $(t_{2g}^+)^3(t_{2g}^-)^2$, also in octahedral coordination,^{55,56} but in a low-spin configuration. It should be noted that the green subspectrum shows almost no quadrupole splitting and supports the above made designation of d orbital occupancies that give different electric field gradients at the iron nucleus.⁵⁶ The average relative intensities of the subspectra, calculated from the room temperature spectrum before the heating cycle, are as follows: $I_{\text{blue}} = 67.9\%$, $I_{\text{green}} = 8.1\%$, $I_{\text{red}} = 24.0\%$. In Fig. 8 it is shown that the green subspectrum disappears with increasing temperature from room temperature to ca. 500 °C. At temperatures above 500 °C, the spectra become narrower. The vanishing of the Fe^{iii} fraction from the spectrum indicates a partial spin-state transition by an increase of $\Delta_{ex} - \Delta_c$ (cf. Fig. 4). The Mössbauer spectra of the sample taken above 500 °C could be fitted by the superposition of just two subspectra (blue and red). The intensity of the red subspectrum increases at the expense of the blue one. At 900 °C, the intensities of the red and blue subspectra are 62.5 % Fe^{IV} and 37.5 % Fe^{III} , respectively (see Table 1 for more details). If the intensities of the subspectra are taken to indicate the relative amount of different iron species, a very slight reduction of iron is noted; the deduced oxygen stoichiometry $3 - \delta$ of the BSFZ compound does not change significantly, from 2.67 at room temperature to 2.65 at 900 °C in air. The change in iron valencies deduced would be minimal, 3.7+ at room temperature and 3.6+ at 900 °C, respectively. But the mixed low- and high-spin state of the Fe^{3+} ion changes to a purely high-spin configuration. For room temperature the deduced δ (and corresponding iron valences) are in good agreement with Fig. 9, but, at high temperature they deviate remarkably by an underestimation of Fe^{3+} species. Remember, the spectral intensities of subspectra are proportional to the recoil-free fraction of various iron species in the sample and can be correlated directly to real

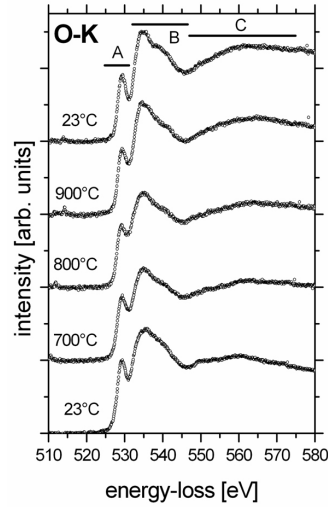


Figure 7: *In situ* oxygen K-ELNES of a BSFZ ceramic. Spectra are background subtracted, scaled to the same integral counts in the range of 522 - 546 eV, and vertically shifted for clarity.

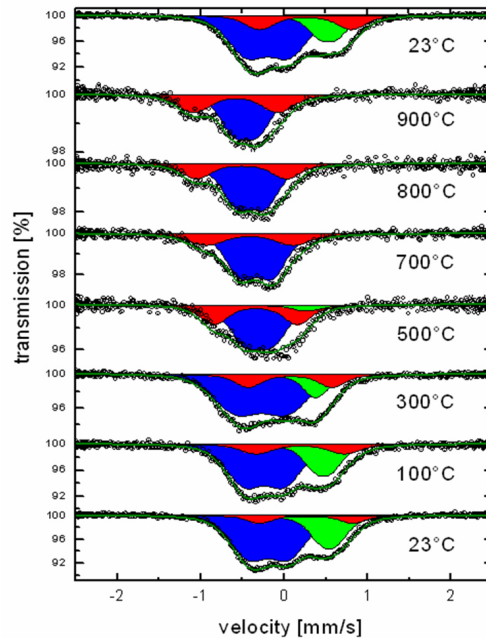


Figure 8: *In situ* Mössbauer spectra of BSFZ powder conducted in air. The subspectra are fitted in color (Fe^{IV} blue, Fe^{iii} green, and Fe^{III} red) and are vertically shifted for clarity.

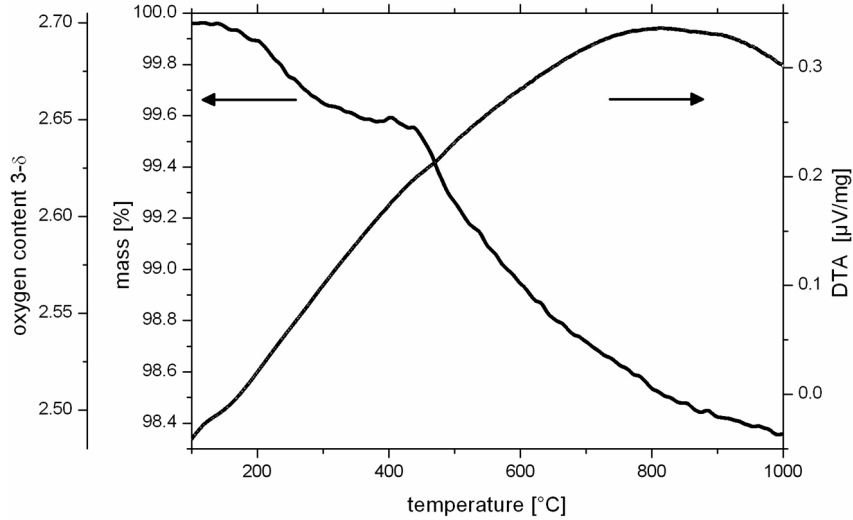


Figure 9: DTA and TGA curves of BSFZ with indication of the oxygen content $3 - \delta$.

concentrations only if constant atomic displacement factors are assumed for all species. Even though in the cubic perovskite the different iron species occupy just one crystallographic site, a measure of likely individual thermal vibration amplitudes has to be estimated by temperature-dependent neutron, X-ray or (convergent beam) electron diffraction on single-crystals combined with appropriate modeling. This is of special concern for the BSFZ perovskite, as the average atomic displacement parameter for the 1b Wyckoff position (iron and zinc) is already high as $B = 2.4 \pm 0.1$ at room temperature.²⁸ The situation is even more complicated by the complex stoichiometry of BSFZ. However, to allow a reliable quantification of the spectra once additional knowledge about the BSFZ material is obtained, we provide complete spectral information in a condensed form in Table 1.

In addition, it should be mentioned that with increasing temperature there is a large center shift of all subspectra to the left. This means essentially that the charge density at the ^{57}Fe nucleus decreases⁵⁷ even though a contribution from second-order Doppler shift⁵⁸ should be considered. One principal reason for the observation could be a decrease of the probability density of ligand orbitals (oxygen) at the position of the ^{57}Fe nucleus when the lattice is thermally dilated. The second principal reason is related to the observed spin-state transition and a change in the population of orbitals with e_g - and t_{2g} -character. Remember, the amount of hybridization of e_g orbitals pointing to the ligand, can be assumed to be twice that of t_{2g} orbitals due to larger overlap integrals with O-2p orbitals.^{43,44}

DTA proves the thermal stability of the perovskite by the absence of exo- or endothermic peaks in the temperature range from 100 - 1000 °C (see Fig. 9,

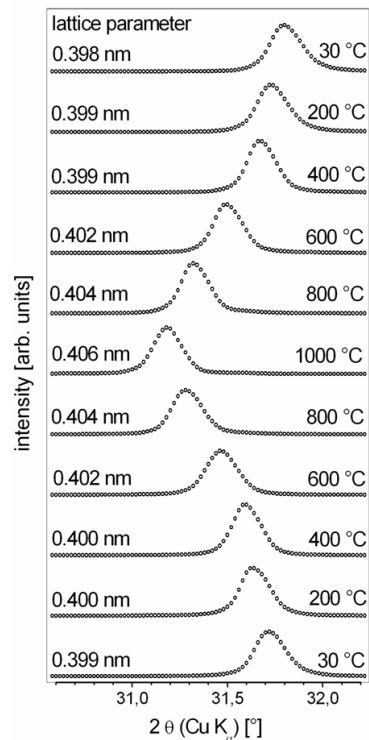


Figure 10: *In situ* XRD pattern in air of a narrow angular range around the (110) reflex of a BSFZ powder with indication of respective lattice parameters for the cubic cell. Diffractograms are vertically shifted for clarity.

Table 1: Fitting results of the *in situ* Mössbauer spectra of BSFZ. A Lorentzian linewidth of $0.24 \text{ mm} \cdot \text{s}^{-1}$ resulting from the fit of the room temperature spectrum of the sample was chosen for the fits of the spectra taken at elevated temperatures. CS refers to the center shift of the whole spectrum.

T	Fe ^{IV} high-spin			Fe ⁱⁱⁱ low-spin			Fe ^{III} high-spin			CS
	IS	QS	intensity	IS	QS	intensity	IS	QS	intensity	
°C	$\text{mm} \cdot \text{s}^{-1}$	$\text{mm} \cdot \text{s}^{-1}$		$\text{mm} \cdot \text{s}^{-1}$	$\text{mm} \cdot \text{s}^{-1}$		$\text{mm} \cdot \text{s}^{-1}$	$\text{mm} \cdot \text{s}^{-1}$		$\text{mm} \cdot \text{s}^{-1}$
23	-0.19	0.48	67.9 %	+0.53	0.21	24.0 %	+0.26	1.11	8.1 %	+0.02
100	-0.23	0.50	62.0 %	+0.47	0.21	24.0 %	+0.20	1.06	14.0 %	0.00
300	-0.27	0.64	69.5 %	+0.38	0.14	14.0 %	+0.08	1.00	16.5 %	-0.12
500	-0.30	0.33	62.5 %	+0.27	0.18	4.8 %	-0.34	1.00	32.7 %	-0.29
700	-0.33	0.39	74.3 %	–	–	–	-0.41	1.05	25.7 %	-0.35
800	-0.40	0.36	71.8 %	–	–	–	-0.51	1.08	28.2 %	-0.43
900	-0.46	0.30	62.5 %	–	–	–	-0.57	1.00	37.5 %	-0.50
23	-0.19	0.51	61.7 %	+0.53	0.21	19.7 %	+0.26	1.10	18.6 %	+0.04

right scale). Hence, phase transformations or decomposition can be ruled out. The constant increase of the DTA signal displays an exothermic process spanning from 100 - 900 °C and is attributed to the release of oxygen from the perovskite lattice. The oxygen release is monitored by a continuous weight loss as seen in the TGA curve (Fig. 9, left scale). The slope of the TGA curve becomes distinctly steeper at around 450 °C, correlating with the vanishing of the Feⁱⁱⁱ fraction (cf. Fig. 8). It should be noted that the resulting high-spin configurations have a higher occupancy of the e_g -based states (see Fig. 4) with stronger hybridization effects and thus a higher electronegativity. This is favorable for a larger release rate of oxygen. The accompanied reduction of iron is obviously easier if no spin-flip are involved. However, above 800 °C the mass loss (Fig. 9, left scale) becomes very small and the oxygen release seems to stagnate at a relative weight loss of ca. 1.6 wt.%. The DTA shows constant values above 800 °C and decreases above 900 °C, signifying the end of the exothermic process, i.e., the oxygen release. The oxygen content in a BSFZ powder at room temperature was estimated by carrier hot gas extraction to 20.25 ± 0.19 wt.% after double heating-cooling in a thermoanalyser apparatus (STA449, Net-

zsch, Selb, Germany) between room temperature and 1000 °C at a heating/cooling rate of $20 \text{ K} \cdot \text{min}^{-1}$. The measurements gave an oxygen content $3 - \delta$ of about 2.70 ± 0.03 . Using this data the TGA curve can be interpreted directly in terms of the oxygen content in the BSFZ perovskite (Fig. 9, very left scale). It shows a decrease of the oxygen content from 2.70 at room temperature to 2.50 at 900 °C. That corresponds to a reduction of iron from an average valence of $3.75+$ down to $3.25+$, if the other cations are considered to have a constant valence: Ba²⁺, Sr²⁺, and Zn²⁺. In other words, iron in BSFZ is in a mixed 75 % Fe⁴⁺ / 25 % Fe³⁺ valence at room temperature. Upon heating to 900 °C in air it will be reduced to a 25 % Fe⁴⁺ / 75 % Fe³⁺ valence. We should mention that the TGA curve in Fig. 9 agrees with the one published by Wei et al.²⁶ for the heating of BSFZ in air. However, their room temperature value for the oxygen content estimated by iodometric titration is lower (2.59). Thus, they estimate the oxygen content at 900 °C to be just 2.40, which would implicitly predict a reduction of iron to less than $3+$ with some Fe²⁺ species being present. However, this can be ruled out by Mössbauer spectroscopy (Fig. 8) as well as by EELS (Figs. 5 and 6). We state that our results are self-consistent.

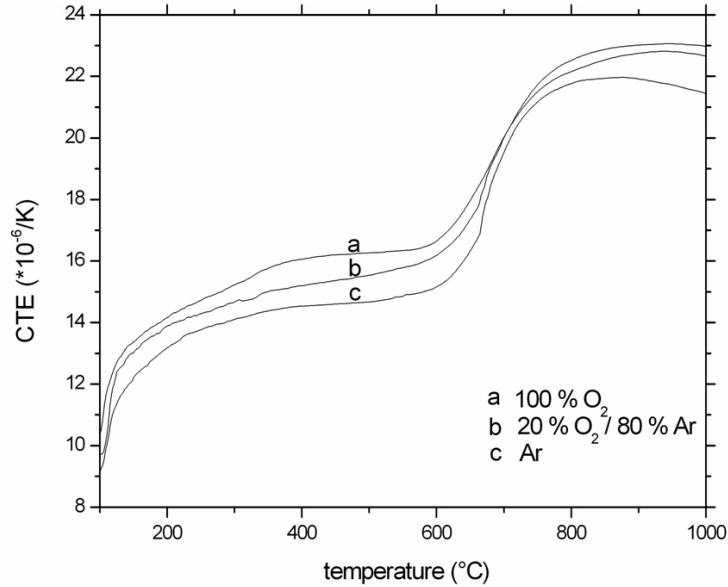


Figure 11: Coefficient of thermal expansion of BSFZ as a function of temperature for different oxygen partial pressures: (a) 100 % O₂, $p_{O_2} \approx 100$ kPa, (b) 20 % O₂, $p_{O_2} \approx 20$ kPa, (c) "pure" argon, < 3 ppm O₂, $p_{O_2} \leq 0.3$ Pa.

In situ XRD patterns of a BSFZ powder in air and in reducing gas mixtures (Ar, 2 % O₂-Ar, and 2 % H₂-Ar) in the 2θ range of 20° - 90° from room temperature to 900 °C have been presented in.²⁴ They show excellent phase stability under all applied conditions by the conservation of the cubic perovskite structure. Figure 10 shows the 2θ angular position of the (110) reflex of the cubic BSFZ during *in situ* heating in air up to 1000 °C with indication of the respective lattice parameters. The absolute reflex position after the heating cycle is shifted by 0.1° towards smaller angles and indicates that the changes are not completely reversible, probably due to kinetic effects. This is consistent with observations by EELS (cf. Fig. 7) and Mössbauer spectroscopy (cf. Fig. 8). A change in the rate of expansion of the BSFZ powder crystals is noted between 400 °C and 600 °C. From these XRD data, the CTE is estimated to be around $11 \times 10^{-6} \text{ K}^{-1}$ and $24 \times 10^{-6} \text{ K}^{-1}$ in the temperature ranges 30 - 400 °C and 600 - 1000 °C, respectively.

The dilatometric measurement of the CTE for a BSFZ ceramic is presented in Fig. 11 as a function of different oxygen partial pressure. The measurements were conducted at 100 % and 20 % O₂, and under Ar. The CTE is nearly independent of the oxygen partial pressure p_{O_2} , although it slightly decreases with decreasing p_{O_2} . There is a constant CTE between 300 - 600 °C of ca. $15 \times 10^{-6} \cdot \text{K}^{-1}$ and between 750 - 1000 °C of ca. $22 \times 10^{-6} \times \text{K}^{-1}$, which corresponds to the XRD data obtained on powders. Strain-induced phase transitions can be ruled out by the *in situ* XRD

and DTA observations. Therefore, the CTE in the current experiment is a combination of a steady thermal expansion caused by anharmonic thermal lattice vibrations and an additional term of a chemical expansion^{59,60} due to the coupled valence/spin-state transition of iron and the accompanied increase of its ionic radius during heating.

4 Conclusions

The performed EELS, esp. ELNES analyses of the Fe-L_{2,3} edge have revealed that iron in the BSFZ perovskite is in a mixed Fe⁴⁺/Fe³⁺ valence state at room temperature. Upon heating to 900 °C the reduction of iron is so weak that no Fe²⁺ species are involved. Moreover, at the O-K edge hybridization effects of O-2p orbitals with empty Fe-3d, Zn-4sp, Ba-4f, Sr-4d, and Fe-4sp orbitals are noticed. The relative amount of hybridization does not change upon heating of the BSFZ perovskite. Mössbauer spectroscopy identified a gradual spin-state transition of the Fe³⁺ species from a mixed low-spin/high-spin configuration to a high-spin configuration. Above ca. 500 °C the Fe³⁺ fraction is in a pure high-spin state. The Fe⁴⁺ fraction is in a pure high-spin state under all applied conditions. Concerning the redox state of iron, weights of Mössbauer subspectra give a reliable estimate at room temperature only. At elevated temperatures obviously the Fe³⁺ recoil-free fraction is lower than the Fe⁴⁺ recoil-free fraction as a consequence of different temperature coefficients of the respective atomic displace-

ment parameters. However, the accurate determination of the oxygen content by carrier hot gas extraction ($3 - \delta = 2.70$) gave an average Fe valence of $3.75+$ in BSFZ at room temperature. Based on these values, monitoring the released amount of oxygen by weight loss upon heating shows that the oxygen content drops to 2.50 and iron is reduced to an average valence of $3.25+$ at $900\text{ }^\circ\text{C}$ in air. The oxygen release rate and the accompanied reduction of iron increase at around $450\text{ }^\circ\text{C}$, which is the Fe^{3+} spin-state transition. The spin-state transition also reflects in an increase of lattice expansion above ca. $600\text{ }^\circ\text{C}$ as monitored by XRD and dilatometry.

The spin-state transition should be elucidated in more detail. Since the intra-atomic exchange coupling Δ_{ex} decreases with larger radial extension of the crystalline wave functions,⁴³ $\Delta_{ex}(\text{Fe}^{4+})$ exceeds $\Delta_{ex}(\text{Fe}^{3+})$. Increasing Δ_{ex} with decreasing hybridization is forced by a lattice expansion in our experiments. Contrary, the cubic ligand field splitting Δ_c increases with increasing hybridization and $\Delta_c(\text{Fe}^{4+}) < \Delta_c(\text{Fe}^{3+})$. An increase of the Fe-O distance, and thus smaller Fe-3d-O-2p interactions leads to a lower Δ_c and a more stable high-spin state. As oxygen is located at the face centers of the cubic unit cell, the Fe-O distance can be read for different temperatures directly from Fig. 10 as half of the respective lattice parameter. It increases from 199.5 pm at room temperature, to 200.0 pm at $400\text{ }^\circ\text{C}$, to 201.0 pm at $600\text{ }^\circ\text{C}$, and so forth. The effective ionic radii from Shannon's compilation⁶¹ for Fe^{IV} (58.5 pm), Fe^{III} (64.5 pm), and Fe^{ii} (55.0 pm) sum with that of O^{2-} (140.0 pm) to 198.5 pm , 204.5 pm , and 195.0 pm , respectively. The lack of additivity to the bond length of the radii of the Fe^{3+} species can be attributed to some covalence (covalent shortening) and maybe electron delocalization.⁶¹ It directly points at the higher electronegativity of Fe^{3+} compared to Fe^{4+} in the perovskite framework. The corresponding Fe-3d-O-2p hybridization is indeed proved by the pre-peak A in the O K-ELNES (Fig. 7). However, the consideration of summarized effective ionic radii indicates that it is favorable for iron to leave the low-spin configuration with increasing Fe-O bond length. Changes in the the occupancy of t_{2g} and e_g states affect the amount of hybridization and the strength of Fe-O bonds, so additional anharmonic terms are introduced into the elastic energy. This might be the reason why the spin-state transition correlates with the observed changes in the rate of lattice expansion (cf. Figs. 10 and 11). The decrease of hybridization with thermal expansion is reflected in the center shift of the Mössbauer spectra (cf. Fig. 8 and Tab. 1). Remember that the elastic energy is anharmonic in principle. Otherwise, no thermal expansion would be observed and the amplitude of atomic vibrations would rise without a shift of the center of gravity with increasing temperature.³⁷

The redox chemistry of transition metals in these

complex perovskites cannot be described by a simple change in valence. Hybridization enables gradual charge transfer in bonds with oxygen and thus changes of the electronegativity of the transition metal during oxidation or reduction.⁶² From the transition metals perspective lattice expansion corresponds to an oxidation and removal of oxygen from the lattice to a reduction. For the heating of BSFZ, reduction of iron from Fe^{4+} to Fe^{3+} is compensated partly by the O-2p band. Lowering p_{O_2} in the surrounding atmosphere, i.e., picking more oxygen from the perovskite lattice, gives two electrons per removed oxygen atom to the lattice and may enhance hybridization of Fe-3d-O-2p bonds. The Fe-O bonds become stronger with decreasing p_{O_2} and we expect a smaller CTE. This systematic trend can be seen in Fig. 11.

We restricted our discussion of the electronic structure in context with Fig. 3 somehow to a simple ionic model with electrons being localized around iron sites to highlight some important points. However, the excellent transport properties of BSFZ for oxygen ions and electrons²⁴⁻²⁶ suggest further investigations of the t_{2g} - and e_g -based energy bands are warranted. The e_g orbitals with higher amount of hybridization give broader bands. The partly filled t_{2g}^+ - and e_g^- -based bands are narrow and not widely separated, which is essential in the observed spin-state transition and indicated by the sharp first peak (2.8 eV FWHM) in the Fe $L_{2,3}$ -ELNES (Figs. 5 and 6). The spin-state transition is manifested in the crossing and finally the separation of t_{2g}^+ - and e_g^- -based bands. Immediately before the separation a metal-like band of maximum width is observed, and a maximum in the electrical conductivity can be expected, which correlates well with the observation by Wei et al.²⁶ of a maximum in the electrical conductivity of BSFZ at around $600\text{ }^\circ\text{C}$ ($9.4\text{ S}\cdot\text{cm}^{-1}$).

Oxygen K-ELNES showed that the amount of O-2p hybridization with Fe-3d relative to other metal cations (Zn-4sp, Ba-4f, and Sr-4d) does not change with the bond length expansion associated with lattice dilatation during heating of BSFZ. This is in clear contrast to observations in the BSCF perovskite, which show a relative switch in hybridization of O-2p with Ba-4f and Sr-4d upon Fe-3d and Co-3d.¹² The comparison with⁴² makes the relative stabilization of transition-metal-oxygen-ligand to earth alkaline-metal-oxygen-ligand hybridization plausible by an anomalous Zn-3d-O2p hybridization caused by a very small energy difference (cf. Fig. 3).

It is worth noting that the lowest temperature of successful synthesis of BSCF ($950\text{ }^\circ\text{C}$)^{19,30} or BSFZ ($750\text{ }^\circ\text{C}$)²⁷⁻²⁹ correlates with spin-state transitions of one of the polyvalent transition metal ions. As already mentioned, it has to be emphasized that both, valence and spin-state, modify the effective radii of transition metal cations, which govern Goldschmidt's tolerance factor, providing a principal criterion for the expectable perovskite symmetry. Therefore, a careful

choice of a membrane material for specific operational conditions has to take into account, that a high stability of the cubic perovskite structure can only be achieved in a pure high-spin state material with its higher ionic radius. This is seen as a big advantage for BSFZ in the IT range compared to BSCF. However, spin-state transition and its effect on the functionality of membrane materials must be investigated in more detail.

Integration over the CTE from room temperature to 700 °C (Fig. 20) gives a dilatation of 0.94 % for BSFZ, compared to 1.6 % for the cobaltite BSCF (based on the CTE given in¹³). The relatively low dilatation of the BSFZ material combined with the peculiar redox behavior of iron, good transport properties, and phase stability^{24–26} makes it superior to cobaltites for prospective applications in the intermediate temperature range (500 - 800 °C).

5 Summary

It has been shown that the iron in the BSFZ perovskite has a mixed 75 % Fe⁴⁺ / 25 % Fe³⁺ valence (3.75+) at room temperature. Upon heating to 900 °C in air it is reduced to a 25 % Fe⁴⁺ / 75 % Fe³⁺ valence (3.25+). The Fe⁴⁺ fraction is always in a high-spin state, and the Fe³⁺ fraction makes a transition from a predominantly low-spin to a pure high-spin configuration at intermediate temperatures. A decrease in the amount of Fe-3d-O-2p hybridization during lattice expansion is seen as the reason for the spin-state transition as the exchange coupling Δ_{ex} increases and the cubic ligand-field splitting Δ_c decreases for each species. The coupled valence/spin-state transition is seen as anomalies of weight-loss, due to release of oxygen, and thermal expansion behavior. It is concluded that to provide excellent phase stability of perovskite-based membrane materials it is crucial to tailor the materials in a way that they exhibit pure high-spin states under operational conditions, even in the presence of mixed valence states. This is the case for BSFZ above ca. 500 °C, making it highly attractive for intermediate temperature applications (500 - 800 °C).

Acknowledgment We would like to thank Prof. Harald Behrens for putting his high-pressure apparatus at our disposal and Falk Heinroth for assistance in TGA measurements. Our discussions with Profs. Jürgen Caro and Haihui Wang were fruitful and are appreciated. The authors greatly acknowledge financial support by DFG grant number FE 928/1-2.

References

- (1) Sunarso, J.; Baumann, S.; Serra, J.; Meulenberg, W.; Liu, S.; Lin, Y.; da Costa, J. D. *J. Membr. Sci.* **2008**, *320*, 13–41.
- (2) Bouwmeester, H. *Catal. Today* **2003**, *82*, 141–150.
- (3) Vente, J.; McIntosh, S.; Haije, W.; Bouwmeester, H. *J. Solid State Electrochem.* **2006**, *10*, 581–588.
- (4) Teraoka, Y.; Zhang, H.; Furukawa, S.; Yamazoe, N. *Chem. Lett.* **1985**, 1743–1746.
- (5) Zhang, H.; Teraoka, Y.; Yamazoe, N. *Chem. Lett.* **1987**, 665–668.
- (6) Teraoka, Y.; Nobunaga, T.; Yamazoe, N. *Chem. Lett.* **1988**, 503–506.
- (7) Teraoka, Y.; Zhang, H.; Okamoto, K.; Yamazoe, N. *Mater. Res. Bull.* **1988**, *23*, 51–58.
- (8) Kingery, W.; Pappis, J.; Doty, M.; Hill, D. *J. Am. Ceram. Soc.* **1959**, *42*, 393–398.
- (9) Shao, Z.; Yang, W.; Cong, Y.; Dong, H.; Tong, J.; Xiong, G. *J. Membr. Sci.* **2000**, *172*, 177–188.
- (10) Shao, Z.; Haile, S. *Nature* **2004**, *431*, 170–173.
- (11) McIntosh, S.; Vente, J.; Haije, W.; Blank, D.; Bouwmeester, H. *Solid State Ionics* **2006**, *177*, 833–842.
- (12) Arnold, M.; Xu, Q.; Tichelaar, F.; Feldhoff, A. *Chem. Mater.* **2008**, submitted.
- (13) McIntosh, S.; Vente, J.; Haije, W.; Blank, D.; Bouwmeester, H. *Chem. Mater.* **2006**, *18*, 2187–2193.
- (14) Teraoka, Y.; Shimokawa, H.; Kang, C.; Kusaba, H.; Sasaki, K. *Solid State Ionics* **2006**, *177*, 2245–2248.
- (15) Vente, J.; Haije, W.; Rak, Z. *J. Membr. Sci.* **2006**, *276*, 178–184.
- (16) Teraoka, Y.; Fukuda, T.; Miura, N.; Yamazoe, N. *J. Ceram. Soc. Jpn.* **1989**, *97*, 533–538.
- (17) Schiestel, T.; Kilgus, M.; Peter, S.; Caspary, K.; Wang, H.; Caro, J. *J. Membr. Sci.* **2005**, *258*, 1–4.
- (18) Švarcová,.; Wiik, K.; Tolchard, J.; Bouwmeester, H.; Grande, T. *Solid State Ionics* **2008**, *178*, 1787–1791.
- (19) Arnold, M.; Gesing, T.; Martynczuk, J.; Feldhoff, A. *Chem. Mater.* **2008**, *20*, 5881–5858.
- (20) Wang, H.; Cong, Y.; Yang, W. *Chem. Comm.* **2002**, 1468–1469.
- (21) Vente, J.; McIntosh, S.; Haije, W.; Bouwmeester, H. *React. Kinet. Catal. Lett.* **2003**, *79*, 351–356.

- (22) Steele, C.; Heinzl, A. *Nature* **2001**, *414*, 345–352.
- (23) J. Caro, H. Wang, C. Tablet, G. Grubert, "Sauerstofftransportierende Oxidkeramiken" (EU patent EP 1630 148 A3, 2006).
- (24) Wang, H.; Tablet, C.; Feldhoff, A.; Caro, J. *Adv. Mater.* **2005**, *17*, 1785–1788.
- (25) Wei, B.; Lü, Z.; Huang, X.; Liu, Z.; Miao, J.; Li, N.; Su, W. *J. Am. Ceram. Soc.* **2007**, *90*, 2264–3366.
- (26) Wei, B.; Lü, Z.; Huang, X.; Liu, M.; Miao, J.; Li, N.; Su, W. *J. Power Sourc.* **2008**, *176*, 1–8.
- (27) Feldhoff, A.; Arnold, M.; Martynczuk, J.; Gesing, T.; Wang, H. *Solid State Sci.* **2008**, *10*, 689–701.
- (28) Feldhoff, A.; Martynczuk, J.; Wang, H. *Prog. Solid State Chem.* **2007**, *35*, 339–353.
- (29) Martynczuk, J.; Arnold, M.; Wang, H.; Feldhoff, A. *Adv. Mater.* **2007**, *19*, 2134–2140.
- (30) Arnold, M.; Wang, H.; Martynczuk, J.; Feldhoff, A. *J. Am. Ceram. Soc.* **2007**, *90*, 3651–3655.
- (31) Schmid, H.; Mader, W. *Micron* **2006**, *37*, 426–432.
- (32) Adler, P.; Ericsson, S. *Z. Anorg. Allg. Chem.* **2000**, *626*, 118–124.
- (33) Bocquet, A.; Fujimoro, A.; Mizokawa, T.; Saitoh, T.; Namatame, H.; Suga, S.; Kimizuka, N.; Takeda, Y.; Takano, M. *Phys. Rev. B* **1992**, *45*, 1561–1570.
- (34) Potapov, P.; Schryvers, N. *Ultramicrosc.* **2004**, *99*, 73–85.
- (35) K. Lagarec, D.G. Rancourt, "Recoil - Mössbauer Spectral Analysis Software for Windows, version 1.02", Department of Physics, University of Ottawa, Ottawa, 1998.
- (36) Gruner, W. *Fresenius J. Anal. Chem.* **1999**, *365*, 597–603.
- (37) H. Küppers, "Thermal expansion"; pp. 99–104 in International tables for crystallography, Volume D. Edited by A. Authier, The International Union of Crystallography, Kluwer Academic Publishers, Dordrecht, 2003.
- (38) Wang, H.; Schiestel, T.; Tablet, C.; Schroeder, M.; Caro, J. *Solid State Ionics* **2006**, *177*, 2255–2259.
- (39) Arnold, M.; Martynczuk, J.; Efimov, K.; Wang, H.; Feldhoff, A. *J. Membr. Sci.* **2008**, *316*, 137–144.
- (40) Martynczuk, J.; Arnold, M.; Feldhoff, A. *J. Membr. Sci.* **2008**, *322*, 375–382.
- (41) de Groot, F. *J. Electr. Spectrosc. Rel. Phenomen.* **1994**, *67*, 529–622.
- (42) Dong, C.; Persson, C.; Vayssieres, L.; Augustsson, A.; Schmitt, T.; Mattesini, M.; Ahuja, R.; Chang, C.; Guo, J. *Phys. Rev. B* **2004**, *70*, 1953251–1953252.
- (43) J.B. Goodenough, and J.M. Longo, "Crystallographic and magnetic properties of perovskite and perovskite-related compounds", pp. 126–314, in Landolt-Börnstein new series, numerical data and functional relationships in science and technology, Volume III/4a. Edited by K.H. Hellwege and A.M. Hellwege, Springer, Berlin, 1970.
- (44) de Groot, F.; Grioni, M.; Fuggle, J.; Ghijsen, J.; Sawatzky, G.; Petersen, H. *Phys. Rev. B* **1989**, *40*, 5715–5723.
- (45) The RT Fe-L_{2,3} spectra of standard substances are accessible as ascii data through the EELS data base at the Centre d'Elaboration de Matériaux et d'Etudes Structurales (CEMES): <http://www.cemes.fr/eelsdb/>.
- (46) Ikeno, H.; Tanaka, I.; Miyamae, T.; Mishimna, T.; Adachi, H.; Ogasawara, K. *Mater. Trans.* **2004**, *45*, 1414–1418.
- (47) Tanaka, I.; Mizoguchi, T.; Yamamoto, T. *J. Am. Ceram. Soc.* **2005**, *88*, 2013–2029.
- (48) Garvie, L.; Buseck, P. *Nature* **1998**, *396*, 667–670.
- (49) Krishnan, K. *Ultramicrosc.* **1990**, *32*, 309–311.
- (50) van Aken, P.; Liebscher, B.; Styrsa, V. *Phys. Chem. Minerals* **1998**, *25*, 323–327.
- (51) Gloter, A.; Ingrin, J.; Bouchet, D.; Colliex, C. *Phys. Rev. B* **2000**, *61*, 2587–2594.
- (52) Sefat, A.; Amow, G.; Wu, M.; Botton, G.; Greedan, J. *J. Solid State Chem.* **2005**, *178*, 1008–1016.
- (53) Wagener, T.; Gao, Y.; Weaver, J.; Arko, A.; Flandermeier, B.; Capone, D. *Phys. Rev. B* **1987**, *36*, 3899–3902.
- (54) Abbate, M.; de Groot, F.; Fuggle, J.; Fujimori, A.; Strebel, O.; Lopez, F.; Domke, M.; Kaindl, G.; Sawatzky, G.; Takano, M.; Takeda, Y.; Eisaki, H.; Uchida, S. *Phys. Rev. B* **1992**, *46*, 4511–4519.
- (55) Menil, F. *J. Phys. Chem. Solids* **1985**, *46*, 763–789.

- (56) Parish, R. *NMR, NQR, EPR, and Mössbauer spectroscopy in inorganic chemistry*; Ellis Horwood, New York, Berlin, 1990; pp 128–164.
- (57) Takano, M.; Nasu, S.; Abe, T.; Yamamoto, K.; Endo, S.; Takeda, Y.; Goodenough, J. *Phys. Rev. Lett.* **1991**, *67*, 3267–3270.
- (58) Šepelak, V.; Wißmann, S.; Becker, K. *J. Mater. Sci.* **1998**, *33*, 2845–2850.
- (59) Adler, S. *J. Am. Ceram. Soc.* **2001**, *84*, 2117–2119.
- (60) Fossdal, A.; Menon, M.; Waernhus, I.; Wiik, K.; Einarsrud, M.; Grande, T. *J. Am. Ceram. Soc.* **2004**, *87*, 1952–1958.
- (61) Shannon, R. *Acta Cryst. A* **1976**, *32*, 751–767.
- (62) Valkeappa, M.; Katsuma, Y.; Asako, I.; Motohashi, T.; Chan, T.; Liu, R.; Chen, J.; Yamauchi, H.; Karpinnen, M. *J. Solid State Chem.* **2007**, *180*, 1608–1615.

4.3 Aluminum doped perovskites as high performance oxygen permeation materials

Julia Martynczuk, Fangyi Liang, Mirko Arnold,

Vladimir Šepelák, and Armin Feldhoff

Chemistry of Materials (submitted)

Aluminum doped perovskites as high performance oxygen permeation materials

Julia Martynczuk,^{*,†} Fangyi Liang,[†] Mirko Arnold,[†]
Vladimir Šepelák,^{‡§} and Armin Feldhoff[†]

[†]*Institute of Physical Chemistry and Electrochemistry,
Leibniz Universität Hannover, D-30167 Hannover, Germany, and*

[‡]*Institute of Physical and Theoretical Chemistry,
Braunschweig University of Technology, D-38106 Braunschweig, Germany*

[§]*On leave from the Slovak Academy of Sciences, Košice, Slovakia*

*Email: julia.martynczuk@pci.uni-hannover.de

Abstract

Previously unreleased compositions of $(\text{Ba}_{0.5}\text{Sr}_{0.5})(\text{Fe}_{1-x}\text{Al}_x)\text{O}_{3-\delta}$ perovskites in the range of $0 \leq x \leq 0.2$ were synthesized and studied with respect to electronic and crystallographic structure, as well as oxygen permeation. The perovskite phase in all synthesized oxides was found to be cubic, without any impurities for aluminum fractions in the range $x = 0.01-0.09$. Electron energy-loss spectroscopy (EELS) revealed a significant amount of covalency by Fe-3d-O-2p hybridization and a mixed $\text{Fe}^{3+}/\text{Fe}^{4+}$ valence state of iron for all synthesized perovskites, which was quantified by Mössbauer spectroscopy. Trivalent aluminum replaces a higher fraction of Fe^{4+} than of Fe^{3+} while both iron species are in high-spin state. The Mössbauer quadrupole splittings indicate a greater disorder around iron with increasing aluminum content and, together with the EELS result of an abatement of covalent character in the bonding of iron and oxygen, the observed lattice expansion can be understood. In-situ XRD and TG/DTA measurements revealed high temperature stability of the materials up to 1350 °C. The oxygen permeation increases with rising aluminum content from 0 to 0.1, and the $(\text{Ba}_{0.5}\text{Sr}_{0.5})(\text{Fe}_{0.9}\text{Al}_{0.1})\text{O}_{3-\delta}$ membranes show a very high oxygen permeation ($1.19 \text{ ml cm}^{-2} \text{ s}^{-1}$ at 950 °C) compared to known perovskite membranes. Even among the previously published iron and aluminum containing membranes, they exhibit the highest oxygen permeation.

1 Introduction

Many industrial processes require the supply or removal of oxygen to or from reaction mixtures with high selectivity and oxygen fluxes. The separation

of oxygen from air by ceramic membranes is a key technology. Membranes with both high flux and selectivity are based on mixed ionic-electronic conductors (MIECs) with perovskite structure.^{1,2} Perovskite-type oxides of the composition ABO_3 can host many different cations on the A- and B-sites, which enables us to tune conductivities from almost pure electronic to almost pure ionic. Numerous applications of perovskite membranes with different elemental compositions have already been reported, e.g. separation of oxygen from air, partial oxidation of carbon hydrides and oxygen-enrichment in air.³⁻⁸ The electrochemical importance of perovskite oxides is apparent in the case of solid-oxide fuel cells (SOFCs) for power generation.⁹ In this application, perovskites are employed as cathode, electrolyte or anode materials, and even full ceramic intermediate-temperature solid oxide fuel cells (IT-SOFCs, ca. 500-800 °C) are possible.¹⁰⁻¹⁴ For membrane-based dehydrogenation processes in the synthesis of basic chemicals like ethylene¹⁵ and propylene¹⁶ at high selectivity, and for IT-SOFCs,¹⁷ the long-time stability of the materials is of special interest. However, perovskite materials offer, in addition to oxygen separation membranes, an even wider range of application in many different fields, which are listed elsewhere.¹⁸

Due to their multiple applications, new perovskite materials are of major interest for natural scientists, like chemists and materials scientists. The current state-of-the-art material, due to its high oxygen permeation flux and phase stability above 900 °C, is $(\text{Ba}_{0.5}\text{Sr}_{0.5})(\text{Co}_{0.8}\text{Fe}_{0.2})\text{O}_{3-\delta}$ (BSCF).^{1,10,19} However, recently, serious stability problems with cobalt-containing materials in the IT range have been discussed in the literature.^{20,21} If the cubic BSCF is kept at temperatures below 900 °C for long time periods, a decomposition into a three-phase mixture takes

place due to a reversible reordering of the hexagonal AO_3 -layer stacking sequence in the cubic perovskite. The breakdown of the cubic perovskite structure leads to the long-term instability of the BSCF material in the IT range. The driving force for this reaction was identified to be the cobalt site ($\text{Co}^{2+}/\text{Co}^{3+}$), because trivalent cobalt shows a high-spin (HS) to low-spin (LS) transition and prefers a low-spin configuration at intermediate temperatures. Furthermore, it was shown by in situ high-temperature electron energy-loss spectroscopy (HT-EELS) on BSCF²² and comparative TGA of different perovskite-type materials²³ that the redox behavior of polyvalent B-site cobalt ions is much more flexible than that of iron, manganese or nickel. The flexible redox behavior of cobalt in BSCF causes a large coefficient of thermal expansion (CTE) in the range of $20\text{-}24 \times 10^{-6} \text{ K}^{-1}$ ^{24,25} resulting in huge thermal stresses and, in the worst case, crack formation.

Therefore, the search for alternative materials and the development of cobalt-free perovskite-type oxides are of great interest. The introduction of lower valence state ions into the perovskite structure ABO_3 induces oxygen vacancies, leading to an improved ionic conductivity that benefits the oxygen permeability. This paper presents novel cobalt-free perovskite materials of $\text{A}^{II}\text{B}^{III/IV}\text{O}_{3-\delta}$ -type, containing iron and aluminum with the stoichiometries $(\text{Ba}_{0.5}\text{Sr}_{0.5})(\text{Fe}_{1-x}\text{Al}_x)\text{O}_{3-\delta}$ (BSFA). Doping of the B-site of the perovskite structure with a metal with a fixed valence state, like the trivalent aluminum, is expected to lead to the diminution of non-stoichiometric oxygen variations and a more stable redox behavior of the material. The lattice expansion caused by the variation in temperature or chemical oxygen potential is likely to be reduced, but the oxygen permeability due to higher ionic conductivity should improve.

We are not the first to investigate the idea of aluminum doping. There are several lanthanum-based²⁶⁻³³ as well as strontium-based³²⁻⁴⁶ aluminum doped perovskite materials reported in the literature. Even though Holc et al. suggest $(\text{La}_{0.8}\text{Sr}_{0.2})(\text{Fe}_{1-x}\text{Al}_x)\text{O}_{3-\delta}$ with $x = 0, 0.3, \text{ and } 0.5$ as candidates for IT-SOFCs,²⁶ most researchers have reported a deterioration in the oxygen permeation for lanthanum-based aluminum doped perovskite materials, e.g. for $(\text{La}_{0.5}\text{Sr}_{0.5})\text{FeO}_{3-\delta}$, $(\text{La}_{1-x}\text{Ca}_x)(\text{Al}_y\text{Fe}_{1-y})\text{O}_{3-\delta}$ and $\text{La}(\text{Ga}_{0.9-x}\text{Mg}_{0.1}\text{Al}_x)\text{O}_{3-\delta}$.^{29,30,32} A decrease in the ionic and electronic conductivity was also published for strontium-based aluminum doped perovskites by Dong et al. for $\text{Sr}(\text{Co}_{0.4}\text{Fe}_{0.6-x}\text{Al}_x)\text{O}_{3-\delta}$ and Kharton et al. for $(\text{Sr}_{0.7}\text{La}_{0.3})(\text{Fe}_{1-x}\text{Al}_x)\text{O}_{3-\delta}$, $\text{Sr}(\text{Fe}_{1-y}\text{Al}_y)\text{O}_{3-\delta}$, and $(\text{Sr}_{0.7}\text{La}_{0.3})(\text{Co}_{0.8}\text{Al}_{0.2})\text{O}_{3-\delta}$.³⁵⁻³⁸ To our knowledge, the only barium containing aluminum doped perovskite reported in the literature is $(\text{Sr}_{0.8}\text{Ba}_{0.2})(\text{Co}_{0.5}\text{Al}_{0.3}\text{Fe}_{0.2})\text{O}_{3-\delta}$, and only the coefficient of thermal expansion (CTE: $22.4 \times 10^{-6} \text{ K}^{-1}$ for

$773 \leq T \leq 1273 \text{ K}$) for this cobalt containing material is tabulated.⁴⁶

The structural characterization of the novel $(\text{Ba}_{0.5}\text{Sr}_{0.5})(\text{Fe}_{1-x}\text{Al}_x)\text{O}_{3-\delta}$ material was carried out by (in-situ) X-ray diffraction (XRD) and Rietveld refinements. Electron energy-loss spectroscopy (EELS) and Mössbauer spectroscopy revealed the iron oxidation and spin-states and the hybridization of iron and oxygen. Scanning electron microscopy (SEM), combined with energy-dispersive X-ray spectroscopy (EDXS) and transmission electron microscopy (TEM) along with EDXS, were conducted to examine the microstructure and elemental composition. Additionally, differential thermal analysis (DTA) and oxygen permeation experiments were conducted for characterization purposes.

2 Experimental Section

$(\text{Ba}_{0.5}\text{Sr}_{0.5})(\text{Fe}_{1-x}\text{Al}_x)\text{O}_{3-\delta}$ powders were synthesized by a combined citric acid and ethylene-diamine-tetraacetic acid (EDTA) method, as described in detail elsewhere.^{18,47,48} Given amounts of $\text{Ba}(\text{NO}_3)_2$, $\text{Zn}(\text{NO}_3)_2$, $\text{Fe}(\text{NO}_3)_3$, and $\text{Sr}(\text{NO}_3)_2$ were dissolved in water, followed by the addition of EDTA acid and citric acid with the molar ratio of EDTA acid: citric acid: total of metal cations controlled at around 1:1.5:1. After agitation for a given time, the pH value of the solution was adjusted to approximately 9, by the addition of $\text{NH}_3 \cdot \text{H}_2\text{O}$. Water was evaporated with stirring at $150 \text{ }^\circ\text{C}$. The transparent solution transformed into a dark purple gel following several hours of evaporation. Further heat treatments were applied, i.e., the pre-calcination for 2 h at ca. $700 \text{ }^\circ\text{C}$ and the final calcination to obtain the pure perovskite phases for 10 h at $950 \text{ }^\circ\text{C}$. The calcined powders were uniaxially pressed under 140 kN into pellets and sintered pressurelessly at $1150 \text{ }^\circ\text{C}$ for 2 h to ceramic discs of 14 mm in diameter and a thickness of 1.1 mm.

X-ray diffraction (XRD) was measured with a Philips X'pert-MPD instrument using a flat sample geometry and monochromator-filtered $\text{Cu K}\alpha$ radiation at 40 kV and 40 mA, a receiving slit of 0.19-0.38 mm and count times of 3-25 s per step. Data were collected in a step-scan mode in the range of $15\text{-}100^\circ$ with intervals of 0.005 to 0.03° . Data for interpretation were taken from the PDF-2 database with PDF numbers BaAl_2O_4 [17-306] and $\text{Ba}_3\text{Al}_2\text{O}_6$ [25-75]. In-situ XRD measurements were taken with steps of 200 K with a heating rate of 5 K/min, respectively, in order to achieve a good overview within the temperature range 20-1000 $^\circ\text{C}$. Before each data acquisition, an equilibrium time of 1/2 h was set, five scans were performed at 1000 $^\circ\text{C}$, and the temperature was held for 10 h. Ambient air was used as the atmosphere within the chamber. Rietveld refinements on the XRD powder data were carried out by using Topas Aca-

Table 1: Tolerance factors of BSFA with the assumption of sole Fe^{3+} , sole Fe^{4+} or with the ratio of $\text{Fe}^{3+}/\text{Fe}^{4+}$ both in high-spin state calculated from integral intensities of ^{57}Fe Mössbauer subspectra.

	tolerance factor t for			elemental fractions		
	Fe^{3+}	$\text{Fe}^{3+}/\text{Fe}^{4+}$	Fe^{4+}	Fe^{3+}	Fe^{4+}	Al^{3+}
BSF	1.011	1.022	1.042	63.6	36.4	0
BSFA0.01	1.012	1.023	1.042	63.9	35.1	1
BSFA0.05	1.014	1.024	1.043	62.7	32.3	5
BSFA0.1	1.019	1.025	1.046	61.7	28.9	9.4
BSFA0.2	1.022	1.033	1.047	44.4	35.6	20

demio 4.1 software. During refinements, general parameters, such as the scale factor, background parameters and the zero point of the counter, were optimized. Profile shape calculations were carried out using the Thompson-Cox-Hastings function implemented in the program by varying the strain parameter as well. Additionally, the cell parameter and the displacement parameters were refined. In the case of site occupation with mixed atoms, linear constraints were used for the occupancy (the occupancy of atom B is equivalent to 1.0 minus the occupancy of atom A) and the displacement parameters (atoms on the same position have the same displacement parameter).

^{57}Fe Mössbauer spectroscopic measurements were performed in transmission geometry using a conventional spectrometer in constant acceleration mode at temperature $T = 293$ K. A $^{57}\text{Co}/\text{Rh}$ γ -ray source was used. The velocity scale of the spectra was calibrated relative to ^{57}Fe in Rh. 'Recoil' spectral analysis software⁴⁹ and the Voigt-based fitting method were used for the quantitative evaluation of the Mössbauer spectra. IS is the isomer shift relative to Fe in Rh at 293 K. QS is the quadrupole splitting. A Lorentzian linewidth of 0.30 mm/s, resulting from the fit of the spectrum of the BSF sample, was chosen for fitting the spectra of the other investigated samples. The estimated standard deviations are lower than 1 % for intensity I and lower than 0.01 mm/s for the IS and QS parameters. Scanning electron microscopy (SEM) was performed with a JEOL JSM-6700F. Secondary electron (SE) micrographs were taken at a low excitation voltage of 2 kV. In order to analyze the microstructure of the sintered membranes, SEM was conducted on both surfaces and on fracture surfaces, and grain size distributions were evaluated using image analysis software (Adobe Photoshop CS2 (Version 9.0) and ImageJ (1.33 u)).⁵⁰ Fracture surfaces were etched with aqueous HCl (0.5 M) for 1-2 min in order to visualize grain boundaries. An EDX spectrometer, Oxford Instruments INCA-300, with an ultra-thin window was used for elemental analysis.

Thermogravimetric analysis (TGA) and differential

thermal analysis (DTA) were measured on calcined BSFA powders in DTA/TG crucibles of Al_2O_3 with a SETSYS TGA-DSC instrument from 20 to 1200 °C with a heating rate of 20 K/min and from 1200 to 1420 °C with a heating rate of 1 K/min under air (flowrate: 100 ml/min).

Transmission electron microscopy (TEM) and electron energy-loss spectroscopy (EELS) were conducted at 200 kV with a JEOL JEM-2100F-UHR field-emission instrument equipped with a Gatan GIF 2001 energy filter and a 1k-CCD camera. EDXS was carried out by a light-element detector using the Cliff-Lorimer quantification technique (INCA 200 TEM, Oxford Instruments). EELS was performed in diffraction coupled mode while taking care to measure accurately the absolute position of core-loss details.⁵¹ The preparation of standards for Fe^{4+} (SrFeO_3) and Fe^{3+} ($\alpha\text{-Fe}_2\text{O}_3$), which were carefully checked by Mössbauer spectroscopy to exhibit only the desired iron valence, is described elsewhere.⁵¹ Furthermore, the specimen for TEM investigations was prepared similar to Martynczuk et al.⁵⁰ Membranes were cut, covered on both sides with silicon single crystals, polished on polymer embedded diamond lapping films and epoxy-glued onto a copper slot grid. Electron transparency was achieved by Ar^+ ion sputtering (Gatan, model 691 PIPS).

The oxygen permeation was measured in a high-temperature permeation cell⁵² from 800 to 950 °C in steps of 25 °C with an equilibrium time of 15 min. Discs were sealed onto a ceramic tube with gold-paste (conducting 130 paste, C5754, Heraeus) at 950 °C for 2 h. The actual temperature was measured 1 cm above the membrane with a quartz glass protected Pt/Rh thermocouple. After sealing, gas flow rates were delivered to the reactor by mass flow controllers (Bronckhorst Hi-Tech) and continuously read by an on-line gas chromatograph (Agilent Technologies, HP 5890, equipped with a Carboxen 1000 column). Air was fed at a rate of 150 mL min^{-1} to the air side; He (29.0 mL min^{-1} , 99.995 %) and Ne (1.0 mL min^{-1} , 99.995 %) as the internal standard gases were fed to the sweep side.

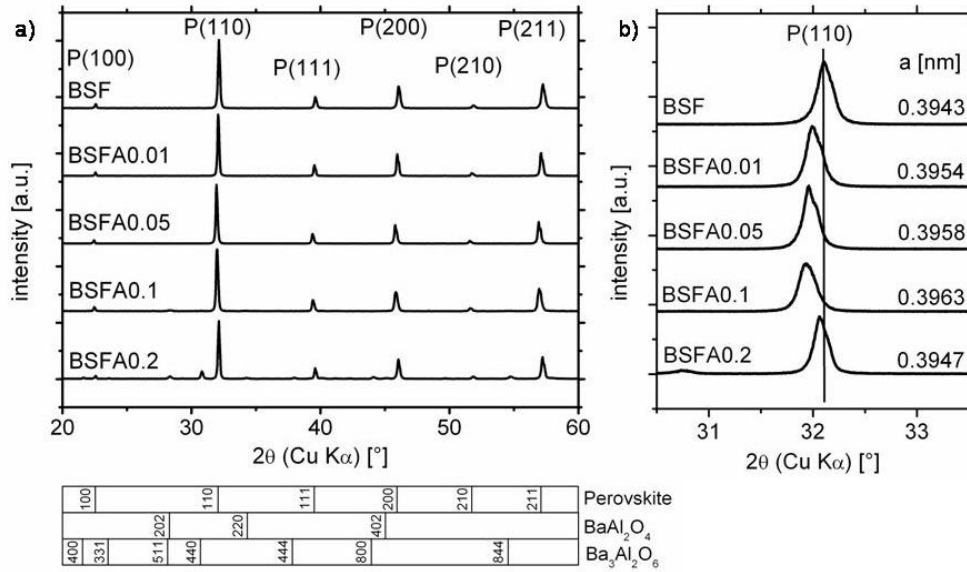


Figure 1: X-ray diffraction data of a) all synthesized BSFA oxides with various aluminum fractions calcined at 950 °C for 10 h, b) zoom of reflex at the Miller index (110) for determination of lattice parameters a . Reflex positions for perovskite (p) belong to BSF with $a = 0.3943$ nm.

The absolute flow rate of the effluents was determined by using neon as an internal standardization. For that purpose, the concentration of neon in the effluents was measured. Since the flow rate of neon is known, it is thus possible to calculate the total flow rate of the effluents. Nitrogen was also detected in the effluents by gas chromatography because of slight imperfections in the sealing, and the leakage of oxygen was subtracted in the calculation of the oxygen permeation flux. The relative leakage of O₂ was found to be less than 5 %. The permeation flux through the membrane could then be calculated by the fraction of O₂ in the effluents and the determination of the effective permeation area of the membrane.

3 Results and Discussion

The incorporation of aluminum into the perovskite lattice was conducted systematically. Due to the small ionic radius of trivalent aluminum ($r(\text{Al}^{3+}) = 0.535$ Å), it was expected to be incorporated at the B-position of ABO₃ (A: $r(\text{Ba}^{2+}) = 1.61$ Å, $r(\text{Sr}^{2+}) = 1.44$ Å, B: $r(\text{Fe}^{3+}, \text{HS}) = 0.645$ Å, $r(\text{Fe}^{4+}, \text{HS}) = 0.585$ Å, $r(\text{O}^{2-}) = 1.40$ Å).⁵³ A good benchmark for the degree of aluminum doping in a cubic perovskite is the tolerance factor t described by Goldschmidt.⁵⁴ For the ideal cubic structure, t should equal one. It was adapted to double perovskites by Anderson⁵⁵ and can be calculated for ABO₃ with weighted arithmetic mean values for the cationic radii \bar{r} according to Feldhoff et al.:⁴⁷

$$t = \frac{\bar{r}_A + r_O}{\sqrt{2}[\bar{r}_B + r_O]} \quad (1)$$

For the composition $(\text{Ba}_{0.5}\text{Sr}_{0.5})(\text{Fe}_{1-x}\text{Al}_x)\text{O}_{3-\delta}$ the values for t are labeled in Table 1 for Fe³⁺, Fe⁴⁺, and for the ratio of Fe³⁺ to Fe⁴⁺ determined by Mössbauer spectroscopy. The values for t are in the range of 1.01 to 1.05 for $0 \leq x \leq 0.2$. When the tolerance factor is $t > 1$, the AO₃ layers typically adopt mixed cubic and hexagonal, or pure hexagonal, close-packed stacking sequences.^{20,56} The more t deviates from unity, the less stable the cubic perovskite; thus, it is reasonable to expect a cubic perovskite with very low aluminum doping. Apparently, the maximum aluminum doping for BSFA is around $x = 0.1$ with a tolerance factor of 1.025. This conclusion can be drawn from Figure 1.

The crystal structure of the synthesized powders with various aluminum fractions calcined at 950 °C for 10 h was examined by X-ray powder diffraction from 20 to 60 ° 2θ at room temperature (Figure 1a). The oxides with aluminum fractions of $0 \leq x \leq 0.05$ crystallize as cubic perovskites with lattice parameters around 0.396 nm, which are labeled in Figure 1b in a zoom of reflex at the Miller index (110) for lattice parameter determination. The perovskite phase in all synthesized oxides is cubic perovskite, and the highest aluminum fraction for a formation of pure cubic perovskite without any impurities is in the range of $x = 0.09$ -0.1. The BSFA oxides with aluminum fractions of $x \geq 0.1$ do not form a pure cubic perovskite phase. In the BSFA0.1

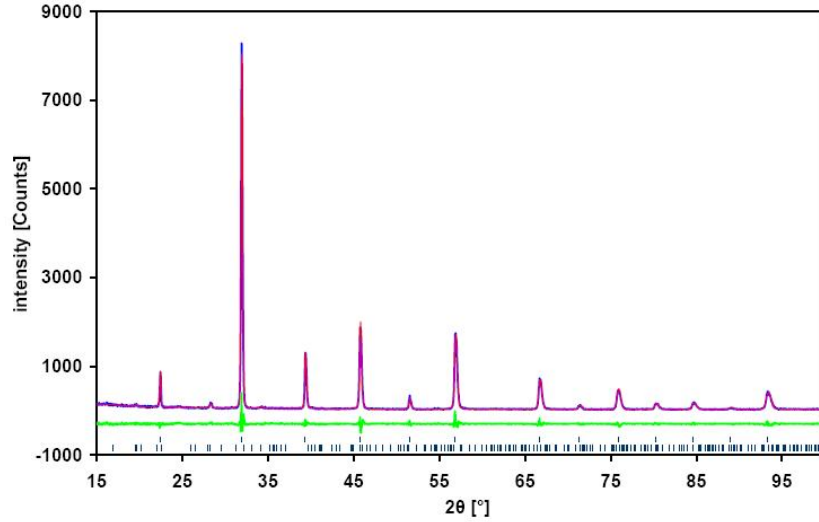


Figure 2: Rietveld refinement for BSFA0.1 (calcined at 950 °C for 10 h). The observed (blue) and calculated intensities (red) together with the difference (green) between the observed and calculated pattern as well as the possible reflex position (tick marks) are given.

Table 2: Parameters obtained by fitting the room-temperature Mössbauer spectra of the BSFA samples. IS is the isomer shift relative to Fe in Rh at 293 K. QS is the quadrupole splitting.

	BSF		BSFA0.01		BSFA0.05		BSFA0.1		BSFA0.2			
	Fe ⁴⁺	Fe ³⁺	Fe ⁴⁺	Fe ³⁺	Fe ⁴⁺	Fe ³⁺	Fe ⁴⁺	Fe ³⁺	Fe ⁴⁺	Fe ³⁺	Fe ⁴⁺	Fe ³⁺
IS (mm/s)	-0.17	0.18	-0.17	0.18	-0.17	0.18	-0.17	0.18	-0.17	-0.14	0.10	0.28
QS (mm/s)	0.48	0.70	0.54	0.72	0.51	0.72	0.49	0.73	0.47	0.83	0.72	0.80
I(%)	36.4	63.6	35.5	64.5	34.0	66.0	31.9	68.1	21.4	23.1	11.9	43.6

powder a minor impurity (3.3 %) of BaAl₂O₄ was determined by Rietveld refinements (Figure 2).

The Rietveld refinement of BSFA0.1 revealed a two phase mixture consisting of the perovskite and a second oxide (BaAl₂O₄). The perovskite was found to crystallize in the cubic space group Pm-3m (No. 221) with a lattice parameter of 0.39630(3) nm. Barium and strontium were refined on the same crystallographic position 1a (0,0,0) with 52(2) % occupation for the strontium atoms corresponding to the chemical analysis and a displacement parameter of B = 1.3 (1). Iron (91 %) and aluminum (9 %) were calculated at the 1b (1/2,1/2,1/2) position, showing a high displacement of B = 1.7 (1). An equivalently high displacement of B = 2.8 (5) was found for the oxygen atoms on the 3c (0,1/2,1/2) site. The refinement converged to reliability factors of RWP = 0.127 and RP = 0.09 for the pattern with a goodness of fit = 1.265, a Durban-Watson parameter of 1.345, and a Bragg R-value of 0.022 for the perovskite structure.

The second oxide was identified as hexagonal BaAl₂O₄

with space group P6₃22 (No. 182), as reported by Arlett et al.⁵⁷ Quantitative analysis revealed that the perovskite structure is the major phase, accounting for 96.7 %, and the BaAl₂O₄ accounts for 3.3 %. For BSFA0.2 two impurities were found and identified as 6 % of hexagonal BaAl₂O₄ and 8 % of cubic Ba₃Al₂O₆⁵⁸ with space group Pa₃ (No. 205, Figure 1a). The tolerance factor is nevertheless a good benchmark for the predictability of perovskite formation. When the aluminum fraction was higher than 0.1 ($t \geq 1.025$), the aluminum was not completely incorporated into the perovskite lattice, and instead of a hexagonal perovskite, the excessive aluminum formed an extra hexagonal phase containing predominantly barium at the A-site. For this reason, the BSFA0.2 perovskite does not contain an Al fraction of $x = 0.2$, but rather less than that, and therefore, the lattice constant decreases again. Astonishingly, the lattice parameter increases with higher aluminum doping ($x \leq 0.1$, Figure 1b), although a decrease due to the smaller ionic radius of aluminum could be expected.

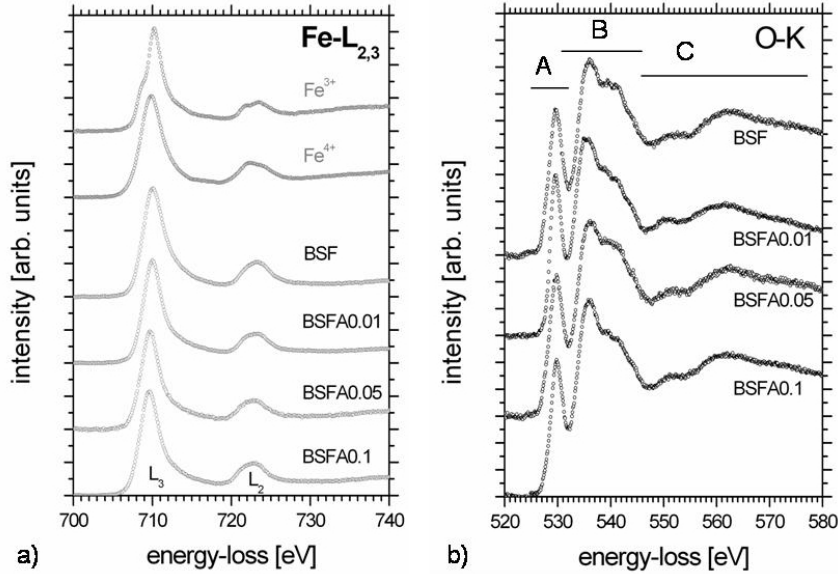


Figure 3: Room-temperature EEL spectra a) of the Fe- $L_{2,3}$ edge for BSF, BSFA0.01, BSFA0.05, and BSFA0.1 compared to Fe^{3+} and Fe^{4+} standards, b) of the O-K edge for BSF, BSFA0.01, BSFA0.05, and BSFA0.1.

Hence, this aspect cannot be explained by the assumption of a purely ionic crystal, but by the results of EELS.

Table 3: Summary of average grain size areas (A_{gs}) and oxygen permeation flux (J_{O_2}) of sintered membranes at 900 °C.

membrane	A_{gs} [μm^2]	J_{O_2} [$\text{ml cm}^{-2} \text{s}^{-1}$]
BSF	166	0.61
BSFA0.01	75	0.76
BSFA0.05	146	0.83
BSFA0.1	10	0.98
BSFA0.2	0.41	0.55

In order to investigate the electronic structure, the iron $L_{2,3}$ - (Figure 3a) and oxygen K-edge (Figure 3b) were examined by EELS measurements. The iron $L_{2,3}$ -edge displays an electronic transition from the Fe-2p core orbitals to the partly unoccupied Fe-3d orbitals (energetic location displayed schematically in Feldhoff et al.⁵¹). The validity of the dipole selective rule in principle attributes the sensitivity of this measurement to the chemical environment of iron with respect to coordination, valence and spin configuration.⁵⁹ Figure 3a shows no significant changes of the overall shape and position of the iron $L_{2,3}$ -edge for the different BSFA samples. However, compared to standards for Fe^{4+}

($SrFeO_3$) and Fe^{3+} ($\alpha\text{-Fe}_2\text{O}_3$) all BSFA samples show a smaller FWHM of the L_3 white line. That indicates a mixed valence of Fe^{3+}/Fe^{4+} and a small energy difference between the intra-atomic exchange splitting and the cubic crystal field splitting, making a competition of iron high-spin and low-spin states likely. The presence of Fe^{2+} or Fe^{6+} can be excluded. The oxygen K-edge is caused by the transition of oxygen 1s orbitals into orbitals with oxygen 2p character. If the iron 3d orbitals are hybridized with the oxygen 2p ligand orbitals, the energy-loss near-edge structure of the oxygen K-edge also reflects the occupation of the iron 3d orbitals. That means the charge distribution between oxygen and iron is reflected in both the iron $L_{2,3}$ -edge and the oxygen K-edge.⁶⁰ Figure 3b displays the oxygen K-edge, which is separated into three parts: the low energy part A (525-532 eV), reflecting the hybridization of the oxygen 1s orbitals with the partly occupied iron 3d orbitals; a middle energy part B (532-547 eV), reflecting the hybridization of the oxygen 2p orbitals with the barium 4f, strontium 4d and aluminum 3p orbitals; and the high energy part C (above 547 eV), reflecting the hybridization with the empty iron 4sp band.^{51,61,62} The occurrence of the A peak of the O K-edge leads to the conclusion that there is a significant amount of covalency due to the iron 3d–oxygen 2p hybridization. As the formal valence of iron decreases, the occupation of the hybridized 3d orbitals with the oxygen 2p ligand is diminished. Therefore, the probability of exciting a core electron into these orbitals is lower. This is reflected in the peak area.^{63,64} The intensity ratio B/A follows from estimating the integral intensities in the energy-loss inter-

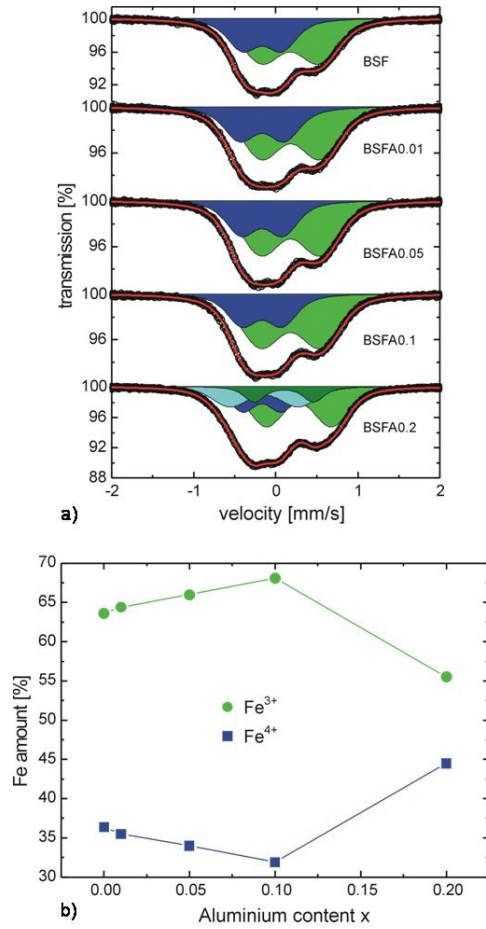


Figure 4: Mössbauer results a) room-temperature spectra of BSF, BSFA0.01, BSFA0.05, BSFA0.1, and BSFA0.2, b) variation of the amount of Fe³⁺ and Fe⁴⁺ cations in BSFA samples with respect to total iron content (\neq total B-site occupancy) as a function of Al content.

vals 532-547 eV and 525-532 eV. It increases from 4.55 (BSF) to 5.26 (BSFA0.1). Thus, the hybridization of Fe-3d with O-2p decreases slightly relatively to that of the other cations (Ba-4f, Sr-4d, Al-3p). Obviously aluminum takes part in the charge transfer, and thus, the covalent mixing of iron and oxygen orbitals decreases, leading to the extension of the lattice with increasing aluminum content.

The mixed Fe³⁺/Fe⁴⁺ valence state of iron can be quantified by Mössbauer spectroscopy. Figure 4a and Figure 4b show the Mössbauer room-temperature spectra of BSFA with $0 \leq x \leq 0.2$ and the variation of the amount of Fe³⁺ and Fe⁴⁺ cations in the BSFA samples as a function of aluminum content. The spectra of the BSF, BSFA0.01, BSFA0.05 and BSFA0.1 samples were fitted with two doublets, with

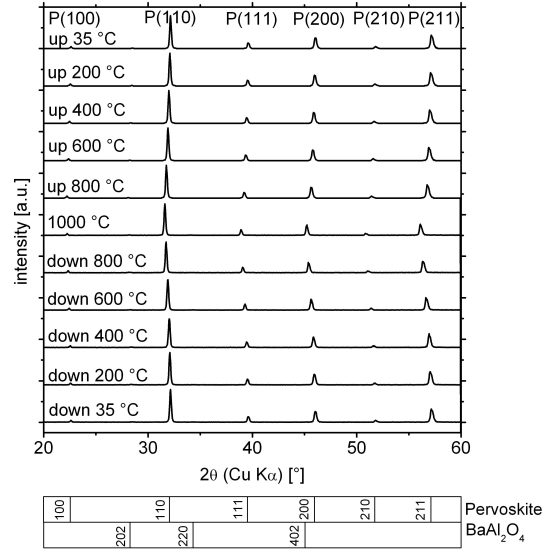


Figure 5: In situ X-ray diffraction data for BSFA0.1 (calcined at 950 °C for 10 h), heated up from 35 to 1000 °C and cooled down again in steps of 200 °C (heating rate 5 K/min) with an equilibrium time of 1/2 h in ambient air.

the values of isomer shift of -0.17 mm/s and 0.18 mm/s characteristic of tetravalent (Fe⁴⁺) and trivalent (Fe³⁺) cations, both in the high-spin state, respectively.^{51,65,66} Note that the isomer shift values corresponding to Fe⁴⁺ cations are in agreement with those reported for SrFe_{1-x}Al_xO_{3- δ} .⁴⁰ The spectrum of the BSFA0.2 sample, however, is not well fitted with only two subspectra. Based on the information that the sample contains more than one phase, we have fitted its spectrum with four components. The analysis of the spectrum revealed the presence of two nonequivalent sites for both Fe³⁺ and Fe⁴⁺ cations. The hyperfine parameters obtained by fitting the spectra of the (Ba_{0.5}Sr_{0.5})(Fe_{1-x}Al_x)O_{3- δ} samples are listed in Table 2. As shown in Table 2 and Figure 4b, the intensity of the doublet corresponding to Fe³⁺ cations increases monotonically with increasing Al-substitution. Thus, Al-addition increases the proportion of trivalent iron in (Ba_{0.5}Sr_{0.5})(Fe_{1-x}Al_x)O_{3- δ} , as it has already been observed for Ga-doped SrFeO_{3- δ} based phases⁶⁷ and similar compositions with tetravalent B-site dopants.^{43,68} The quadrupole splitting value characteristic of Fe³⁺ cations slightly increases with Al content, indicating greater disorder around Fe³⁺. Similarly as in the work of Waerenborgh et al.,⁴⁰ it can be assumed that the Al-doping leads to a localization of electron states around oxygen by introducing greater ionic character to the Fe-O-Fe network. In summary, Mössbauer results show Fe⁴⁺ and Fe³⁺ cations both in

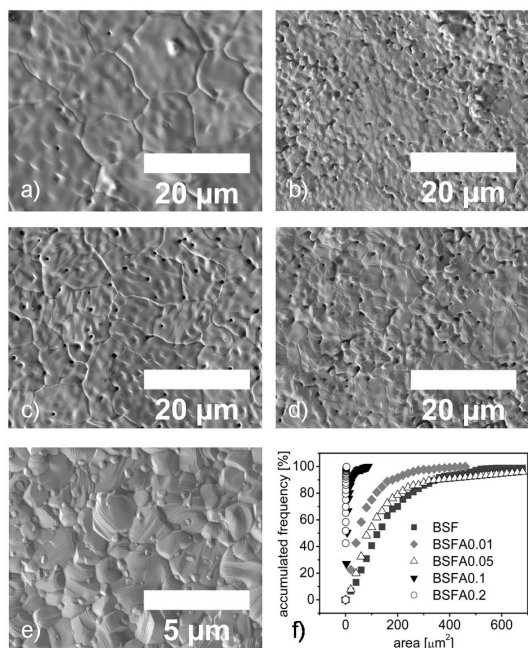


Figure 6: Scanning electron micrographs showing surfaces and grain size distributions at 1150 °C for 10 h of sintered membranes a) BSF, b) BSFA0.01, c) BSFA0.05, d) BSFA0.1, e) BSFA0.2 (note different scale), f) and grain size area distribution.

the high-spin state and greater disorder around Fe^{3+} , which - with respect to EELS - also can be interpreted as less covalent mixing of the iron d- and oxygen p-orbitals resulting in an expanded perovskite lattice.

Table 1 labels the weighted values for the crystallographic B-position in the perovskite lattice including aluminum. It is evident that the ratio of Fe^{3+} is almost constant. This leads to the conclusion that aluminum replaces predominantly Fe^{4+} in the lattice. There are two competing effects during the aluminum incorporation. First, Fe^{4+} and Al^{3+} have similar ionic radii, but the oxygen deficit has to be increased due to the lowering of charge. Second, Fe^{3+} and Al^{3+} have the same oxidation state, but different ionic radii. The second effect seems to be the weaker driving force, compared to the effect of the similar radius, hence most of the Al^{3+} replaces Fe^{4+} in the lattice. This causes a higher oxygen vacancy concentration, which is increased even more with rising temperature due to oxygen removal. The material might not be stable at higher temperatures and even collapse into brownmillerite phase with $\text{ABO}_{2.5}$ stoichiometry.⁶⁹ To examine the high temperature stability of the $(\text{Ba}_{0.5}\text{Sr}_{0.5})(\text{Fe}_{1-x}\text{Al}_x)\text{O}_{3-\delta}$ perovskites, in-situ XRD and TG/DTA measurements were conducted. The in-situ XRD measurements of BSFA0.1 are shown in Figure 5. The sample was heated up from 35 to 1000 °C and cooled down again in steps of 200 °C in

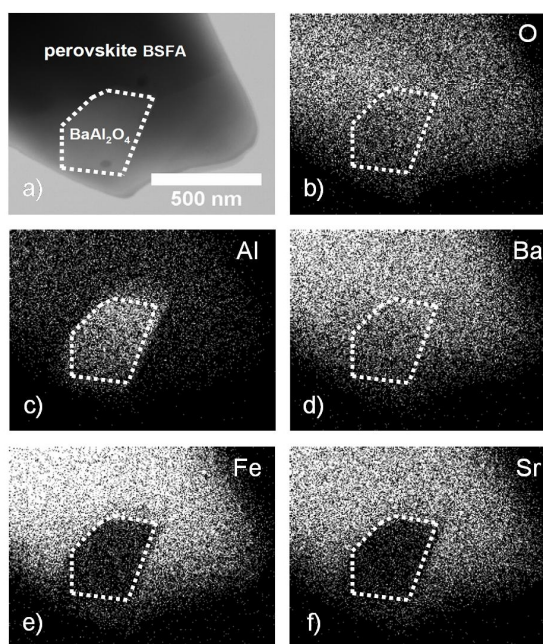


Figure 7: Scanning transmission electron micrograph of BSFA0.1 (a) and element distribution of b) oxygen, c) aluminum, d) barium, e) iron, and f) strontium.

ambient air. The cubic perovskite phase is stable over the whole temperature range. Due to the thermal expansion of the material, a shift of lattice parameters of 0.0063 nm is evident, and the CTE was determined to be $16 \times 10^{-6} \text{ K}^{-1}$.

TG/DTA measurements revealed that the perovskites are stable until 1350 °C. Above that temperature a decomposition slowly sets in, and the definitive melting points (T_{mp}) are between 1380 and 1400 °C ($T_{mp}(\text{BSF}) = 1381 \text{ °C}$, $T_{mp}(\text{BSFA0.01}) = 1392 \text{ °C}$, $T_{mp}(\text{BSFA0.05}) = 1389 \text{ °C}$, $T_{mp}(\text{BSFA0.1}) = 1399 \text{ °C}$, $T_{mp}(\text{BSFA0.2}) = 1356 \text{ °C}$). BSFA0.1 exhibits the highest stability. Due to the knowledge of the decomposition and melting points, the sinter temperature for the perovskite membranes could be chosen as high as 1150 °C. XRD measurements of the surfaces and fracture surfaces of the membranes were similar to those in Figure 1. Previous to oxygen permeation measurements, membranes were carefully checked for density, i.e., crack or channel formation, and depletion or accumulation of any element by SEM. Additionally, the grain size distribution and the correlation between grain size and oxygen permeation was investigated.

Figure 6 illustrates the scanning electron micrographs of the membrane surfaces and the grain size distributions of all synthesized perovskite powders. The membranes do not show cracks or channels, only some small pores are visible at the surface, which are

not connected throughout the membrane. This was evidenced by SEM of the fracture surfaces.

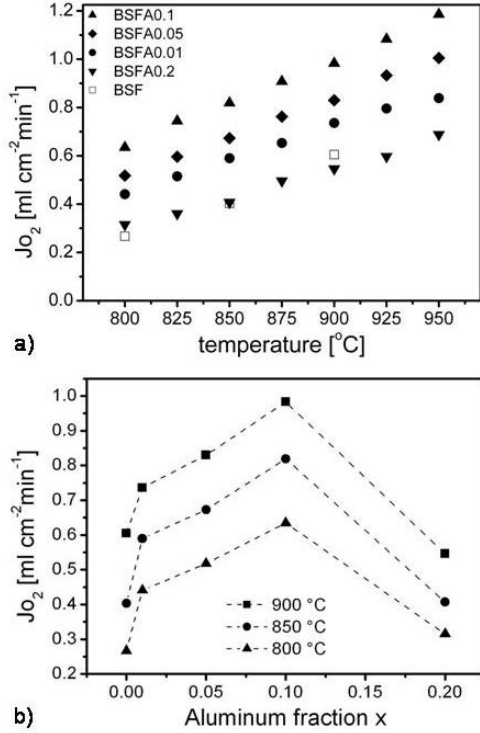


Figure 8: Oxygen permeation flux a) temperature dependence for BSF,⁷¹ BSFA0.01, BSFA0.05, BSFA0.1 and BSFA0.2, membrane thickness = 1.1 mm, b) for membranes with various aluminum fractions at different temperatures. The lines are guides for the eye and indicate a maximum at an Al fraction of 0.1.

Grain size distribution was the same for surfaces and fracture surfaces for each kind of membrane. This was already demonstrated for $(\text{Ba}_{0.5}\text{Sr}_{0.5})(\text{Fe}_{0.8}\text{Zn}_{0.2})\text{O}_{3-\delta}$ and $(\text{Ba}_{0.5}\text{Sr}_{0.5})(\text{Co}_{0.8}\text{Fe}_{0.2})\text{O}_{3-\delta}$.⁷⁰ Table 3 summarizes the average grain size areas A_{gs} and shows that they are very different for the BSFA membranes and do not correlate with the aluminum doping. Membranes of BSF have the biggest A_{gs} with 166 μm . Grain sizes for the pure phases BSFA0.01 and BSFA0.05 are increasing and decreasing again as soon as impurities are formed for BSFA0.1 and BSFA0.2. The formation of the other phases inhibits the grain growth. Since mappings by EDXS of the surfaces and fracture surfaces showed a homogeneous distribution of all elements without any depletion or accumulation, they are not presented here. The quantification confirms the stoichiometries $(\text{Ba}_{0.5}\text{Sr}_{0.5})(\text{Fe}_{1-x}\text{Al}_x)\text{O}_{3-\delta}$ with $0 \leq x \leq 0.2$, respectively. Hence, a BSFA0.1 and a BSFA0.2 membrane were prepared for TEM. We were

interested in seeing if the impurities are located in the grain boundaries or as separate particles. Figure 7 shows a transmission electron micrograph of BSFA0.1 and the element distribution of oxygen, aluminum, barium, iron, and strontium. The impurity phases were found to be located as separated grains between the perovskite grains. The higher aluminum fraction of the BaAl_2O_4 can be seen in Figure 7c. Figure 7e and f show a weak signal of iron and strontium for the BaAl_2O_4 phase, which was quantified as a small solubility of 3 % strontium of the barium site and 8 % iron of the aluminum site. The latter was also reported by Yaremchemko et al. for a iron solubility in SrAl_2O_4 below 5 % of the aluminum sites and by Kharton et al. below 7 %.^{32,42} The perovskite in BSFA0.1 and BSFA0.2 was quantified as $(\text{Ba}_{0.48}\text{Sr}_{0.52})(\text{Fe}_{0.91}\text{Al}_{0.09})\text{O}_{3-\delta}$ with slight deviations very close to impurity grains.

For an impression of the application of BSFA materials, the oxygen permeation behavior was investigated. The oxygen permeation results are displayed in Figure 8. Figure 8a shows the temperature dependence for membranes with different aluminum fractions in comparison to the data of a BSF membrane measured by Chen et al.⁷¹ The oxygen permeation increases with rising Al content from 0 to 0.1 to a maximum of $1.19 \text{ ml cm}^{-2} \text{ s}^{-1}$ at 950 $^{\circ}\text{C}$ and decreases again for BSFA0.2 to values comparable to BSF. The change in oxygen permeation for membranes with varying aluminum fractions at different temperatures is presented in Figure 8b. The maximum for BSFA0.1 demonstrates that the very small impurity of 3.3 % does not disturb the oxygen transport through the membranes, but a higher impurity content of 14 % (BSFA0.2) leads to a decrease in oxygen permeation.

We also found that the grain size is not directly correlated with oxygen permeation (Table 3). Oxygen permeation depends primarily on the materials composition. In spite of the reduction in grain size from BSF to BSFA0.01 the oxygen permeation rises, but with increasing grain size from BSFA0.01 to BSFA0.05 a further rise in permeation is observed. Due to the impurity in BSFA0.1 the grain growth was inhibited, but the permeation increases even more. Further measurements for oxygen permeation dependence on grain size are required to draw final conclusions. The BSFA0.1 membranes show high oxygen permeation in comparison to the currently known perovskite membranes labeled in Table 4. Among the Fe and Al containing membranes, they have the highest oxygen permeation. Only $(\text{Ba}_{0.5}\text{Sr}_{0.5})(\text{Co}_{0.8}\text{Fe}_{0.2})\text{O}_{3-\delta}$, the current state-of-the-art material above 900 $^{\circ}\text{C}$, reaches higher values.¹ However, in the intermediate temperature range the novel aluminum doped perovskite BSFA0.1 is expected to show a better performance in application than the cobalt containing BSCF due to an improved long-time stability preserved by a less flexible redox behavior and a stable high-spin configuration of iron.

Table 4: Oxygen permeation flux across different membranes with iron and aluminum at the B-site compared to other perovskite materials containing barium on the A-site of the lattice. Values marked with * are extrapolated with the assumption of linearity. ** not stable for long time (≥ 300 h).¹⁹⁻²¹

perovskite membranes	thickness [mm]	oxygen permeation flux at [ml cm ⁻² s ⁻¹]			
		800 °C	850 °C	900 °C	950 °C
(Ba _{0.5} Sr _{0.5})(Fe _{1-x} Al _x)O _{3-δ} (x = 0.1)	1.1	0.63	0.82	0.98	1.19
Sr(Fe _{1-x} Al _x)O _{3-δ} (x = 0.3) ³⁶	1.0	0*	0.05	0.13	0.20
(La _{0.3} Sr _{0.7})(Fe _{1-x} Al _x)O _{3-δ} (x = 0.2) ³⁵	1.0	0.05	0.08	0.13	0.21
(Ba _{0.5} Sr _{0.5})(Fe _{0.8} Zn _{0.2})O _{3-δ} ⁵⁰	1.15	0.49	0.65	0.80	0.96
(Ba _{0.5} Sr _{0.5})(Co _{0.8} Fe _{0.2})O _{3-δ} ¹⁹	1.5	0.92**	1.18**	1.39	1.57
Ba(Co _x Fe _y Zr _z)O _{3-δ} (x + y + z = 1) ⁷²	1.0	0.5	0.6	0.7	0.8*

4 Conclusions

The systematic aluminum doping of (Ba_{0.5}Sr_{0.5})(Fe_{1-x}Al_x)O_{3-δ} was conducted in the range of 0 < x ≤ 0.2 with regard to the calculation of the tolerance factors. With XRD, the perovskite phase in all synthesized oxides was found to be cubic perovskite, and the highest aluminum fraction for a formation of pure cubic perovskite without any impurities was in the range of x = 0.09-0.1. In the BSFA0.1 powder a minor impurity (3.3 %) of BaAl₂O₄ was determined by Rietveld refinements, and for BSFA0.2 two impurities were found and identified as BaAl₂O₄ and Ba₃Al₂O₆. The impurity phases are located as separated grains between the perovskite grains (TEM). Because of the smaller ionic radius of aluminum, the lattice parameters were expected to decrease. However, the reverse was found by XRD. EELS together with Mössbauer spectroscopy revealed that, with the increasing replacement of iron with aluminum at the B-position of the perovskite (x ≤ 0.1), a higher fraction of Fe³⁺ instead of Fe⁴⁺ is observed and due to the decreased covalent mixing of the iron 3d and oxygen 2p orbitals the lattice expands. Fe⁴⁺ is predominantly substituted by Al³⁺ due to their similar ionic radii, but with this substitution the oxygen deficit has to be increased. This results in a higher oxygen vacancy concentration, which might cause instability of the material at higher temperatures. However, in-situ XRD and TG/DTA measurements reveal high temperature stability up to 1350 °C. The oxygen permeation increases with rising Al content from 0 to 0.1 to a maximum of 1.19 ml cm⁻² s⁻¹ at 950 °C and decreases again for BSFA0.2 to values comparable to BSF. The maximum for BSFA0.1 demonstrates that the very small impurity does not disturb the oxygen transport through the membranes. We also found that the oxygen permeation is primarily dependent on the materials composition, since the grain size is not directly correlated with the oxygen

permeation. The BSFA0.1 membranes show very high oxygen permeation, in comparison to the currently known perovskite membranes. Additionally, among the iron and aluminum containing membranes they have the highest oxygen permeation. Due to an improved long-time stability preserved by a less flexible redox behavior and a stable high-spin configuration of iron, a good performance in the intermediate temperature range, where cobalt containing perovskites have serious stability problems, is expected in application.

Acknowledgment The authors greatly acknowledge financial support by DFG grant number FE 928/1-2. Fruitful discussions with Prof. Jürgen Caro are appreciated. One of the authors (V.Š.) thanks the APVV (Project 0728-07) and VEGA (2/0065/08) for their support of his work.

References

- (1) Merkle, R.; Maier, J.; Bouwmeester, H.J.M., *Angew. Chem. Int. Ed.* **2004**, *43*, 5069-5073.
- (2) Sunarso, J.; Baumann, S.; Serra, J.M.; Meulenberg, W.A.; Liu, S.; Lin, Y.S.; Diniz da Costa, J.C., *J. Membr. Sci.* **2008**, *320*, 13-41.
- (3) Liu, M.; Joshi, V.; Shen, Y.; Krist, K., *US Patent* **1993**, 5,273,628.
- (4) Balachandran, U.; Dusek, J.T.; Mieville, R.L.; Poeppel, R.B.; Kleefisch, M.S.; Pei, S.; Kobylinski, T.P.; Udovich, C.A.; Bose, A.C., *Appl. Catal. A* **1995**, *133*, 19-29.
- (5) Wang, H.; Cong, Y.; Yang, W., *J. Membr. Sci.* **2002**, *209*, 143-152.
- (6) Wang, H.; Cong, Y.; Zhu, X.; Yang, W., *React. Kinet. Catal. Lett.* **2003**, *79*, 351-356.

- (7) Hamel, C.; Seidel-Morgenstern, A.; Schiestel, T.; Werth, S.; Wang, H.; Tablet, C.; Caro, J., *AICHE J.* **2006**, *52*, 3118-3125.
- (8) Wang, H.; Werth, S.; Schiestel, T.; Caro, J., *Angew. Chemie Int. Ed.* **2005**, *44*, 6906-6909.
- (9) Yokokawa, H.; Sakai, N.; Kawada, T.; Dokiya, M., *Solid State Ionics* **1992**, *52*, 43-56.
- (10) Shao, Z.; Haile, S., *Nature* **2004**, *431*, 170-173.
- (11) Esquirol, A.; Brandon, N.P.; Kilner, J.A.; Mogenssen, M., *J. Electrochem. Soc.* **2004**, *151*, A1847-A1855.
- (12) Tao, S.; Irvine, J.T.S., *Adv. Mater.* **2006**, *18*, 1581-1584.
- (13) Fu, Q.X.; Tietz, F.; Stöver, F., *J. Electrochem. Soc.* **2006**, *153*, D74-D83.
- (14) Hsu, M.-F.; Wu, L.-J.; Wu, J.-M.; Shiu, Y.-H.; Lin, K.-F., *Electrochem. Solid-State Lett.* **2006**, *9*, A193-A195.
- (15) Wang, H.; Cong, Y.; Yang, W., *Chem. Comm.* **2002**, 1468-1469.
- (16) Vente, J.; McIntosh, S.; Haije, W.; Bouwmeester, H.J.W., *React. Kinet. Catal. Lett.* **2003**, *79*, 351-356.
- (17) Steele, C.; Heinzl, A., *Nature* **2001**, *414*, 345-352.
- (18) Martynczuk, J.; Arnold, M.; Wang, H.; Caro, J.; Feldhoff, A., *Adv. Mater.* **2007**, *19*, 2134-2140.
- (19) Shao, Z.; Yang, W.; Cong, Y.; Dong, H.; Tong, J.; Xiong, G., *J. Membr. Sci.* **2000**, *172*, 177-188.
- (20) Arnold, M.; Gesing, T.M.; Martynczuk, J.; Feldhoff, A., *Chem. Mater.* **2008**, *20*, 5851-5858.
- (21) Švarcová, S.; Wiik, K.; Tolchard, J.; Bouwmeester, H. J. M.; Grande, T., *Solid State Ionics* **2008**, *178*, 1787-1791.
- (22) Arnold, M.; Xu, Q.; Tichelaar, F.; Feldhoff, A., *Chem. Mater.* **2008**, *submitted*.
- (23) Teraoka, Y.; Shimokawa, H.; Kang, C.; Kusaba, H.; Sasaki, K., *Solid State Ionics* **2006**, *177*, 2245-2248.
- (24) McIntosh, S.; Vente, J.; Haije, W.; Blank, D.; Bouwmeester, H.J.W., *Chem. Mater.* **2006**, *18*, 2187-2193.
- (25) Vente, J.; Haije, W.; Rak, Z., *J. Membr. Sci.* **2006**, *276*, 178-184.
- (26) Holc, J.; Kušcer, D.; Hrovat, M.; Bernik, S.; Kolar, D., *Solid State Ionics* **1997**, *95*, 259-268.
- (27) Ciambelli, P.; Cimino, S.; Lasorella, G.; Lisi, L.; De Rossi, S.; Faticanti, M.; Minelli, G.; Porta, P., *Appl. Catal., B* **2002**, *37*, 231-241.
- (28) Park, H.J.; Choi, G.M., *Solid State Ionics* **2004**, *175*, 399-403.
- (29) Cihlar, J.; DelFavero, D.; Cihlar Jr., J.; Buchal, A.; Van herle, J., *J. Eur. Ceram. Soc.* **2006**, *26*, 2999-3004.
- (30) Kajitani, M.; Matsuda, M.; Miyake, M., *Solid State Ionics* **2007**, *178*, 355-358.
- (31) Urasaki, K.; Fukuda, Y.; Sekine, Y.; Matsukata, M.; Kikuchi, E., *J. Jpn. Pet. Inst.* **2008**, *51(2)*, 83-87.
- (32) Kharton, V.V.; Shaula, A.L.; Snijkers, F.M.M.; Cooymans, J.F.C.; Luyten, J.J.; Marozau, I.P.; Viskup, A.P.; Marques, F.M.B.; Frade, J.R., *J. Eur. Ceram. Soc.* **2006**, *26*, 3695-3704.
- (33) Kharton, V.V.; Waerenborgh, J.C.; Viskup, A.P.; Yakovlev, S.O.; Patrakeeve, M.V.; Gaczyński, P.; Marozau, I.P.; Yaremchenko, A.A.; Shaula, A.L.; Samakhval, V.V., *J. Solid State Chem.* **2006**, *179*, 1273-1284.
- (34) Dunyushkina, L.A.; Gorbunov, V.A.; Babkina, A.A.; Esina, N.O., *Ionics* **2003**, *9*, 67-70.
- (35) Yaremchenko, A.A.; Patrakeeve, M.V.; Kharton, V.V.; Marques F.M.B.; Leonidov, I.A.; Kozhevnikov, V.L., *Solid State Sci.* **2004**, *6*, 357-366.
- (36) Shaula, A.L.; Kharton, V.V.; Vyshatko, N.P.; Tsipis, E.V.; Patrakeeve, M.V.; Marques, F.M.B.; Frade, J.R., *J. Eur. Ceram. Soc.* **2005**, *25*, 489-499.
- (37) Kharton, V.V.; Tsipis, E.V.; Yaremchenko, A.A.; Marozau, I.P.; Viskup, A.P.; Frade, J.R.; Naumovich, E.N., *Mater. Sci. Eng., B* **2006**, *134*, 80-88.
- (38) Dong, X.; Xu, Z.; Chang, X.; Zhang, C.; Jin, W., *J. Am. Ceram. Soc.* **2007**, *90 [12]*, 3923-3929.
- (39) Takamura, H.; Enomoto, K.; Aizumi, Y.; Kamegawa, A.; Okada, M., *Solid State Ionics* **2004**, *175*, 379-382.
- (40) Waerenborgh, J.C.; Rojas, D.P.; Shaula, A.L.; Mather, G.C.; Patrakeeve, M.V.; Kharton, V.V.; Frade, J.R., *Mater. Lett.* **2005**, *59*, 1644-1648.
- (41) Kharton, V.V.; Shaula, A.L.; Snijkers, F.M.M.; Cooymans, J.F.C.; Luyten, J.J.; Yaremchenko, A.A.; Valente, A.A.; Tsipis, E.V.; Frade, J.R.; Marques, F.M.B.; Rocha, J., *J. Membr. Sci.* **2005**, *252*, 215-225.

- (42) Yaremchenko, A.A.; Kharton, V.V.; Shaula, A.L.; Snijkers, F.M.M.; Cooymans, J.F.C.; Luyten, J.J.; Marques, F.M.B., *J. Electrochem. Soc.* **2006**, *153*(6), J50-J60.
- (43) Patrakeev, M.V.; Kharton, V.V.; Bakhteeva, Yu.A.; Shaula, A.L.; Leonidov, I.A.; Kozhevnikov, V.L.; Naumovich, E.N.; Yaremchenko, A.A.; Marques, F.M.B., *Solid State Sci.* **2006**, *8*, 476-487.
- (44) Naumovich, E.N.; Patrakeev, M.V.; Kharton, V.V.; Islam, M.S.; Yaremchenko, A.A.; Frade, J.R.; Marques, F.M.B., *Solid State Ionics* **2006**, *177*, 457-470.
- (45) Marozau, I.P.; Kharton, V.V.; Viskup, A.P.; Frade, J.R.; Samakhval, V.V., *J. Eur. Ceram. Soc.* **2006**, *26*, 1371-1378.
- (46) Ancharova, U.V.; Ancharov, A.I.; Lyakhov, N.Z.; Nemudry, A.P.; Pyatiletova, E.B.; Savinskaya, O.A.; Tsybulya, S.V., *Nucl. Instrum. Methods Phys. Res., Sect. A* **2007**, *575*, 144-148.
- (47) Feldhoff, A.; Martynczuk, J.; Wang, H., *Prog. Solid State Chem.* **2007**, *35*, 339-353.
- (48) Arnold, M.; Wang, H.; Martynczuk, J.; Feldhoff, A., *J. Am. Ceram. Soc.* **2007**, *90*[11], 3651-3655.
- (49) Lagarec, K.; Rancourt, D. G., *Recoil - Mossbauer Spectral Analysis Software for Windows, version 1.02*, Department of Physics, University of Ottawa: Ottawa, ON, **1998**.
- (50) Martynczuk, J.; Arnold, M.; Feldhoff, A., *J. Membr. Sci.* **2008**, *322*, 375-382.
- (51) Feldhoff, A.; Martynczuk, J.; Arnold, M.; Mynydyk, M.; Bergmann, I.; Šepelák V.; Gruner, W.; Vogt, U.; Hähnel, A.; Woltersdorf, J., *J. Am. Ceram. Soc.* **2008**, *submitted*.
- (52) Wang, H.; Tablet, C.; Feldhoff, A.; Caro, J., *J. Membr. Sci.* **2005**, *262*, 20-26.
- (53) Shannon, R.D.; *Acta Crystallogr., Sect. A: Found. Crystallogr.* **1976**, *32*, 751-767.
- (54) Goldschmidt, V.M., *Naturwissenschaften* **1926**, *14*, 477-485.
- (55) Anderson, M.T.; Greenwood, K.B.; Taylor, G.A.; Poepfelmeier, K.R., *Prog. Solid State Chem.* **1993**, *22*, 197-233.
- (56) Davies, P.K.; Wu, H.; Borisevich, A.Y.; Molodetsky, I.E.; Farber, L., *Annu. Rev. Mater. Res.* **2008**, *38*, 369-401.
- (57) Arlett, R.H.; White, J.G.; Robbins M., *Acta Cryst.* **1967**, *22*, 315.
- (58) Hilpert, K.; Beske, H.; Naoumidis, A., *High Temp. Sci.* **1975**, *7*(3), 159-166.
- (59) Egerton, R.F.; *Electron energy-loss spectroscopy in the transmission electron microscope*, Plenum Press, New York, London **1986**.
- (60) Groot, de F.M.F.; Grioni, M.; Fuggle, J.C.; Ghijssen, J.; Sawatzky, G.A.; Petersen, H., *Phys. Rev. B*, **1989**, *40*, 5715-5723.
- (61) Samantaray, C.B.; Sim, H.; Hwang, H., *Appl. Surf. Sci.* **2005**, *242*, 1211-1218.
- (62) Sasaki, T.; Mizoguchi, T.; Matsunaga, K.; Tanaka, S.; Yamamoto, T.; Kohyama, M.; Ikuhara, Y., *Appl. Surf. Sci.* **2005**, *241*, 8790.
- (63) Gloter, A.; Ingrin, J.; Bouchet, D.; Colliex, C., *Phys. Rev. B*, **2000**, *61*, 2587-2594.
- (64) Colliex, C.; Manoubi, T.; Ortiz, C., *Phys. Rev. B*, **1991**, *44*, 11402-11411.
- (65) Menil, F., *J. Phys. Chem. Solids* **1985**, *46*, 763-789.
- (66) Parish, R., *NMR, NQR, EPR, and Mössbauer spectroscopy in inorganic chemistry* Ellis Horwood, New York, Berlin, p.133 **1990**.
- (67) Patrakeev, M.V.; Mitberg, E.B.; Lakhtin, A.A.; Leonidov, I.A.; Kozhevnikov, V.L.; Kharton, V.V.; Avdeev, M.; Marques, F.M.B., *J. Solid State Chem.* **2002**, *167*, 203-213.
- (68) Adler, P.; Eriksson, S., *Z. Anorg. Allg. Chem.* **2000**, *626*, 118-124.
- (69) McIntosh, S.; Vente, J.F.; Haije, W.G.; Blank, D.H.A.; Bouwmeester, H.J.M., *Solid State Ionics* **2006**, *177*, 833-842.
- (70) Arnold, M.; Martynczuk, J.; Efimov, K.; Wang, H.; Feldhoff, A., *J. Membr. Sci.* **2007**, *316*, 137-144.
- (71) Chen, Z.; Ran, R.; Zhou, W.; Shao, Z.; Liu, S., *Electrochim. Acta.* **2007**, *52*, 7343-7351.
- (72) Wang, H.; Schiestel, T.; Tablet, C.; Schroeder, M.; Caro, J., *Solid State Ionics* **2006**, *177*, 2255-2259.

Publications and Conferences

Publications included in the thesis (reversed chronological order)

- (1) Aluminum doped perovskites as high performance oxygen permeation materials
J. Martynczuk, F. Liang, M. Arnold, V. Šepelák, and A. Feldhoff
Chemistry of Materials (**submitted**).
- (2) Spin-state transition of iron in $(\text{Ba}_{0.5}\text{Sr}_{0.5})(\text{Fe}_{0.8}\text{Zn}_{0.2})\text{O}_{3-\delta}$ perovskite
A. Feldhoff, J. Martynczuk, M. Arnold, M. Myndyk, I. Bergmann, V. Šepelák,
W. Gruner, U. Vogt, A. Hähnel, and J. Woltersdorf
Journal of the American Ceramic Society (**submitted**).
- (3) Influence of grain size on the oxygen permeation performance of perovskite-type
 $(\text{Ba}_{0.5}\text{Sr}_{0.5})(\text{Fe}_{0.8}\text{Zn}_{0.2})\text{O}_{3-\delta}$ membranes
J. Martynczuk, M. Arnold, and A. Feldhoff
Journal of Membrane Science **322**, 375-382 (**2008**).
- (4) The sol-gel synthesis of perovskites by an EDTA/citrate complexing method in-
volves nanoscale solid state reactions
A. Feldhoff, M. Arnold, J. Martynczuk, Th.M. Gesing, and H. Wang
Solid State Sciences **10**, 689-701 (**2008**).
- (5) Grain boundaries as barrier for oxygen transport in perovskite-type membranes
M. Arnold, J. Martynczuk, K. Efimov, H. Wang, and A. Feldhoff
Journal of Membrane Science **316**, 137-144 (**2008**).
- (6) How $(\text{Ba}_{0.5}\text{Sr}_{0.5})(\text{Fe}_{0.8}\text{Zn}_{0.2})\text{O}_{3-\delta}$ and $(\text{Ba}_{0.5}\text{Sr}_{0.5})(\text{Co}_{0.8}\text{Fe}_{0.2})\text{O}_{3-\delta}$ perovskites form
via an EDTA/citric acid complexing method
J. Martynczuk, M. Arnold, H. Wang, J. Caro, and A. Feldhoff
Advanced Materials **19**, 2134-2140 (**2007**).

Publications not included in the thesis

- (7) Long-time permeation performance of $(\text{Ba}_{0.5}\text{Sr}_{0.5})(\text{Fe}_{0.8}\text{Zn}_{0.2})\text{O}_{3-\delta}$ at intermediate temperatures and under CO_2 atmosphere
J. Martynczuk, L. Robben, and A. Feldhoff
(in preparation).
- (8) Crystalline intermediate phases in the sol gel-based synthesis of $\text{La}_2\text{NiO}_{4+\delta}$
K. Efimov, M. Arnold, J. Martynczuk, and A. Feldhoff
Journal of the American Ceramic Society (accepted).
- (9) Correlation of the formation and the decomposition process of the BSCF perovskite at intermediate temperatures
M. Arnold, Th.M. Gesing, J. Martynczuk, and A. Feldhoff
Chemistry of Materials **20**, 5851-5858 (2008).
- (10) In situ study of the reaction sequence in the sol-gel synthesis of a $(\text{Ba}_{0.5}\text{Sr}_{0.5})(\text{Co}_{0.8}\text{Fe}_{0.2})\text{O}_{3-\delta}$ perovskite by X-ray diffraction and transmission electron microscopy
M. Arnold, H. Wang, J. Martynczuk, and A. Feldhoff
Journal of the American Ceramic Society **90**, 3651-3655 (2007).
- (11) Advanced $\text{Ba}_{0.5}\text{Sr}_{0.5}\text{Zn}_{0.2}\text{Fe}_{0.8}\text{O}_{3-\delta}$ perovskite-type ceramics as oxygen selective membranes: Evaluation of the synthetic process
A. Feldhoff, J. Martynczuk, and H. Wang
Progress in Solid State Chemistry **35**, 339-353 (2007).
- (12) The effect of grain size and grain boundary microstructure on the oxygen permeation of perovskite-type membranes
J. Martynczuk, H. Wang, and A. Feldhoff
Proceedings of the 10th ECerS Conference, Berlin, 17 to 21 June 2007, (ed. by J.G. Heinrich, C. Aneziris), pp. 910-912, ISBN 3-87264-022-4, Göller Verlag, Baden-Baden, Germany (2007).
- (13) Influence of processing conditions on the microstructure and function of $(\text{Ba}_{0.5}\text{Sr}_{0.5})(\text{Fe}_{0.8}\text{Zn}_{0.2})\text{O}_{3-\delta}$ membranes
J. Martynczuk, H. Wang, M. Arnold, and A. Feldhoff
Proceedings of the 9th International Conference on Inorganic Membranes (ICIM9), Lillehammer, 25.-29. July 2006, (ed. by R. Bredesen, H. Raeder), pp. 503-506, ISBN 978-82-14-04026-5, SINTEF, Blindern, Norway (2006).

Contributions to Conferences

- (1) Crystalline intermediate phases in the sol-gel synthesis of the mixed ionic-electronic conductor $\text{La}_2\text{NiO}_{4+\delta}$ studied by transmission electron microscopy and X-ray diffraction
K. Efimov*, M. Arnold, J. Martynczuk, and A. Feldhoff
Electroceramics XI, Manchester, UK, 1st - 4rd September (**2008**) (Poster).
- (2) Valence stability of polyvalent cations in oxygen semi-permeable perovskites
A. Feldhoff*, M. Arnold, and J. Martynczuk
2nd International Congress on Ceramics (ICC2), Verona, Italy, 29th June - 4th July (**2008**) (Talk).
- (3) Reaction sequences in the sol gel-based formation of mixed-conducting oxides of complex stoichiometries for oxygen separation membranes
A. Feldhoff*, M. Arnold, J. Martynczuk, and K. Efimov
International Materials Research Conference (IMRC2008), Chongqing, China, 9th - 12th June (**2008**) (Talk).
- (4) The effect of grain size and grain boundary microstructure on the oxygen permeation of perovskite-type membranes
J. Martynczuk*, M. Arnold, H. Wang, and A. Feldhoff
Eidgenössische Materialprüfanstalt (EMPA), Dübendorf, 28th September (**2007**) (Talk).
- (5) Analytical TEM study of the formation of perovskite-type oxides by the EDTA/citrate complexing method
A. Feldhoff*, M. Arnold, and J. Martynczuk
2007 E-MRS Fall Meeting, Warsaw, Poland, 17th - 21st September (**2007**) (Talk).
- (6) Tuning the functional properties of perovskite-type oxygen permeation membranes by advanced powder processing
J. Martynczuk*, M. Arnold, H. Wang, and A. Feldhoff
Euromat 2007, Nuremberg, Germany, 9th - 14th September (**2007**) (Oral Poster).
- (7) The effect of grain size and grain boundary microstructure on the oxygen permeation of perovskite-type membranes
J. Martynczuk*, H. Wang, and A. Feldhoff
10th International Conference and Exhibition of the European Ceramic Society (ECerS), Berlin, Germany, 17th - 21st June (**2007**) (Talk).

- (8) In situ study of the reaction sequence in the sol-gel synthesis of the $(\text{Ba}_{0.5}\text{Sr}_{0.5})(\text{Co}_{0.8}\text{Fe}_{0.2})\text{O}_{3-\delta}$ perovskite
M. Arnold*, J. Martynczuk, H. Wang, and A. Feldhoff
10th International Conference and Exhibition of the European Ceramic Society (ECerS), Berlin, Germany, 17th - 21st June (**2007**) (Talk).
- (9) Local in situ study of charge disproportion in mixed-conducting perovskite ceramics
A. Feldhoff*, I. Bergmann, V. Šepelák, J. Martynczuk, M. Arnold, and H. Wang
10th International Conference and Exhibition of the European Ceramic Society (ECerS), Berlin, Germany, 17th - 21st June (**2007**) (Talk).
- (10) In situ HR-EELS of cobalt and iron valence in a complex perovskite for oxygen separation membranes
A. Feldhoff*, J. Martynczuk, M. Arnold, and H. Wang
99th Bunsen colloquium, Eberbach, Germany, 7th - 8th June (**2007**) (Talk).
- (11) The soft chemical formation of $(\text{Ba}_{0.5}\text{Sr}_{0.5})(\text{Fe}_{0.8}\text{Zn}_{0.2})\text{O}_{3-\delta}$ perovskite studied by analytical TEM
J. Martynczuk*, M. Arnold, H. Wang, and A. Feldhoff
5. Workshop für EELS/EFTEM 2006, EF - EELS Arbeitskreistreffen der Deutschen Gesellschaft für Elektronenmikroskopie (DGE), Vienna, Austria, 27th - 29th September (**2006**) (Poster).
- (12) Influence of processing conditions on the microstructure and function of $(\text{Ba}_{0.5}\text{Sr}_{0.5})(\text{Fe}_{0.8}\text{Zn}_{0.2})\text{O}_{3-\delta}$ - membranes
J. Martynczuk*, H. Wang, M. Arnold, and A. Feldhoff
9th International Conference on Inorganic Membranes (ICIM9), Lillehammer, Norway, 25th - 29th July (**2006**) (Poster, Young scientist award).

List of Figures

1.1	World energy demand (in Mtoe: Million tonnes of oil equivalent) expands by 45% between now and 2030 with an average rate of increase of 1.6% per year [1].	2
1.2	Structure of perovskite-type oxide.	3
1.3	Perspective view of perovskite structure, a) ideal cubic perovskite, b) distorted perovskite with tilted BO_6 octahedra $t < 1$ [31].	4
1.4	Perovskite structures viewed along (110): a) Ideal cubic with cubic close packing of AO_3 layers and resultant corner sharing of BO_6 octahedra, b) $t > 1$, cubic (c) and hexagonal (h) layers are indicated (A cations are omitted for clarity) [31].	5
1.5	Flow chart of the sol-gel synthetic process for the perovskite preparation.	7
1.6	EDX spectra monitoring the decrease of nitrogen and oxygen content of the gel.	8
1.7	Schematic diagram showing the mechanism of formation of tridymite, spinel and ZnO between spinel and carbonate (phase boundaries in black).	9
1.8	Mechanisms during the sintering. Only 1 to 3 lead to densification, but all cause the necks to grow and so influence the rate of densification [41].	10
1.9	Equilibrium shape of a pore in a polycrystalline solid [41].	11
1.10	Oxygen vacancy V_{O} in the perovskite structure (a) and the mechanism for the oxygen transport through change of places (b).	12
1.11	Principle of oxygen permeation through a perovskite membrane. $\nabla\mu_{\text{O}_2}$ is the chemical potential gradient between the air side with high oxygen partial pressure p_A and the permeation side with low oxygen partial pressure p_P . The chemical potential on the air side $\mu_{\text{O}_2}^A$ is much higher than on the permeation side ($\mu_{\text{O}_2}^P$).	13
1.12	Oxygen permeation measurement setup for disc membranes with the high-temperature permeation cell (left), the closer look on the membrane and the sealing (middle) and a disc membrane and the on-line gas chromatograph (right).	15
1.13	Schematic diagram for the diffusion through a ceramic with scarcely permeable grain boundaries with oxygen diffusion along vacancies in the crystal lattice (intracrystalline) (a) or highly permeable grain boundaries with oxygen diffusion along grain boundaries (intercrystalline) (b).	16

Curriculum vitae

Personal data

Date of birth	19 March 1981
Place of birth	Hannover, Germany
Nationality	German
Marital status	Unmarried, no children

Awards

06/2008	Zonta Award for Young Scientists Award for excellent scientific performance and outstanding voluntary service, Zonta International, Hannover
07/2006	Young Scientist Award Best poster presentation at the 9th International Conference on Inorganic Membranes (ICIM9), Lillehammer, Norway

Higher Education

01/2008	Swiss Federal Laboratories for Materials Testing and Research (EMPA) Research visit at the group of Ph.D. Thomas Graule, Laboratory for High Performance Ceramics
since 01/2006	Leibniz Universität Hannover Scientific assistant at the group of Prof. Dr. Caro, Institute of Physical Chemistry and Electrochemistry
04/2005 - 11/2005	Leibniz Universität Hannover Diploma thesis together with Prof. Dr. Caro: „Herstellung, Mikrostruktur und Eigenschaften von Perowskitmembranen zur Sauerstoffabtrennung“, mark: excellent
10/2000 - 11/2005	Leibniz Universität Hannover Student of chemistry Degree: Diplom-Chemiker, mark: excellent

Education

08/1993 - 06/2000	St. Ursula-Schule High school , Hannover Intensive courses: chemistry and mathematics Degree: Abitur, mark: 1.6
08/1991 - 06/1993	Ludwig-Windthorst-Schule Middle school , Hannover
07/1987 - 07/1991	Grundschule In den Sieben Stücken Elementary school , Hannover

Erklärung zur Dissertation

Hierdurch erkläre ich, dass ich die vorliegende Arbeit selbstständig verfasst, alle benutzten Hilfsmittel sowie evtl. zur Hilfeleistung herangezogene Institutionen vollständig angegeben habe und die den benutzten Werken entnommenen Stellen als solche kenntlich gemacht habe.

Die vorgelegte Dissertation wurde nicht schon als Diplom- oder ähnliche Prüfungsarbeit verwendet.

Hannover, im Dezember 2008

Julia-Maria Martynczuk

(Unterschrift)

Name: Julia-Maria Martynczuk